REPUBLIQUE ALGERIENNE DEMOCRATIQUE ET POPULAIRE
MINISTERE DE L'ENSEIGNEMENT SUPERIEUR ET DE LA RECHERCHE SCIENTIFIQUE
UNIVERSITE DE MEDEA



FACULTE DE TECHNOLOGIE

THESE DE DOCTORAT

Présentée en vue de l'obtention du diplôme de

Docteur en : Automatique

Specialité : Automatique et Systèmes

Présentée par : HADJ MIHOUB SIDI MOUSSA Fayçal

Thème

Développement des Systèmes Dédiés a l'Intégration des Sources d'Energie Renouvelable au Réseau Electrique

Présentée devant le jury composé de :

Nom & Prénom	Grade	Institution d'affiliation	Designation
HENINI Noureddine	Professeur	University de Médéa	President
MORSLI Abdelkader	MCA	University de Médéa	Directeur de thèse
TLEMÇANI Abdelhalim	Professeur	University de Médéa	Co- Directeur de thèse
BENTOUATI Smain	MCA	University de Médéa	Examinateur 1
HOUASSINE Hamza	Professeur	University de Bouira	Examinateur 2

Année académique : 2025/2026

PEOPLE'S DEMOCRATIC REPUBLIC OF ALGERIA
MINISTRY OF HIGHER EDUCATION AND SCIENTIFIC RESEARCH
UNIVERSITY YAHIA FARES OF MEDEA



FACULTY OF TECHNOLOGY

THESIS

To obtain the degree of

DOCTOR in : Automatic

Speciality : Automation and Systems

Presented by : HADJ MIHOUB SIDI MOUSSA Fayçal

Thesis title

Development of Systems Dedicated to the Integration of Renewable Energy Sources into the Electrical Grid

Defended in front of a jury composed of :

Last and first name	Grade	Institution of affiliation	Designation
HENINI Noureddine	Professor	University of Medea	President
MORSLI Abdelkader	MCA	University of Medea	Supervisor
TLEMÇANI Abdelhalim	Professor	University of Bouira	Co-supervisor
BENTOUATI Smain	MCA	University of Medea	Examiner 1
HOUASSINE Hamza	Professor	University of Medea	Examiner 2

Academic year : 2025/2026

Dedication

To my beloved **wife Kawther**,
Whose love, patience, and unwavering support have been my greatest strength. You stood beside me through every challenge, and your encouragement made this journey possible.

To my precious **daughter Eline** and my dear **son Mohamed**,
You are my greatest source of inspiration and joy. May this work one day encourage you to dream big and persevere.

To my wonderful **mother** and **father**,
For their sacrifices, prayers, and endless support. I owe everything to your love and guidance.

To my dear **sisters, Soraya and Lilia**,
For always believing in me and cheering me on with love and kindness.

To my brother **Abd Raouf**,
Your presence and encouragement have meant more than words can express.

To my respected **father-in-law** and **mother-in-law**,
Thank you for your kindness, prayers, and sincere support throughout my academic journey.

To my **friends**,
Thank you for your support, companionship, and understanding along the way.

This thesis is dedicated to all of you, with love, respect, and deep gratitude.

Acknowledgements

First and foremost, I thank الله سبحانه وتعالى for granting me the strength, patience, and perseverance to complete this doctoral journey.

I would like to express my deepest gratitude to my thesis director, Dr. Morsli Abdelkader, for his invaluable guidance, support, and trust throughout this research. His insightful supervision and encouragement were instrumental in the completion of this work.

I also extend my sincere thanks to my co-director, Professor Tlemcani Abdelhalim, for his expertise, availability, and constructive advice, which enriched this thesis significantly.

My appreciation goes to Pr. Kabeche Nadir, Director of the Laboratory of Research in Electrotechnics and Automation (LREA), for providing a stimulating research environment and the necessary support for this work.

I am equally thankful to the members of the thesis committee for their time, careful evaluation, and valuable recommendations, which have helped improve the quality of this work.

I would also like to thank all the professors, researchers, and staff of the Department of Electrical Engineering at Yahia Fares University of Medea for their support and the academic foundation they provided during my studies.

To my colleagues and friends from the laboratory and beyond, thank you for your collaboration, encouragement, and shared moments throughout this research journey.

الملخص

تهدف هذه الأطروحة إلى تصميم ونمذجة وتطوير أنظمة مخصصة لدمج مصادر الطاقة المتجددة، وعلى وجه الخصوص الطاقة الشمسية الكهروضوئية وطاقة الرياح، في الشبكة الكهربائية. مع الاعتماد المتزايد عالمياً على الطاقة النظيفة، ظهرت تحديات تقنية كبيرة نتيجة الطبيعة المتقطعة واللامركزية لهذه المصادر، وخاصة فيما يتعلق باستقرار الشبكة وجودة الطاقة وتزامن الربط مع الشبكة.

ولمعالجة هذه التحديات، تقترح هذه الدراسة استراتيجيات تحكم متقدمة وهياكل أنظمة فعالة تضمن تحويل الطاقة بشكل موثوق وكفء. تتضمن الدراسة نمذجة مفصلة للأنظمة الشمسية والرياحية، وتطبيق خوارزميات التتبع الأقصى لنقطة القدرة (MPPT)، وتصميم محولات متعددة المستويات لأنظمة ذات مرحلة واحدة أو هجينة. كما يتم التركيز على تقنيات تزامن الشبكة مثل التحكم بالإطار المرجعي المتزامن (SRF) وخوارزمية القفل الطوري باستخدام المرشح المزدوج من الرتبة الثانية (DSOGI-PLL).

تم تنفيذ محاكاة باستخدام برنامج MATLAB/Simulink للتحقق من أداء النظام تحت ظروف بيئية وشبكية متغيرة. أظهرت النتائج فعالية في تنظيم الجهد والتردد، وتقليل التشوه التوافقي الكلي(THD) ، وتحقيق توازن ديناميكي في القدرة، مما يؤكد موثوقية الحلول المقترحة.

تُعد هذه الأطروحة مساهمة في تطوير أنظمة ذكية وقابلة للتوسع لدمج الطاقة المتجددة، بما يتماشى مع متطلبات الشبكات الذكية وأهداف الاستدامة. كما تُوفر أساسًا عمليًا لتطوير أنظمة كهربائية مستقبلية تعتمد على الطاقات المتجددة مع إمكانية دمج أنظمة التخزين وإدارة الطاقة.

الكلمات المفتاحية : دمج مصادر الطاقة المتجددة ، أنظمة الطاقة الشمسية الكهروضوئية ، تحويل طاقة الرياح ، التحكم بنقطة التشغيل القصوى(MPPT) ، محولات مرتبطة بالشبكة ، جودة الطاقة.

Abstract

This thesis focuses on the design, modeling, and development of systems dedicated to the integration of renewable energy sources, primarily photovoltaic (PV) and wind energy, into the electrical grid. The growing global reliance on clean energy has brought significant attention to the technical challenges posed by the intermittent and decentralized nature of renewable sources, especially in terms of grid stability, power quality, and synchronization.

To address these issues, the research proposes advanced control strategies and system architectures that ensure reliable and efficient energy conversion and delivery. The study includes detailed modeling of PV and wind subsystems, the implementation of maximum power point tracking (MPPT) algorithms, and the design of multi-level inverter topologies for single-stage and hybrid configurations. Emphasis is placed on grid synchronization through advanced techniques such as the Synchronous Reference Frame (SRF) control and the Dual Second Order Generalized Integrator Phase-Locked Loop (DSOGI-PLL).

Simulations are carried out using MATLAB/Simulink to validate system performance under varying environmental and grid conditions. The results demonstrate effective voltage and frequency regulation, reduced total harmonic distortion (THD), and dynamic power balancing, confirming the robustness of the proposed solutions.

This work contributes to the development of intelligent and scalable renewable energy integration systems, in line with smart grid requirements and sustainable energy goals. It offers a practical foundation for future renewable-based grid systems, with potential extensions to storage integration and energy management.

Keywords: Renewable Energy Integration, Photovoltaic Systems, Wind Energy Conversion, MPPT Control, Grid-Connected Inverters, Power Quality.

Résumé

Cette thèse porte sur la conception, la modélisation et le développement de systèmes dédiés à l'intégration des sources d'énergie renouvelables, principalement l'énergie photovoltaïque et l'énergie éolienne, au sein du réseau électrique. L'essor mondial des énergies propres a mis en lumière de nombreux défis techniques liés à la nature intermittente et décentralisée de ces sources, notamment en ce qui concerne la stabilité du réseau, la qualité de l'énergie et la synchronisation.

Pour répondre à ces enjeux, cette recherche propose des stratégies de commande avancées et des architectures de conversion énergétique performantes, assurant un transfert d'énergie efficace et fiable. Le travail comprend la modélisation détaillée des sous-systèmes PV et éoliens, la mise en œuvre d'algorithmes de suivi du point de puissance maximale (MPPT), ainsi que la conception de topologies de convertisseurs multi-niveaux pour des configurations à une seule ou plusieurs étapes. Une attention particulière est portée à la synchronisation réseau à l'aide de techniques telles que le contrôle en cadre de référence synchrone (SRF) et le verrouillage de phase basé sur le DSOGI-PLL (Dual Second Order Generalized Integrator - Phase Locked Loop).

Des simulations sous MATLAB/Simulink ont été réalisées afin d'évaluer les performances du système dans diverses conditions environnementales et de réseau. Les résultats obtenus confirment une bonne régulation de la tension et de la fréquence, une réduction notable de la distorsion harmonique totale (THD), et un équilibrage dynamique de la puissance injectée.

Ce travail contribue au développement de systèmes intelligents et évolutifs pour l'intégration des énergies renouvelables, en adéquation avec les exigences des réseaux intelligents et les objectifs de transition énergétique durable. Il offre une base solide pour des extensions futures intégrant le stockage et la gestion énergétique intelligente.

Mots-clés : Intégration des énergies renouvelables, Systèmes photovoltaïques, Conversion de l'énergie éolienne, Commande MPPT, Onduleur connecté au réseau, Qualité de l'énergie.

Table of Contents

General Introduction.....1

Chapter 1 General Information on Grid-Connected Hybrid Systems Based on Photovoltaic and Wind Power

1.1 Introduction.....6
1.2 Renewable Energy Sources.....6
1.2.1 Definition of Renewable Energy Sources.....7
1.2.2 Types of Renewable Energy Sources.....7
1.2.3 CO_2 Emissions from Renewable Energy.....8
1.2.4 Advantages and Disadvantages of Renewable Energy Sources.....9
1.3 Global Renewable Energy Assessment.....9
1.4 Solar Energy.....10
1.4.1 Types of Solar Energy Systems.....11
1.4.2 Definition and Operating Principle of PV Solar.....12
1.4.3 Historical Background.....13
1.4.4 PV panel Technologies types.....14
1.4.5 Advantages and Disadvantages of Photovoltaic Systems.....14
1.4.6 Solar Energy in the World and Algeria.....15
1.5 Wind Energy.....17
1.5.1 Definition and Operating Principle.....18
1.5.2 Historical Background.....18
1.5.3 Aerodynamic Classification and Deployment of Wind Turbines.....19
1.5.4 Wind Generator Technologies.....21
1.5.5 Comparative characteristics of Wind Generator Technologies.....22
1.5.6 Advantages and Disadvantages of Wind Systems.....22
1.5.7 Wind Energy in the World and Algeria.....23
1.6 Hybrid Renewable Energy Systems.....25
1.6.1 Definition of Hybrid Renewable Energy Systems.....25
1.6.2 Classification of Hybrid Systems.....25
1.6.3 Optimization Criteria for HRES.....26
1.6.4 Advantages of Hybrid Systems.....27
1.6.5 Challenges in Hybrid System Design.....27
1.7 Grid-Connected Hybrid Renewable Energy Systems.....27
1.7.1 Architectures.....27
1.7.2 Power Electronic Interfaces.....28

1.7.3 Control Strategies 28
1.7.4 Modeling and Simulation 28
1.8 Economic and Ecological Benefits of Renewable Hybrid Systems 28
1.9 Challenges and Future Trends 31
1.10 Conclusion....31
Chapter 2 Design and Modeling of Grid-Connected Photovoltaic Systems
2.1 Introduction....32
2.2 Photovoltaic System Components and Operation 33
2.2.1 PV Cell and Array Modeling....33
2.2.2 Electrical Characteristics of PV Modules....37
2.2.3 PV System Operating Conditions....39
2.2.4 Balance of System (BoS) Components 39
2.3 Power Conversion Architectures 43
2.3.1 Single-Stage and Two-Stage Architectures....43
2.3.2 DC-DC Converter Types....45
2.3.3 Inverter Topologies....47
2.3.4 Filtering and Grid Interfacing....51
2.3.5 Emerging Architectures....54
2.4 Maximum Power Point Tracking Techniques 54
2.4.1 Conventional MPPT Methods 55
2.4.2 Intelligent MPPT Techniques....57
2.4.3 Metaheuristic Optimization Techniques....59
2.5 Control Strategies for Grid Integration....62
2.5.1 Synchronous Reference Frame Control....63
2.5.2 Direct Power Control....64
2.5.3 dq Current Control (Vector Current Control)....64
2.5.4 Repetitive and Predictive Control Methods 65
2.6 PLL Methods for Grid Synchronization 65
2.6.1 Synchronous Reference Frame PLL (SRF-PLL) 66
2.6.2 Dual second-order generalized integrator PLL (DSOGI-PLL)....66
2.7 Case Study: Simulated Design of a 100kW Two-Stage Grid-Connected PV system 68
2.7.1 System Overview....68
2.7.2 System Design....68
2.7.3 Simulation Parameters....70
2.8 Case Study: Modeling and Simulation of a 100kW Single-Stage Grid-Connected PV System 70

2.8.1 System Overview....70
2.8.2 System Design....71
2.8.3 Simulation Parameters....72
2.9 Comparative Study Between Single-Stage and Two-Stage PV Systems....73
2.9.1 Topological Architecture and PV Array Configuration....73
2.9.2 Control Strategy and MPPT Integration....74
2.9.3 Simulation Results and Performance Comparison....74
2.9.4 Comparative Summary of Inverter Topologies....78
2.10 Conclusion....78
Chapter 3 Design and Modeling of Grid-Connected Wind Conversion Systems
3.1 Introduction....80
3.2 Wind Energy Principles and System Components....80
3.2.1 Wind Energy Conversion Principle....81
3.2.2 Aerodynamic Model of Wind Turbine....81
3.2.3 Mechanical Drive Train Modeling....82
3.2.4 Analytical Model of the Power Coefficient....83
3.3 Types of Wind Turbine Systems....84
3.3.1 Constant-Speed Wind Turbine System....84
3.3.2 Variable-speed wind turbine system....85
3.4 Wind Turbine Control Techniques....85
3.4.1 Wind Turbine Power Characteristics....86
3.4.2 Control in region I (Power Optimization)....86
3.4.3 Indirect Reference Speed Control....87
3.4.4 Control in Region III (Power Limitation)....88
3.5 Generator Constitution and Modeling for WECS....89
3.5.1 Permanent Magnet Synchronous Generator....90
3.5.2 Doubly-Fed Induction Generator....93
3.6 Grid-connected Wind Energy System Topologies based on PMSG and DFIG....96
3.6.1 PMSG-based Grid-Connected Wind Energy System Topologies....96
3.6.2 DFIG-Based Grid-Connected Wind Energy System Topologies....99
3.7 Control Strategies for Wind Energy Systems....100
3.7.1 Rotor Side Control of DFIG-based Wind Energy Systems....100
3.7.2 Control Strategies for PMSG-Based Wind Energy Systems....101
3.7.3 Grid-Side Converter Control for DFIG and PMSG....102
3.7.4 Advanced Control Techniques for Wind Energy Systems....103

3.8 Modeling of Grid-Connected Wind Energy System....103
3.8.1 Description of the Grid-Connected Wind Energy System....103
3.8.2 Direct Power Control of the Three-Phase Rectifier....104
3.8.3 DC-Link Capacitance Design....106
3.8.4 LCL Filter Design....107
3.9 Simulation Results of Grid-Connected Wind Energy System....109
3.9.1 DC-Link Voltage Regulation Performance....110
3.9.2 DSOGI-PLL Synchronization Performance....110
3.9.3 LCL Filter Frequency Response Analysis....111
3.9.4 Active and Reactive Power Exchange with the Grid and Efficiency....112
3.9.5 Grid Current Quality and Harmonic Distortion....112
3.10 Simulation Results Discussion....113
3.11 Conclusion....113
Chapter 4 Design and Control of a Grid-Connected Hybrid PV–Wind System Based on a DFIG
4.1 Introduction....115
4.2 System Description and Operating Principle....116
4.3 Description and Operating Characteristics of the PV Array Subsystem....117
4.4 Description and Operating Characteristics of the Wind Generator Subsystem....118
4.5 Description of the Back-to-Back Converter Part....119
4.5.1 Rotor-Side Converter Control....120
4.5.2 DC-Link and Energy Coupling....121
4.5.3 Grid-Side Converter Control....121
4.5.4 Role of the RL Filter....122
4.6 Steady-State Analysis of the DFIG....122
4.7 Simulation Scenarios and Parameter Definition....124
4.8 Mechanical Dynamic Response of the DFIG....125
4.9 Electrical Performance Analysis of the Hybrid PV–Wind System....126
4.9.1 PV Subsystem Performance....126
4.9.2 DC-link Voltage Behavior....128
4.9.3 Power Output and Efficiency....129
4.9.4 Power Quality and Harmonic Analysis....131
4.9.5 Voltage and frequency stability....133
4.10 Discussion of Results....134
4.11 Limitations of the proposed system....135
4.12 Conclusion....136

General Conclusion 138
Perspectives of Future Work 140
Annex I
Annex II
Annex III
Bibliography

List of abbreviations and acronyms

Abbreviation	Full Term
AC	Alternating Current
BoS	Balance of System
CHB	Cascaded H-Bridge
CPV	Concentrated Photovoltaic
CSP	Concentrated Solar Power
DC	Direct Current
DFIG	Doubly-Fed Induction Generator
DNI	Direct Normal Irradiance
DPC	Direct Power Control
DSP	Digital Signal Processor
DSOGI-PLL	Dual Second-Order Generalized Integrator Phase-Locked Loop
DTC	Direct Torque Control
EMI	Electromagnetic Interference
FCMI	Flying Capacitor Multilevel Inverter
FPGA	Field-Programmable Gate Array
GSC	Grid-Side Converter
GWO	Grey Wolf Optimization
HAWTs	Horizontal-Axis Wind Turbines
HCS/P&O	Hill Climb Search / Perturb and Observe
HRES	Hybrid Renewable Energy Systems
IGBTs	Insulated Gate Bipolar Transistors
INC	Incremental Conductance
IP	Ingress Protection
IPCC	Intergovernmental Panel on Climate Change
IoT	Internet of Things
IRENA	International Renewable Energy Agency
LCOE	Levelized Cost of Energy
MOSFETs	Metal-Oxide-Semiconductor Field-Effect Transistors
MPP	Maximum Power Point
MPPT	Maximum Power Point Tracking
MPC	Model Predictive Control
OTC	Optimal Torque Control
P&O	Perturb and Observe
PCC	Point of Common Coupling
PLL	Phase-Locked Loop
PSF	Power Signal Feedback
PSO	Particle Swarm Optimization
PV	Photovoltaic

Abbreviation	Full Term
PWM	Pulse Width Modulation
RC	Repetitive Control
RSC	Rotor-Side Converter
SCIG	Squirrel Cage Induction Generator
SOGI	Second-Order Generalized Integrator
SPDs	Surge Protection Devices
SRF	Synchronous Reference Frame
STC	Standard Test Conditions
THD	Total Harmonic Distortion
TSR	Tip-Speed Ratio
VAWTs	Vertical-Axis Wind Turbines
VSI	Voltage-Source Inverter
WECS	Wind Energy Conversion System
WRSG	Wound Rotor Synchronous Generator

List of symbols and units of measurement

Symbol	Description	Unit
A	Swept area of turbine blades	m^2
β	Blade pitch angle	°
C_{dc}	DC-link capacitance	μF, mF
C_f	Filter capacitance	μF
C_i	Split DC-link capacitor	μF
C_r	Rectifier DC bus capacitor	μF
$C_p(\lambda)$	Power coefficient of a wind turbine	—
E_g	Semiconductor energy band gap	eV
f	Electrical grid frequency	Hz
f_{sw}	Switching frequency	Hz, kHz
F	Friction coefficient	$N{\cdot}m{\cdot}s/rad$
G	Gearbox ratio	—
I_0	Reverse saturation current of a diode	A
I_d	Junction (diode) current	A
I_{dq}	Line current in the dq reference frame	A
I_{dq_ref}	Reference current in the dq frame	A
I_m	Current amplitude	A
I_{ph}	Photocurrent	A
I_{pv}	Photovoltaic current	A
I_{sc}	Short-circuit current	A
J	Moment of inertia	$kg{\cdot}m^2$
K	Boltzmann constant	J/K
K_I	Integral gain of the PI controller	—
K_P	Proportional gain of PI controller	—
K_P^{dc}	DC voltage loop proportional gain	—
K_I^{dc}	DC voltage loop integral gain	—
K_P^{PLL}	PLL proportional gain	—
K_I^{PLL}	PLL integral gain	—
L	Line or interfacing inductance	H
L_d	d-axis stator inductance	mH
L_q	q-axis stator inductance	mH
L_f	Filter inductance	μH
L_g	Grid-side inductance	μH
L_i	Inverter-side inductance	μH
L_m	Magnetizing inductance	mH
$L_{\sigma s}$	Stator leakage inductance	mH
$L_{\sigma r}$	Rotor leakage inductance	mH

Symbol	Description	Unit
m	Meter (length)	m
m^2	Area	m^2
m^3	Volume	m^3
mF	Millifarad	mF
mH	Millihenry	mH
N_n	Synchronous speed	rpm
p	Number of pole pairs	—
P_{mpp}	Maximum power at MPP	W, kW
P_n	Nominal power	MW
P_r	Rated DC bus power	MW
P_W	Wind turbine active power	W
q	Electron charge	C
R	Line resistance	Ω
r	Wind turbine blade radius	m
R_d	Damping resistor	Ω
R_f	Filter resistance	Ω
R_r	Rotor resistance	$m\Omega$
R_s	Stator resistance	$m\Omega$
s	Second (time unit)	s
S	Slip of the Doubly-Fed Induction Generator	—
Sn	Rated apparent power	kVA
T	Wind turbine torque	$N{\cdot}m$
T_c	PV cell temperature	$°C$
V	Electric voltage	V
V_o	Open-circuit voltage	V
V_{abc}	Three-phase grid voltage	V
V_{dc}	DC bus voltage	V
ΔV_{dc}	DC voltage ripple	V
V_{dc_ref}	Reference DC bus voltage	V
V_m	Voltage amplitude	V
V_{pv}	PV output voltage	V
V_{rms}	Root mean square voltage	V
V_w	Wind speed	m/s
v_{cdq}	Converter voltage in the dq reference frame	V
λ	Tip-speed ratio	—
ψ_f	Permanent magnet flux linkage	$V{\cdot}s$
ρ	Air density	kg/m^3
ΔV_{dc_ref}	DC voltage step size (INC MPPT)	—

Physical Constants

Symbol	Description	Unit	Value
e	Electron charge	C	1.602×10^{-19}
K	Boltzmann constant	J/K	1.381×10^{-23}
ρ_{air}	Air density at STC	kg/m³	1.225

Figures list

Figure 1-1 Different types of renewable energy. 7

Figure 1-2 Carbon Intensity of Electricity Generation by Source (in gCO_2e/kWh, life-cycle average). 8

Figure 1-3 Global renewable electricity capacity, 2010-2023. 10

Figure 1-4 Photovoltaic fields. 11

Figure 1-5 Concentrated solar power plant. 12

Figure 1-6 Solar thermal collectors. 12

Figure 1-7 The principle of operation of the PV cell. 13

Figure 1-8 Models of solar modules based on silicon cell type. 14

Figure 1-9 Average Annual Sunshine Hours (Direct Normal Irradiance > *360W/m²*) 2015–2025. 16

Figure 1-10 Solar PV deployment in 2023: New installations and cumulative capacity in the top 10 countries and worldwide. 16

Figure 1-11 Traditional windmills and modern wind Turbines. 18

Figure 1-12 Horizontal and vertical axis wind turbine. 20

Figure 1-13 Onshore and offshore wind turbines. 20

Figure 1-14 Mean wind speed estimates at *100m*, every *6* hours from *01-01-2007* to *31-12-2016*, at a *0,75°×0,75°* precision. 24

Figure 1-15 Wind power deployment in 2023: New installations and cumulative capacity in the top 10 countries and worldwide. 24

Figure 1-16 Diagram of AC- and DC-coupling topologies for integrating wind, solar, and battery systems. 27

Figure 1-17 Global energy transition investment from 2020 to 2024. 29

Figure 1-18 Evolution of global renewable energy employment by technology from 2012 to 2023. 29

Figure 1-19 Increase in primary energy consumption from *1998* to *2018*, with projections to *2040*. 30

Figure 2-1 Equivalent circuit for PV cell based on one-diode model. 34

Figure 2-2 Equivalent circuit for PV cell based on two-diode model. 35

Figure 2-3 I-V and P-V characteristic curves of a PV module. 37

Figure 2-4 I–V and P–V characteristics of a PV module under varying irradiance conditions. 37

Figure 2-5 I–V and P–V characteristics of a PV module under varying temperature conditions. 38

Figure 2-6 I-V and P-V characteristics of a PV array under partial shading, showing multiple MPPs.....38
Figure 2-7 Configuration of bypass and blocking diodes in a PV array. 40
Figure 2-8 Mounting systems for PV panels. 41
Figure 2-9 DC Cabling and junction boxes. 41
Figure 2-10 Basic schematic of a grid-connected PV system with an inverter. 42
Figure 2-11 Surge protection device symbol. 43
Figure 2-12 Block diagram of a single-stage grid-connected PV system. 44
Figure 2-13 Block diagram of a two-stage PV grid-connected system. 44
Figure 2-14 Equivalent circuit of a boost DC-DC converter. 45
Figure 2-15 Equivalent circuit of a buck DC-DC converter. 46
Figure 2-16 Equivalent circuit of a buck-boost DC-DC converter. 47
Figure 2-17 Two-level inverter power circuit. 48
Figure 2-18 Three-level NPC inverter power circuit. 49
Figure 2-19 T-Type three-level inverter power circuit. 49
Figure 2-20 Flying Capacitor Three-level Inverter power circuit. 50
Figure 2-21 Cascaded H-Bridge inverter power circuit. 50
Figure 2-22 LCL filter configuration for grid-connected PV inverter systems. 52
Figure 2-23 Configuration of a shunt active filter connected to the grid. 53
Figure 2-24 Flowchart of the P&O MPPT algorithm. 55
Figure 2-25 Flowchart of the INC MPPT algorithm. 56
Figure 2-26 Conceptual diagram of the CV MPPT method. 57
Figure 2-27 Control block diagram of the PI-based MPPT method. 57
Figure 2-28 Block diagram of FLC. 58
Figure 2-29 Structure of an ANN-based MPPT system. 58
Figure 2-30 Flowchart of the PSO-based MPPT. 60
Figure 2-31 Flowchart of the GWO-based MPPT algorithm. 62
Figure 2-32 Block diagram of the SRF-PLL. 66
Figure 2-33 Block diagram of the DSOGI-PLL. 67
Figure 2-34 Block diagram of a two-stage grid-connected inverter for a PV system. 68
Figure 2-35 I-V and P-V curve characteristics of PV array at 25°C for two-stage inverter. 69
Figure 2-36 Block diagram of SRF-dq control. 70

Figure 2-37 Block diagram of a single-stage grid-connected inverter for a PV system.....71
Figure 2-38 I-V and P-V curve characteristics of PV array at *25°C* for single-stage inverter. 71
Figure 2-39 Block diagram of SRF-INC control. 72
Figure 2-40 DC bus voltage (Single-stage and Two-stage).....75
Figure 2-41 Inverter line outputs voltage: (a) single-stage, (b) two-stage. 75
Figure 2-42 Three-Phase Grid Voltage (Phase-to-phase). 76
Figure 2-43 Inverter outputs line current: (a) single-stage, (b) two-stage. 76
Figure 2-44 Line currents THD: (a) single-stage, (b) two-stage. 77
Figure 2-45 Exchanged Active Power – Single-Stage Inverter. 77
Figure 2-46 Exchanged Active Power – Two-Stage Inverter. 78
Figure 3-1 Main components of the wind turbine. 82
Figure 3-2 Block diagram of the turbine model. 83
Figure 3-3 Power coefficient C_p curves for different pitch blade angles β. 84
Figure 3-4 Schematic diagram for fixed-speed wind turbine system. 85
Figure 3-5 Schematic diagram for variable-speed wind turbine system. 85
Figure 3-6 Power characteristic of the wind turbine and operating regions. 86
Figure 3-7 Block diagram of indirect reference speed control for MPPT. 88
Figure 3-8 Block diagram of the blade pitch actuator. 89
Figure 3-9 Block diagram of the pitch control regulation system. 89
Figure 3-10 Physical constitution of a PMSG 90
Figure 3-11 Equivalent circuit of the PMSG in the d-q reference frame 91
Figure 3-12 Block diagram of the DFIG dynamic simulation model.....96
Figure 3-13 Grid-connected wind energy conversion system based on a PMSG with a diode rectifier and voltage source inverter. 97
Figure 3-14 Grid-connected PMSG-based wind energy system employing a diode rectifier and DC–DC boost converter for DC-link voltage regulation.....97
Figure 3-15 Grid-connected wind energy conversion system using a PMSG with controlled PWM rectifier and grid-side inverter.....98
Figure 3-16 PMSG-based wind energy conversion system with full-scale back-to-back power converter for grid integration.....98
Figure 3-17 Conventional grid-connected DFIG-based wind energy system with partial-scale back-to-back rotor-side converter.....99
Figure 3-18 DFIG-based wind energy conversion system with direct AC-AC rotor converter and grid-connected stator. 100

Figure 3-19 Configuration of the grid-connected PMSG-based wind energy system.....103
Figure 3-20 The division of the αβ plane into sectors. 106
Figure 3-21 Variable wind speed profile. 110
Figure 3-22 DC-link voltage response. 110
Figure 3-23 Estimated grid frequency using DSOGI-PLL. 111
Figure 3-24 Bode diagram of the LCL filter transfer function. 111
Figure 3-25 Active and reactive powers injected into the grid. 112
Figure 3-26 Current injected into the grid waveforms. 112
Figure 4-1 Block diagram of grid-connected PV/DFIG hybrid system. 117
Figure 4-2 Block diagram of method controls for back-to-back converter. 119
Figure 4-3 Steady-state magnitudes as a function of rotation speed: (a) Slip, (b) electromagnetic torque, (c) stator active power, and (d) rotor active power. 123
Figure 4-4 Electromagnetic torque. 125
Figure 4-5 Mechanical rotational speed at the rotor. 125
Figure 4-6 PV current. 127
Figure 4-7 PV power injected into the DC bus. 128
Figure 4-8 DC bus voltage. 128
Figure 4-9 DFIG slip. 129
Figure 4-10 Stator power injected into the grid. 130
Figure 4-11 GSC power injected into the grid. 131
Figure 4-12 GSC reactive power injected into the grid. 131
Figure 4-13 GSC output line current. 132
Figure 4-14 THD of GSC output currents. 132
Figure 4-15 Three-phase grid voltage (phase-to-phase). 133

Tables list

Table 1-1 PV Projects in Algeria. 17

Table 1-2 Comparative characteristics of wind generator technologies. 22

Table 2-1 Comparison of PV cells models. 36

Table 2-5 Performance comparison summary 78

Table 3-1 Switching table. 106

Table 2-2 Electrical Characteristics of the Kyocera KD205GX-LP Module (STC). I

Table 2-3 Simulation parameters of the two-stage inverter. I

Table 2-4 Simulation parameters of single-stage inverter. I

Table 3-2 Simultion parameters of wind system II

Table 4-1 DFIG parameters. III

Table 4-2 Simulation parameters of the hybrid PV–wind grid-connected system. III

General Introduction

The 21st century is witnessing a paradigm shift in global energy systems, driven by growing environmental concerns, technological innovation, and the rising demand for sustainable development. Fossil fuels, which have long served as the backbone of industrial progress and economic expansion, are now under scrutiny due to their finite nature and detrimental impact on the environment. The increased emission of greenhouse gases such as carbon dioxide (CO_2), resulting from the combustion of coal, oil, and natural gas, has significantly contributed to climate change, global warming, and ecological degradation. As a result, the need for transitioning toward cleaner and more sustainable energy sources has become both urgent and indispensable for ensuring a secure energy future [23][57][88][90].

Among the most promising alternatives are renewable energy sources (RES), particularly solar and wind power, which are abundant, naturally replenished, and environmentally friendly [23]. These resources offer an effective means to diversify the energy mix, reduce carbon emissions, and achieve national energy independence. Over the last decade, the global deployment of photovoltaic (PV) and wind energy systems has accelerated, supported by advances in materials, manufacturing processes, and energy conversion technologies. Additionally, global policy initiatives such as the Paris Climate Agreement have played a pivotal role in setting decarbonization goals, prompting countries to invest heavily in clean energy infrastructure and integrate renewable resources into their electricity grids.

However, the integration of renewable energy into traditional power systems presents a complex set of challenges. Solar and wind resources are inherently intermittent and unpredictable, leading to fluctuations in power generation that can compromise grid stability. Conventional electric grids, originally designed for centralized, dispatchable energy sources, are ill-equipped to manage the variability associated with decentralized RES. Furthermore, technical issues such as voltage instability, harmonic distortion, and frequency deviations arise when RES penetration increases. These issues necessitate the development of robust control mechanisms, efficient power electronic interfaces, and intelligent energy management systems to ensure compatibility, reliability, and grid compliance [11][16].

In this context, hybrid renewable energy systems (HRES) that combine multiple sources, most notably PV and wind, have gained significant attention. These systems offer enhanced reliability and efficiency by mitigating the shortcomings of individual sources. For instance, solar energy is typically abundant during the daytime, while wind energy is often more available during the night or on cloudy days. Combining these complementary profiles results in a more balanced power output. The use of hybrid systems, equipped with appropriate control strategies and power electronics, can thus facilitate the stable and seamless integration of RES into the electric grid. This thesis explores the modeling, control, and simulation of a PV-wind hybrid energy system interconnected to the utility grid.

The growing demand for energy, especially in emerging economies, underscores the necessity of developing systems that not only provide reliable electricity but also align with global sustainability objectives. In regions like North Africa and the Middle East, where solar irradiation levels are among the highest globally, and wind patterns are favorable, hybrid RES offer a strategic solution to energy challenges. Algeria, for instance, has launched ambitious

national programs to promote renewable energy and reduce dependency on fossil fuels. These programs aim to harness the country's vast renewable potential to achieve energy security, promote rural electrification, and reduce environmental pollution. The design and deployment of hybrid systems that integrate PV and wind energy are, therefore, not only technically viable but also socioeconomically beneficial.

From an economic perspective, global investments in renewable energy technologies continue to grow steadily. According to the "Energy Transition Investment Trends *2025"* report, global spending on clean energy technologies reached nearly *$2* trillion in 2024, with more than *60%* directed toward renewable power generation, grid modernization, and electrification. The economic appeal of hybrid systems lies in their ability to reduce long-term operational costs, hedge against fossil fuel price volatility, and create new jobs in system design, installation, and maintenance. Furthermore, as technology costs decline and supportive policy frameworks are implemented, hybrid renewable energy systems are expected to deliver increasingly favorable returns on investment (ROI), especially in regions with high renewable resource potential [56][86][88].

On the ecological front, hybrid systems play a vital role in reducing greenhouse gas emissions and improving local environmental conditions. By replacing diesel generators or fossil-fuel-based power plants, these systems contribute to cleaner air, reduced noise pollution, and lower carbon intensity in power generation. Lifecycle assessments of PV and wind systems demonstrate significantly lower CO_2 emissions per kilowatt-hour compared to conventional sources. Additionally, decentralized deployment of hybrid systems can minimize land degradation and transmission losses, especially when integrated as part of microgrids or community-scale installations [56].

Hybrid systems bring additional advantages beyond resource complementarity. They reduce the dependence on expensive and space-consuming energy storage systems, improve load-following capabilities, and enhance the overall efficiency of energy conversion. Moreover, in grid-connected scenarios, hybrid systems can provide ancillary services such as reactive power support, voltage regulation, and peak shaving. Nevertheless, the effectiveness of hybrid systems is contingent upon the design of intelligent control frameworks and advanced power electronics that can respond dynamically to changes in environmental conditions and load demands.

A crucial component of hybrid systems is the power electronic interface, which manages the conversion and regulation of power from various sources before delivering it to the grid. Among the various topologies available, multi-level inverters, such as the Neutral Point Clamped (NPC) inverter, are particularly advantageous due to their ability to produce high-quality output waveforms with reduced harmonic distortion. The three-level NPC inverter, used in this thesis, enables efficient power delivery with improved voltage control, lower switching losses, and better thermal performance. When combined with advanced filtering techniques like LCL filters, these inverters significantly enhance power quality and grid compliance.

Control strategies also play a pivotal role in ensuring the stable and optimal operation of hybrid energy systems. Maximum Power Point Tracking (MPPT) algorithms are essential for extracting the maximum possible energy from the PV array and wind turbine under varying environmental conditions. In this thesis, a wide range of MPPT strategies is investigated. These include conventional techniques such as Perturb and Observe (P&O), Incremental Conductance (INC), and Proportional-Integral (PI) control. In parallel, intelligent and metaheuristic approaches such as Fuzzy Logic Control (FLC), Particle Swarm Optimization (PSO), Grey Wolf Optimizer (GWO), Hybrid Simulated Optimization (HSO), and co-cooperative research-inspired algorithms are explored. These advanced techniques enable the system to dynamically optimize performance, achieve faster convergence, and adapt to complex environmental variations with high tracking accuracy.

The wind energy subsystem in this study is developed in two configurations to assess comparative performance: one employing a Permanent Magnet Synchronous Generator (PMSG), and another utilizing a Doubly-Fed Induction Generator (DFIG). Each generator is integrated using appropriate converter topologies. For the PMSG system, a full-scale back-to-back converter comprising a rectifier and an inverter is used to regulate power flow and implement control strategies. For the DFIG system, a partially-rated back-to-back converter controls the rotor side, enabling efficient variable-speed operation and flexible reactive power support. These configurations allow the evaluation of trade-offs in cost, complexity, and control flexibility.

The organization of the thesis reflects the evolving complexity of grid-connected hybrid renewable energy systems. Chapter 1 introduces general information on hybrid systems that combine photovoltaic and wind energy, highlighting their benefits, challenges, and deployment trends. Chapter 2 focuses on the design and modeling of grid-connected photovoltaic systems, covering single-stage and two-stage inverter architectures, various DC-DC converter configurations (boost, buck, buck-boost), and MPPT techniques, both classical and intelligent. Chapter 3 presents the design and modeling of wind energy conversion systems, discussing the use of generators such as PMSG and DFIG, and their respective topologies, full-scale and partial-scale back-to-back converters, with control strategies including FOC, DPC, and direct/indirect MPPT. Finally, Chapter 4 analyzes the combined hybrid system topologies, their control techniques, and integration into the grid.

To validate the proposed system architecture, a comprehensive simulation environment is developed using MATLAB/Simulink. The model incorporates real environmental input data such as irradiance and wind speed variations, as well as grid disturbances like voltage sags and harmonic distortions. Various case studies are conducted to evaluate the performance of the hybrid system under dynamic conditions. Key metrics such as output power quality, DC-link voltage stability, Total Harmonic Distortion (THD) of the injected current, and reactive power compensation are analyzed in detail. The simulation results demonstrate the robustness of the system and its ability to maintain compliance with grid standards under fluctuating operating conditions.

The PV subsystem is managed using Incremental Conductance (INC) MPPT due to its precision in rapidly changing irradiance environments. The converter topology and control are selected based on the configuration, boost, buck, or buck-boost, to adapt the voltage to the required DC-link level. On the wind side, the indirect speed control strategy is implemented to optimize energy extraction without requiring mechanical speed sensors. This approach enhances system reliability and reduces maintenance costs. Depending on the generator type, control schemes such as DPC or vector control are applied to regulate power flow and ensure synchronization with the grid.

In addition to technical evaluation, the system's economic feasibility is assessed using key indicators such as Levelized Cost of Energy (LCOE) and return on investment (ROI). These metrics are compared against conventional energy systems to highlight the cost benefits of deploying hybrid RES. The ecological impact is also quantified, showing significant reductions in CO_2 emissions per kWh. These findings reinforce the value of hybrid systems in achieving both environmental and economic sustainability, particularly in resource-rich regions like Algeria.

Another focus of the simulation work is the interoperability of the two subsystems. The hybrid configuration relies on a common DC-link that acts as a power exchange platform between the PV and wind modules and the grid inverter. The control strategy ensures that each subsystem can operate independently or cooperatively, adjusting its output based on availability and demand. For instance, when solar output is low during evening hours, the wind subsystem compensates, thereby enhancing overall system continuity.

Advanced control coordination is essential in this context. The Synchronous Reference Frame (SRF) control is used to manage the inverter, ensuring proper grid synchronization and power injection with minimal harmonic content. The Dual Second Order Generalized Integrator Phase-Locked Loop (DSOGI-PLL) is integrated into the SRF framework to enhance performance under distorted grid conditions. These algorithms work in tandem to ensure compliance with international grid codes and maintain high power quality.

Furthermore, this thesis examines the scalability and adaptability of the proposed system architecture. It is shown that the design can be adjusted for various power levels and site-specific conditions, making it suitable for both rural electrification and urban energy support. By using modular components and standardized control schemes, the system allows for incremental upgrades and easy integration into existing infrastructure.

In the broader context of national energy planning, the outcomes of this thesis align with strategic initiatives for sustainable development and decarbonization. In Algeria, for example, the Renewable Energy and Energy Efficiency Program targets the installation of several gigawatts of renewable capacity by 2035. The hybrid PV-wind system proposed in this work represents a practical solution for achieving these goals, especially in remote or underserved areas. It offers a flexible, scalable, and efficient approach to integrating renewable energy while enhancing grid resilience.

This work also provides a valuable academic contribution by offering a unified approach to hybrid system modeling and control. By combining conventional techniques with intelligent optimization algorithms and by validating them through high-fidelity simulations, this thesis presents a holistic and replicable framework for future research and industrial implementation. It bridges the gap between theoretical development and practical application, paving the way for smarter, greener, and more sustainable energy systems.

Ultimately, this general introduction provides a foundation for the subsequent chapters of the thesis. It outlines the motivations, objectives, and methodological framework, while highlighting the relevance of the research in addressing global and local energy challenges. The following chapters will delve deeper into each subsystem and control strategy, presenting detailed analyses and simulation outcomes to substantiate the proposed system's performance and viability.

Chapter 1 General Information on Grid-Connected Hybrid Systems Based on Photovoltaic and Wind Power

1.1 Introduction

The shift toward clean energy has become a central pillar of energy policy, driven by increasing awareness of environmental issues, finite fossil fuel reserves, and rising global energy demand. Renewable energy sources, particularly solar photovoltaic (PV) and wind, have emerged as leading solutions for clean electricity generation. Their integration into power systems, however, presents challenges due to their intermittency and variability. To address these challenges, hybrid renewable energy systems (HRES) have gained prominence. By combining multiple renewable sources, such as PV and wind, these systems achieve improved reliability, efficiency, and continuity in power delivery.

A HRES integrates two or more energy sources in a complementary manner, allowing each component to compensate for the shortcomings of the others. In the case of PV-wind hybrid systems, solar energy can be harnessed during daylight hours, while wind energy is often more abundant at night or during overcast periods, creating a more continuous and stable energy supply. When connected to the grid, these systems not only supply renewable electricity but also contribute to grid support services, including reactive power compensation, voltage regulation, and frequency stabilization. Their ability to address grid code requirements and support dynamic operating conditions makes them essential for future energy systems.

The deployment of HRES is facilitated by recent advancements in power electronics, control strategies, and system modeling. Power converters enable the efficient transformation and regulation of energy flow from variable DC or AC sources to grid-compatible formats. Meanwhile, intelligent control algorithms manage power balance, optimize energy extraction, and ensure system stability in real time. The adoption of advanced Maximum Power Point Tracking (MPPT) techniques further improves the energy yield from PV modules and wind turbines. Moreover, hybrid systems offer modularity and scalability, allowing them to be implemented in a wide range of applications, from remote microgrids to urban utility-scale power plants.

This chapter provides a comprehensive overview of renewable energy fundamentals, with a particular emphasis on hybrid PV-wind systems. It presents key definitions, classifications, and the environmental implications of renewable energy technologies. The global and regional contexts are explored, including Algeria’s significant potential for solar and wind exploitation. In addition, this chapter introduces the architecture, operating principles, and design considerations of hybrid systems, setting the groundwork for the technical modeling and control strategies presented in the subsequent chapters of this thesis.

1.2 Renewable Energy Sources

This section provides foundational knowledge about renewable energy. It defines renewable sources and classifies the main types, emphasizing solar and wind technologies, which are

central to this thesis. A brief comparison highlights their complementary nature in hybrid systems.

1.2.1 Definition of Renewable Energy Sources

Renewable energy sources are derived from natural processes that are continually replenished on a human timescale. These include sunlight, wind, rainfall, tides, geothermal heat, and biomass. Unlike fossil fuels, which are non-renewable and contribute significantly to greenhouse gas emissions, renewable energy sources offer a clean and inexhaustible alternative for power generation. Renewable energy systems are key to achieving long-term energy sustainability, reducing environmental impact, and minimizing dependence on imported fuels. The global shift toward renewables reflects not only technological progress but also a growing commitment to environmental stewardship and social equity.

1.2.2 Types of Renewable Energy Sources

As illustrated in Figure 1-1, renewable energy encompasses a variety of sources that are naturally replenished and environmentally sustainable. These sources are generally classified into the following categories [5][16][18]:

- Solar Energy: Harnessed using photovoltaic panels or solar thermal systems, solar energy is one of the most widely available and scalable renewable resources.
- Wind Energy: Generated by converting the kinetic energy of wind into mechanical and subsequently electrical energy through wind turbines.
- Hydropower: Utilizes the flow of water from rivers or dams to turn turbines and generate electricity. It remains the largest source of renewable electricity globally.
- Biomass: Refers to organic material, such as agricultural waste, wood, and biofuels, that can be used to produce heat, electricity, or transportation fuels.
- Geothermal Energy: Extracted from the Earth's internal heat, geothermal energy is used for electricity generation and direct heating applications.
- Marine Energy: Includes tidal and wave energy, which exploit the movement of ocean water to generate power.

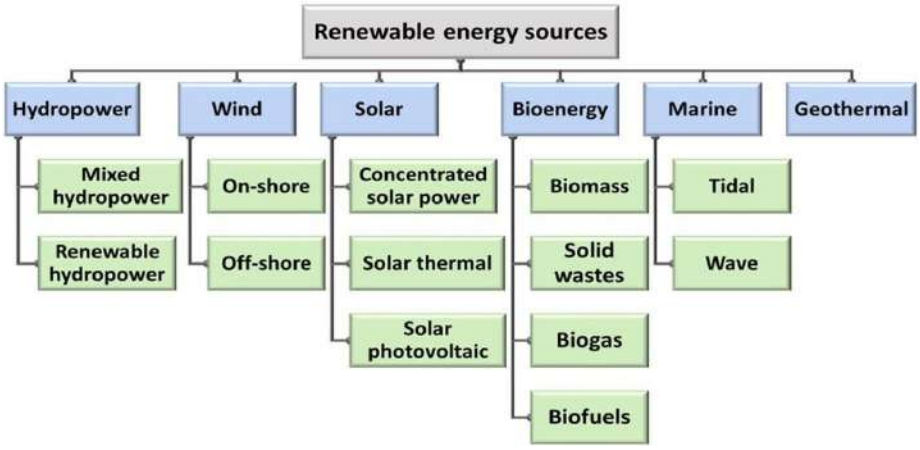


Figure 1-1 Different types of renewable energy.

Among these sources, solar and wind are the most promising for large-scale and distributed generation due to their widespread availability, rapid cost decline, and ease of installation.

1.2.3 CO_2 Emissions from Renewable Energy

One of the most compelling advantages of renewable energy systems lies in their significantly lower contribution to atmospheric carbon dioxide (CO_2) emissions compared to conventional fossil-fuel-based electricity generation. This benefit is particularly critical in the global effort to mitigate climate change and reduce the carbon intensity of the energy sector [57][90].

As illustrated in Figure 1-2, fossil fuels such as coal and oil are the most carbon-intensive sources, emitting approximately *1001gCO_2/kWh* and *840gCO_2/kWh*, respectively, over their full life cycle. Even natural gas, often considered a "bridge fuel," produces around *469gCO_2/kWh*, making it substantially more polluting than any renewable alternative [24].

In stark contrast, renewable energy technologies emit only a fraction of these levels. Solar photovoltaic (PV) systems have life-cycle emissions estimated between *20* and *48gCO_2/kWh*, accounting for the manufacturing of panels, installation, maintenance, and eventual decommissioning. Wind energy performs even better, with emissions typically ranging from *8* to *12gCO_2/kWh*, owing to the minimal operational emissions once turbines are installed [90].

Even among renewables, some variation exists. For instance, geothermal and biomass systems range from *18* to *45gCO_2/kWh*, depending on specific fuel sources and processing methods. Hydropower, ocean, and nuclear energy demonstrate the lowest emissions, with hydro emitting as little as *4gCO_2/kWh*, making it one of the cleanest energy options available [18].

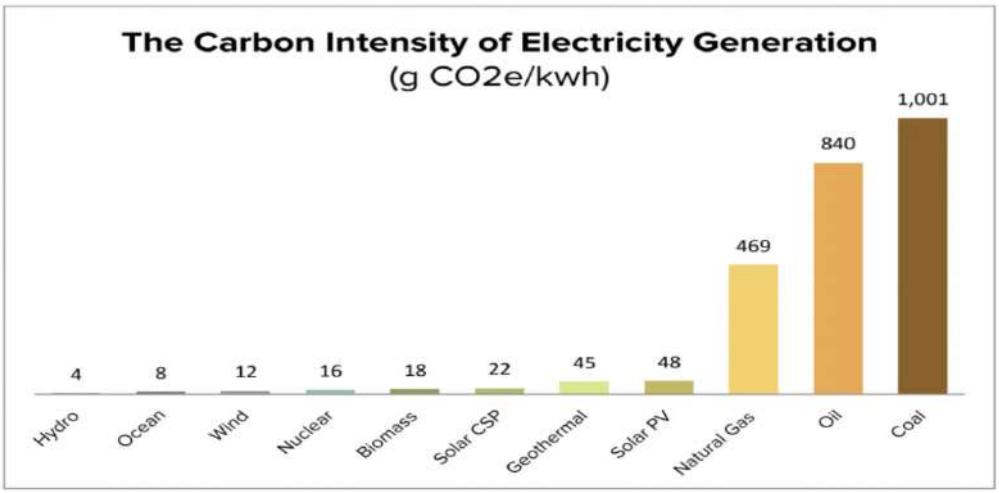


Figure 1-2 Carbon Intensity of Electricity Generation by Source (in gCO_2e/kWh, life-cycle average).

Source: Adapted from IPCC Special Report on Renewable Energy Sources and Climate Change Mitigation.

This figure underscores the urgent need to accelerate the shift toward renewable energy to meet the targets of the Paris Agreement, which aim to limit global temperature rise to well below *2°C* above pre-industrial levels. By integrating low-emission technologies like solar PV

and wind, nations can drastically reduce their carbon footprint, enhance energy sustainability, and improve public health by lowering pollution levels [18][24].

Moreover, the comparative data visually emphasize the climate advantage of renewables. The transition to clean energy is not only an environmental imperative but also an economic and strategic opportunity to modernize national power infrastructures while safeguarding the planet for future generations.

1.2.4 Advantages and Disadvantages of Renewable Energy Sources

Advantages of Renewable Energy Sources [16]*:*

- Environmentally friendly with low greenhouse gas emissions
- Sustainable and inexhaustible energy supply
- Reduced reliance on fossil fuel imports
- Creation of new job opportunities and economic development
- Decentralized energy production for rural and remote areas
- Scalability and flexibility in system design

Disadvantages of Renewable Energy Sources [16]*:*

- Intermittency and variability in energy production
- High initial capital investment for equipment and infrastructure
- Need for energy storage or backup systems
- Technical challenges in grid integration and power quality
- Dependence on site-specific resource availability

Despite these challenges, continuous innovation in materials science, control systems, and energy storage technologies is making renewable energy more reliable and cost-effective. Hybrid systems, in particular, offer a practical solution to many of these limitations by combining complementary sources and optimizing system performance under diverse operating conditions.

1.3 Global Renewable Energy Assessment

In recent decades, the global energy landscape has witnessed a transformative shift towards renewable energy sources. According to the International Renewable Energy Agency (IRENA), the total installed renewable energy capacity worldwide surpassed *3,800GW* by the end of *2023*, with solar photovoltaic and wind energy accounting for the majority of new additions. This expansion is driven by a combination of technological advancements, favorable policy environments, and increasing awareness of the environmental and economic consequences of fossil fuel dependency [16][18][88].

As illustrated in Figure 1-3, Solar PV capacity alone exceeded *1200GW*, making it the fastest-growing renewable source globally. The cost of solar modules has decreased by more than

85% since *2010*, resulting in a levelized cost of electricity (LCOE) that is competitive with or lower than fossil fuel alternatives in most regions. Similarly, wind power capacity grew beyond *900GW*, with substantial investments in both onshore and offshore installations. Innovations in turbine design, increased hub heights, and larger rotor diameters have improved the capacity factors and reduced the LCOE of wind energy systems [5][16].

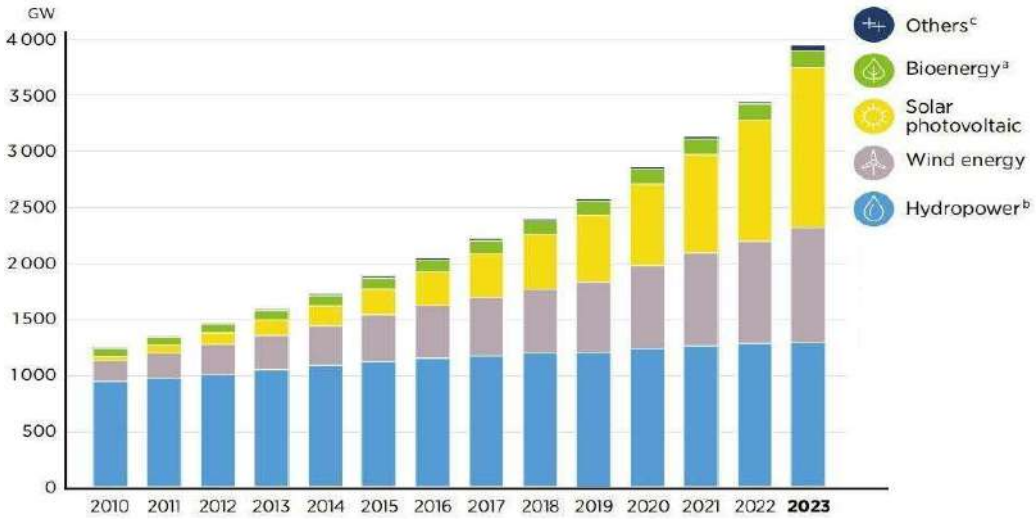


Figure 1-3 Global renewable electricity capacity, 2010-2023.
Source: IRENA, Renewable Energy and Jobs, Annual Review 2024 [88].

In terms of regional deployment, Asia continues to dominate, with China being the global leader in both solar and wind capacity. The European Union and the United States also play significant roles, supported by robust regulatory frameworks and investment incentives. Meanwhile, emerging economies in Africa and Latin America are increasingly turning to renewable energy to meet rising demand and support economic development. Global investment in renewables reached a record USD *570* billion in *2024*, with over *70%* directed toward solar and wind energy projects [19][88].

The decarbonization potential of renewables is further underscored by the decline in carbon intensity of power generation. Countries with high renewable shares in their energy mix, such as Denmark, Uruguay, and Iceland, demonstrate the feasibility of near-zero emission electricity systems. The shift towards renewables is not only an environmental imperative but also an economic opportunity, as it creates jobs, reduces import bills, and enhances energy security. However, variability in renewable output necessitates the integration of energy storage, smart grid technologies, and hybrid configurations for stable grid operation [10][88].

1.4 Solar Energy

Solar energy harnesses the electromagnetic radiation emitted by the sun, offering abundant, clean, and increasingly cost-effective power. It can be captured and converted into usable energy through several technologies. This section explores the three primary solar energy systems in use today, Photovoltaic (PV), Solar Thermal (CSP), and Solar Heating, before systems the foundational principles and historical development of solar PV.

1.4.1 Types of Solar Energy Systems

Solar energy can be harnessed through various technological pathways, each with its own operational principles, advantages, and limitations. The three primary categories include PV systems, solar thermal or concentrated solar power (CSP) systems, and solar heating systems. These technologies differ in how they convert sunlight and in the types of applications they best serve [16][18].

a Photovoltaic System

PV systems convert sunlight directly into electricity using semiconductor materials, typically silicon-based. When solar radiation strikes the surface of a PV cell, photons excite electrons, creating an electric current through the photovoltaic effect. These systems are highly versatile and are deployed in residential rooftops, commercial buildings, and large-scale utility solar farms. Their modularity allows for a wide range of installations, from a few watts to several megawatts. PV systems are scalable, non-polluting, and silent during operation. However, their efficiency is highly dependent on sunlight availability, and they require energy storage solutions, such as batteries, to ensure a continuous power supply during cloudy periods or at night [5][12][18].



Figure 1-4 Photovoltaic fields.

b Concentrated Solar

Concentrated Solar Power (CSP) systems, also known as solar thermal power plants, operate on a different principle. They use mirrors or lenses to focus a large area of sunlight onto a smaller receiver, where the concentrated heat is used to generate steam that drives turbines or other heat engines for electricity production. Several CSP variants exist, including parabolic troughs, power towers, and parabolic dish systems. These systems are particularly well-suited for utility-scale installations in regions with high direct solar irradiance, such as deserts. One of the key advantages of CSP is its ability to store thermal energy, commonly in molten salts, allowing it to deliver power even when sunlight is unavailable. Nonetheless, CSP systems entail high capital investment, require substantial land and water for cooling, and are typically limited to sunny and dry geographical areas [5][18].



Figure 1-5 Concentrated solar power plant.

c Solar thermal

Solar heating systems, or solar thermal collectors, focus on capturing sunlight to produce heat rather than electricity. These systems typically use flat-plate or evacuated tube collectors to heat water or air for domestic, commercial, or industrial use. They are among the most cost-effective solar technologies, offering high efficiency for direct thermal applications. Common uses include residential hot water systems, space heating, and process heating in manufacturing industries. Despite their affordability and efficiency, their output is limited to thermal energy and is subject to seasonal variations. Additionally, integrating them with electrical systems often requires auxiliary technologies for heat-to-electricity conversion [5][18].



Figure 1-6 Solar thermal collectors.

1.4.2 Definition and Operating Principle of PV Solar

Solar energy refers to the electromagnetic radiation emitted by the sun, which can be converted into electricity using photovoltaic (PV) cells. PV cells operate on the principle of the photovoltaic effect, where incident photons excite electrons in a semiconductor material, generating a direct current (DC). These cells are typically made of silicon and are arranged in modules and arrays to form a PV system. The DC output must be converted into alternating current (AC) using an inverter to be compatible with grid systems [4][5][16].

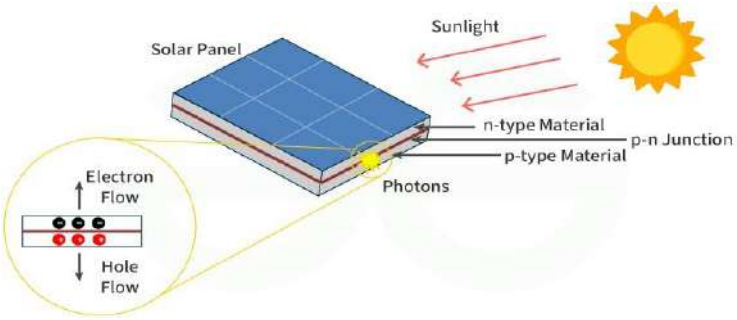


Figure 1-7 The principle of operation of the PV cell.

1.4.3 Historical Background

The concept of converting sunlight into electrical energy was first introduced in *1839* when French physicist Edmond Becquerel discovered the photovoltaic (PV) effect. However, the practical implementation of this phenomenon remained elusive for decades. In *1877*, early documentation on photovoltaic technology appeared, describing the properties of selenium when exposed to light. This marked one of the first instances where the solar effect on materials was formally investigated [20].

By *1883*, Charles Fritts constructed the first working solar cell using selenium coated with a thin layer of gold, achieving a conversion efficiency of approximately *1%*. Although far from efficient by today's standards, it represented a significant step forward in understanding solar energy conversion. The early 20^{th} century saw incremental advances in semiconductor physics, culminating in a breakthrough by the Chaplin-Fuller-Pearson team in the *1950*s. Using crystalline silicon as the active material, they developed a silicon-based solar cell capable of reaching *6%* efficiency, laying the foundation for modern PV technology [20].

The turning point for widespread PV adoption came in *1954* at Bell Laboratories, where researchers created the first commercial silicon solar cell. Due to their reliability and autonomy, these cells were first deployed in satellite and space missions during the *1960*s, particularly by NASA. Their high cost, however, limited terrestrial applications for several decades [20].

As research and industrial interest grew, efficiency continued to improve through material innovation, doping techniques, and anti-reflective coatings. Over time, commercial silicon-based PV modules have reached efficiencies exceeding *17%*, with laboratory prototypes achieving even higher figures. Meanwhile, the raw materials used for manufacturing, such as silicon and germanium, are abundant in Earth's crust, making PV a viable large-scale energy solution.

Moreover, PV systems offer distinct environmental advantages: they operate without generating greenhouse gases, air or water pollutants, or noise, owing to the absence of moving parts. These characteristics make them a key pillar in clean energy transition strategies.

Today, photovoltaic technology has moved far beyond its origins in laboratories and spacecraft. It is now deployed globally in residential rooftops, commercial installations, and large-scale solar farms. The evolution of PV continues, with ongoing research into perovskites, tandem cells, and advanced materials promising even higher efficiencies and reduced manufacturing costs.

1.4.4 PV panel Technologies types

Several PV technologies are in commercial and developmental stages, and are presented in Figure 1-8 [14][16][18][20]:

- Monocrystalline silicon: High efficiency (*18–22%*), high cost, long lifespan.
- Polycrystalline silicon: Moderate efficiency (*15–18%*), lower cost.
- Thin-film (CdTe, CIGS): Lightweight, flexible, suitable for building-integrated PV (BIPV).
- Concentrated PV (CPV): Uses lenses or mirrors to focus sunlight on high-efficiency cells, ideal for high-irradiance locations.

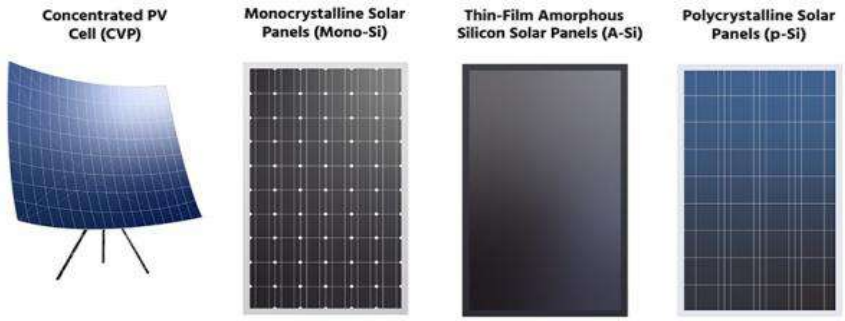


Figure 1-8 Models of solar modules based on silicon cell type.

Each technology has trade-offs in terms of cost, efficiency, durability, and environmental impact. The choice depends on application requirements, site conditions, and economic constraints [18].

1.4.5 Advantages and Disadvantages of Photovoltaic Systems

Photovoltaic (PV) systems offer numerous benefits, but they also present specific limitations that must be considered during planning and design [16][18][19].

Advantages:

- Clean energy production: PV systems generate electricity without emitting greenhouse gases during operation.
- Low operational costs: Once installed, PV systems require minimal maintenance and incur negligible fuel costs.
- Modularity and scalability: PV installations can be sized to match any energy demand, from small homes to utility-scale farms.

- Energy access for remote areas: PV systems are ideal for off-grid applications in rural or isolated regions.
- Silent operation: PV panels operate silently, making them suitable for residential and urban settings.

Disadvantages:

- Intermittency: PV output depends on sunlight availability, which is affected by time of day and weather conditions.
- High initial investment: The cost of installation and grid interconnection can be high despite declining module prices.
- Energy storage needs: Batteries or other energy storage systems are required to ensure a continuous power supply.
- Land use: Large PV farms may require considerable land area, potentially impacting ecosystems.

Despite these drawbacks, continuous improvements in technology, policy incentives, and integration with other sources (such as wind or batteries) have made PV systems more viable and attractive [18].

1.4.6 Solar Energy in the World and Algeria

Solar photovoltaic technology has emerged as one of the most dynamic and rapidly expanding sources of renewable electricity worldwide. Its success is driven by continuous cost reductions, technological innovations, and political commitment to the global shift toward low-carbon energy systems. However, beyond technological and economic factors, the geographical distribution of solar resources, measured in sunshine hours and solar irradiance, plays a fundamental role in determining the feasibility and performance of solar energy systems [12][14].

The average annual sunshine hours, particularly under Direct Normal Irradiance (DNI) above *360W/m²*, reveal striking spatial differences across the globe. Between *2015* and *2025*, data show that the most solar-favored regions, those exceeding *3000* sunshine hours per year, include North Africa (notably Algeria, Egypt, and Libya), the Middle East, Australia, the Atacama Desert in Chile, the southwestern United States, and parts of South and Central Asia. These areas benefit from high solar elevation angles, low atmospheric moisture, and minimal cloud coverage, making them prime locations for high-efficiency, utility-scale solar PV installations [12][16][20].

Conversely, regions such as Northern and Western Europe, Canada, and Russia receive significantly less sunshine, typically less than *1500hours/year*, due to high cloudiness and seasonal variation. While these countries have advanced PV markets, their deployments rely heavily on policy incentives, advanced technologies like bifacial modules, solar tracking systems, and grid-connected hybrid solutions to overcome resource limitations [4][12][14].

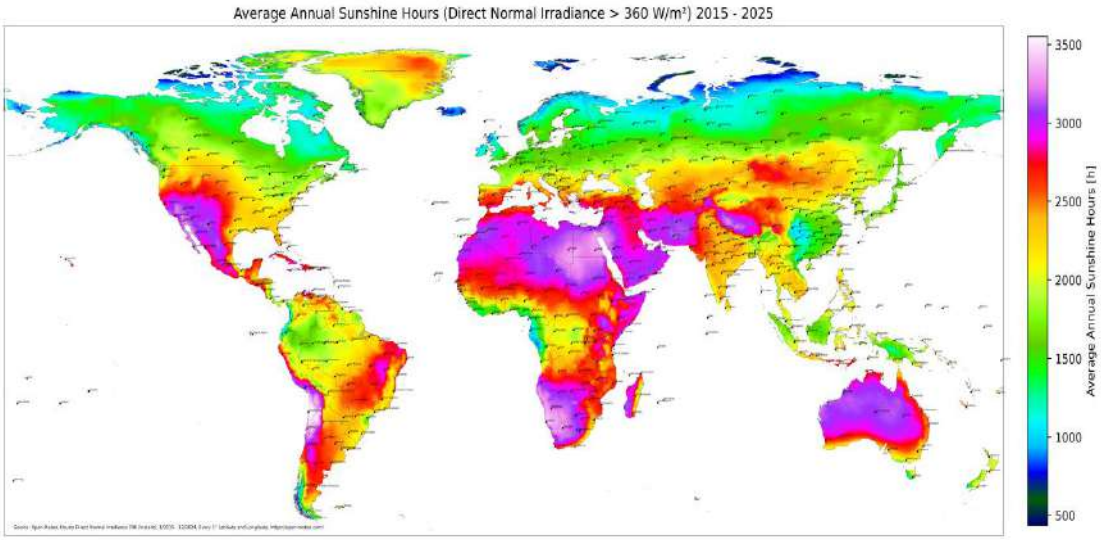


Figure 1-9 Average Annual Sunshine Hours (Direct Normal Irradiance > *360W/m²*) 2015–2025.

Source: Adapted from https://open-meteo.com

In parallel with high resource potential, the global solar PV market has witnessed remarkable expansion. According to the IRENA *2024* Annual Review, solar PV accounted for nearly *60%* of all newly added renewable energy capacity in *2023*, highlighting its centrality to global energy transitions. Countries such as China, India, the United States, and Germany continue to lead both in annual installations and cumulative capacity. China alone has surpassed *500GW* of installed PV capacity, supported by strong industrial policies and domestic manufacturing. India and the United States are rapidly scaling up utility and distributed PV, while Germany remains a leader in rooftop solar and citizen-driven energy cooperatives [14][88].



Figure 1-10 Solar PV deployment in 2023: New installations and cumulative capacity in the top 10 countries and worldwide.

Source: IRENA, Renewable Energy and Jobs, Annual Review 2024 [88].

In Algeria, solar energy is not only a clean alternative but a strategic national resource. The country benefits from *2500* to *3500* sunshine hours annually, especially in the Sahara region, where solar irradiance levels can reach up to *2600kWh/m²/year*. These conditions place Algeria among the top five global locations for solar PV deployment. Vast, arid, and sparsely populated desert zones provide ideal landscapes for large-scale solar farms, with potential for both domestic energy supply and electricity exports to Europe via trans-Mediterranean HVDC interconnectors [14][20][55].

To harness this opportunity, Algeria has launched the Renewable Energy and Energy Efficiency Program (PNEREE), aiming to install *22GW* of renewable capacity by *2030*, of which *13.6GW* will come from solar PV. Major initiatives include the "Tafouk 1" solar project, which seeks to install over *4GW* across several wilayas, and hybrid PV-diesel systems for off-grid rural electrification in remote communities. These systems reduce reliance on fossil fuels, cut operational costs, and improve energy access for isolated populations [14][18].

Table 1-1 PV Projects in Algeria.

Project Name	Year Started	Maximum Capacity (MW)
Boughezoul	2016	150
El Oued	2017	300
Tafouk 1	2018	4000
Ghardaia	2019	100
Tindouf	2020	100

Sources: International Renewable Energy Agency (IRENA). Renewable Energy Statistics 2023. Retrieved from IRENA. International Energy Agency (IEA). World Energy Statistics 2023. Retrieved from IEA.

In terms of policy, the Algerian government has adopted several investment incentives, including feed-in tariffs, VAT exemptions, and measures to promote local manufacturing of PV components. Institutions like Sonelgaz, the Commissariat aux Énergies Renouvelables (CEREFE), and CDER (Centre de Développement des Énergies Renouvelables) are actively involved in project implementation, grid integration, and technical evaluation.

Despite these strengths, Algeria faces a range of implementation barriers, including bureaucratic delays, grid constraints, financing limitations, and insufficient coordination between public institutions and private investors. Overcoming these challenges requires regulatory reform, capacity building, enhanced R&D programs, and stronger international partnerships, particularly in the framework of Euro-Mediterranean cooperation for sustainable energy development [14].

In summary, Algeria's combination of exceptional solar resources, geopolitical positioning, and national ambitions makes it a strong candidate for becoming a regional hub in solar energy generation and export. However, realizing this vision demands a concerted effort to align technical capabilities, policy frameworks, and market instruments to ensure long-term sustainability, resilience, and social equity in energy access [88][91].

1.5 Wind Energy

This section offers a comprehensive overview of wind energy, starting with its operating principles and historical development. It then presents the various turbine types and installation configurations, evaluates the advantages and limitations of wind power systems, and concludes with an analysis of global and Algerian wind energy landscapes. This foundational understanding is essential for appreciating how wind power integrates with other renewables in hybrid systems, which will be explored in subsequent chapters.

1.5.1 Definition and Operating Principle

Wind energy is harnessed by converting the kinetic energy of moving air masses into mechanical energy, and subsequently into electricity using wind turbines. Wind turbines consist of blades mounted on a rotor connected to a shaft, which spins a generator. The amount of energy generated depends on wind speed, air density, and the swept area of the rotor. Wind energy systems can be deployed as standalone turbines, wind farms, or integrated into hybrid configurations with other renewable sources [3][5].

1.5.2 Historical Background

The use of wind energy spans millennia, beginning with its application in navigation by ancient civilizations such as the Egyptians, who used sails to harness wind power as early as 5000 years ago. By 2000 B.C., wind-powered devices had emerged in ancient Babylon and China, primarily for mechanical tasks like grinding grain and drawing water. These early innovations marked the inception of wind energy technology and laid the groundwork for later advancements [3][13].

During the Middle Ages, windmills became widespread in Europe, where they were integral to agricultural and irrigation systems. A major leap occurred in the late *19*th century when wind energy began to be harnessed for electricity generation. Denmark was among the first to construct small wind turbines designed specifically to supply electricity to rural areas. Simultaneously, in the United States, an early wind electric generator with a *17*-meter rotor and *144* wooden blades was built, capable of producing up to *12kW*, a remarkable milestone in wind power engineering [3].

The modern era of wind energy was catalyzed by the oil crises of the *1970s*, which heightened global awareness of fossil fuel limitations and triggered increased investment in renewable alternatives. This period marked the beginning of systematic research and development in wind turbine technology. By the *1980s*, the first commercial wind farms appeared, particularly in Europe and the United States, where supportive policies and technological readiness facilitated deployment [3][13].



Figure 1-11 Traditional windmills and modern wind Turbines.

Over the past two decades, the field has undergone transformative growth, driven by innovations in materials science, aerodynamics, and power electronics. These advancements have led to highly efficient, computer-controlled wind turbines capable of grid-scale electricity generation. Today, wind energy is no longer a niche technology; it is a central pillar of renewable energy portfolios in numerous countries and plays a critical role in decarbonization strategies aimed at mitigating climate change and enhancing energy security.

1.5.3 Aerodynamic Classification and Deployment of Wind Turbines

Wind turbine technologies are not only defined by their orientation but also by their aerodynamic performance, suitability for specific environments, and structural design. In this section, we revisit turbine classification from an engineering perspective, emphasizing performance, design constraints, and application domains [16][18].

a Aerodynamic Orientation and Rotor Axis Configuration

From an aerodynamic and control standpoint, wind turbines fall into two main categories [10][13][19][20][10]:

- Horizontal-Axis Wind Turbines (HAWTs): These turbines have their rotor shaft parallel to the ground and typically face the wind head-on through an active yaw control system. HAWTs dominate utility-scale projects due to [10][16]:

  - Higher energy conversion efficiency in laminar wind conditions.
  - Optimized blade designs using airfoil profiles for maximum lift-to-drag ratio.
  - Larger swept area and greater tower height, enabling access to higher wind speeds.

However, HAWTs require precise wind alignment mechanisms and have higher structural stress on blades and towers under turbulent conditions [3][5][18].

- Vertical-Axis Wind Turbines (VAWTs): With a rotor axis perpendicular to the ground, VAWTs can operate independently of wind direction, removing the need for yaw control. Their characteristics include [10][16]:

  - Easier integration into complex terrains and urban environments.
  - Simple mechanical design and low center of gravity.
  - Lower starting torque and overall efficiency compared to HAWTs.

VAWTs are often used in small-scale or distributed systems, especially where wind direction is highly variable [3][5][18].

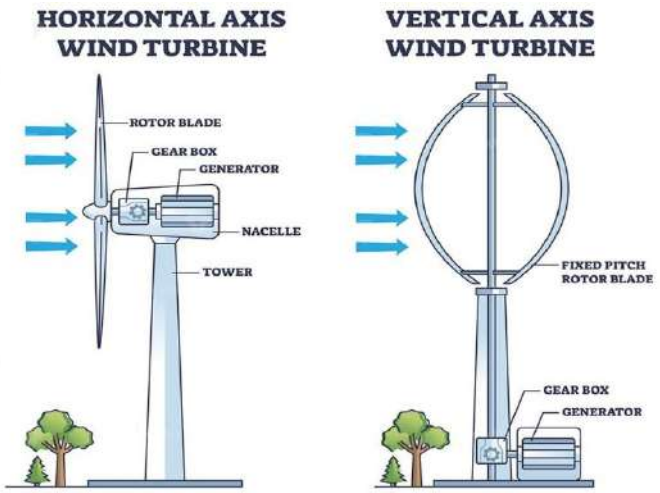


Figure 1-12 Horizontal and vertical axis wind turbine.

b Site Deployment: Onshore and Offshore Wind Turbines

In addition to axis orientation, turbines are also categorized by their installation environments [3][19]:

- Onshore Wind Turbines**:** Installed on land, these systems are easier and less expensive to install and maintain. Onshore installations are typically used in areas with accessible wind corridors, such as ridgelines and coastal plains.
- Offshore Wind Turbines**:** Located in shallow or deep-sea environments, offshore turbines benefit from [9][19]:

    - Stronger and more consistent wind resources.
    - Minimal visual and acoustic impact on populated areas.
    - Larger turbine sizes due to easier transportation of components via ships.

Despite higher capital costs and maintenance complexity due to harsh marine conditions, offshore wind farms have become a critical component in the energy transition of many countries, particularly in Europe and Asia [1][19].

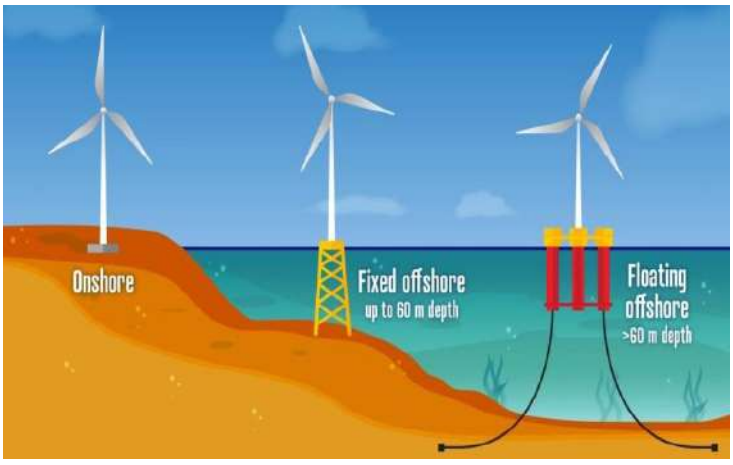


Figure 1-13 Onshore and offshore wind turbines.

1.5.4 Wind Generator Technologies

The electrical generator is a key component in a wind energy conversion system (WECS), responsible for transforming the mechanical energy produced by the turbine into electrical energy. Several generator technologies are used in wind applications, each characterized by distinct operating principles, control requirements, and suitability for specific turbine configurations. The main types include the Squirrel Cage Induction Generator (SCIG), Doubly-Fed Induction Generator (DFIG), Wound Rotor Synchronous Generator (WRSG), and Permanent Magnet Synchronous Generator (PMSG) [1].

a Squirrel Cage Induction Generator (SCIG)

The Squirrel Cage Induction Generator is the simplest and most robust generator used in early wind energy systems. It consists of a squirrel-cage rotor and a stator directly connected to the grid. The SCIG operates at nearly constant speed, as its rotor is short-circuited and cannot control excitation. It requires reactive power from the grid or external capacitors for magnetization. Due to its simplicity and low cost, it is suitable for small fixed-speed wind turbines, but it offers limited energy capture and poor adaptability to wind speed variations [5].

b Doubly-Fed Induction Generator (DFIG)

The Doubly-Fed Induction Generator features a wound rotor connected to the grid through a partial-scale back-to-back converter, while the stator is directly connected to the grid. This configuration allows independent control of active and reactive power through the converter, enabling variable-speed operation around the synchronous speed. The DFIG is widely used in modern onshore wind turbines due to its high efficiency, controllability, and reduced converter cost [1][3][5].

c Wound Rotor Synchronous Generator (WRSG)

The Wound Rotor Synchronous Generator employs a field winding on the rotor supplied by an external DC excitation source through slip rings. This configuration allows direct control of the magnetic field and terminal voltage by adjusting the excitation current. The WRSG operates synchronously with the stator field and is often connected to the grid through a full-scale converter, enabling variable-speed operation and reactive power control. It is suitable for large-scale and offshore wind turbines where reliability and flexibility are essential [1][5].

d Permanent Magnet Synchronous Generator (PMSG)

The Permanent Magnet Synchronous Generator uses permanent magnets on the rotor to create the excitation field, eliminating the need for slip rings and external excitation. It provides high efficiency and reliability, making it ideal for direct-drive configurations without gearboxes. PMSGs operate over a wide speed range and are connected to the grid via a full-scale power

converter, which manages active and reactive power. These generators are widely used in modern variable-speed and offshore wind turbines due to their compact design and excellent performance [1][5].

1.5.5 Comparative characteristics of Wind Generator Technologies

The selection of an appropriate generator technology for a wind energy conversion system (WECS) depends on factors such as turbine size, desired speed range, control flexibility, cost, and grid integration requirements. Each generator type presents specific advantages and limitations related to its excitation method, converter configuration, and operational characteristics. Table 1-2 summarizes the main comparative features of the four commonly used wind generators in modern wind turbines [1].

Table 1-2 Comparative characteristics of wind generator technologies.

Feature	SCIG	DFIG	WRSG	PMSG
Excitation System	Self-excited (requires reactive power from the grid or capacitors)	External via rotor converter	DC excitation via slip rings	Permanent magnets (no excitation losses)
Converter Requirement	None or simple soft starter	Partial-scale (~30% of rated power)	Full-scale converter	Full-scale converter
Speed Range	Fixed or narrow range	Variable (±30% around synchronous speed)	Fully variable	Fully variable
Reactive Power Control	Limited (depends on the grid)	Excellent through the rotor converter	Excellent via excitation current	Controlled through a converter
Efficiency	Moderate	High	High	Very high
Maintenance	Low	Moderate (brushes and converter)	High (brushes and cooling)	Low (no brushes)
Typical Application	Small fixed-speed turbines	Medium to large onshore turbines	Large offshore turbines	Direct-drive and offshore turbines

1.5.6 Advantages and Disadvantages of Wind Systems

Advantages [3][10][13]*:*

- Renewable and clean: Wind turbines generate electricity without greenhouse gas emissions.
- Cost-effective: Modern wind energy is among the cheapest sources of new electricity generation.

- Quick installation: Compared to fossil or nuclear plants, wind farms can be developed and commissioned rapidly.
- Complementary to solar energy: Wind and solar have different peak generation times, improving overall hybrid system reliability.

Disadvantages [3][10][13]*:*
- Intermittency and unpredictability: Wind speed variations can cause power fluctuations.
- Noise and visual impact: Turbines may affect local communities or wildlife.
- Land use and grid access: Large wind farms require extensive land and suitable transmission infrastructure.
- Maintenance in harsh environments: Offshore turbines, in particular, face logistical and maintenance challenges.

1.5.7 Wind Energy in the World and Algeria

Wind energy continues to play an increasingly important role in the global energy landscape, contributing approximately *20%* of all renewable electricity production in *2024*. This growth is driven by technological innovation, reductions in installation costs, supportive policies, and the growing urgency to decarbonize power systems. Countries such as China, the United States, Germany, and Spain have emerged as leaders in wind energy deployment, with China alone accounting for a majority of recent global additions. In *2023*, China was responsible for *65.5%* of new wind power installations, while also holding *43.4%* of the cumulative installed capacity worldwide. The United States followed with *14.6%* of global capacity, and other key contributors included Germany, India, Brazil, and Spain. The expansion of offshore wind energy, especially in the North Sea, along the eastern seaboard of the United States, and in East Asian waters, reflects a broader trend toward harnessing more consistent and powerful wind resources at sea [3][10][15][87][88][93].

Global wind resource distribution is closely tied to geographic and climatic conditions. Regions with the highest average wind speeds, often exceeding *10m/s* at *100m* height, are typically located in open oceans, coastal areas, and wide plains. These include the Southern Ocean, the North Atlantic, parts of Central Asia, and high-latitude coastal regions of the southern hemisphere. By contrast, areas with dense forests, mountainous terrain, or frequent low-pressure systems tend to have lower wind speeds. Figure 1-14 shows the global map of mean wind speed at 100 meters, highlighting the most promising zones for utility-scale wind power development. The map is based on high-resolution global datasets collected over the period from *2007* to *2016*, with a spatial resolution of *0.75*°. The red and orange zones represent regions with the strongest and most consistent wind speeds, whereas blue shades indicate areas with relatively modest wind potential [3][13][20].

The global market trends for wind energy deployment are illustrated in Figure 1-15, which compares both new installations and cumulative installed capacity for the top ten countries and the rest of the world. The dominance of China in both metrics is visible, followed by steady contributions from major economies in Europe, North America, and emerging markets. These trends underscore the increasing competitiveness of wind energy in diverse energy

systems and market structures. As wind technology becomes more efficient and cost-effective, it is expected that both onshore and offshore capacities will continue to grow substantially over the next decade [20].

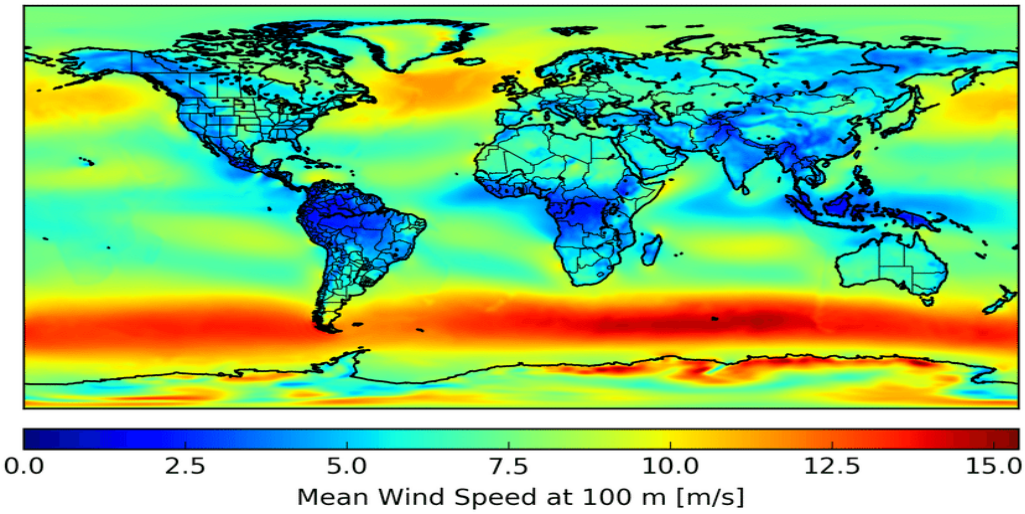


Figure 1-14 Mean wind speed estimates at *100m*, every *6* hours from *01-01-2007* to *31-12-2016*, at a *0,75°×0,75°* precision.

In Algeria, wind energy remains significantly underutilized despite the country's substantial natural potential. Regions such as Tindouf, Adrar, and El Oued are among the most promising for wind power generation, with average wind speeds consistently exceeding *6m/s*. These areas are characterized by flat, open landscapes with minimal surface roughness, which contributes to stable and favorable wind flow conditions. The Kabertene wind farm in the Adrar region, with a capacity of *10MW*, serves as a pilot project demonstrating Algeria's capacity to implement wind energy technology under local environmental and grid conditions. However, beyond this initial deployment, progress has been limited due to infrastructural and regulatory barriers [3][10][13][20][55].

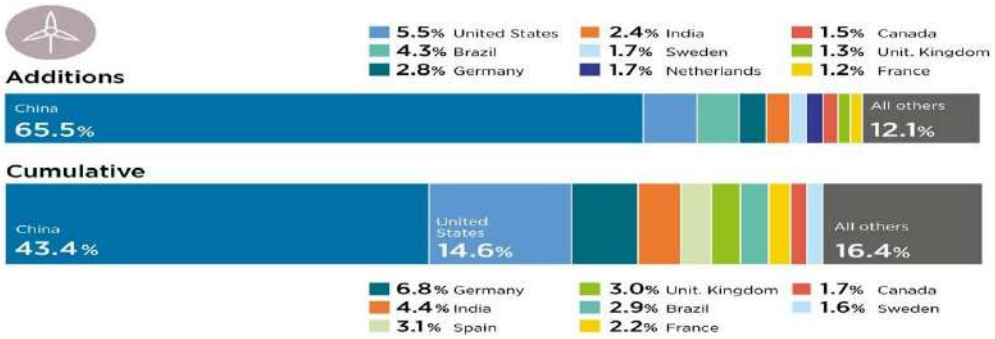


Figure 1-15 Wind power deployment in 2023: New installations and cumulative capacity in the top 10 countries and worldwide [88].

The Algerian national strategy for renewable energy, outlined in the Renewable Energy and Energy Efficiency Program, targets *5GW* of wind capacity by *2030*. One of the pioneering initiatives within this framework is the Adrar Wind Farm, a *10MW* onshore wind project

launched in *2015*. Located in a high-potential wind zone in southwestern Algeria, this facility serves as the country's first operational wind power plant and provides valuable technical and operational insights for future developments. Reaching the national target requires coordinated investment in transmission infrastructure, particularly to connect remote high-wind areas to major urban centers. Technical challenges, such as the limited domestic experience in offshore wind projects and the lack of large-scale wind component manufacturing, must also be addressed [10][13].

Integrating wind with solar photovoltaic systems provides a viable pathway to optimize renewable generation and ensure a more consistent energy supply. In Algeria, such hybrid configurations are particularly advantageous due to the complementary nature of solar and wind profiles. While solar generation peaks during the day, wind resources are often stronger at night or during winter months, which helps smooth out variability and reduce dependence on storage systems. This integrated approach enhances the flexibility and resilience of energy systems and is especially beneficial for off-grid applications in remote areas [3].

1.6 Hybrid Renewable Energy Systems

This section presents an in-depth look at hybrid systems, beginning with their definition, classification, and optimization criteria. It also highlights their technical advantages and the challenges associated with their design and deployment in modern power systems.

1.6.1 Definition of Hybrid Renewable Energy Systems

Hybrid Renewable Energy Systems (HRES) are energy systems that combine two or more renewable energy sources, such as solar, wind, hydro, biomass, or geothermal, often supported by energy storage such as batteries. The goal is to optimize energy generation by taking advantage of the complementary nature of different sources, improving system reliability, reducing intermittency, and ensuring a more stable and continuous power supply [4][17][20].

1.6.2 Classification of Hybrid Systems

Hybrid renewable energy systems (HRES) are designed to integrate multiple energy sources in a coordinated manner to enhance overall reliability, efficiency, and power quality. A typical HRES can be classified based on various criteria, including grid connectivity, energy coupling, storage integration, and control architecture [17][18][20].

a Based on grid connectivity

- Off-grid HRES are used in remote or isolated locations where grid access is limited or unavailable. These systems often include batteries or diesel generators as backup.
- Grid-connected HRES are integrated into the public electricity network and can inject surplus energy, reduce demand peaks, and provide ancillary services [4][17][20].

b Based on energy coupling

- AC-coupled systems involve AC sources connected through transformers and synchronized to a common bus.
- DC-coupled systems share a common DC link, enabling direct coupling of solar panels, wind rectifiers, and storage units before inversion [17].

c Based on storage integration

- With energy storage: Systems that include batteries, supercapacitors, or other forms of storage to buffer energy.
- Without energy storage: Directly supply the load and grid, relying on source complementarity [17].

d Based on the control strategy

- Centralized control: A single controller coordinates all subsystems.
- Distributed or decentralized control: Each subsystem manages its output locally, with limited or no central supervision [17].

This thesis focuses on a grid-connected, DC-coupled hybrid system that uses a shared DC-link architecture and advanced control strategies to optimize performance.

1.6.3 Optimization Criteria for HRES

The successful deployment of a hybrid system requires careful consideration of design and operational parameters. The main optimization criteria include [17][18][20]:
- *Reliability and availability*: The system must deliver continuous power with minimal interruptions, even in the absence of one energy source.
- Energy efficiency: Efficient conversion, minimal losses, and maximum energy harvesting from available resources.
- *Economic performance*: Low levelized cost of energy (LCOE), favorable return on investment, and short payback period.
- *Environmental impact*: Low lifecycle emissions, reduced land use, and sustainable material sourcing.
- *Control complexity***:** Scalability and manageability of the control system, particularly under dynamic grid and environmental conditions.

These criteria guide the sizing, topology selection, and algorithm development discussed in subsequent chapters. Multi-objective optimization approaches are often used, leveraging algorithms like PSO, GWO, and fuzzy logic to strike a balance between conflicting goals.

1.6.4 Advantages of Hybrid Systems

Hybrid systems provide many technical and operational benefits, including [16]:
- Increased reliability and continuity of power.
- Enhanced energy efficiency and reduced curtailment.
- Improved grid interaction and voltage support.
- Decreased emissions and fossil fuel dependency.
- Flexibility and scalability for diverse applications.

1.6.5 Challenges in Hybrid System Design

The main challenges in scaling up adoption and designing effective hybrid systems, with an emphasis on integration complexity and technical limitations, include [16][20][24][31]:
- Management of multiple dynamic energy sources [8].
- Integration of control algorithms for coordination.
- System sizing and optimization.
- Compliance with grid standards.
- High initial capital costs.

1.7 Grid-Connected Hybrid Renewable Energy Systems

This section introduces the main architectures of hybrid systems and the power electronic interfaces used. It also presents advanced control strategies used for optimal operation and integration into the grid [5][16][24].

1.7.1 Architectures

Hybrid systems can be configured as [16][19]:
- *DC-Coupled*: All energy sources feed a common DC bus that connects to the grid via a single inverter.
- *AC-Coupled*: Each energy source is connected via individual inverters to an AC bus [27].

DC-coupled systems offer better integration of control and energy management, while AC-coupled systems allow modular upgrades [24].

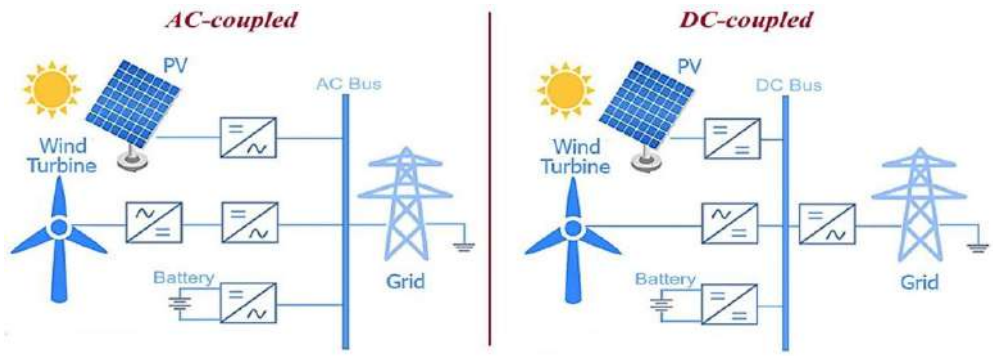


Figure 1-16 Diagram of AC- and DC-coupling topologies for integrating wind, solar, and battery systems.

1.7.2 Power Electronic Interfaces

Hybrid systems employ various converters [16][24]:
- *DC-DC Converters*: Boost, buck, or buck-boost types regulate DC voltage.
- *Inverters*: Two-level or multilevel (e.g., NPC) topologies convert DC to AC.

Multilevel inverters reduce harmonic distortion and improve output quality. Inverter control strategies include SPWM, SVPWM [25][67], and direct torque control (DTC).

1.7.3 Control Strategies

Modern hybrid systems require advanced control techniques [16][31]:
- *MPPT Algorithms*: Conventional like Perturb and Observe (P&O), Incremental Conductance (INC), PI-based control. Intelligent as: Fuzzy Logic, Particle Swarm Optimization (PSO), Grey Wolf Optimization (GWO), Hybrid algorithms.
- *Grid Synchronization*: Phase-Locked Loop, Dual Second-Order Generalized Integrator.
- *Voltage and Current Control*: Synchronous Reference Frame (SRF), Direct Power Control (DPC), Hysteresis control.

These strategies maximize energy harvesting and ensure power quality [31].

1.7.4 Modeling and Simulation

Accurate modeling is essential for performance evaluation and controller design. Simulink and MATLAB are widely used for time-domain simulations, enabling the analysis of steady-state and transient behaviors of PV, wind, and hybrid systems [16].

1.8 Economic and Ecological Benefits of Renewable Hybrid Systems

HRES are increasingly recognized as a central component of the global clean energy transition, delivering substantial economic and environmental benefits. By combining complementary resources such as solar and wind, these systems ensure a more stable and cost-effective electricity supply while reducing dependence on fossil fuels. This is particularly valuable in energy-exporting countries like Algeria, where hybrid systems help preserve valuable hydrocarbon resources for export, thereby boosting revenues, enhancing national energy security, and contributing to the diversification of exports beyond hydrocarbons into clean energy markets [16][56][57][87].

According to Bloomberg NEF's Energy Transition Investment Trends *2025*, global investment in renewable energy, including solar, wind, and hybrid systems, reached *USD728* billion in *2024*, forming a significant share of the record *USD2.08* trillion total clean energy transition investment that year. Renewable energy, energy storage, and grid infrastructure were the leading sectors, with China maintaining its position as the top investor, followed by the United States, the European Union, and India. The Asia-Pacific region as a whole

accounted for over half of the global investment, reflecting a rapid acceleration in deployment [86].

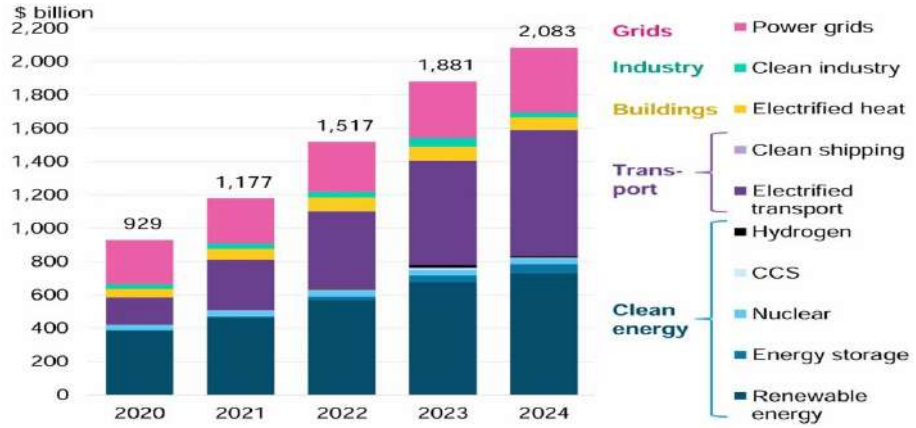


Figure 1-17 Global energy transition investment from 2020 to 2024 [86].

From a labor market perspective, the Renewable Energy and Jobs: Annual Review *2024* reported that the renewable energy sector employed 16.2million people worldwide in *2023*, marking a steady increase from *7.3* million in *2012*. Solar PV remained the largest employer with *7.11* million jobs, followed by bioenergy with *4.9* million, hydropower with *3.88* million, and wind energy with *1.46* million. The expansion of hybrid systems is expected to create even more high-quality jobs across manufacturing, project development, installation, operation, and maintenance, particularly in emerging markets that leverage their abundant renewable resources [16][88].

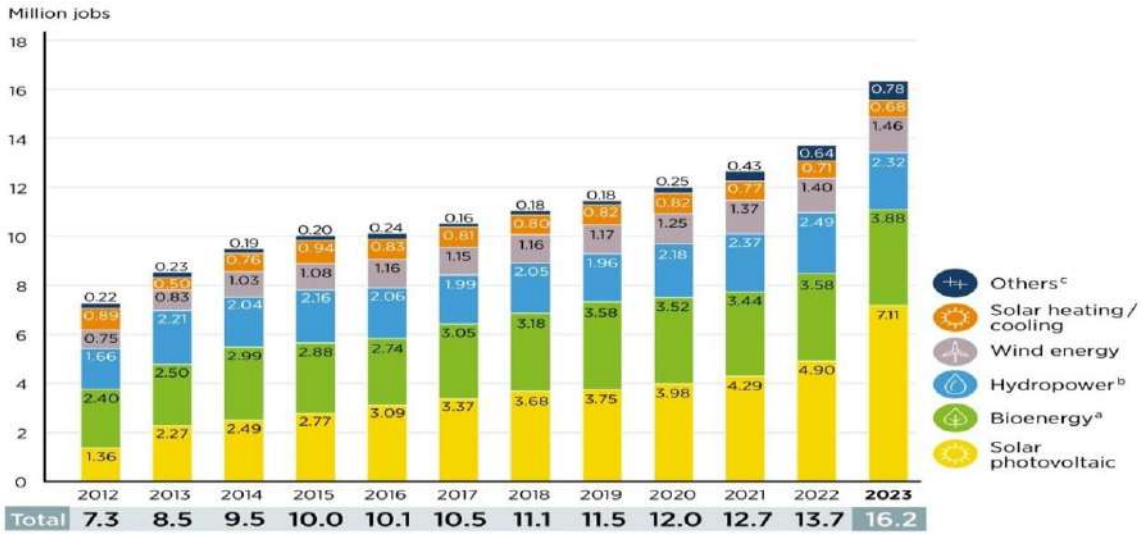


Figure 1-18 Evolution of global renewable energy employment by technology from 2012 to 2023 [88].

On the ecological front, the steady growth of the global population, combined with rapid industrialization, has driven a significant increase in worldwide energy consumption over the past decades. As illustrated in Figure 1-19, global primary energy demand rose steadily between *1998* and *2018* and is projected to continue increasing through *2040*. In this scenario,

the share of fossil fuels-coal, oil, and natural gas-declines even as total energy use rises, while the share of renewable energy grows substantially. This trend reflects a global commitment to reducing dependence on polluting fuels and accelerating the transition toward sustainable energy sources.

Meeting the *1.5°C* climate target by *2050* requires immediate and substantial reductions in greenhouse gas emissions. The Intergovernmental Panel on Climate Change (IPCC) indicates that coal and oil consumption should have already peaked, with natural gas expected to peak around *2025*. The technologies needed to accelerate this transition are already available, including large-scale renewable energy deployment, advanced power grids, efficient energy storage, and widespread electrification of end uses [88].

According to the International Renewable Energy Agency (IRENA), achieving the *1.5°C* goal will require a *25%* reduction in global CO_2 emissions by *2030*, accompanied by a profound restructuring of the global energy mix by *2040*. This entails a rapid decline in the share of fossil fuels and a steady rise in renewable energy, which will become the dominant source of power. These shifts demand ambitious policy frameworks and the accelerated deployment of existing solutions [86][88].

In this context, HRES are a key enabler of decarbonization. By replacing diesel- or coal-based generation, they can significantly reduce greenhouse gas emissions. For example, a *1MW* PV–wind hybrid plant can avoid over *2000* metric tons of CO_2 annually compared to an equivalent diesel generator. They also lower emissions of sulfur dioxide, nitrogen oxides, and particulate matter, improving air quality and reducing health risks, particularly in densely populated or industrial regions. Furthermore, distributed hybrid systems reduce the need for large centralized plants and extensive transmission infrastructure, helping to preserve natural habitats and biodiversity.

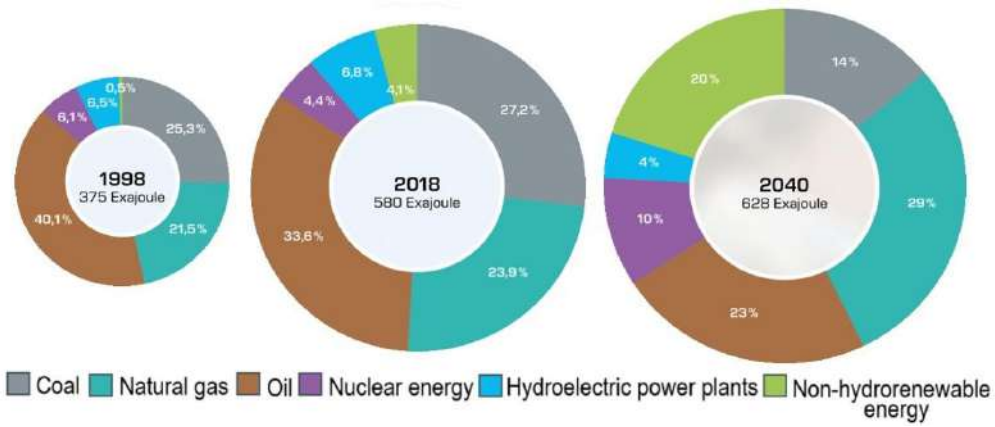


Figure 1-19 Increase in primary energy consumption from *1998* to *2018*, with projections to *2040*.

Over the long term, the levelized cost of energy (LCOE) for hybrid systems is expected to decline thanks to improvements in materials, power electronics, and digital control strategies. The integration of energy storage and intelligent management will ensure optimal resource

use, minimize curtailment, and enhance efficiency. By delivering both economic returns and ecological protection, hybrid renewable energy systems are a cornerstone of a sustainable energy future and a vital tool for achieving the *1.5°C* climate pathway [86][88].

1.9 Challenges and Future Trends

Despite their advantages, hybrid renewable energy systems face several challenges related to intermittency, control complexity, and grid integration. The variability of solar irradiance and wind speed requires advanced control strategies to ensure stable and reliable system operation [24]. In this context, intelligent optimization and control techniques such as PSO, GWO, and Fuzzy Logic Controllers have been widely applied to improve MPPT performance, enhance power quality, and increase overall system stability.

Hardware constraints, such as converter size, thermal limits, and battery degradation, must also be addressed. Modular inverter designs and adaptive control schemes help manage power flow and extend component lifespan. Interoperability with the utility grid introduces further technical considerations, such as harmonic distortion, reactive power control, and compliance with standards like IEEE 1547 and IEC 61727 [21].

Looking ahead, the future of hybrid renewable systems will be shaped by several trends [93]:
- *Digitalization*: Incorporation of smart sensors, Internet of Things (IoT) platforms, and cloud-based energy management systems [11][16].
- *Sector coupling*: Integration with electric vehicles, heating/cooling systems, and hydrogen production.
- *Energy storage integration*: Wider deployment of batteries, supercapacitors, and emerging technologies such as flow batteries and green hydrogen.
- *Policy innovation*: Development of flexible tariffs, green certificates, and grid access schemes to incentivize hybrid deployment.

1.10 Conclusion

This chapter has laid the foundation for understanding the role of photovoltaic and wind energy in the evolving energy landscape. It introduced the key concepts, classifications, and operational principles of solar and wind systems, alongside an in-depth exploration of their applications in hybrid configurations. The Algerian context has been highlighted to underscore the relevance of such systems in national development goals.

The subsequent chapters delve into the design, modeling, and control of standalone PV and wind energy systems, followed by the integration techniques employed in hybrid configurations. By bridging theoretical knowledge with practical engineering solutions, this work aims to make a meaningful contribution to the field of renewable energy integration.

Chapter 2 Design and Modeling of Grid-Connected Photovoltaic Systems

2.1 Introduction

The global energy transition has prioritized the integration of renewable energy systems into existing power infrastructures to reduce dependence on fossil fuels and mitigate environmental impacts. Among the various renewable energy sources, PV systems have gained significant attention due to their scalability, reliability, and steadily decreasing installation costs. As PV module efficiency improves and power electronic devices evolve, grid-connected PV systems are increasingly deployed in residential, commercial, and utility-scale applications. The challenge, however, lies not only in harnessing solar energy effectively but also in designing and controlling these systems to operate efficiently and harmoniously within the grid's dynamic conditions.

A grid-connected PV system refers to a solar energy setup that delivers electricity directly into the utility grid. Unlike standalone systems, it does not necessarily include battery storage and must comply with strict grid codes concerning power quality, reactive power support, frequency stability, and fault ride-through capabilities. The success of such systems depends on the proper design of the overall architecture, selection of appropriate power conversion topologies, and the implementation of advanced control algorithms. In addition, environmental variability such as fluctuating irradiance, temperature shifts, and partial shading necessitates the use of robust MPPT techniques to ensure the system operates at its optimal point under all conditions.

This chapter presents a comprehensive approach to designing and modeling grid-connected PV systems, starting from the basic building blocks up to complete system simulation. The design process begins with an in-depth understanding of the PV cell’s electrical behavior, typically modeled using single-diode or double-diode equivalents. From these models, the characteristics of modules and arrays are derived to assess system performance under different environmental conditions. Proper modeling of the I-V and P-V curves is essential for selecting components and ensuring accurate simulation results.

Power conversion is a critical aspect of grid-connected PV systems. The chapter explores two main conversion architectures: single-stage systems, which integrate MPPT and grid interface functionalities into one inverter, and two-stage systems, which separate the DC-DC converter from the DC-AC inverter, enabling more flexible control. Each architecture has trade-offs related to complexity, cost, and performance, all of which are discussed in detail. Additionally, various DC-DC converters, such as boost, buck, and buck-boost, are examined alongside inverter topologies, including two-level and three-level configurations. The choice of filtering technique (L, LC, or LCL) is also crucial for achieving low Total Harmonic Distortion (THD) in compliance with grid standards [21][40][71].

One of the most important aspects of PV system control is MPPT, which ensures maximum energy is harvested from the solar array. This chapter categorizes MPPT methods into three groups: conventional (e.g., Perturb and Observe, Incremental Conductance), intelligent (e.g., Fuzzy Logic, Artificial Neural Networks), and metaheuristic techniques (e.g., Particle Swarm Optimization, Grey Wolf Optimization, and hybrid methods). A comparative analysis is

provided to evaluate the strengths and limitations of each method based on convergence speed, tracking accuracy, implementation complexity, and adaptability to dynamic conditions.

Control strategies for grid interfacing are also covered in detail, including current and voltage regulation methods, synchronization techniques such as Phase-Locked Loop (PLL) and Dual Second Order Generalized Integrator PLL (DSOGI-PLL), and grid support functionalities like reactive power injection. Anti-islanding mechanisms are discussed as a critical safety feature that prevents unintended power export during grid outages [40].

Finally, this chapter presents modeling and simulation approaches using MATLAB/Simulink to evaluate system performance under real-world conditions. A case study of a *100kW* PV system is analyzed, highlighting how different MPPT techniques impact energy yield, voltage stability, and power quality [21][31]. Key performance indicators such as THD, inverter efficiency, and voltage regulation are used to assess design choices and control strategies.

In summary, this chapter establishes the theoretical and practical foundation for designing high-performance grid-connected PV systems. By integrating accurate modeling techniques with advanced power electronics and intelligent control, engineers and researchers can optimize system performance, ensure compliance with grid requirements, and contribute to a more sustainable and reliable electricity grid. The concepts and models presented here will serve as a cornerstone for the subsequent chapters, especially the hybrid integration of PV with wind systems.

2.2 Photovoltaic System Components and Operation

PV systems are composed of multiple electrical and electronic components working in concert to convert solar energy into usable electrical power. A comprehensive understanding of these components, their physical principles, and interactions is essential for designing efficient and reliable grid-connected PV systems. This section outlines the main functional elements of a PV system, focusing on PV cells, modules, and arrays, and elaborates on their behavior under real-world environmental conditions. It also examines how irradiance, temperature, and partial shading impact the electrical output of PV generators and highlights the importance of accurate modeling in performance prediction and control.

2.2.1 PV Cell and Array Modeling

The accurate modeling of PV cells is essential for the simulation, design, and optimization of PV systems. Several equivalent circuit models have been proposed to represent the behavior of PV cells under different operating conditions. These models differ in complexity and accuracy, and the selection of the appropriate model depends on the desired balance between computational simplicity and precision [2][16][19][65][91].

a Single-Diode Equivalent Model

The single-diode model is the most widely used and simplest approach to simulate PV cell behavior. As shown in Figure 2-1, it consists of a current source that represents the photocurrent I_{ph} generated by sunlight, a diode, a series resistance R_s representing internal resistance and contact losses, and a shunt resistance R_{sh} representing leakage current paths. This configuration captures the essential electrical behavior of a PV cell with sufficient accuracy for most engineering applications [1][14][16][20].

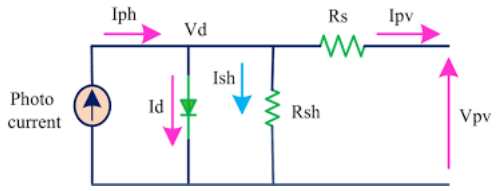


Figure 2-1 Equivalent circuit for PV cell based on one-diode model.

The relationship governing this model is expressed in equation (2-1**)** [14][18].

$$I_{PV} = I_{ph} - I_0 \left(e^{\frac{q\,(V_{PV} + I_{PV}\,R_S)}{n\,k\,T}} - 1 \right) - \frac{V_{PV} + I_{PV}\,R_s}{R_{sh}} \qquad (2\text{-}1)$$

Where I_{PV} is the output current (A), V_{PV} is the output voltage (V), I_0 is the reverse saturation current of the diode (A), q is the electron charge ($1.602 \times 10^{-19}\ C$), k is the Boltzmann constant ($1.381 \times 10^{-23}\ J/K$), T is the cell temperature in Kelvin (K), and n is the ideality factor of the diode (usually between *1* and *2*).

The single-diode model presents several advantages, making it widely used in PV system simulations. It is simple to implement in most simulation tools and requires only a limited number of parameters, which reduces computational complexity. Moreover, it provides sufficiently accurate results for steady-state analysis, making it suitable for general design and performance evaluation. However, the model also has limitations. Its accuracy decreases under low irradiance or high-temperature conditions, where non-ideal effects become more pronounced. In addition, it cannot accurately capture recombination losses within the PV cell, which can lead to discrepancies when modeling under dynamic or extreme operating scenarios [14][35].

b Two-Diode Equivalent Model

The two-diode model improves upon the single-diode equivalent by introducing a second diode that accounts for recombination losses in the depletion region of the p-n junction. This addition enhances accuracy, particularly under low irradiance and non-ideal conditions where the single-diode model falls short [12][16][91].

Figure 2-2 illustrates the equivalent circuit of the PV cell in the two-diode model. Its electrical behavior is expressed by formula (2-2) [12][16][32]:

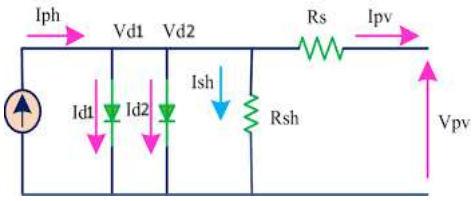


Figure 2-2 Equivalent circuit for PV cell based on two-diode model.

$$I_{PV} = I_{ph} - I_{01}\left(e^{\frac{q\,(V_{PV}+I_{PV}\,R_S)}{n_1\,k\,T}} - 1\right) - I_{02}\left(e^{\frac{q\,(V_{PV}+I_{PV}\,R_S)}{n_2\,k\,T}} - 1\right) - \frac{V_{PV} + I_{PV}\,R_s}{R_{sh}} \quad (2\text{-}2)$$

In this expression, I_{01} and I_{02} represent the saturation currents of the two diodes, while n_1 and n_2 are their ideality factors, generally close to *1* and *2*, respectively.

The model provides a more realistic representation of PV cell performance by accurately capturing recombination and leakage effects, offering better prediction under dynamic operating scenarios. However, it requires more parameters to be identified and is computationally more complex than the single-diode model [12][16][32].

c Multi-Diode (n-Diode) Models

For very high-precision simulations or when modeling advanced photovoltaic technologies such as multijunction solar cells, the multi-diode model is often applied. This approach generalizes the two-diode model by introducing several diodes, each representing a distinct recombination mechanism or junction behavior. The electrical behavior of the model is described by Formula (2-3).

$$I = I_{ph} - \sum_{i=1}^{n} I_{0i}\left(e^{\frac{q\,(V_{PV}+I_{PV}\,R_S)}{n_i\,k\,T}} - 1\right) - \frac{V_{PV} + I_{PV}\,R_{sr}}{R_{sh}} \quad (2\text{-}3)$$

Here, each diode term in the summation corresponds to a particular loss pathway, such as surface recombination, bulk recombination, or grain boundary effects. By explicitly incorporating these mechanisms, the model provides the highest accuracy among equivalent PV cell representations and is particularly suitable for laboratory-grade simulations or the study of innovative solar technologies.

Despite its precision, the multi-diode model presents important limitations. It is computationally intensive, involves the identification of numerous parameters through experimental characterization, and is generally impractical for commercial PV design or real-time applications. For this reason, its use remains largely restricted to research contexts where detailed performance analysis is required.

d PV Module and Array Modeling

While the PV cell represents the fundamental building block of solar power systems, practical applications rely on modules, formed by connecting multiple cells, and arrays, which are

composed of several interconnected modules to achieve the desired voltage and power levels. In these configurations, the method of interconnection determines the electrical characteristics of the system. When cells are connected in series, the output voltage increases while the current remains constant. Conversely, parallel connections increase the current while maintaining the same voltage level [12][16].

The current–voltage (I–V) and power–voltage (P–V) characteristics of a PV module or array can be derived by scaling the single-cell model according to the number of cells connected in series Ns and in parallel Np. Specifically, the overall array voltage is obtained by multiplying the single-cell voltage by the number of series-connected cells, as expressed in Equation (2-4) [12][16].

$$V_{array} = N_s . V_{cell} \tag{2-4}$$

Similarly, the total current output of the array is the sum of the currents of all parallel-connected strings, as shown in Equation (2-5)[16].

$$I_{array} = N_p . I_{cell} \tag{2-5}$$

This modularity makes PV systems highly flexible, allowing engineers to design installations ranging from small rooftop systems to multi-megawatt solar farms. However, real-world performance can deviate from ideal conditions due to mismatch effects caused by partial shading, temperature variations, or slight differences in manufacturing tolerances between individual cells and modules [16][35].

e Comparison of PV Cell Models

Table 2-1 provides a comparative overview of the most commonly used PV cell models: the single-diode, two-diode, and multi-diode approaches [16].

Table 2-1 Comparison of PV cells models.

Feature	Single-Diode Model	Two-Diode Model	Multi-Diode Model
Complexity	Low	Medium	High
Accuracy	Moderate	High	Very High
Parameters Required	Few	More	Many
Suitable For	General-purpose modeling	Enhanced simulation accuracy	Research applications
Recombination Losses	Not included	Included	Fully represented

Selecting the appropriate PV cell model is crucial for accurately simulating system behavior under diverse operating conditions. The single-diode model is generally adequate for basic design studies and real-time control algorithms due to its simplicity and efficiency. However,

the two-diode and multi-diode models provide greater accuracy, making them preferable for detailed performance evaluation, fault diagnosis, and analysis of systems operating under extreme or highly variable environmental conditions [16].

2.2.2 Electrical Characteristics of PV Modules

The electrical performance of PV modules is typically described through their current-voltage (I-V) and power-voltage (P-V) curves, which are essential for identifying the maximum power point (MPP), where conversion efficiency is highest. Under standard test conditions (STC), the I-V curve shows a smooth decrease in current with increasing voltage, while the P-V curve displays a bell-shaped profile with a single peak at the MPP. The short-circuit current I_{sc} corresponds to the maximum current when the terminals are shorted ($V=0$), and the open-circuit voltage V_{oc} is the maximum voltage when no current flows ($I=0$). Between these extremes lies the MPP, expressed mathematically by equation (2-6) [4][14]:

$$P = V \times I \tag{2-6}$$

Figure 2-3 illustrates the standard I-V and P-V characteristics of a PV module. Accurately tracking the MPP under real operating conditions is the central goal of maximum power point tracking (MPPT) techniques [4][14][16][19][64].

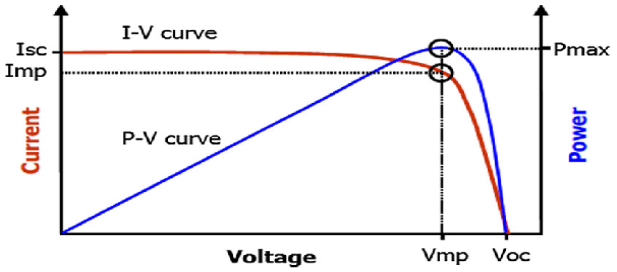


Figure 2-3 I-V and P-V characteristic curves of a PV module.

a Impact of Irradiance

Irradiance, or solar radiation intensity, is the most direct factor influencing PV performance. The short-circuit current I_{sc} is nearly proportional to irradiance, while V_{oc} increases only slightly. Consequently, as irradiance rises, the I-V curve shifts upward, and the P-V curve expands, increasing both current and maximum power. Conversely, reduced irradiance lowers the curves, compressing the power output. These effects are illustrated in Figure 2-4, which shows I–V and P–V characteristics under varying irradiance levels [1][12][18][19].

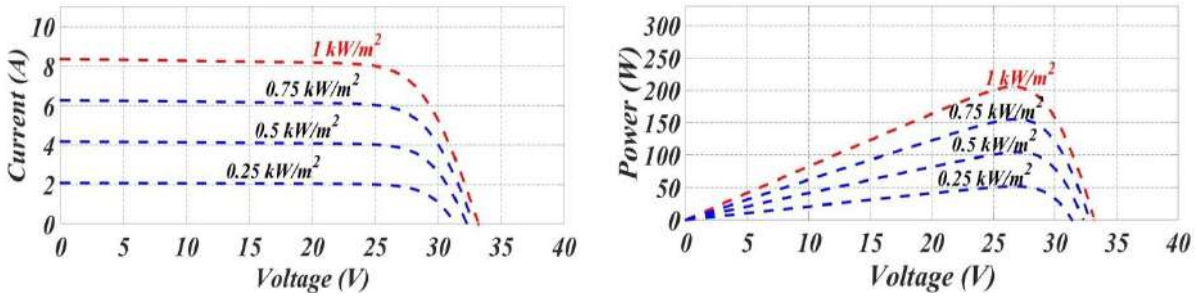


Figure 2-4 I–V and P–V characteristics of a PV module under varying irradiance conditions.

b Impact of Temperature

Temperature has a different but equally important effect. As cell temperature increases, the open-circuit voltage V_{oc} decreases significantly due to enhanced recombination processes, while the short-circuit current I_{sc} rises slightly. The result is a downward shift in the P-V curve and a reduction in overall efficiency. At lower temperatures, voltage and efficiency are higher. This behavior is clearly depicted in Figure 2-5, which presents I-V and P-V characteristics under varying temperature conditions [1][12][18][19].

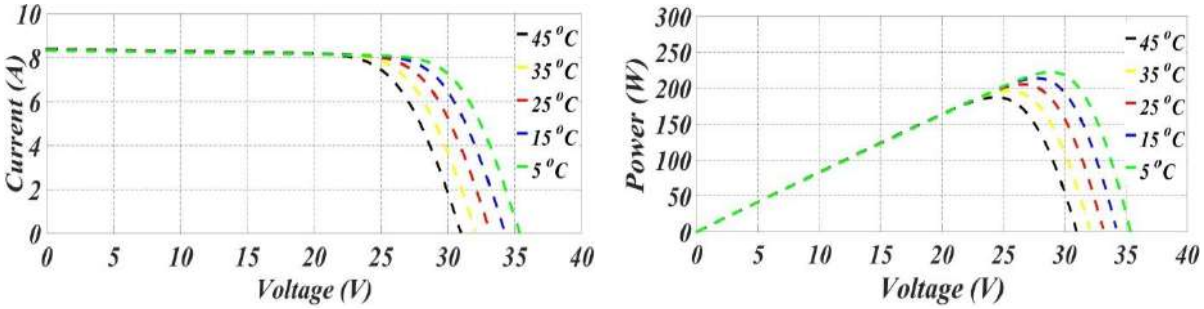


Figure 2-5 I–V and P–V characteristics of a PV module under varying temperature conditions.

c Impact of Partial Shading

Partial shading exposes different cells or modules within a PV array to non-uniform irradiance, which significantly alters its electrical behavior. As shown in Figure 2-6, the I–V and P–V curves become distorted, with the P–V curve displaying multiple local maxima alongside a single global maximum. This complicates maximum power point tracking (MPPT), since conventional algorithms may become trapped at a local peak rather than identifying the true global MPP [12][19][42][58][91].

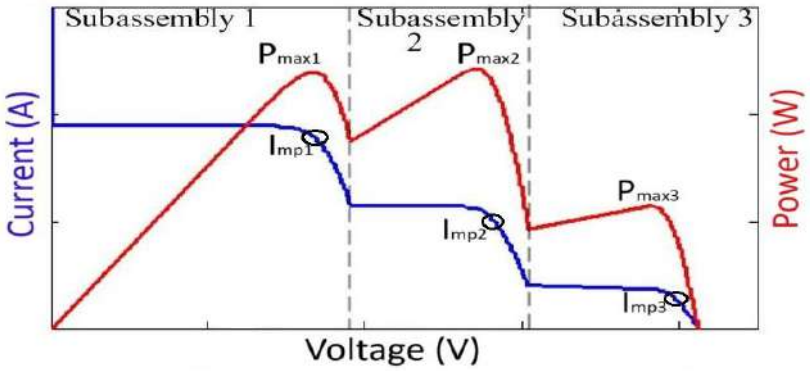


Figure 2-6 I-V and P-V characteristics of a PV array under partial shading, showing multiple MPPs.

Shading also reduces the string current in series-connected modules, leading to mismatch losses and lower overall efficiency. In such cases, shaded cells may act like resistive loads, dissipating power and further degrading system performance. To mitigate these effects, bypass diodes are integrated into PV modules, allowing current to bypass shaded cells and reducing both mismatch losses and the risk of hot spots [12][42][91].

2.2.3 PV System Operating Conditions

PV systems operate under dynamic environmental conditions that directly influence their power output. The main factors include [12][14][20]:

- *Irradiance*: Solar radiation intensity strongly affects the current output of PV cells. Under STC, irradiance is set at *1000W/m²*, with a cell temperature of *25°C* and an air mass of *1.5*. These standardized values allow comparison of PV module performance across manufacturers. In practice, however, irradiance varies throughout the day due to changes in sunlight angle, cloud cover, and atmospheric conditions, leading to significant fluctuations in output [2].
- *Temperature***:** Higher cell temperatures cause a noticeable decrease in the open-circuit voltage (V_{oc}), which reduces overall efficiency. While the short-circuit current (I_{sc}) increases slightly with temperature, the negative effect on voltage dominates, resulting in lower power generation compared to STC.
- *Partial Shading***:** When one or more cells in a module are shaded, current flow is disrupted, and bypass diodes are activated to prevent hot spots. Nevertheless, shading introduces multiple peaks in the P-V curve, complicating MPPT and often reducing system efficiency.

To ensure reliable operation, PV system design must consider both worst-case and frequent scenarios. This involves using thermal models, irradiance profiles, and layout strategies to minimize shading, as well as incorporating advanced MPPT techniques to maximize performance under non-ideal conditions.

2.2.4 Balance of System (BoS) Components

In addition to PV modules, a typical grid-connected PV system requires several BoS components that ensure safe, efficient, and reliable operation. These include electrical, structural, and protective devices that complement the generation units [77].

a Use of Bypass and Blocking Diodes

To mitigate shading effects and prevent reverse current, photovoltaic arrays use bypass and blocking diodes, which play a vital role in protecting modules and enhancing overall system performance. Their placement within a PV array is illustrated in Figure 2-7 [20].

Bypass diodes, shown in green, are connected in parallel with groups of solar cells inside each module. When a cell or part of a module is shaded, it produces less current and may act as a resistive load. In this case, the bypass diode provides an alternate path for current, preventing overheating and protecting the shaded cells from damage. This protection reduces mismatch losses but introduces characteristic steps in the I-V curve and multiple peaks in the P–V curve. The number of peaks depends on how many bypass diodes are activated, with only one representing the true global MPP [20].

Blocking diodes, shown in red, are installed in series with each module string. Their main function is to stop reverse current flow from the battery or the grid back into the PV modules, which can occur at night or during periods of very low irradiance. Without blocking diodes, reverse currents could discharge storage devices or damage PV modules [20].

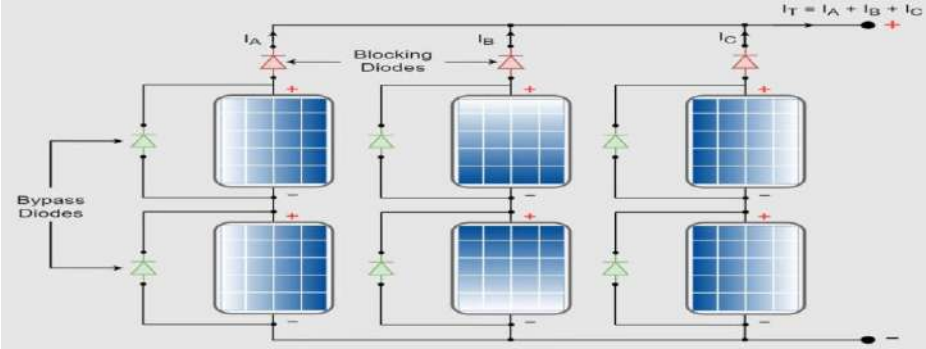


Figure 2-7 Configuration of bypass and blocking diodes in a PV array.

Together, these diodes ensure safe and reliable operation of PV systems. Bypass diodes protect against partial shading and localized heating, while blocking diodes prevent reverse current losses. Their combined use improves system efficiency, maintains stable energy production, and extends the lifespan of PV installations.

b Mounting Structures

Mounting systems are essential components of PV installations, as they provide the physical support required to hold solar panels in place while optimizing their exposure to sunlight. Their primary role is to maintain PV modules at the correct tilt angle and orientation, which significantly affects the amount of solar energy captured and, consequently, the overall system efficiency. The optimal tilt angle typically depends on the geographic latitude, seasonal variations, and specific energy yield objectives. In many systems, fixed-tilt mounting structures are used due to their simplicity and cost-effectiveness, while in more advanced installations, single-axis or dual-axis solar trackers are employed to continuously adjust panel orientation, thereby maximizing energy harvest throughout the day and across different seasons.

In addition to optimizing solar capture, mounting systems must ensure mechanical stability and durability under various environmental conditions. This includes resistance to wind loads, snow accumulation, seismic activity, and long-term exposure to UV radiation and corrosion. Materials such as galvanized steel and anodized aluminum are commonly used to provide both structural strength and weather resistance.

Proper design of mounting systems also facilitates ease of installation and maintenance, enabling technicians to safely access panels for cleaning, inspection, or replacement. Furthermore, the mounting configuration must consider spacing between panels to avoid self-shading, allow adequate airflow for passive cooling, and minimize thermal stresses, which can impact PV efficiency.

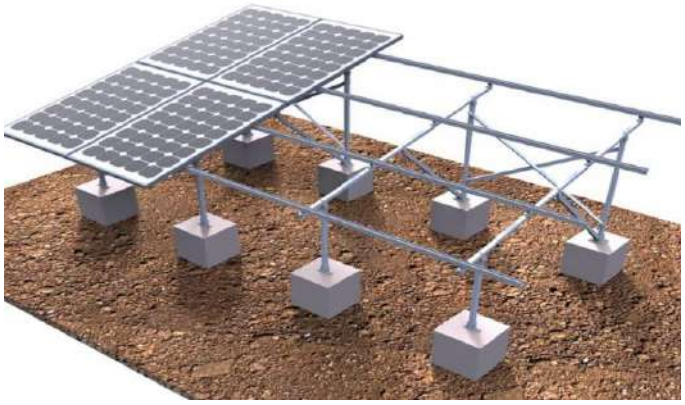


Figure 2-8 Mounting systems for PV panels.

c DC Cabling and Junction Boxes

DC cabling and junction boxes form the electrical backbone of a photovoltaic system, ensuring efficient and safe transmission of the generated power from PV modules to the inverter. Their design and sizing are critical to minimize electrical losses, guarantee safety, and comply with international standards.

DC Cabling connects individual solar modules within a string and subsequently links multiple strings together. These cables are specifically designed to handle direct current under outdoor conditions, featuring UV resistance, double insulation, flame retardancy, and high mechanical strength. The cross-sectional area of the conductors must be carefully selected to minimize voltage drop and resistive losses, particularly in large-scale installations where cable lengths can be significant. Inadequately sized cables can lead to overheating, reduced efficiency, or even fire hazards. Proper routing and protection against abrasion, rodents, and environmental stress are also vital considerations.

Junction Boxes act as central nodes that collect and combine outputs from multiple PV strings. Located either at the module level or array level, they typically house electrical connectors, fuses, surge protection devices (SPDs), and monitoring sensors. Their enclosure is designed to meet high ingress protection (IP) ratings, ensuring resistance against dust, moisture, and temperature fluctuations. Junction boxes not only simplify the wiring configuration but also provide overcurrent protection and safe disconnection points for maintenance.

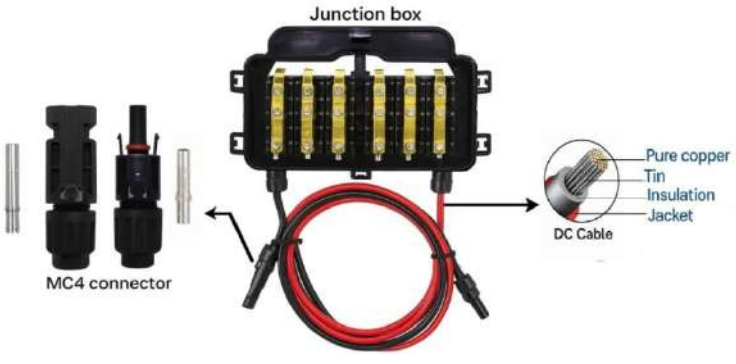


Figure 2-9 DC Cabling and junction boxes.

d Inverters

A grid-connected PV inverter serves as a crucial link between the PV array and the utility grid, converting the direct current produced by solar modules into alternating current that complies with grid standards for voltage, frequency, and power quality. Its main function is MPPT, which ensures the PV system operates at the optimal point on the I-V curve to maximize energy output despite changes in irradiance and temperature. Most grid-tied inverters utilize voltage-source inverter (VSI) technology with pulse width modulation (PWM) to generate controlled AC waveforms. Since PWM can generate high-frequency harmonics, filters like inductors or LCL networks are installed at the output to produce a clean, sinusoidal current for feeding into the grid [23][36].

In many systems, a DC-DC converter is positioned between the PV array and the inverter to regulate the DC bus voltage and perform MPPT. This component adjusts the fluctuating PV voltage to a stable level needed by the inverter, boosting efficiency and dynamic response. However, in single-stage configurations, the inverter directly manages MPPT and grid injection without a separate DC-DC stage [90].

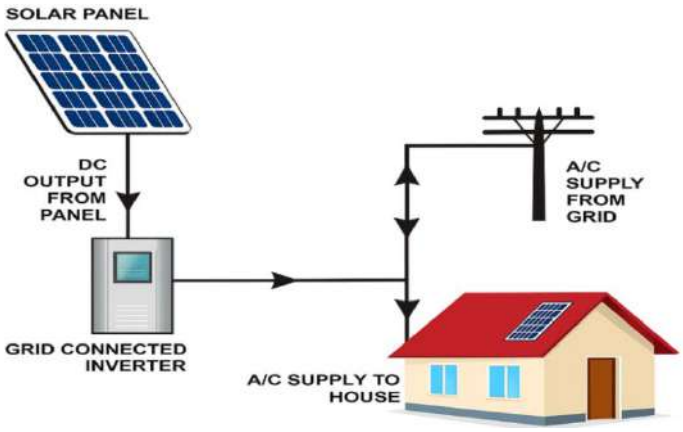


Figure 2-10 Basic schematic of a grid-connected PV system with an inverter.

Beyond converting DC to AC, modern PV inverters also offer auxiliary functions such as reactive power compensation, grid synchronization, and protection against reverse currents, thereby improving both energy efficiency and grid stability [9].

e Protection Devices

Protection devices are essential components of PV systems, ensuring both the safety of equipment and the reliability of power delivery. They are designed to protect against overcurrents, short circuits, ground faults, and voltage surges that could damage system components or pose risks to users [77].

Fuses and circuit breakers safeguard the system by disconnecting faulty sections during overcurrent conditions, preventing overheating and fire hazards. SPDs, illustrated in Figure 2-11, protect sensitive electronics, such as inverters and monitoring systems, against transient overvoltages caused by lightning strikes or grid disturbances. Ground fault protection is also critical, as it minimizes the risk of electric shock and reduces the likelihood of fire in case of insulation failures.

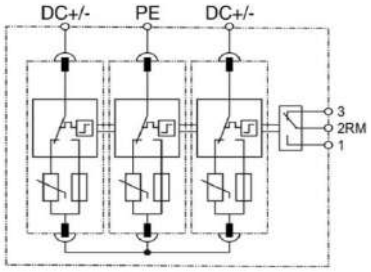


Figure 2-11 Surge protection device symbol.

The proper selection and coordination of these devices are crucial to guarantee safe operation, minimize downtime, and comply with international standards for grid-connected PV systems.

- ***Monitoring Systems***

Monitoring systems are integral to modern PV installations, as they collect real-time performance data and enable both local and remote supervision. These systems track key parameters such as voltage, current, power output, energy yield, irradiance, and module temperature. By continuously analyzing this information, monitoring platforms help detect performance degradation, identify faults, and ensure that the PV system operates at its expected efficiency.

Advanced monitoring solutions also provide remote access, allowing operators to supervise system performance, schedule maintenance, and implement corrective actions without the need for on-site inspection. This capability is particularly valuable in large-scale solar farms and distributed generation systems, where manual monitoring would be impractical.

The selection and proper integration of monitoring systems are crucial for reliability and efficiency. Combined with appropriately sized BoS components, they help minimize downtime, reduce energy losses, and ensure safe, long-term operation of grid-connected PV systems.

2.3 Power Conversion Architectures

The efficiency and stability of a grid-connected PV system depend heavily on its power conversion architecture. The role of the power conversion stage is to condition the variable DC power generated by the PV modules into a form that is suitable for grid injection, typically regulated AC power with specific voltage, frequency, and harmonic characteristics. Different converter topologies and system architectures can be adopted based on design criteria such as control flexibility, component cost, efficiency, power level, and grid compliance. This section discusses the most common conversion structures, the associated power electronic devices, and their implications on system performance [2].

2.3.1 Single-Stage and Two-Stage Architectures

Grid-connected PV systems are generally classified into two main power conversion structures, single-stage and two-stage architectures. Each approach has specific advantages

and limitations, and the choice depends on factors such as system size, power quality requirements, and control flexibility [2][41].

a Single-Stage Architecture

In a single-stage configuration, a single inverter performs all the essential functions of a grid-connected PV system, including MPPT, DC-AC conversion, and synchronization with the grid. Figure 2-12 presents the block diagram of this configuration, illustrating how a single power conversion stage manages all these tasks. This architecture reduces the number of components, lowers the overall cost, makes the design more compact, and minimizes switching losses by eliminating intermediate conversion stages. However, its main drawback lies in the limited control flexibility, making it more difficult to handle wide variations in input voltage. For this reason, single-stage systems are generally less suitable for high-power installations or environments with rapidly fluctuating irradiance [2][43][45][48][62].

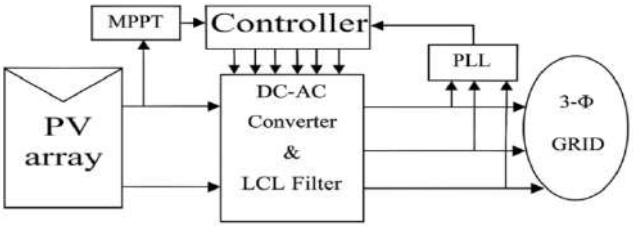


Figure 2-12 Block diagram of a single-stage grid-connected PV system.

b Two-Stage Architecture

In a two-stage architecture, the conversion process is divided into two separate stages. The first stage is a DC-DC converter, which is primarily responsible for Maximum Power Point Tracking (MPPT) and for maintaining a stable DC-link voltage. The second stage is a DC-AC inverter that ensures efficient power injection into the grid while meeting grid synchronization requirements. This separation of functions provides better control over each stage and makes it easier to stabilize the DC-link voltage. Figure 2-13 presents the block diagram of this configuration. The two-stage system also demonstrates superior performance under dynamic irradiance conditions and partial shading, making it more reliable in challenging operating environments. However, these advantages come at the expense of higher component count, greater design complexity, and increased cost, in addition to additional conversion losses due to multiple processing stages [1][2][14][46].

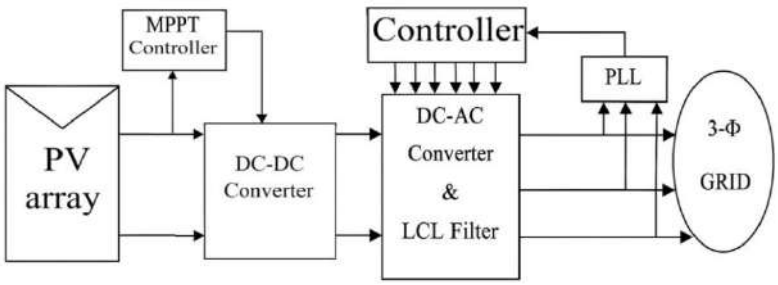


Figure 2-13 Block diagram of a two-stage PV grid-connected system.

2.3.2 DC-DC Converter Types

DC–DC converters are fundamental in photovoltaic (PV) systems, as they regulate the PV output voltage, perform maximum power point tracking (MPPT), and condition the energy before delivering it to the inverter. The three most commonly used topologies are the boost, buck, and buck–boost converters, each with distinct characteristics and applications [12][14].

a Boost Converter

The boost converter steps up the PV array voltage to the higher DC-link voltage required by the inverter. Its operation relies on storing energy in the inductor during the ON-state of the switch and transferring it to the load during the OFF-state. The steady-state voltage conversion ratio is defined in expression (2-7) [1][12][14][26][90].

$$V_{dc} = \frac{V_{PV}}{1 - D} \tag{2-7}$$

Where V_{dc} is the output voltage, V_{PV} is the PV input voltage, and D is the duty cycle.

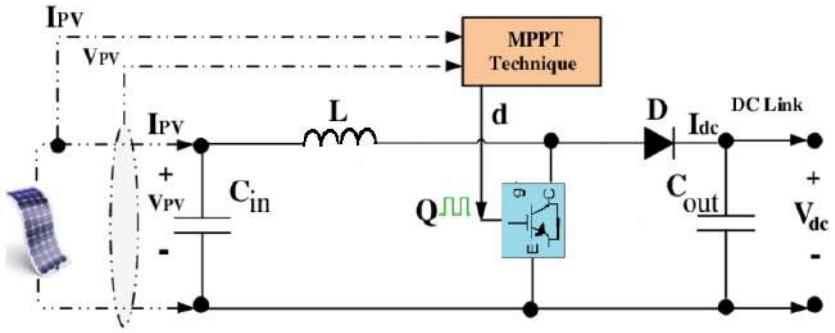


Figure 2-14 Equivalent circuit of a boost DC-DC converter.

The design of a boost converter, shown in Figure 2.14, requires proper sizing of its passive components to guarantee stable and efficient operation. The inductor value is given by equation (2-8) [16][22][45][53].

$$L = \frac{V_{PV} \,.\, D}{\Delta I_L \,.\, f_{sw}} \tag{2-8}$$

Where V_{PV} is the PV input voltage, D is the duty cycle, ΔI_L is the inductor current ripple, and fsw is the switching frequency. The output capacitor, which filters the voltage before supplying the DC-link, is calculated using equation (2-9) [45][53].

$$C_{out} = \frac{I_{dc} \,.\, D}{\Delta V_{dc} \,.\, f_{sw}} \tag{2-9}$$

With I_{dc} the output current and ΔV_{dc} are the maximum acceptable DC voltage ripple. In addition, the input capacitor must be sized to reduce fluctuations on the PV side and is expressed by (2-10) [12][45][53].

$$C_{in} \geq \frac{I_{PV} \,.\, D}{\Delta V_{PV} \,.\, f_{sw}} \tag{2-10}$$

Where I_{PV} is the PV current and ΔV_{PV} the permissible input voltage ripple.

Boost converters in PV systems typically use Metal-Oxide-Semiconductor Field-Effect Transistors (MOSFETs) for switching when operating at higher frequencies between *20kHz* and *100kHz*, and lower power, due to their fast switching speed and low conduction losses. At higher power levels and lower switching frequencies below *20kHz*, IGBTs are often preferred because they handle higher currents efficiently [12][14][26][45].

b Buck Converter

The buck converter, shown in Figure 2-15, reduces the input voltage to a lower output voltage, typically used when the PV voltage exceeds the required DC-link voltage. Its input-output relation is defined in expression (2-11) [12][14][90].

$$V_{out} = D.V_{in} \tag{2-11}$$

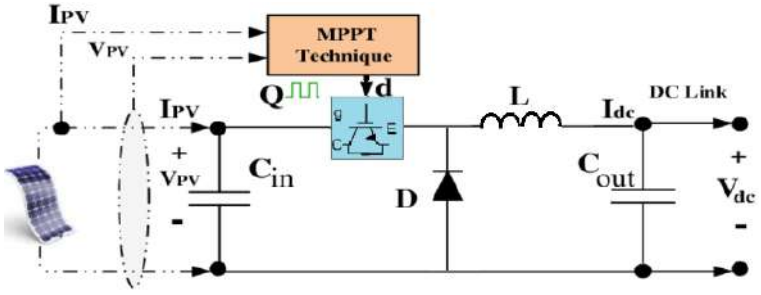


Figure 2-15 Equivalent circuit of a buck DC-DC converter.

The main design equations for the inductor, output capacitor, and input capacitor are given by equations (2-12), (2-13), and (2-14), respectively [12].

$$L = \frac{(V_{PV} - V_{dc}).D}{\Delta I_L \,.\, f_{sw}} \tag{2-12}$$

$$C_{out} = \frac{(1 - D).I_{dc}}{\Delta V_{out} \,.\, f_{sw}} \tag{2-13}$$

$$C_{in} \geq \frac{I_{PV} \,.D.(1 - D)}{\Delta V_{PV} \,.f_{sw}} \tag{2-14}$$

Buck converters in PV systems generally rely on MOSFETs because they must operate at relatively high frequencies to minimize inductor size. At larger scales, IGBTs are used but usually combined with lower switching frequencies to limit losses [14][16].

c Buck-Boost Converter

The buck-boost converter provides operational flexibility by allowing both voltage step-up and step-down, depending on the duty cycle, which makes it particularly suitable for PV systems operating under variable irradiance conditions. Its steady-state voltage conversion ratio is expressed by equation (2-15) [12][14][90].

$$V_{dc} = \frac{V_{PV} \,.\, D}{1 - D} \tag{2-15}$$

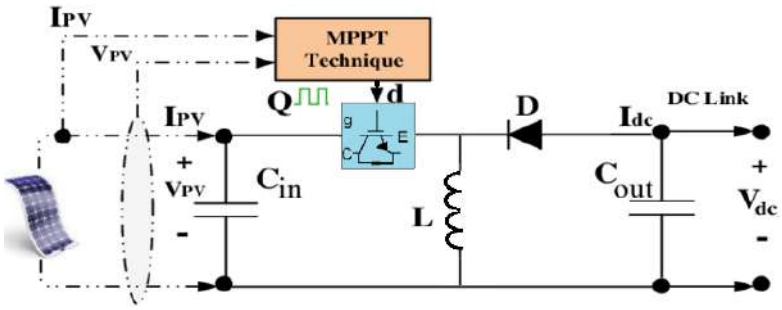


Figure 2-16 Equivalent circuit of a buck-boost DC-DC converter.

Figure 2-16 illustrates the equivalent circuit of a buck–boost DC-DC converter. The inductor value, determined by equation (2-16), depends on the PV voltage, duty cycle, current ripple, and switching frequency [12].

$$L = \frac{V_{PV} \,.\, D}{\Delta I_L \,.\, f_{sw}} \tag{2-16}$$

The output capacitor, shown in equation (2-17), ensures a stable DC-link voltage, while the input capacitor, given by equation (2-18), maintains voltage stability at the converter input.

$$C_{out} = \frac{D \,.\, I_{dc}}{\Delta V_{out} \,.\, f_{sw} \,.\, (1 - D)} \tag{2-17}$$

$$C_{in} \geq \frac{I_{PV} \,.\, D}{\Delta V_{PV} \,.\, f_{sw}} \tag{2-18}$$

In terms of switching devices, MOSFETs are commonly employed in low- and medium-power PV systems due to their fast switching capability and efficiency at frequencies above *50kHz*, which allows for smaller passive components. Conversely, Insulated Gate Bipolar Transistors (IGBTs) are preferred in high-power applications for their superior current-handling capacity, although their switching frequencies are typically limited to the *5-20 kHz* range to minimize switching losses [12][14].

2.3.3 Inverter Topologies

The inverter is the core component of a grid-connected PV system, tasked with converting DC power from the PV array into AC power compatible with grid voltage and frequency [8].

Its design greatly affects the power quality, efficiency, and compliance with grid codes. Modern PV systems use a variety of inverter topologies, which can be broadly categorized into conventional two-level inverters and more advanced multilevel inverters [16][17].

a Two-Level Voltage Source Inverter (VSI)

The two-level voltage source inverter (VSI) represents the simplest and most commonly used inverter topology in grid-connected PV systems. It consists of six semiconductor switches, either IGBTs or MOSFETs, arranged in a three-phase bridge configuration [66][67]. Each leg of the inverter alternately connects the output to either the positive or negative terminal of the DC-link voltage, thereby generating the desired AC waveform. Figure 2-17 presents the typical power circuit of a two-level inverter [1][16][44][62].

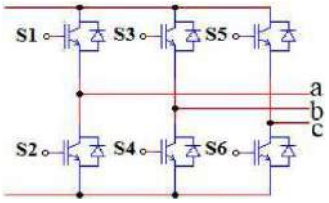


Figure 2-17 Two-level inverter power circuit.

This configuration offers several advantages, including a simple structure, ease of control, and well-established industrial implementation, making it cost-effective for low and medium-power applications. However, it also presents certain limitations. The output voltage waveform contains significant harmonic distortion, leading to higher total harmonic distortion (THD) and the need for bulky filters to comply with grid standards. Additionally, each switch is subjected to the full DC-link voltage, resulting in higher voltage stress and potential reliability concerns in high-power applications [44][45][66].

b Multilevel Inverter Topologies

Multilevel inverters are advanced converter configurations that generate stepped voltage waveforms using multiple voltage levels. They are particularly well-suited for medium- and high-power PV systems due to their excellent output voltage quality, reduced switching losses, and lower harmonic distortion compared to conventional two-level inverters. These topologies are designed to improve efficiency, minimize the size of passive filters, and enhance voltage stress distribution across semiconductor devices [45][68][91].

i. Neutral Point Clamped (NPC) Three-Level Inverter

The NPC inverter uses clamping diodes to connect the neutral point of the DC-link capacitors, thereby producing three voltage levels per phase: positive, zero, and negative. This topology is one of the most established configurations in grid-connected PV applications due to its reliability and moderate control complexity [1][12][45][66].

As illustrated in Figure 2.18, the NPC inverter achieves lower total harmonic distortion (THD) and reduced switching losses compared to a conventional two-level inverter [32]. However, it faces challenges related to neutral-point voltage imbalance, which requires dedicated control strategies to maintain voltage stability. Despite this, it remains a preferred solution in medium-voltage PV systems [12][41][44][66][91].

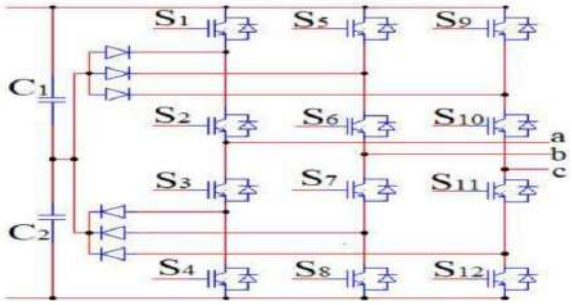


Figure 2-18 Three-level NPC inverter power circuit.

ii. T-Type Three-Level Inverter

The T-Type inverter is an enhanced variant of the NPC topology that replaces the clamping diodes with bidirectional switches, improving the efficiency and reducing the number of conduction paths. This inverter delivers superior performance, particularly under partial load, due to its lower conduction and switching losses [91].

As shown in Figure 2-19, the T-Type inverter features a more compact structure, which makes it attractive for modern PV systems where efficiency and space optimization are crucial. However, it requires precise control of gate signals to avoid switching overlap and ensure safe operation, which adds slight control complexity [68][91].

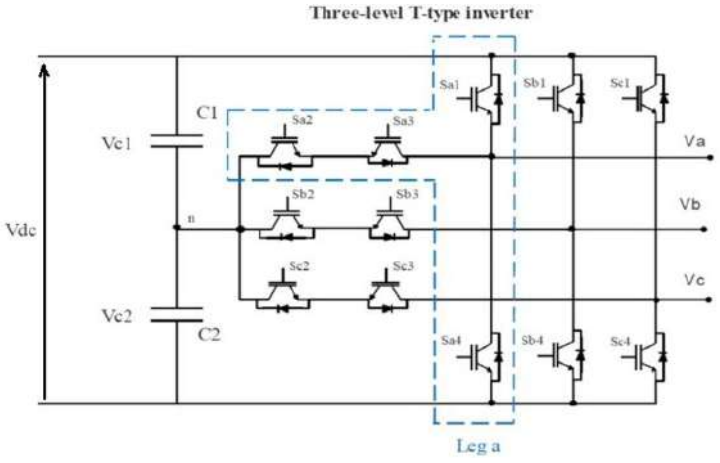


Figure 2-19 T-Type three-level inverter power circuit.

iii. Flying Capacitor Multilevel Inverter (FCMI)

The FCMI employs capacitors connected in series to generate intermediate voltage levels between the main DC rails. Each “flying” capacitor helps to balance voltage across the switches, resulting in an improved output waveform and excellent voltage quality [93].

Figure 2-20 presents the structure of the flying capacitor inverter, which offers redundancy and modularity, making it suitable for high-performance PV and industrial applications. However, it requires complex voltage balancing control and additional sensing circuits, increasing design complexity and cost [68][93].

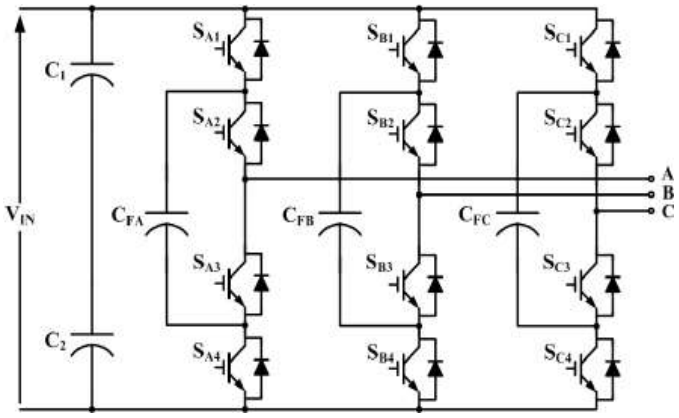


Figure 2-20 Flying Capacitor Three-level Inverter power circuit.

iv. Cascaded H-Bridge (CHB) Inverter

The CHB inverter consists of several H-bridge cells connected in series, with each cell powered by an isolated DC source such as a PV string. This modular configuration enables scalability and high-quality sinusoidal output with minimal harmonic distortion.

As depicted in Figure 2-21, each H-bridge generates a distinct voltage level, and the combination of these levels forms a near-sinusoidal output. This topology is ideal for large-scale PV installations and distributed generation systems. However, it requires multiple isolated DC sources or converters, which increases the system footprint and cost [68].

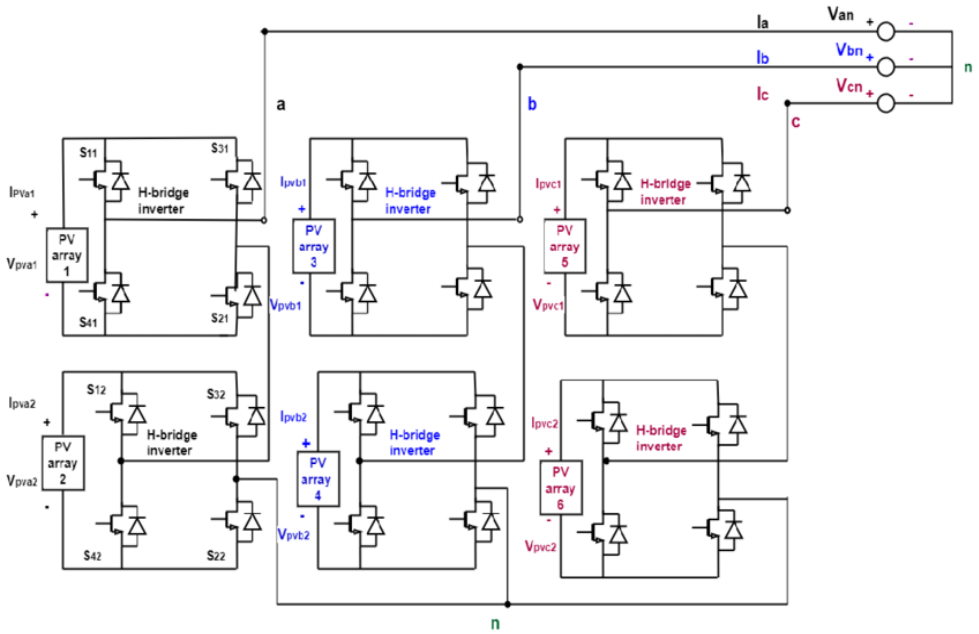


Figure 2-21 Cascaded H-Bridge inverter power circuit.

c Benefits and Selection of Multilevel Inverters in PV Systems

Multilevel inverters offer significant advantages in PV grid-connected systems, particularly in terms of power quality, efficiency, and grid compliance. By producing stepped voltage waveforms that closely approximate a sinusoidal output, they minimize harmonic distortion and reduce the need for bulky filtering components. Their lower switching frequencies and reduced voltage stress on semiconductor devices contribute to improved overall efficiency and reliability. Additionally, the smaller voltage jumps between levels result in reduced electromagnetic interference (EMI), enhancing the electromagnetic compatibility of the system. These characteristics make multilevel inverters highly scalable, allowing their deployment in medium- and large-scale PV plants, and ensuring compliance with grid standards such as IEEE 1547 and IEC 61727 regarding THD and power factor performance.

The selection of an appropriate inverter topology depends largely on the application scale, performance requirements, and cost considerations. For residential and small commercial systems, conventional two-level inverters remain the preferred choice due to their simplicity, compactness, and lower cost. In contrast, medium- and large-scale PV installations typically benefit from three-level NPC or T-Type inverters, which provide a balanced compromise between performance, efficiency, and system complexity. For high-voltage or modular PV systems, such as those used in utility-scale solar farms, more advanced configurations like CHB or FCMI may be adopted, despite their higher control and design complexity [68].

Overall, multilevel inverter topologies have transformed grid-connected PV systems by enabling superior voltage waveform quality, reducing harmonic distortion, and facilitating the direct integration of renewable power into higher-voltage grids. Their versatility and scalability make them a cornerstone technology for the next generation of high-performance PV systems, meeting both the growing energy demands and the increasingly stringent international grid codes.

2.3.4 Filtering and Grid Interfacing

Grid-connected PV systems rely on power electronic inverters to convert DC power from solar arrays into AC power compatible with the utility grid. These inverters operate using high-frequency switching, which introduces unwanted harmonic components into the output voltage and current. To comply with international grid code standards such as IEEE 519 and IEC 61000, it is necessary to mitigate these harmonics to maintain acceptable power quality [76]. Filters are therefore integrated between the inverter and the grid to smooth out high-frequency components and enable efficient, high-quality energy transfer [2][8][9][37].

a Passive Filters

Passive filters are composed of passive elements such as inductors (L) and capacitors (C), or combinations of both. Their primary function is to attenuate the high-frequency switching

harmonics generated by the inverter. They are widely used in PV applications due to their simplicity, robustness, and low implementation cost [18][43][71].

The most common configurations include the L filter, consisting of a single inductor; the LC filter [37][40], which provides enhanced attenuation through the combination of an inductor and a capacitor; and the LCL filter, which adds a second inductor for superior harmonic suppression. Among these, the LCL topology is most frequently employed in grid-connected PV systems because it offers an optimal balance between filtering efficiency and compactness. Figure 2-22 illustrates a typical LCL filter used in grid-connected PV inverters [9][36][75][77][93].

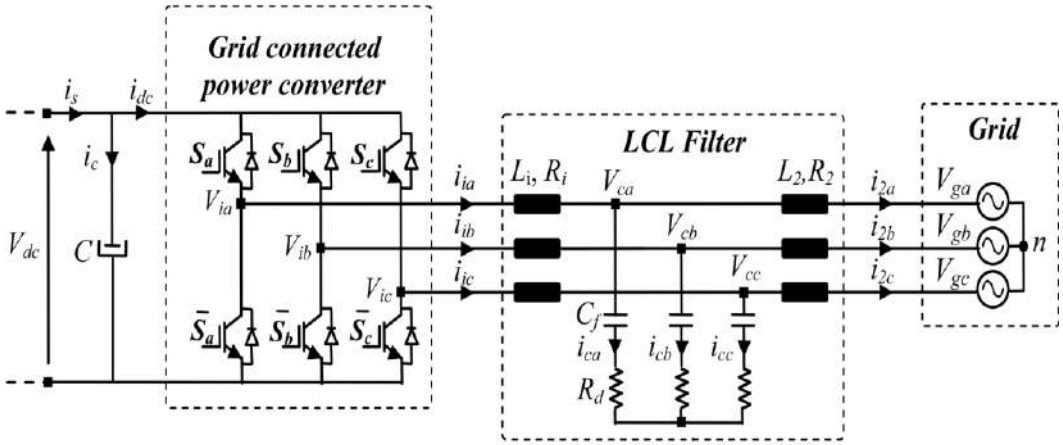


Figure 2-22 LCL filter configuration for grid-connected PV inverter systems.

Although passive filters are reliable and require no external control or power supply, they have certain drawbacks. Their filtering characteristics are fixed, making them less effective under varying operating conditions, and they may introduce resonance at specific frequencies, necessitating damping circuits. Moreover, in high-power applications, passive filters can become bulky and costly due to the large inductors required [75].

b Active Filters

Active filters are advanced power electronic devices designed to dynamically cancel harmonics by injecting compensating currents or voltages. Unlike passive filters, they can adapt in real time to changing grid and load conditions. Active filters are typically implemented using voltage source inverters (VSI) controlled by high-speed digital signal processors (DSP) or field-programmable gate arrays (FPGA) [2][8].

Depending on their connection, active filters can be shunt, series, or hybrid. Shunt active filters are connected in parallel with the grid to eliminate current harmonics, while series active filters are connected in series to correct voltage distortions. Hybrid configurations combine both passive and active elements to achieve a compromise between cost and dynamic performance. A schematic representation of an active filtering system is shown in Figure 2-23 [2][47].

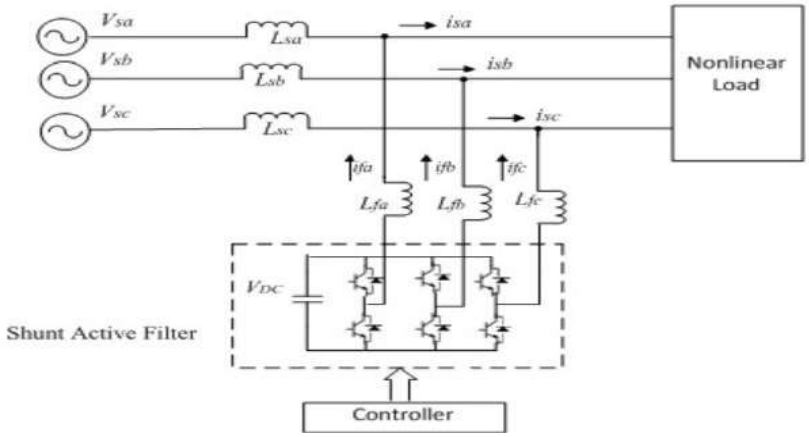


Figure 2-23 Configuration of a shunt active filter connected to the grid.

Active filters offer significant advantages, including adaptability, programmability, and the ability to provide both harmonic compensation and reactive power support. They are particularly effective in systems subject to variable loads or distorted grid voltages. However, their main limitations are higher cost, greater control complexity, and potential switching noise if not properly designed or filtered [47].

c Filter Selection and Grid Synchronization in Grid-Connected PV Inverters

The integration of PV systems into the electrical grid requires not only efficient power conversion but also compliance with strict power quality and synchronization standards. One of the main challenges in grid-connected inverter operation is the mitigation of switching harmonics and the assurance of sinusoidal current injection into the grid. To achieve this, appropriate filtering and precise grid synchronization mechanisms are essential.

The selection of a filtering method depends largely on the system size, performance requirements, and cost considerations. In residential and small-scale PV systems, simple passive filters, particularly LCL configurations, are typically sufficient to attenuate high-frequency harmonics and maintain THD within the limits prescribed by grid codes such as IEEE 519 and IEC 61000 [21]. These filters are cost-effective and reliable, though they require careful design to avoid resonance issues. For large-scale or high-performance systems operating under dynamic grid conditions, active filters are preferred because they can adaptively compensate for both current and voltage harmonics. In utility-scale solar plants, hybrid filters, which combine passive and active components, are often implemented to achieve an optimal balance between cost, harmonic suppression, and dynamic performance [2].

Beyond harmonic mitigation, the grid interface of a PV inverter plays a critical role in ensuring synchronized and stable power delivery. Synchronization is achieved through algorithms such as the Phase-Locked Loop (PLL) or the Dual Second-Order Generalized Integrator PLL (DSOGI-PLL), which align the inverter output phase and frequency precisely with that of the grid. This ensures that the current injected into the grid is in phase with the grid voltage, maintaining a unity power factor under normal operation. Moreover, grid-

connected inverters are designed to control both active and reactive power, allowing them to contribute to voltage regulation and overall grid stability [2].

Reactive power support is particularly important in weak or distributed networks, where voltage fluctuations can affect power quality. Modern PV inverters are capable of dynamically adjusting reactive power injection or absorption based on grid conditions, improving local voltage profiles and supporting grid reliability. Additionally, advanced control systems integrate islanding detection mechanisms to identify unintentional grid disconnections. When islanding occurs, the inverter immediately ceases power injection to prevent unsafe standalone operation and protect maintenance personnel.

In summary, proper filter design and robust grid synchronization control are indispensable for the safe and efficient operation of grid-connected PV systems. While passive filters remain suitable for small and medium installations, active and hybrid filtering solutions are increasingly adopted in high-performance and utility-scale systems due to their adaptability and superior harmonic compensation. Combined with accurate PLL-based synchronization, these measures ensure that PV inverters deliver clean, stable, and compliant power, thereby supporting the continued expansion of renewable energy integration into modern electrical grids.

2.3.5 Emerging Architectures

Recent research explores novel configurations that improve system flexibility and reliability:
- *Multi-string converters*: Each PV string has its own DC-DC converter, improving MPPT accuracy and reducing mismatch losses.
- *Modular multilevel converters (MMC)*: Offer scalability and high-quality waveforms, but are complex and expensive.
- *Transformerless inverters*: Improve efficiency and reduce cost, but require advanced leakage current control.

These innovations are particularly useful in large-scale installations or where energy management is complex.

The power conversion architecture forms the backbone of a grid-connected PV system, determining its efficiency, flexibility, and compliance with grid standards. While single-stage systems offer simplicity and cost-effectiveness, two-stage systems provide superior control and adaptability under dynamic environmental conditions. Proper selection and design of DC-DC converters, inverters, and filters are essential for maximizing energy harvest, minimizing losses, and ensuring safe, stable grid interaction. The next section will delve into the MPPT techniques, a critical element of energy optimization in PV systems.

2.4 Maximum Power Point Tracking Techniques

The performance of a PV system greatly depends on its ability to continuously operate at its MPP under changing environmental conditions. Since solar irradiance and temperature vary

throughout the day, the output characteristics of the PV array (especially the power-voltage curve) also change, making it essential to use MPPT algorithms to ensure maximum energy harvesting at all times [12][18][63].

This section summarizes the main MPPT techniques used in grid-connected PV systems. These methods are grouped into conventional, intelligent (AI-based), and metaheuristic optimization approaches [32]. Each category is analyzed based on its operating principle, performance, and adaptability to changing environmental conditions. The comparison underscores their respective strengths and limitations, focusing on efficiency improvement and system reliability enhancement [12].

2.4.1 Conventional MPPT Methods

Conventional MPPT algorithms are widely used due to their simplicity and ease of implementation. These methods are suitable for most applications but may suffer from performance limitations under rapidly changing or partial shading conditions [64].

a Perturb and Observe Method

The Perturb and Observe (P&O) method is one of the most commonly used MPPT techniques due to its simplicity and ease of implementation. It operates by periodically perturbing the operating voltage (or duty cycle) of the PV system and observing the corresponding change in output power. If the power increases after a perturbation, the next perturbation continues in the same direction; otherwise, the direction is reversed. This iterative process drives the system toward the Maximum Power Point (MPP). However, under steady-state conditions, the method tends to oscillate around the MPP, causing small power losses. Moreover, under rapidly changing irradiance, it may misinterpret power variations caused by irradiance fluctuations rather than by voltage perturbations, leading to tracking errors. Figure 2-24 illustrates the flowchart of the P&O algorithm [1][2][14][47][58][63].

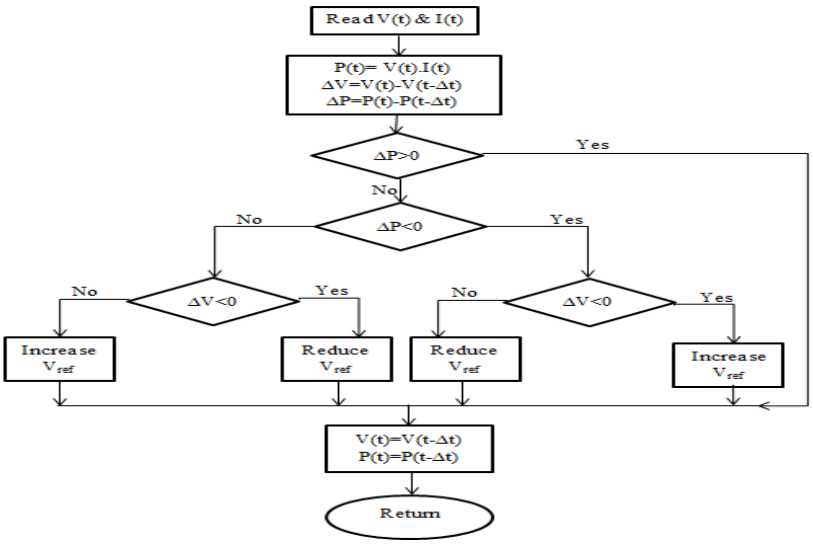


Figure 2-24 Flowchart of the P&O MPPT algorithm.

b Incremental Conductance Method

The Incremental Conductance (INC) method determines the MPP by comparing the instantaneous conductance *I/V* to the incremental conductance *dI/dV*. At the MPP, the slope of the P–V curve is zero, which means $dP/dV = 0$ or equivalently $dI/dV = -I/V$. When $dI/dV > -I/V$, the operating point is to the left of the MPP, and when $dI/dV < -I/V$, it is to the right [12][16][18][26]. The algorithm continuously adjusts the voltage until the equality condition is satisfied. This method achieves faster and more accurate tracking compared to P&O, particularly under rapidly varying irradiance. However, it requires real-time differentiation and precise current and voltage measurements, making it more computationally complex and sensitive to noise. Figure 2-25 presents the flowchart of the Incremental Conductance MPPT algorithm [32][58][63][64][65].

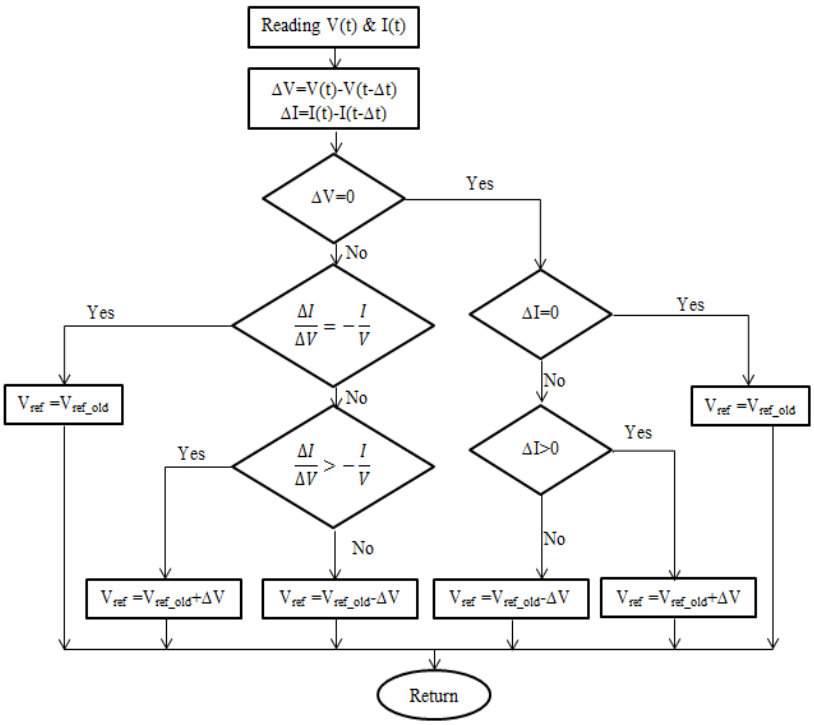


Figure 2-25 Flowchart of the INC MPPT algorithm.

c Constant Voltage (CV) and Constant Current (CC) Methods

The Constant Voltage (CV) and Constant Current (CC) methods are among the simplest MPPT strategies. In these techniques, the operating point of the PV system is fixed at a predetermined fraction of the open-circuit voltage V_{oc} or short-circuit current I_{sc}, typically between *70%* and *80%*. Since V_{oc} and I_{sc} are approximately proportional to irradiance, this approximation yields a suboptimal but acceptable operating point for low-cost systems. Although these methods eliminate the need for continuous tracking and reduce sensor requirements, they are not adaptive to dynamic environmental variations, leading to significant efficiency losses under fluctuating irradiance or temperature. Figure 2-26 shows the basic concept of the Constant Voltage MPPT method [58].

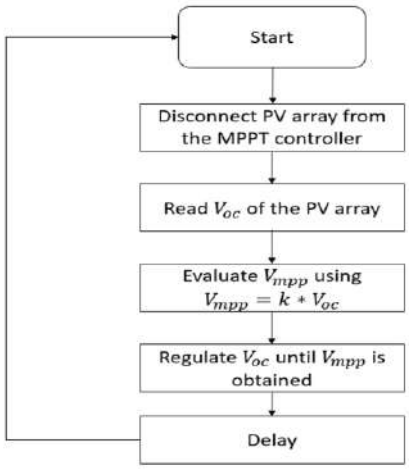


Figure 2-26 Conceptual diagram of the CV MPPT method.

d PI-Based MPPT Control

The PI-based MPPT control method employs a Proportional-Integral (PI) controller to regulate the duty cycle of the DC-DC converter, ensuring that the PV array operates at its optimal power point. The control variable, usually the PV voltage or power, is compared to a reference value derived from the MPP condition. The error is processed by the PI controller, which adjusts the converter's duty ratio to minimize the error. This approach provides smooth convergence, stable operation, and reduced oscillations around the MPP. Nevertheless, the effectiveness of this method depends on proper tuning of the PI gains, and its performance may degrade during fast irradiance changes if the controller parameters are not adapted. Figure 2-27 illustrates the control structure of a PI-based MPPT system [1][14].

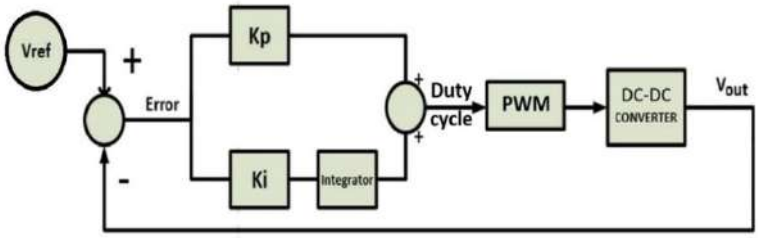


Figure 2-27 Control block diagram of the PI-based MPPT method.

2.4.2 Intelligent MPPT Techniques

Intelligent MPPT methods employ artificial intelligence (AI) principles to efficiently track the Maximum Power Point of photovoltaic systems under nonlinear and time-varying conditions of irradiance and temperature. Unlike conventional approaches, these techniques can learn, adapt, and make decisions without requiring an explicit mathematical model of the PV system, which makes them highly effective in complex and uncertain environments [18][58].

a Fuzzy Logic Control

The Fuzzy Logic Control (FLC) technique determines the optimal control action based on linguistic rules and fuzzy sets, rather than precise numerical models. It operates using three

main stages: fuzzification, rule evaluation, and defuzzification. During fuzzification, the input variables, such as voltage and change in power, are converted into linguistic terms (e.g., low, medium, high). The rule base then determines the appropriate control response according to predefined "if–then" rules, and the defuzzification stage converts this fuzzy output into a crisp control signal that adjusts the converter's duty cycle [3][12][16].

FLC offers excellent robustness to parameter variations and nonlinearity, maintaining high efficiency even under partial shading or fast irradiance changes. However, its effectiveness depends heavily on the accurate design of membership functions and expert-defined rules, which can be challenging for complex PV systems. Figure 2-28 presents the general structure of the fuzzy logic MPPT controller [3][5][35].

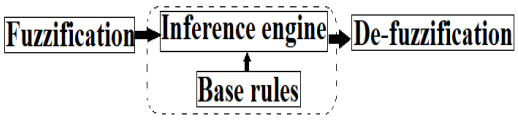


Figure 2-28 Block diagram of FLC.

b Artificial Neural Networks

The Artificial Neural Network (ANN) method is inspired by the structure and function of the human brain. It uses interconnected neurons arranged in layers to learn the nonlinear mapping between inputs, such as irradiance, temperature, and voltage, and the corresponding MPP voltage or current. Once trained, the ANN can instantly predict the optimal operating point of the PV array without iterative searching, making it much faster than traditional algorithms [3].

The ANN's main strength lies in its high adaptability and ability to capture complex nonlinear relationships from data, providing accurate and fast tracking under dynamic conditions. However, it requires a large and representative training dataset, and its performance may deteriorate when operating under conditions not covered during training. Figure 2-29 illustrates the general architecture of an ANN-based MPPT system [3][6][16][31][33][58].

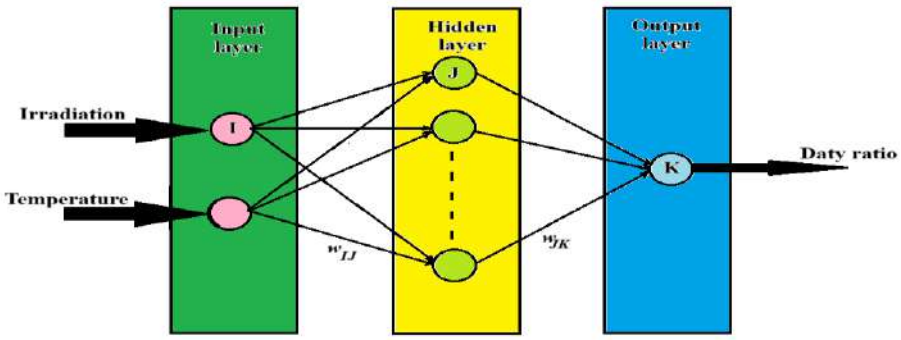


Figure 2-29 Structure of an ANN-based MPPT system.

c Adaptive Neuro-Fuzzy Inference System

The Adaptive Neuro-Fuzzy Inference System (ANFIS) combines the advantages of neural networks and fuzzy logic to create an intelligent hybrid MPPT controller capable of both

learning and reasoning. ANFIS uses a fuzzy inference system whose parameters are automatically tuned through neural learning algorithms based on training data. This integration allows the controller to adapt to environmental changes and continuously optimize its performance [16][29].

ANFIS offers fast convergence, strong adaptability, and superior accuracy under dynamic conditions, making it particularly suitable for partially shaded PV arrays. However, its computational requirements are higher than those of simpler methods, and its design process is more complex due to the hybrid nature of its structure.

2.4.3 Metaheuristic Optimization Techniques

Metaheuristic optimization algorithms represent a class of bio-inspired global search methods that have gained prominence in Maximum Power Point Tracking for photovoltaic systems. Unlike conventional or deterministic algorithms, these techniques can efficiently handle the nonlinear and multimodal nature of PV characteristics, particularly under partial shading conditions where multiple local maxima exist. By mimicking natural processes such as animal behavior, swarm movement, or evolutionary adaptation, metaheuristic MPPT methods can dynamically explore the search space and converge toward the true global Maximum Power Point [2][7][10][11].

a Particle Swarm Optimization

The Particle Swarm Optimization (PSO) algorithm is inspired by the collective movement patterns seen in bird flocks and fish schools. In this method, each particle represents a candidate operating point of the PV system, generally defined by its voltage or duty cycle [79]. The evaluation of each particle is performed using a fitness function based on the instantaneous power of the PV array. The fitness function used in PSO-based MPPT is expressed in expression (2-19) [2][4][7][12].

$$f_{PSO} = P(V) = V \times I \tag{2-19}$$

The objective is to maximize this fitness value. Each particle adjusts its trajectory by updating its velocity and position according to its personal best position and the global best position found by the entire swarm. The velocity and position update laws are given by expressions (2-20) and (2-21) [2][5][7][10][16][58][79].

$$v_i(k+1) = \omega . v_i(k) + c_1 . r_1 . \left[P_{best,i} - D_i(k)\right] + c_2 . r_2 . [G_{best} - D_i(k)] \tag{2-20}$$

$$D_i(k+1) = D_i(k) + v_i(k+1) \tag{2-21}$$

Where ω is the inertia weight, c_1 and c_2 are acceleration coefficients, and r_1,$r_2 \in [0,1]$ are random numbers [11][79]. This dynamic learning behavior enables the swarm to converge rapidly toward the global maximum power point, even under partial shading conditions. However, the effectiveness of PSO strongly depends on the appropriate tuning of its

parameters to avoid premature convergence. The operational sequence of the PSO-based MPPT process, including velocity update, position update, and fitness evaluation, is illustrated in Figure 2-30 [2][4][7].

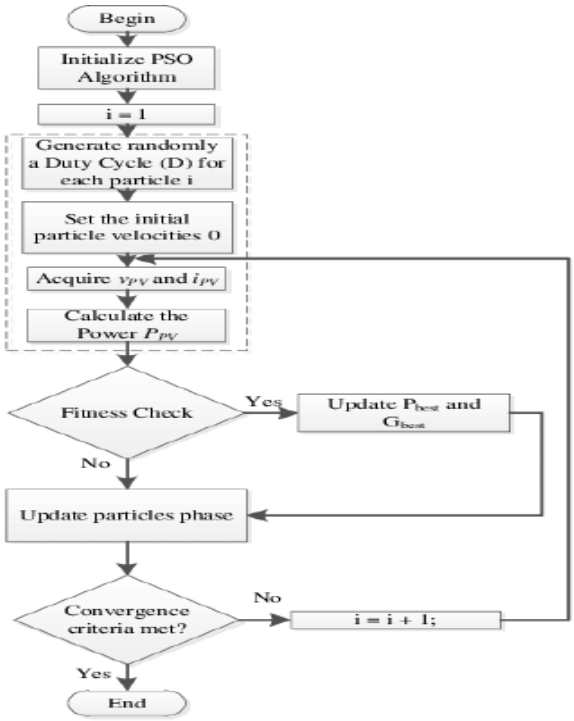


Figure 2-30 Flowchart of the PSO-based MPPT.

b Grey Wolf Optimization (GWO)

The Grey Wolf Optimization (GWO) algorithm is a nature-inspired metaheuristic that models the hierarchical structure and cooperative hunting behavior of grey wolves. In real wolf packs, which typically contain between five and twelve members, social organization is arranged into four levels α, β, δ, and ω. This hierarchy forms the conceptual basis of the GWO algorithm. The α wolves represent the leading and most dominant members of the pack and correspond to the best candidate solutions during optimization. The β wolves assist the α wolves and represent the second-best solutions, while the δ wolves participate in decision-making and correspond to the third-best solutions. All remaining search agents are assigned to the ω category and follow the directions imposed by the upper hierarchy [4][10][12].

The hunting strategy of grey wolves consists of three behavioral phases that the GWO algorithm reproduces mathematically. These phases involve tracking the prey, encircling and approaching it, and finally attacking, which in optimization represents convergence toward the global solution. In the context of MPPT, the prey corresponds to the global maximum power point (GMPP). This analogy enables the GWO algorithm to address multiple-peak characteristics in photovoltaic arrays under partial shading conditions while achieving smooth convergence with minimal steady-state oscillation. The encircling mechanism is expressed by the position update relation, defined in expression (2-22) [4][10].

$$\vec{X}(t+1) = \overrightarrow{X_p}(t) - \vec{A} \,.\, \vec{D} \tag{2-22}$$

Where $\vec{X}(t+1)$ is the updated position of the search agent, $\overrightarrow{X_p}(t)$ represents the estimated position of the prey (the best solution at iteration *t*), $\vec{A}$ is the exploration–exploitation coefficient vector, and $\vec{D}$ denotes the estimated distance between the search agent and the prey. The distance vector is computed as in expression (2-23)[10][12].

$$\vec{D} = \left| \vec{C} \,.\, \overrightarrow{X_p}(t) - \vec{X}(t) \right| \tag{2-23}$$

Where $\vec{C}$ is an adaptive coefficient vector. The coefficient vectors are defined by (2-24) and (2-25).

$$\vec{A} = 2a \,.\, \overrightarrow{r_1} - a \tag{2-24}$$

$$\vec{C} = 2 \,.\, \overrightarrow{r_2} \tag{2-25}$$

With *a* decreasing linearly from *2* to *0* as iterations progress, thereby managing the shift from global exploration to local exploitation. The vectors $\overrightarrow{r_1}$ and $\overrightarrow{r_2}$ are random quantities uniformly distributed in the interval [*0,1*].

Since the *α*, *β*, and *δ* wolves correspond to the three best solutions, the algorithm computes three separate position estimates based on each of these leaders. The final updated position of each search agent is then obtained by averaging the influence of the three best solutions according to expression (2-26) [10][12].

$$\overrightarrow{X_{(k+1)}} = \frac{\overrightarrow{X_\alpha} + \overrightarrow{X_\beta} + \overrightarrow{X_\delta}}{3} \tag{2-26}$$

The quality of each candidate solution is evaluated using the PV array output power, which serves as the fitness function. This is expressed as in (2-27).

$$f_{GWO} = P(V) = V \times I \tag{2-27}$$

Where V_{pv} and I_{pv} denote the PV array output voltage and current, respectively.

Through the cooperative roles of the *α*, *β*, and *δ* wolves and the adaptive control provided by the coefficient vectors, the GWO algorithm maintains a robust balance between exploration and exploitation. This characteristic enables fast and reliable tracking of the global maximum power point even in conditions of rapidly varying irradiance and strong partial shading. The operational structure of the GWO-based MPPT controller is illustrated in Figure 2-31 [4][10].

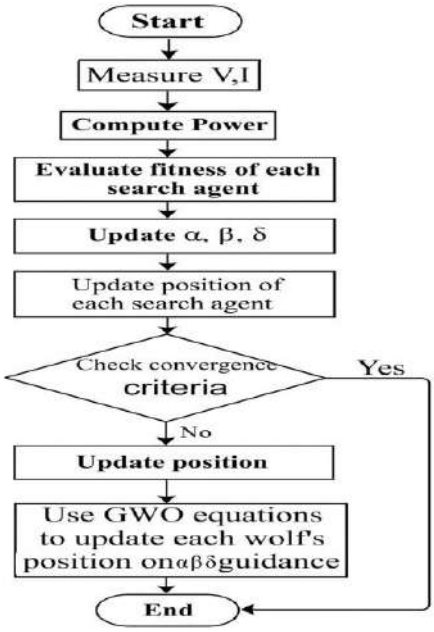


Figure 2-31 Flowchart of the GWO-based MPPT algorithm.

c Hybrid Optimization Algorithms

Hybrid MPPT algorithms combine two or more intelligent and metaheuristic methods to leverage their complementary strengths. For example, combining PSO with Artificial Neural Networks (PSO-ANN) allows the system to use global optimization for training and fast prediction during operation, while a GWO-Fuzzy Logic Controller (GWO-FLC) integrates adaptive reasoning with swarm intelligence for improved robustness [5][18].

These hybrid approaches enhance convergence speed, tracking accuracy, and stability across diverse environmental conditions. However, their design is more complex, and the computational demand increases due to the integration of multiple control layers [2].

Recent advancements in metaheuristic MPPT research focus on cooperative, adaptive, and multi-agent learning models that further enhance tracking performance under real-world conditions. Techniques such as co-operative PSO, reinforcement learning-enhanced swarms, and hybrid evolutionary algorithms enable faster global convergence, improved disturbance rejection, and reduced steady-state oscillations. These new models integrate self-learning mechanisms that adapt algorithm parameters in real time, allowing efficient operation even under rapidly changing irradiance or temperature [12][42][58].

2.5 Control Strategies for Grid Integration

In a grid-connected PV system, the inverter serves as the fundamental interface that converts the DC power generated by the PV array into synchronized AC power suitable for grid injection. Its control system is typically organized into two hierarchical loops. The inner current control loop regulates the grid-injected current, ensuring that it follows reference values with minimal distortion and maintains compliance with power quality standards. The

outer control loop manages either the DC-link voltage to balance power flow between the PV source and the grid or directly controls active and reactive power to support grid stability and power factor correction [36].

Accurate synchronization between the inverter output and the grid voltage is achieved through PLL algorithms, or more advanced techniques such as the DSOGI-PLL, which offer superior performance under grid voltage unbalance and harmonic distortion. These synchronization schemes ensure precise alignment of the inverter's output phase, frequency, and amplitude with the grid, enabling seamless power transfer and stable operation.

2.5.1 Synchronous Reference Frame Control

The Synchronous Reference Frame (SRF) control, also known as the *dq* control strategy, regulates the grid-injected currents by transforming the three-phase quantities from the stationary *abc* frame into a rotating *dq* frame synchronized with the grid voltage. This synchronization is achieved through a PLL, which ensures that the transformation angle θ accurately tracks the grid phase. Once transformed into the rotating frame, the AC variables become DC quantities, enabling the use of simple PI controllers for precise current regulation. The abc-dq transformation is expressed as in (2-28) [2][36][45][47].

$$\begin{bmatrix} i_d \\ i_q \end{bmatrix} = \frac{2}{3} \begin{bmatrix} \cos\theta & \cos(\theta - \frac{2\pi}{3}) & \cos(\theta + \frac{2\pi}{3}) \\ -\sin\theta & -\sin(\theta - \frac{2\pi}{3}) & -\sin(\theta + \frac{2\pi}{3}) \end{bmatrix} \begin{bmatrix} i_a \\ i_b \\ i_c \end{bmatrix} \tag{2-28}$$

The direct component i_d controls the active power, while the quadrature component i_q regulates the reactive power. The instantaneous active and reactive powers are expressed as in (2-29) and (2-30).

$$P = \frac{3}{2} (v_d \cdot i_d + v_q \cdot i_q) \tag{2-29}$$

$$Q = \frac{3}{2} (v_q \cdot i_d - v_d \cdot i_q) \tag{2-30}$$

The control law for the inverter voltages in the dq frame is given by (2-31) and (2-32) [36].

$$v_d^* = (v_{g_d} + L \cdot \frac{di_d}{dt} - \omega \cdot L \cdot i_q + R \cdot i_d) \tag{2-31}$$

$$v_q^* = (v_{g_q} + L \cdot \frac{di_q}{dt} + \omega \cdot L \cdot i_d + R \cdot i_q) \tag{2-32}$$

Where L represents the total equivalent inductance seen by the inverter, which is typically the sum of the filter inductance L_f and the grid-side inductance L_g. R represents the total equivalent resistance, comprising the parasitic resistances of the filter R_f and the grid connection R_g, as well as any added virtual resistance for damping. These reference voltages

are then transformed back to the *abc* frame and applied through Space Vector PWM (SVPWM) [2][23][25][44].

SRF control provides excellent steady-state performance, low THD, and effective reactive power regulation, though it requires precise PLL synchronization and accurate parameter estimation [36].

2.5.2 Direct Power Control

Direct Power Control (DPC) directly regulates active (*P*) and reactive (*Q*) power without requiring an inner current loop or modulation stage. It operates in the stationary *αβ* frame, using Clarke's transformation for voltage projection is expressed as in (2-33) [2][83][84].

$$\begin{bmatrix} v_\alpha \\ v_\beta \end{bmatrix} = \frac{2}{3}\begin{bmatrix} 1 & -1/2 & -1/2 \\ 0 & \sqrt{3}/2 & -\sqrt{3}/2 \end{bmatrix}\begin{bmatrix} v_a \\ v_b \\ v_c \end{bmatrix} \tag{2-33}$$

The instantaneous active and reactive powers are given as in (2-34) and (2-35).

$$P = v_\alpha \cdot i_\alpha + v_\beta \cdot i_\beta \tag{2-34}$$

$$Q = v_\beta \cdot i_\alpha + v_\alpha \cdot i_\beta \tag{2-35}$$

The errors *ΔP* and *ΔQ* are processed through hysteresis controllers, and a switching table selects the optimal voltage vector from the inverter's six available states to minimize power errors.

This control offers fast dynamic response, simple implementation, and direct regulation of power flow, but it exhibits variable switching frequency and higher current ripples. Enhanced versions such as SVM-DPC address these drawbacks by ensuring constant switching frequency and smoother operation [2].

2.5.3 dq Current Control (Vector Current Control)

The dq current control, also called vector current control, builds upon the SRF concept but focuses explicitly on regulating inverter output currents in the synchronous frame.

The measured grid currents are transformed into dq components aligned with the grid voltage vector. Two independent PI controllers regulate i_d and i_q, producing reference voltages for PWM generation. The dynamic model of the inverter in the dq frame is expressed as in (2-36) and (2-37).

$$\frac{di_d}{dt} = \frac{1}{L}\left(v_d - v_{g_d} + \omega \cdot L \cdot i_q - R \cdot i_d\right) \tag{2-36}$$

$$\frac{di_q}{dt} = \frac{1}{L}\left(v_q - v_{g_q} - \omega \cdot L \cdot i_d - R \cdot i_q\right) \tag{2-37}$$

The decoupling terms $\omega L i_q$ and $\omega L i_d$ compensate for the coupling effect between the two axes. This method provides excellent dynamic performance, precise current tracking, and superior harmonic suppression, making it ideal for multilevel PV inverters. However, it requires accurate parameter estimation and high-fidelity current sensing.

2.5.4 Repetitive and Predictive Control Methods

Repetitive Control (RC) and Model Predictive Control (MPC) are advanced strategies that extend beyond traditional PI-based current controllers in grid-connected inverters [42][43].

Repetitive Control is based on the internal model principle and is particularly effective for rejecting periodic disturbances such as grid harmonics. The controller stores the error pattern of the previous grid cycle and injects corrective actions in the next cycle. Its simplified control law is expressed as in (2-38) [48].

$$u(k) = u(k - N) + K_r\, e(k) \tag{2-38}$$

Where N is the number of samples per grid period, and K_r is the repetitive gain. Because it continuously "learns'' the periodic error profile, RC achieves extremely low steady-state harmonic distortion; however, its transient response is slower due to the cycle-based learning mechanism.

MPC predicts future inverter currents using a discrete model of the system. For the filter inductance L, sampling period T_s, inverter voltage $v(k)$, grid voltage $v_g(k)$, and resistance R, the predicted inverter currents are obtained using a discrete system model as in (2-39) [42].

$$i(k+1) = i(k) + \frac{T_s}{L}\left[v(k) - v_g(k) - R\, i(k)\right] \tag{2-39}$$

A cost function evaluates all possible switching states of the inverter, and the optimal state is selected by minimizing the quadratic objective expressed in (2-40).

$$J = [i^* - i(k+1)]^2 \tag{2-40}$$

This forces the predicted current toward its reference. MPC provides fast dynamic response, direct control of switching states, and high robustness to system variations, though at the expense of increased computational complexity [42][43][48].

2.6 PLL Methods for Grid Synchronization

Accurate phase synchronization is essential for the proper operation of the SRF controller, as errors in the estimated angle θ directly affect the computation of id and iq. Two well-established PLL methods are commonly used in grid-connected PV/wind systems: the conventional Synchronous Reference Frame PLL (SRF-PLL) and the DSOGI-PLL [40][60].

2.6.1 Synchronous Reference Frame PLL (SRF-PLL)

The SRF-PLL is one of the most commonly used synchronization methods due to its simplicity and reliability under balanced grid conditions. It operates by transforming the three-phase grid voltages into the synchronous *dq* reference frame using Park's transformation [6][12][16][61].

Under perfect synchronization, the q-axis voltage component becomes zero. The PLL therefore forces the quadrature component of the grid voltage to converge toward zero, ensuring perfect phase alignment, as expressed in (2-41).

$$v_q \rightarrow 0 \tag{2-41}$$

A PI controller processes the error signal v_q and adjusts the estimated grid frequency $\hat{\omega}$, as given in (2-42) [12][45][91].

$$\hat{\omega} = K_P\, v_q + K_I \int v_q\ dt\ V_{abc} \tag{2-42}$$

The estimated phase angle is then obtained by integrating the frequency, as shown in (2-43) [12].

$$\hat{\theta}(t) = \int \hat{\omega}(t)\, dt \tag{2-43}$$

This technique, whose block diagram is presented in Figure 2-32, ensures fast and accurate phase estimation under ideal or moderately disturbed grid conditions. However, harmonic distortion, DC offsets, and voltage unbalances introduce oscillatory components in v_d and v_q, thereby degrading the PLL performance θ [12][16][45][61].

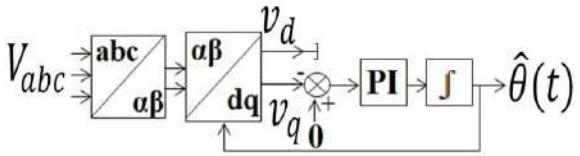


Figure 2-32 Block diagram of the SRF-PLL.

2.6.2 Dual second-order generalized integrator PLL (DSOGI-PLL)

The DSOGI-PLL is designed to deliver highly robust grid synchronization under distorted, unbalanced, or weak-grid conditions. Unlike the classical SRF-PLL, which suffers performance degradation in the presence of harmonics or negative-sequence components, the DSOGI-PLL employs a pre-filtering stage to isolate the fundamental positive-sequence voltage component before the phase estimation stage [40][91].

The method employs two Second-Order Generalized Integrator (SOGI) blocks to generate in-phase and quadrature versions of each grid voltage component in the stationary *αβ* frame. For a single-axis input voltage v_i, the SOGI block produces an in-phase output v_o and a quadrature output qv_o, which is phase-shifted by *-90°*. Their transfer functions are given by expressions (2-44) and (2-45) [40][91].

$$v_o(s) = \frac{k\ \omega_0\ s}{s^2 + k\ \omega_0\ s + \ {\omega_0}^2}\ \ v_i(s) \tag{2-44}$$

$$q\ v_o(s) = \frac{k\ {\omega_0}^2}{s^2 + k\ \omega_0\ s + \ {\omega_0}^2}\ \ v_i(s) \tag{2-45}$$

Where ω_0 is the fundamental grid frequency and k (or 2ζ) is a damping factor. An identical SOGI processes the orthogonal β-component, yielding the four orthogonal signals (v_α,qv_α,v_β,qv_β). These signals are used to extract the fundamental positive-sequence components (v_α^+,v_β^+) using the operation (2-46)[40].

$$\begin{bmatrix} v_\alpha^+ \\ v_\beta^+ \end{bmatrix} = \frac{1}{2}\begin{bmatrix} 1 & -q \\ q & 1 \end{bmatrix}\begin{bmatrix} v_\alpha \\ v_\beta \end{bmatrix} \tag{2-46}$$

This calculation effectively rejects negative-sequence components and harmonic distortion. The clean positive-sequence voltage is then transformed into the synchronous dq frame using the PLL's estimated phase angle $\hat{\theta}$. The quadrature component v_q^+ is regulated to zero by a Proportional-Integral (PI) controller. The output of this controller, which represents the estimated frequency deviation $\Delta\hat{\omega}$, is added to the nominal grid frequency and integrated to obtain the final estimated phase angle $\hat{\theta}$, closing the PLL loop [51].

While the standard DSOGI-PLL provides excellent performance under unbalanced conditions, its ability to reject specific harmonic orders is limited. To address this, an advanced improvement involves cascading Advanced Harmonic Elimination (AHE) modules before the positive-sequence extraction. Each AHE module algebraically cancels a targeted harmonic (e.g., the 5^{th}, 7^{th}, or 11^{th}) [29][31]. This enhanced AHE-DSOGI-PLL structure ensures precise and ripple-free extraction of the grid's phase and frequency, even during complex faults characterized by simultaneous voltage unbalance and severe harmonic distortion, which is critical for the reliable operation of grid-supporting converters like Virtual Synchronous Generators (VSGs). The overall structure of the DSOGI-PLL is illustrated in Figure 2-33 [40][51].

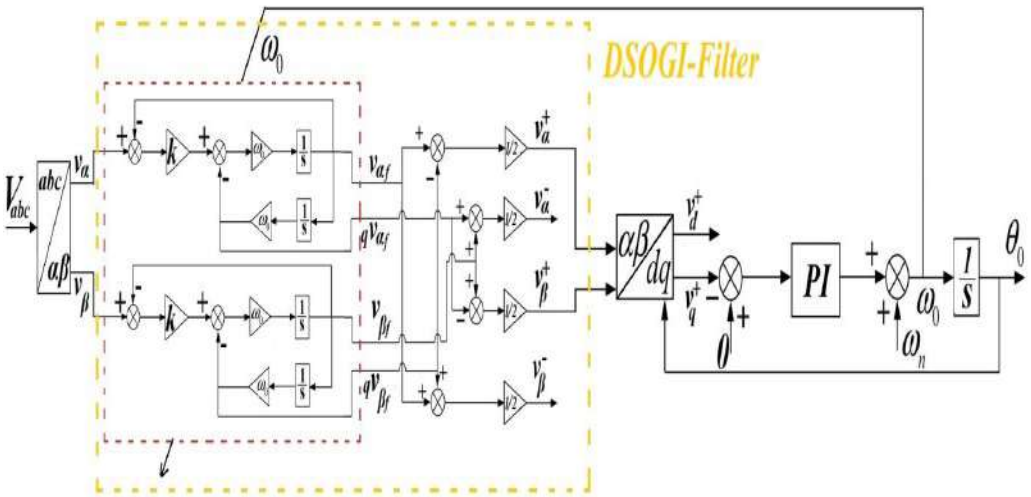


Figure 2-33 Block diagram of the DSOGI-PLL.

2.7 Case Study: Simulated Design of a 100kW Two-Stage Grid-Connected PV system

This section presents the modeling framework and design methodology of a *100kW* two-stage grid-connected photovoltaic system, which employs a DC-DC boost converter followed by a grid-connected inverter. The objective is to illustrate the characteristics, control interactions, and sizing considerations typical of two-stage architectures prior to conducting full simulation analysis. The section is organized into three parts: system overview, detailed system design, and simulation parameter specification.

2.7.1 System Overview

The two-stage system consists of a PV generator supplying a boost DC-DC converter that elevates the PV voltage before feeding a three-phase voltage source inverter. As illustrated in Figure 2-34, the PV array operates at approximately *290-300V* under standard conditions, necessitating voltage boosting to meet the inverter's required DC-link voltage of *600V*.

The Incremental Conductance MPPT algorithm governs the boost duty cycle, ensuring maximum power extraction across varying irradiance levels. The inverter is controlled using the Synchronous Reference Frame method, enabling precise active and reactive power control. An LCL filter provides harmonic attenuation at the grid interface [45][46][62].

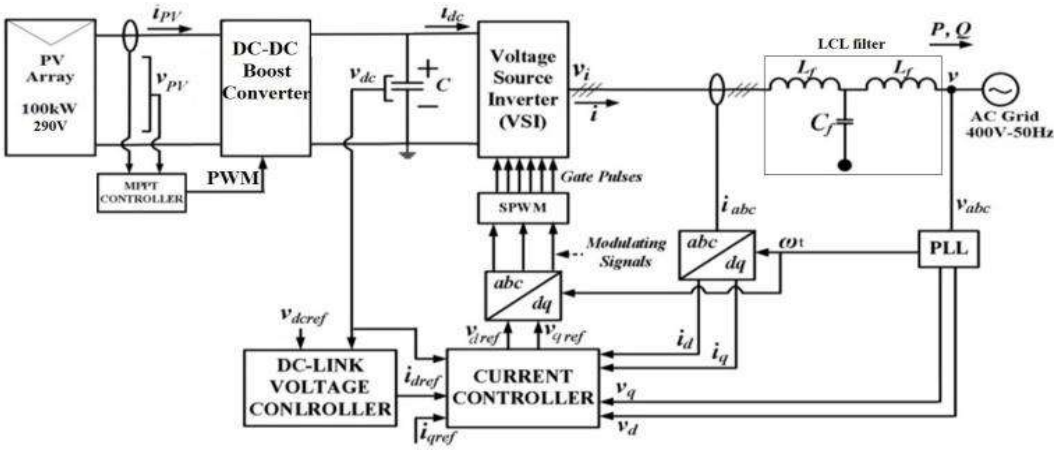


Figure 2-34 Block diagram of a two-stage grid-connected inverter for a PV system.

2.7.2 System Design

a PV Array and Boost Converter

The PV array is dimensioned to supply a nominal output power of *100kW* under STC. The array is constructed using the *Kyocera KD205GX-LP* module, whose electrical characteristics are summarized in Table 2-2 (Annex I). Each module delivers *205W* at its maximum power point; therefore, a total of *495* modules are required. The configuration adopted consists of *11* modules connected in series per string and *45* strings connected in parallel, resulting in an MPP voltage of approximately *290-300V*, suitable for interfacing with the boost converter. The electrical behavior of the complete array, including its I–V and P–V characteristics at

25°C under different irradiances, is illustrated in Figure 2-35, showing a maximum extractable power close to *100kW* [45][46].

To elevate the PV array voltage to the DC-link level required by the grid-connected inverter, a boost DC–DC converter is implemented. The design of this converter follows standard ripple-based criteria typically applied in high-power PV systems. The inductor is sized to limit the current ripple to about five percent of the nominal PV current, leading to a minimum inductance of approximately *1.45mH*. Similarly, the input capacitor is chosen as *1000μF* to stabilize the PV voltage, while the DC-link capacitor is dimensioned to maintain the voltage ripple near one percent, resulting in a required capacitance of at least *3227μF*. With these component values, the boost converter ensures a stable elevation of the PV voltage to the regulated *600V* DC-link, which is necessary for proper operation of the grid-connected inverter and for achieving rapid and stable MPPT response [45][46].

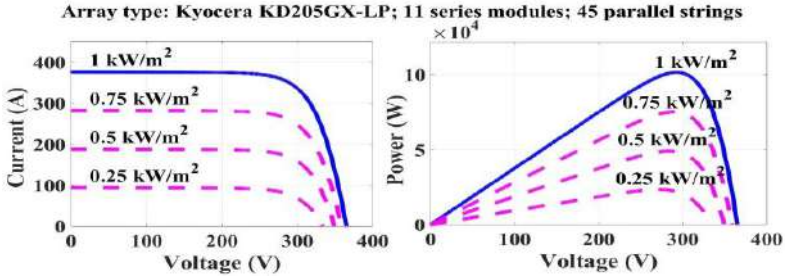


Figure 2-35 I-V and P-V curve characteristics of PV array at 25°C for two-stage inverter.

b Grid-Tied Inverter

The three-phase, two-level inverter operates at a switching frequency of *10kHz* using SPWM [67][80]. Its control structure is based on the Synchronous Reference Frame-dq (SRF-dq) method, as illustrated in Figure 2-36. This control strategy transforms the measured three-phase AC currents into a rotating *dq* reference frame aligned with the grid voltage vector, using a Park transformation. The grid angle is tracked in real time via a PLL to maintain synchronization.

In the *dq* frame, the active power component i_d and the reactive power component i_q are decoupled, allowing for independent control. The DC-link voltage V_{DC} is regulated by an outer voltage loop, which generates the reference direct-axis current i_{d_ref} using expression (2-47), while for unity power factor operation, the quadrature-axis current reference i_{q_ref} is set to zero as presented in (2-48) [44][45][46].

$$i_{d_ref} = \left(k_p^{dc} + \frac{1}{s}\, k_I^{dc}\right).\left(V_{DC_ref} - V_{DC}\right) \tag{2-47}$$

$$i_{q_ref} = 0 \tag{2-48}$$

The inner current control loop uses PI regulators to track both i_d and i_q, producing the reference voltages for the inverter according to expressions (2-49) and (2-50) [45].

$$v_{d\,ref} = \left[\left(k_p + \frac{1}{s}\, k_I\right).\left(i_{d\,ref} - i_d\right) + L.\omega.i_q + v_d\right]\left(\frac{2}{V_{DC}}\right) \tag{2-49}$$

$$v_{q\,ref} = \left[\left(k_p + \frac{1}{s}\,k_I\right).\left(i_{q\,ref} - i_q\right) - L.\omega.i_d + v_q\right]\left(\frac{2}{V_{DC}}\right) \tag{2-50}$$

After computing these control signals, the inverse Park transformation is applied to convert them back into three-phase quantities, which are fed to the PWM generator to produce switching pulses for the inverter.

To mitigate switching harmonics and guarantee compliance with grid power quality standards, an LCL filter is installed at the inverter output. The filter is composed of an inductance of *500μH* and a capacitance of *100μF*, providing effective attenuation of high-frequency components before the current is injected into the grid [45][46].

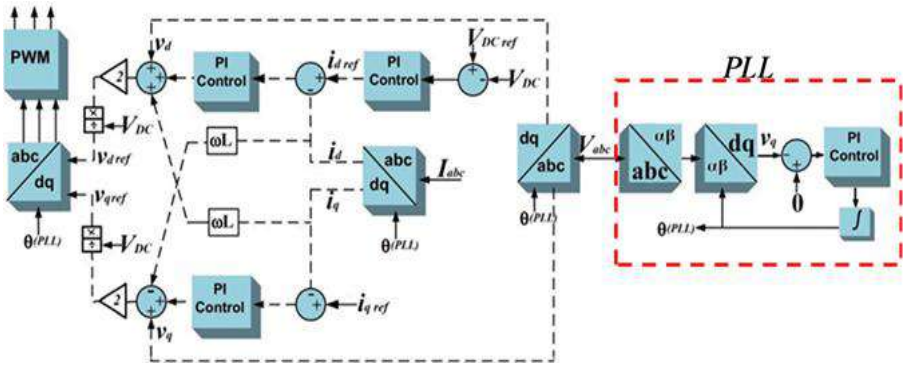


Figure 2-36 Block diagram of SRF-dq control.

2.7.3 Simulation Parameters

Table 2-3 (Annex I) provides a concise overview of the key parameters used in the MATLAB/Simulink model of the proposed two-stage PV system. These values define the operating conditions of the PV generator, the boost converter, the grid-tied inverter, and the associated control loops, ensuring consistent and realistic simulation behavior. The table includes electrical ratings, switching frequencies, controller gains, and grid interface specifications, forming the basis for accurate system performance evaluation.

2.8 Case Study: Modeling and Simulation of a *100kW* Single-Stage Grid-Connected PV System

This section describes the modeling and implementation of a *100kW* single-stage photovoltaic system, where the PV array is directly connected to the grid-tied inverter without an intermediate boost converter. This architecture reduces the number of power-processing stages and can improve efficiency, provided that the PV array is designed to match the DC-link voltage requirements. The section is divided into system overview, system design, and simulation parameters.

2.8.1 System Overview

The single-stage configuration eliminates the DC-DC converter and directly feeds the inverter from the PV array, as shown in Figure 2-37. The PV array is arranged to supply approximately *700V* at its MPP, making direct coupling possible.

In this design, the INC MPPT algorithm is integrated within the inverter's SRF control loop. The MPPT generates the DC-link reference voltage, which the inverter controls through active current modulation. An LCL filter is placed at the inverter output to ensure harmonic performance, while a PLL synchronizes the inverter with the grid [41][45][46].

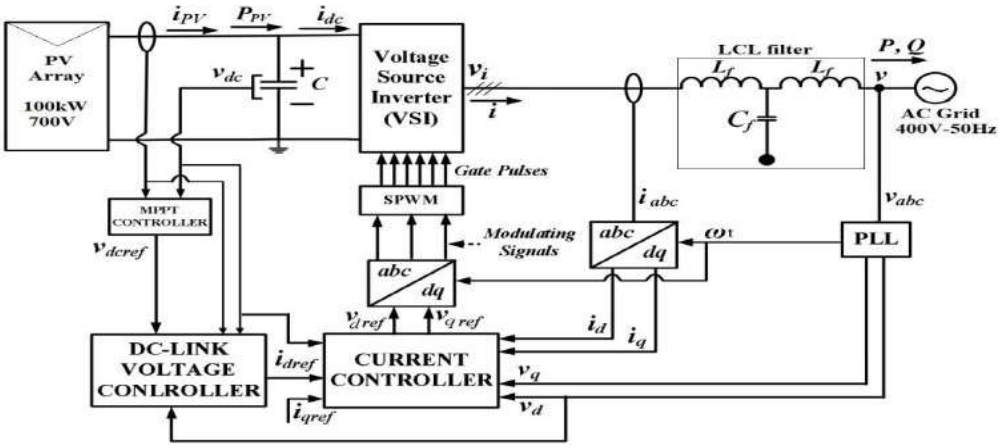


Figure 2-37 Block diagram of a single-stage grid-connected inverter for a PV system.

2.8.2 System Design

a PV Array

The photovoltaic array is constructed using the same *Kyocera KD205GX-LP* modules as in the two-stage system; however, the series-parallel configuration is modified to provide a higher operating voltage suitable for direct single-stage grid connection. To achieve a nominal DC-link voltage close to *700V*, a total of *27* modules are connected in series per string, resulting in an MPP voltage of around *736V*, which is adequate for feeding the inverter without any intermediate DC-DC converter. The total power rating of *100kW* is obtained by using 18 parallel strings, giving a total of 486 modules in the array. The electrical behavior of the complete PV generator is illustrated through its I–V and P–V characteristics at *25°C* under different irradiances, shown in Figure 2-38, where the maximum output power is clearly observed near the *100kW* operating point. These curves highlight the voltage range, current capability, and nonlinear nature of the PV array, serving as a reference for MPPT integration within the inverter control loop [46].

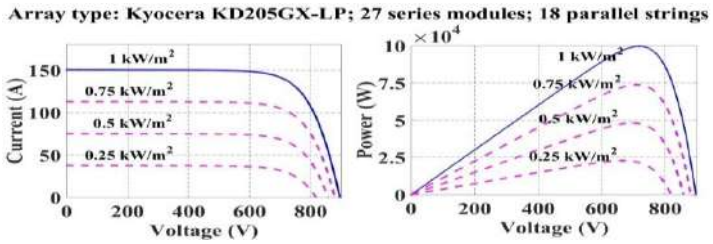


Figure 2-38 I-V and P-V curve characteristics of PV array at *25°C* for single-stage inverter.

b Grid-Tied Inverter

The SPWM-modulated two-level inverter operates at *10kHz*, as shown in Figure 2-37 [25]. In this single-stage structure, the PV array is directly connected to the inverter without an

intermediate DC–DC boost converter, meaning that variations in the PV voltage are immediately reflected on the DC-link. To ensure proper power regulation under these conditions, the MPPT controller is integrated with the Synchronous Reference Frame-dq (SRF-dq) strategy, where the MPPT algorithm provides the reference DC voltage used to generate the direct-axis current reference i_{d_ref} according to expression (2-51). Because the topology lacks a voltage-boosting stage, the DC-link voltage regulation and power extraction are more strongly coupled. The reactive power is maintained at zero by setting the quadrature-axis reference current i_{q_ref} [46].

$$i_{d\,ref}^{single} = \left(k_p^{dc} + \frac{1}{s}\, k_I^{dc}\right).\left(V_{dc\,ref} - V_{dc}\right) + \left(\frac{2}{3}.\frac{V_{dc}.I_{PV}}{V_d}\right) \tag{2-51}$$

The LCL filter and the Phase-Locked Loop (PLL) employed in this system are identical to those used in the two-stage system, as illustrated in Figure 2-37 and Figure 2-39. This arrangement ensures consistent operating conditions for a comparative evaluation of the two systems.

The overall control scheme of the inverter, encompassing SRF-dq-based current regulation, DC-link voltage control, reactive power management, and PLL-based grid synchronization, is summarized in the block diagram presented in Figure 2-39. This diagram highlights the flow of reference signals and feedback loops, providing a comprehensive overview of the inverter control architecture [41][46].

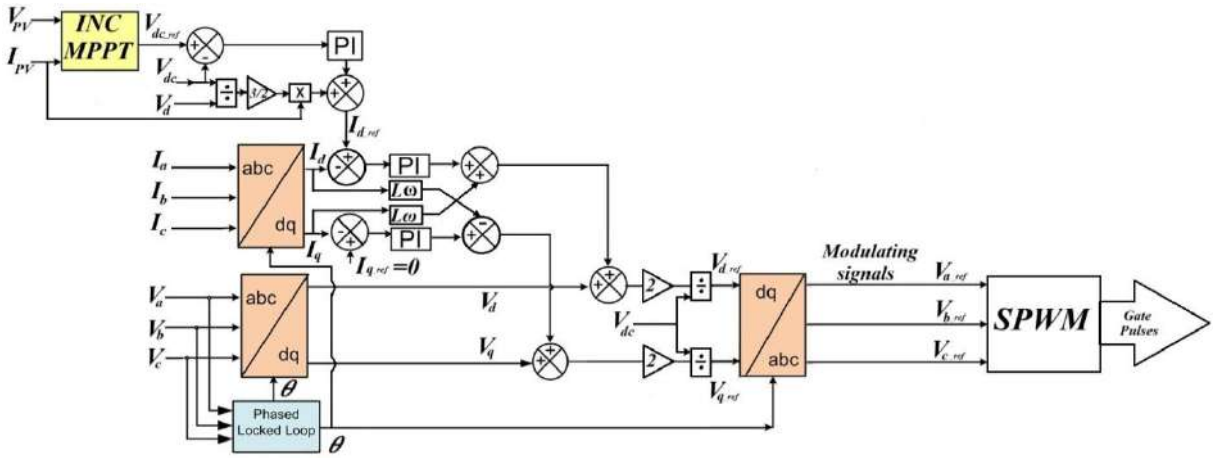


Figure 2-39 Block diagram of SRF-INC control.

2.8.3 Simulation Parameters

The simulation parameters for the single-stage PV system model are listed in Table 2-4 (Annex I). These parameters define the operating conditions of the PV array, the grid-tied inverter, and the associated control loops, including SRF-based regulation of the DC-link voltage and reactive power. The table also specifies the electrical ratings of the PV modules, inverter switching frequency, LCL filter components, and PLL settings for grid synchronization. Collectively, these values ensure that the simulation accurately reflects the dynamic behavior of the PV system under varying irradiance and temperature conditions, providing a reliable basis for performance analysis and comparative studies.

2.9 Comparative Study Between Single-Stage and Two-Stage PV Systems

The selection of inverter topology is a critical design decision for grid-connected photovoltaic systems, directly impacting cost, efficiency, and power quality. A principal distinction lies between single-stage and two-stage architectures. This section provides a comparative analysis of these topologies based on structural differences, control strategies, and key performance metrics derived from simulation studies.

2.9.1 Topological Architecture and PV Array Configuration

The two-stage and single-stage PV system architectures differ fundamentally in the way energy is processed between the PV generator and the AC grid. These structural differences directly determine the required PV array configuration, as each topology demands a specific operating voltage at its input. In the two-stage system, the PV array supplies a boost DC–DC converter that elevates the array's operating voltage from approximately *290-300V* to the regulated *600V* required at the inverter DC-link. This cascaded arrangement decouples the PV generator from the grid-side inverter, allowing the boost converter to execute the Incremental Conductance MPPT algorithm while simultaneously adapting the PV voltage to the inverter's needs. This design enhances operational flexibility, particularly under low irradiance conditions, since the converter can maintain an appropriate DC-link voltage even when the PV voltage fluctuates [45][46].

To achieve the required *290-300V* MPP voltage for the boost stage, the *100kW* two-stage system uses *495 Kyocera KD205GX-LP* modules arranged in *11* modules in series per string and *45* strings in parallel. This configuration delivers the desired array voltage while ensuring that the PV generator can operate close to its maximum power point across varying irradiance levels. Once processed by the boost converter, the elevated *600V* output guarantees stable inverter operation and reliable grid-power injection.

In contrast, the single-stage topology removes the DC–DC converter and connects the PV array directly to the inverter's DC-link capacitor. In this case, the inverter must simultaneously regulate the DC-link voltage, perform MPPT through its modulation strategy, and synchronize current injection with the grid. Because no boost converter is present to adapt the voltage, the PV generator itself must supply a sufficiently high voltage to match the inverter's DC-link requirement. To satisfy this constraint, the *100kW* single-stage configuration employs the same PV module type but arranges them in *27* modules in series and *18* parallel strings, for a total of *486* panels. This layout provides an MPP voltage of approximately *736V*, enabling direct feeding of the inverter without intermediate voltage conversion.

The choice of configuration, therefore, reflects the inherent strengths of each topology. The two-stage design, with more parallel strings and lower series voltage, offers greater control robustness, improved MPPT stability, and better decoupling between the PV array and grid-side dynamics. The single-stage architecture, relying on higher series voltage and fewer parallel strings, benefits from reduced hardware complexity, lower conversion losses, and

higher overall efficiency, though with less flexibility in adapting to irradiance-induced voltage variations. These distinct structural and electrical characteristics constitute the foundation for the operational and performance differences examined in the subsequent sections [46].

2.9.2 Control Strategy and MPPT Integration

The control strategies adopted in the two-stage and single-stage PV systems differ significantly due to the distinct distribution of power processing responsibilities between their respective components. In the two-stage architecture, the presence of the boost DC–DC converter establishes a natural separation between the functions of MPPT, DC-link regulation, and grid-current control. The Incremental Conductance MPPT algorithm governs the duty cycle of the boost converter, ensuring that the PV array operates continuously at its maximum power point regardless of the dynamic requirements of the inverter. This decoupling allows the grid-side inverter to focus exclusively on AC-side control using the Synchronous Reference Frame strategy, where the i_d channel regulates active power through DC-link voltage control and the i_q channel enforces unity power factor. As a result, disturbances originating from the grid, such as voltage fluctuations or harmonic distortion, have a limited influence on the PV operating point, providing a robust and stable control environment [46].

In the single-stage topology, the absence of the boost converter consolidates all control functions into the inverter. The MPPT algorithm is integrated directly into the DC-link voltage regulation loop, meaning that the active current reference generated by the SRF controller must simultaneously satisfy both MPPT and inverter power-balancing requirements. Consequently, any variation in irradiance or temperature directly affects the DC-link dynamics, and the inverter must respond to these changes while maintaining synchronized grid current injection. This tighter coupling between the PV source and the grid-side converter (GSC) increases the sensitivity of the control system to external disturbances and reduces the degree of operational independence between subsystems. The inverter in this topology, therefore, performs a more complex role, combining DC-side voltage regulation, MPP tracking, and AC-side current control within a single stage.

Despite these differences, both systems rely on common foundational elements such as PLL-based grid synchronization and SRF-based current regulation. However, their control architectures reflect fundamentally different design philosophies: the two-stage topology prioritizes modularity and control robustness by isolating PV and grid functions, whereas the single-stage topology minimizes hardware and conversion losses by merging these functions at the expense of tighter dynamic interaction. These distinctions in control structure significantly influence the dynamic response, tracking accuracy, and stability margins of each system, which will be further examined through simulation results in the following section.

2.9.3 Simulation Results and Performance Comparison

A comparative simulation of both *100kW* inverter topologies under standard test conditions (irradiance *1kW/m²*, temperature *25°C*) reveals clear differences in voltage waveforms, harmonic distortion, and overall efficiency.

a Comparative Analysis of the Waveforms

Figure 2-40 shows the DC-bus voltage profiles for the two topologies. The INC MPPT algorithm regulates the DC-bus voltage to *700V* in the single-stage system and *600V* in the two-stage inverter. Both voltages remain stable during operation, confirming correct MPPT and DC-link regulation.

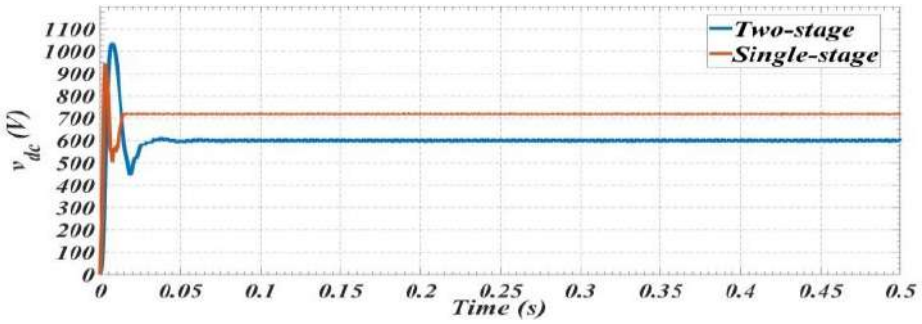
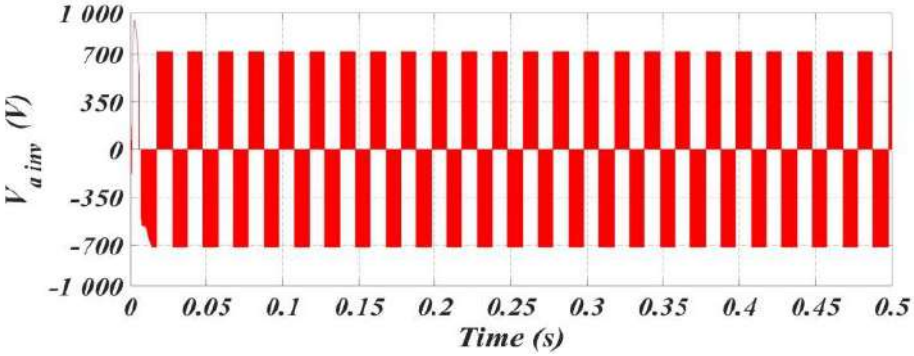
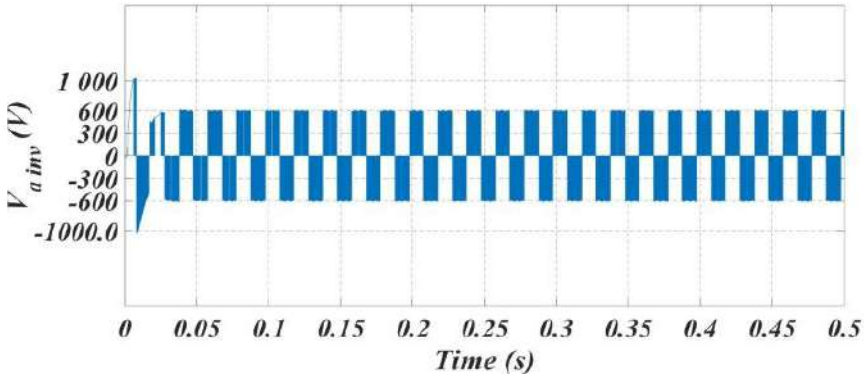


Figure 2-40 DC bus voltage (Single-stage and Two-stage).

In Figure 2-41, the line-to-neutral inverter output voltage of phase *a* is presented. Although both systems achieve proper synchronization with the grid, the single-stage inverter exhibits a more square-shaped voltage waveform with fewer harmonics, thanks to its higher DC-link voltage and the absence of an intermediate DC–DC conversion stage.



(a)



(b)

Figure 2-41 Inverter line outputs voltage: (a) single-stage, (b) two-stage.

The filtered three-phase grid voltages shown in Figure 2-42 are identical for both topologies after the LCL filter. The voltage amplitude, frequency, and phase are correctly adjusted to grid requirements, demonstrating effective filtering and accurate synchronization.

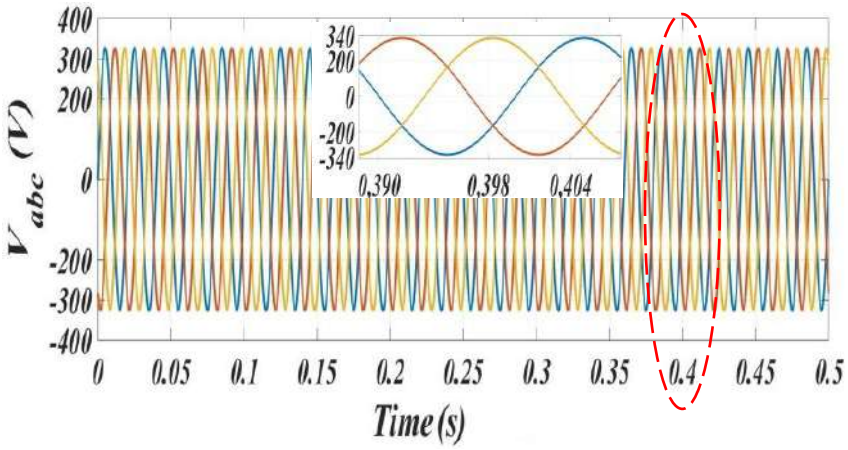


Figure 2-42 Three-Phase Grid Voltage (Phase-to-phase).

b Comparative Analysis of the Line Current THD

The injected line current of phase a, presented in Figure 2-43, is properly synchronized with the grid for both inverter topologies and remains within the harmonic limits imposed by the IEEE-519 standard, which requires the current THD to be below *5%* [21]. Despite this compliance in both cases, the single-stage inverter demonstrates superior current quality.

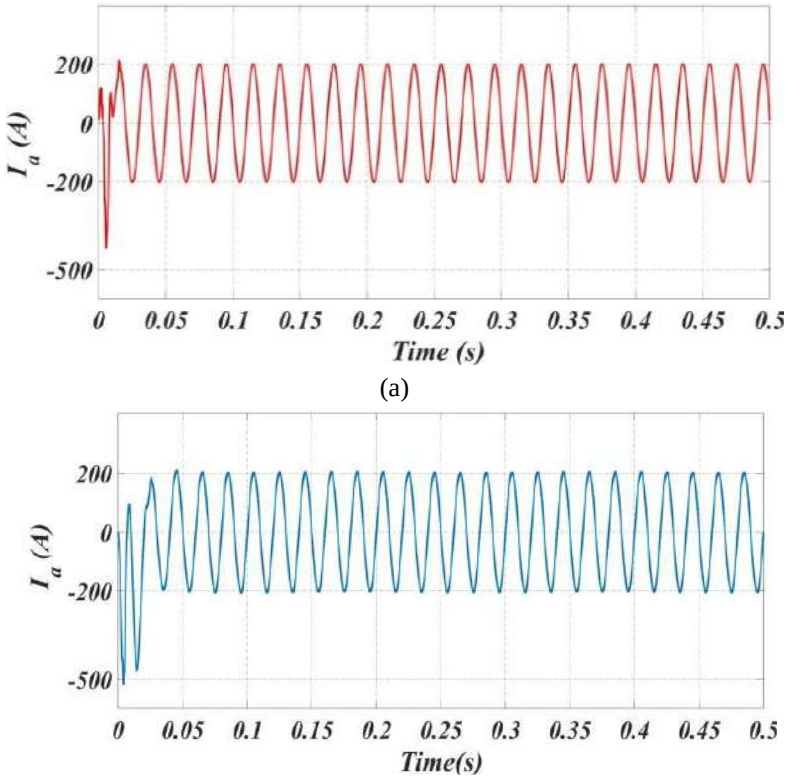


Figure 2-43 Inverter outputs line current: (a) single-stage, (b) two-stage.

As shown in Figure 2-44, its Total Harmonic Distortion reaches only *0.78%*, whereas the two-stage inverter exhibits a THD of *2.54%* [21]. This reduction in harmonic content is mainly attributed to the absence of the boost converter in the single-stage structure, which eliminates an additional switching stage and consequently limits the generation of harmonics. The

fundamental current is nearly identical for both systems, *203.2A* for the single-stage inverter and *203.5A* for the two-stage configuration, indicating that the improvement in THD is not related to current magnitude but rather to the simpler and more direct power conversion path in the single-stage topology.

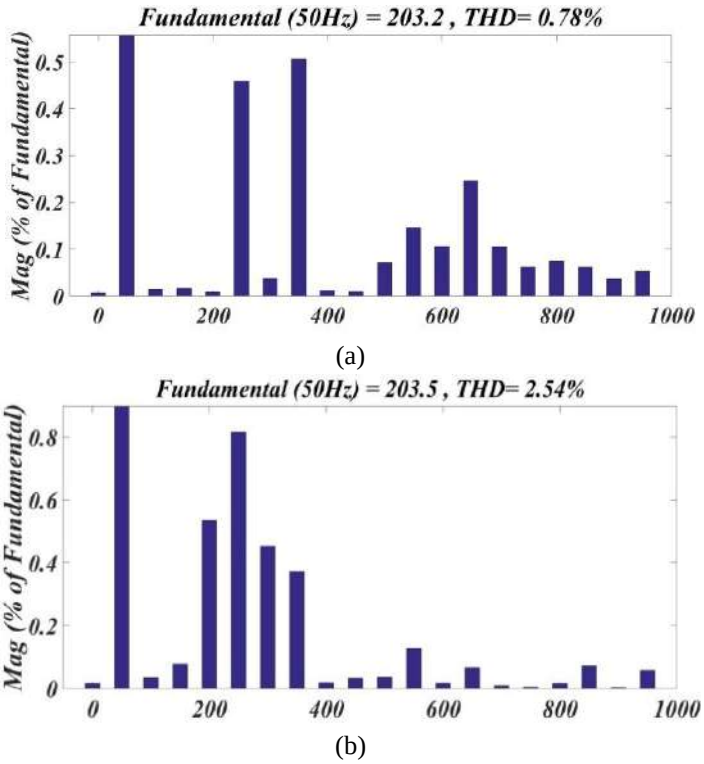


Figure 2-44 Line currents THD: (a) single-stage, (b) two-stage.

c Comparative Analysis of the Efficiency

The exchanged active powers for both inverter topologies, presented in Figure 2-45 and Figure 2-46, show that each system achieves a high efficiency level under standard test conditions. Nevertheless, the single-stage inverter provides slightly better performance, mainly because the removal of the DC–DC boost converter eliminates additional switching and conduction losses. The efficiency of the single-stage configuration reaches *99.56%*, compared to *98.96%* for the two-stage topology. Although the numerical difference is relatively small, both inverters demonstrate excellent efficiency, confirming their suitability for high-performance grid-connected PV applications.

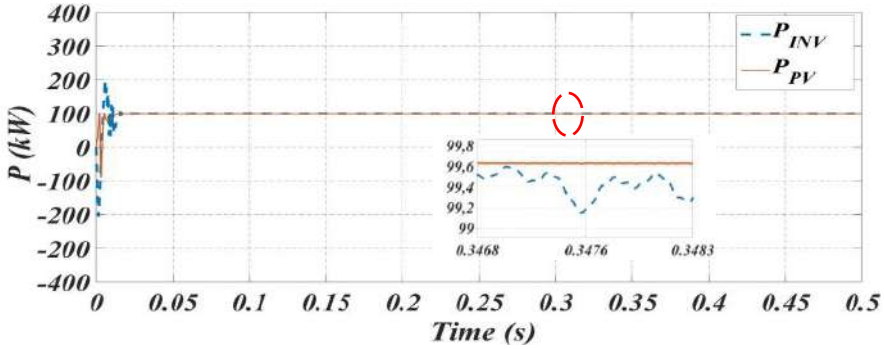


Figure 2-45 Exchanged Active Power – Single-Stage Inverter.

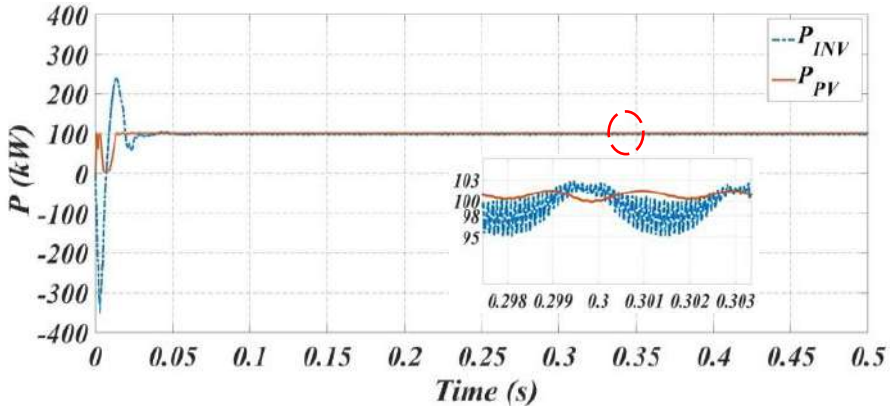


Figure 2-46 Exchanged Active Power – Two-Stage Inverter.

2.9.4 Comparative Summary of Inverter Topologies

The comparative performance of the two inverter topologies is summarized in Table I. The single-stage inverter operates with a high PV array voltage of *700V* and a DC-bus voltage of *700V*, achieving a low grid current THD of *0.78%* and a high system efficiency of *99.56%*, while maintaining lower hardware complexity. In contrast, the two-stage inverter, designed for a lower PV array voltage of *290V*, exhibits a higher THD of *2.54%* and slightly reduced efficiency due to the additional DC–DC boost stage, resulting in increased component count. These results highlight that the single-stage inverter is advantageous when the PV array can supply a sufficiently high voltage, whereas the two-stage topology provides flexibility for low-voltage PV arrays, albeit with modest trade-offs in power quality and efficiency [41][45][46].

Table 2-2 Performance comparison summary

Performance Metric	Single-Stage Inverter	Two-Stage Inverter
PV Array Voltage	*700V*	*290V*
DC-Bus Voltage (v_{dc_ref})	*700V*	*600V*
Output Current THD	*0.78%*	*2.54%*
System Efficiency (η)	*99.56%*	*98.96%*
Output Voltage Waveform	Near-square, lower harmonic content	More distorted harmonic spectrum

2.10 Conclusion

This chapter has presented a detailed examination of the design, modeling, and performance analysis of grid-connected photovoltaic systems. It began by describing the fundamental modeling approaches for PV cells and arrays, highlighting their electrical behavior under standard test conditions as well as under partial shading, where nonlinearities and multiple power peaks significantly influence system operation. The discussion then progressed to power conversion architectures, explaining both single-stage and two-stage configurations together with the main DC-DC converter topologies and inverter technologies, ranging from conventional two-level structures to three-level NPC and more advanced multilevel inverters.

A comprehensive review of MPPT techniques followed, covering conventional algorithms such as Perturb and Observe and Incremental Conductance, intelligent methods including fuzzy logic and neural networks, and metaheuristic optimizers such as PSO and GWO. These techniques were compared in terms of tracking precision, dynamic response, and implementation complexity. The chapter also examined the control strategies required for effective grid integration, including current control loops, synchronous reference frame control, PR regulators, and synchronization mechanisms based on PLL and DSOGI-PLL, with emphasis on meeting IEEE grid compliance standards.

Two simulation studies, involving 100kW single-stage and two-stage PV systems, illustrated the practical implications of the different architectures and control methods, demonstrating their performance under varying environmental and grid conditions.

Overall, the material developed in this chapter provides the essential foundation for the integration of wind energy systems in Chapter 3. The comparative understanding of PV system components, control structures, and performance characteristics will directly support the development and optimization of the hybrid PV-wind architecture addressed in Chapter 4.

Chapter 3 Design and Modeling of Grid-Connected Wind Conversion Systems

3.1 Introduction

The global shift toward sustainable energy solutions has placed wind energy at the forefront of modern power generation strategies. With its significant potential to reduce greenhouse gas emissions, diversify energy portfolios, and enhance energy security, wind power has become one of the most mature and widely deployed renewable technologies. Grid-connected wind energy systems, in particular, play a crucial role in meeting growing electricity demands while supporting environmental and economic objectives [10].

The integration of wind energy into the electrical grid involves complex design and control challenges due to the stochastic nature of wind and the dynamic behavior of wind turbines. Unlike conventional power plants, wind turbines operate under highly variable conditions, requiring robust control strategies and advanced power electronics to maintain efficient energy conversion and ensure grid compliance. As a result, modern wind energy systems increasingly rely on sophisticated generator types such as the DFIG and the PMSG, both of which are capable of operating over a wide range of wind speeds and providing high-quality power to the grid.

This chapter presents a comprehensive study of the design and modeling of grid-connected WECS. It begins by exploring the fundamental principles of wind energy conversion and the components of a typical wind energy system. The chapter then delves into the key generator technologies used in modern WECS, with a focus on variable-speed operation and control. Detailed attention is given to DFIG and PMSG configurations, highlighting their operating principles, advantages, and integration requirements.

Furthermore, the chapter addresses the power electronic interfaces necessary for grid connection, such as back-to-back converters, rectifiers, and inverters. The role of filtering, synchronization, and compliance with grid codes is also examined. The discussion then moves to MPPT strategies, which are essential for maximizing energy capture. Both conventional and intelligent MPPT algorithms are presented and compared based on tracking performance and adaptability to environmental changes.

Finally, the chapter includes a simulation-based case study that illustrates the design, control, and performance of PMSG systems under varying wind conditions. These simulations, performed in MATLAB/Simulink, provide valuable insights into system dynamics, control response, and power quality. The outcomes set the stage for the hybrid system modeling and integration presented in the following chapter.

3.2 Wind Energy Principles and System Components

This section introduces the fundamental operating principles and structural elements of wind energy systems. It outlines the physical mechanisms by which wind energy is harnessed and converted into electrical power. The main components of a Wind Energy Conversion System (WECS), including the aerodynamic subsystem, mechanical drive train, and generator, are

discussed in detail. Understanding these building blocks is essential for the proper design, modeling, and control of grid-connected wind systems.

3.2.1 Wind Energy Conversion Principle

Wind energy originates from the kinetic energy of moving air masses caused by uneven solar heating of the Earth's surface. When wind flows through the rotor swept area of a wind turbine, part of its kinetic energy can be extracted and converted into mechanical power. The total power available in the wind is expressed by (3-1) [1][6][10][38][82].

$$P_W = \frac{1}{2}.\rho.A.{V_W}^3 \tag{3-1}$$

Where P_W is the power in watts (W), ρ is the air density in kg/m^3, A is the swept area of the turbine blades in m^2, and V_W is the wind speed in m/s.

Equation (3-1) shows that wind power is highly sensitive to wind speed, which makes wind energy conversion inherently variable [13][16].

Due to aerodynamic and physical constraints, only a fraction of this power can be extracted by the turbine. According to Betz's limit, the maximum achievable fraction is *59.3%*. In practice, the extracted mechanical power is given by expression (3-2) [1][6][19][22][38].

$$P_t = \frac{1}{2}.\rho.A\,.\,C_p(\lambda,\beta).{V_W}^3 \tag{3-2}$$

Where $C_p(\lambda,\beta)$ is the power coefficient, λ is the tip speed ratio, and β is the blade pitch angle. The coefficient C_p represents the aerodynamic efficiency of the wind turbine and depends on blade design and operating conditions [38].

3.2.2 Aerodynamic Model of Wind Turbine

The aerodynamic behavior of a wind turbine is commonly characterized by the tip speed ratio, as defined in expression (3-3) [1][6][22].

$$\lambda = \frac{R_T\,.\,\Omega_t}{V_W} \tag{3-3}$$

Where R is the blade radius (m), and Ω_t is the angular speed of the turbine rotor (rad/s). For a given pitch angle, the power coefficient C_p reaches a maximum at an optimal tip speed ratio λ_{opt} [16][38].

The mechanical torque generated by the turbine can be derived from the extracted power as defined in expression (3-4).

$$T_t = \frac{P_t}{\Omega_t} = \frac{1}{2}.\rho.\pi.{R_T}^2.{V_W}^2\frac{C_p(\lambda,\beta)}{\lambda} \tag{3-4}$$

This aerodynamic torque drives the mechanical shaft and represents the main input to the electromechanical conversion stage. Figure 3-1 illustrates a typical wind turbine and highlights the relationship between wind speed, rotor speed, and aerodynamic torque [10][13].

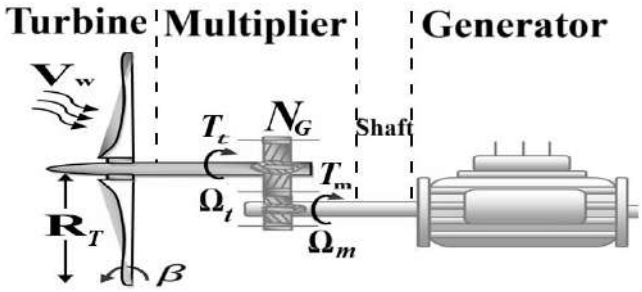


Figure 3-1 Main components of the wind turbine.

3.2.3 Mechanical Drive Train Modeling

The mechanical drive train is responsible for transmitting the torque generated by the wind turbine to the electrical generator. It typically consists of a low-speed shaft connected to the turbine rotor, a gearbox (also referred to as a speed multiplier), and a high-speed shaft coupled to the generator. In variable-speed wind energy conversion systems, the gearbox plays a crucial role by increasing the rotational speed of the turbine rotor to a level compatible with the generator operating requirements, while proportionally reducing the transmitted torque [3][10][38].

Let Ω_t and Ω_m denote the angular speeds of the turbine and generator shafts, respectively, and T_t and T_m the corresponding torques. The gearbox ratio N_G relates these quantities as presented in expressions (3-5) and (3-6) [6][10][16].

$$\Omega_t = \frac{\Omega_m}{N_G} \tag{3-5}$$

$$T_m = \frac{T_t}{N_G} \tag{3-6}$$

The mechanical shafts are assumed to be rigid, and the inertia of the gearbox is considered negligible compared to that of the turbine and generator. Under these assumptions, the mechanical dynamics of the drive train can be described by the fundamental equation (3-7) of motion [6][15].

$$J\frac{d\Omega_m}{dt} = T_t - T_{em} - B.\Omega_m \tag{3-7}$$

Where J is the equivalent inertia of the turbine–generator system referred to the generator side, Ω_m is the mechanical angular speed of the generator shaft, T_{em} is the electromagnetic

torque produced by the generator, and *B* represents the viscous friction coefficient accounting for mechanical losses in the shafts and bearings.

By applying the Laplace transform to equation (3-7) under zero initial conditions, the mechanical angular speed can be expressed in the frequency domain as presented in expression (3-8) [16].

$$\Omega_m = (T_t - T_{em})\,\frac{1}{J\,s + B} \tag{3-8}$$

This transfer function describes the dynamic relationship between the applied mechanical torque, the electromagnetic torque of the generator, and the resulting mechanical speed, and it forms the basis for the development of speed and torque control strategies in wind energy conversion systems [18][28].

This equation highlights the strong coupling between the aerodynamic torque generated by the wind turbine and the electromagnetic torque imposed by the generator, which is a key aspect for the design of speed and torque control strategies. A simplified representation of the turbine–gearbox–shaft–generator system is illustrated in Figure 3-2 [1][13][18][19][55].

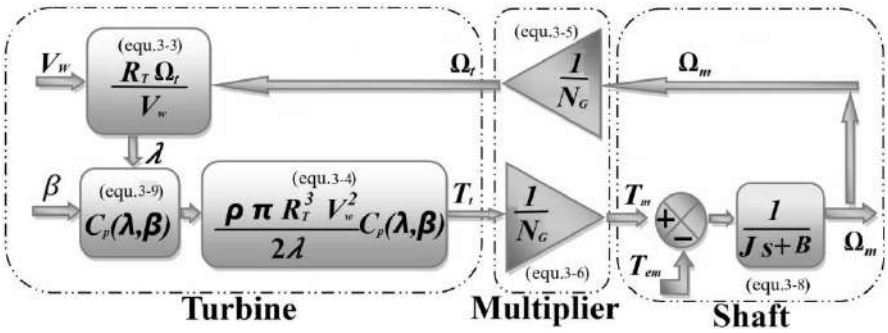


Figure 3-2 Block diagram of the turbine model.

3.2.4 Analytical Model of the Power Coefficient

The power coefficient C_p represents the aerodynamic efficiency of a wind turbine and quantifies the fraction of the available wind power that is converted into useful mechanical power. It is a nonlinear function of the tip speed ratio λ and the blade pitch angle β, and it plays a central role in both turbine modeling and maximum power point tracking strategies [6][15][18].

In analytical and simulation studies, the power coefficient is commonly approximated by an empirical expression that accurately represents the aerodynamic behavior of modern horizontal-axis wind turbines. In this work, the power coefficient is modeled as in expression (3-9) [6][15][18][27].

$$C_p(\lambda,\beta) = 0.73\left(\frac{151}{\lambda_i} - 0.58\,\beta - 0.002\,\beta^{2.14} - 13.2\right) * e^{-\frac{18.4}{\lambda_i}} \tag{3-9}$$

Where λ_i is an intermediate variable defined by expression (3-10) [6][15][18].

$$\lambda_i = \left(\frac{1}{\lambda - 0.02\beta} + \frac{0.003}{\beta^3 + 1}\right)^{-1} \quad (3\text{-}10)$$

This analytical formulation captures the influence of both the rotational speed of the turbine and the blade pitch angle on the aerodynamic performance. For a fixed pitch angle, the power coefficient reaches a maximum value $C_{p,max}$ at an optimal tip speed ratio λ_{opt} [6].

Figure 3-3 illustrates the variation of the power coefficient C_p as a function of the tip speed ratio λ for different values of the blade pitch angle β, using the intermediate variable λ_i defined in (3-10). From these curves, it is observed that for each pitch angle, there exists an optimal tip speed ratio at which the power coefficient reaches its maximum value. In particular, the maximum aerodynamic efficiency $C_{p,max}=0.44$ is obtained for a pitch angle $\beta=0°$ and an optimal tip speed ratio $\lambda_{opt}=7.2$. Under these operating conditions, the wind turbine extracts the maximum mechanical power from the available wind energy, which constitutes the fundamental principle of indirect speed and torque-based MPPT control strategies.

The analytical expression of $C_p(\lambda,\beta)$ is particularly suitable for dynamic simulation and control design, as it allows continuous evaluation of the turbine's aerodynamic efficiency under variable wind and operating conditions.

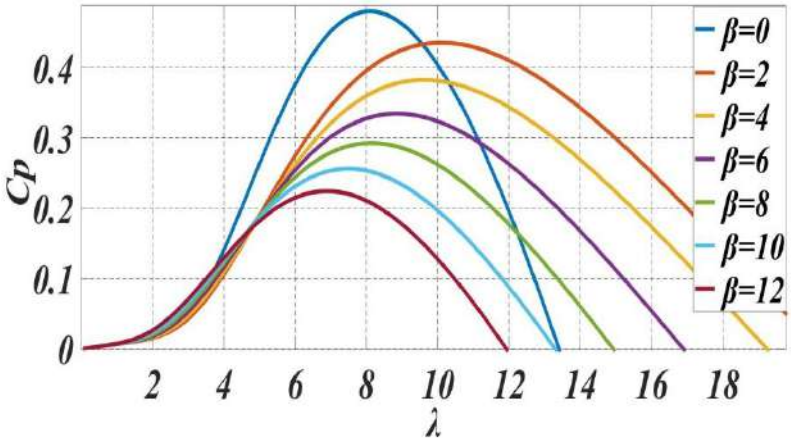


Figure 3-3 Power coefficient C_p curves for different pitch blade angles β.

3.3 Types of Wind Turbine Systems

Wind turbines can be classified according to their operating speed characteristics. The two main categories are constant-speed and variable-speed wind turbine systems. Each type has specific structural configurations, control strategies, and implications for power extraction and grid integration [5][10][20].

3.3.1 Constant-Speed Wind Turbine System

In constant-speed wind turbines, the rotor operates at a nearly fixed rotational speed, typically dictated by the grid frequency for directly connected induction generators. These turbines generally employ a fixed-pitch blade or a simple pitch control mechanism for overload protection. Due to the fixed rotor speed, the turbine cannot maintain the optimal tip speed

ratio across varying wind speeds. Consequently, power extraction is suboptimal at low or high wind speeds, but the system is mechanically simpler and less expensive [5][13][20].

Figure 3-4 illustrates a schematic of a fixed-speed wind turbine system. The rotor is directly coupled to an induction generator, which is connected to the grid through a transformer. Basic control is achieved via a pitch mechanism and optional reactive power compensation [13].

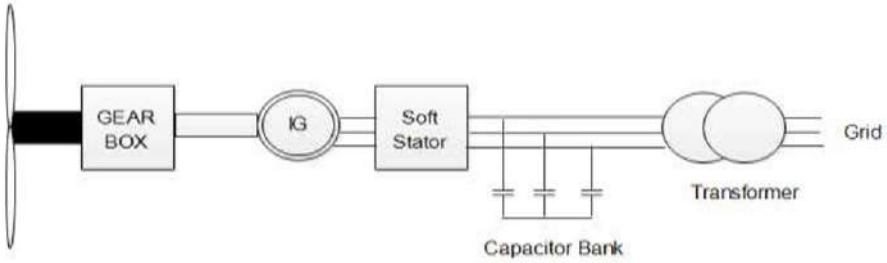


Figure 3-4 Schematic diagram for fixed-speed wind turbine system.

3.3.2 Variable-speed wind turbine system

Variable-speed wind turbines allow the rotor speed to change according to wind conditions, maintaining operation near the optimal tip speed ratio for maximum power extraction. These turbines typically use power electronic converters to decouple the generator from the grid frequency, enabling flexible rotor speed control and improved efficiency. Variable-speed operation also facilitates reduced mechanical stress, lower torque fluctuations, and better grid support through reactive power control [5][13][20].

Figure 3-5 shows a schematic diagram of a variable-speed wind turbine system, where the rotor drives a generator interfaced with the grid via a back-to-back converter, allowing independent control of rotor speed and grid synchronization [13].

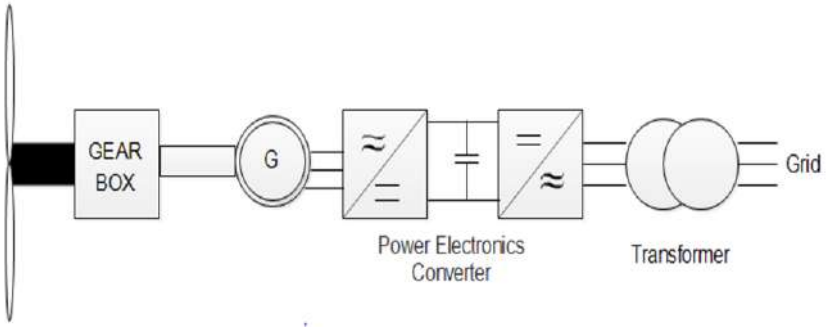


Figure 3-5 Schematic diagram for variable-speed wind turbine system.

3.4 Wind Turbine Control Techniques

The control of a wind turbine aims to maximize the extracted wind energy while ensuring safe mechanical and electrical operation. Depending on the wind speed range, two main control strategies are implemented: maximum power extraction control at low wind speeds and power limitation control at high wind speeds [15].

3.4.1 Wind Turbine Power Characteristics

In wind energy conversion systems, each turbine is characterized by a power curve that represents the converted mechanical power as a function of wind speed. This curve defines distinct operating regions, each associated with specific control objectives [6][10][15][19].

Figure 3-6 shows the power characteristic of the studied wind turbine, highlighting three operating regions corresponding to different wind speed ranges and control requirements [3].

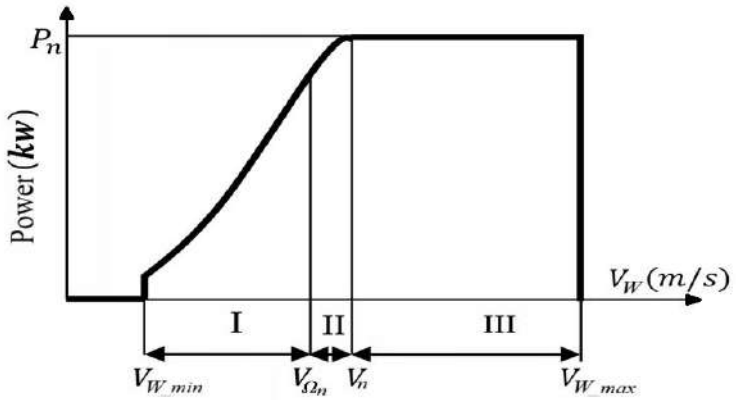


Figure 3-6 Power characteristic of the wind turbine and operating regions.

Region I is a low wind speed region, where the available wind power is lower than the rated power of the turbine. The control objective is to extract the maximum possible power from the wind using MPPT techniques [6][13][49][54].

Region II: is a transition Region, this region lies between partial-load and rated operation. The turbine rotational speed is maintained constant for mechanical and acoustic reasons, such as blade stress limitation and noise reduction. No active power control is required in this region.

Region III is a high wind speed region. At high wind speeds, the turbine power must be limited to its rated value to prevent mechanical and electrical overloading. This is achieved through blade pitch angle control [6][19][20].

3.4.2 Control in region I (Power Optimization)

In Region I, the primary control objective is to maximize the energy extracted from the wind. Although wind energy is abundant, it exhibits significant variability due to continuous fluctuations in wind speed throughout the day. At low wind speeds, efficient control strategies are therefore essential to ensure optimal power extraction under changing operating conditions [15][49].

To achieve maximum aerodynamic efficiency, the blade pitch angle β and the tip-speed ratio λ must be maintained at their optimal values β_{opt} and λ_{opt}, respectively. Under these operating conditions, the wind turbine reaches its maximum power coefficient C_{pmax}. The control strategy used in this operating region is known as MPPT [10][13][54].

MPPT refers to a set of algorithms or control systems designed to enable the energy conversion chain to extract the maximum possible electrical power from the available kinetic energy of the wind. In variable-speed wind energy conversion systems, MPPT is widely employed due to its robustness, simplicity, and high efficiency. The fundamental principle of MPPT is to determine and maintain the turbine rotational speed at an optimal value that ensures maximum power extraction [50].

MPPT techniques can be classified into two main categories depending on whether wind speed measurement and aerodynamic characteristics are required to generate the reference signals. These techniques include Tip-Speed Ratio (TSR) control, Power Signal Feedback (PSF), Hill Climb Search or Perturb and Observe (HCS/P&O), and Optimal Torque Control (OTC) [39].

Direct MPPT methods, such as TSR control and PSF, rely on direct wind speed measurement. However, obtaining accurate and instantaneous wind speed measurements is challenging in practical applications due to sensor limitations and spatial wind variations across the rotor swept area. As a result, their industrial implementation is often limited.

Indirect MPPT methods overcome this limitation by using estimated reference speed or torque signals without requiring direct wind speed measurement. These approaches offer improved reliability and ease of implementation and are therefore widely adopted in modern wind turbines. In this work, an indirect reference speed control method is selected due to its effectiveness, robustness, and suitability for practical wind energy systems [13][15].

3.4.3 Indirect Reference Speed Control

Wind speed measurement is usually performed using an anemometer installed on the turbine nacelle. However, this measurement is often inaccurate because it represents the wind speed at a single point, whereas the rotor sweeps a large area. This leads to estimation errors and reduced energy capture. For this reason, modern wind turbines typically operate without direct wind speed feedback and instead rely on estimation-based control strategies [1][13].

The estimated wind speed can be deduced from the tip-speed ratio definition. The relationship between wind speed and turbine rotational speed is expressed in (3-11) [54].

$$V_{W_est} = \frac{R_T \,.\, \Omega_t}{\lambda_{opt}} \tag{3-11}$$

Where λ_{opt} is the optimal tip-speed ratio.

By substituting the estimated wind speed from Equation (3-11) into Equation (3-4) and considering operation at λ_{opt}, the optimal aerodynamic torque becomes as given in equation (3-12) [13].

$$T_{t_opt} = \frac{1}{2}.\rho.\pi.{R_T}^5.\frac{C_p(\lambda_{opt})}{{\lambda_{opt}}^3}.{\Omega_t}^2 \quad (3\text{-}12)$$

The optimal aerodynamic torque T_{t_opt} is proportional to the square of the turbine rotational speed Ω_t. This relationship can be rewritten as presented in equation (3-13).

$$T_{t_opt} = K_{opt}.{\Omega_t}^2 \quad (3\text{-}13)$$

Where K_{opt} is a constant defined by the turbine and aerodynamic parameters [13].

Under steady-state conditions, the mechanical equation of the turbine-generator system is given by expression (3-14).

$$\frac{T_{t_opt}}{N_G} - B.\Omega_m - T_m = 0 \quad (3\text{-}14)$$

By substituting Equation (3-13) into Equation (3-14), the optimal electromagnetic torque reference imposed on the generator becomes as defined in equation (3-15) [16].

$$T_{m_opt} = \frac{K_{opt}}{{N_G}^3}.{\Omega_m}^2 - B.\Omega_m \quad (3\text{-}15)$$

This expression defines the torque reference that must be applied to the generator to ensure optimal turbine operation. The block diagram illustrating this indirect reference speed control strategy is presented in Figure 3-7 [13].

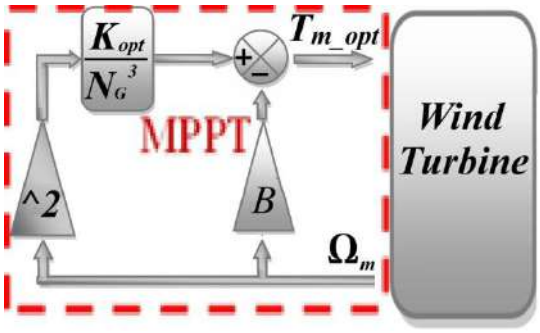


Figure 3-7 Block diagram of indirect reference speed control for MPPT.

3.4.4 Control in Region III (Power Limitation)

In Region III, the wind speed exceeds its rated value, making power regulation necessary to prevent mechanical and electrical overstressing of the turbine. The control objective in this region is therefore to maintain the extracted power at its nominal level [13][16][50].

Two principal techniques are employed for this purpose. Aerodynamic stall control exploits blade geometry to increase aerodynamic losses at high wind speeds and is mainly used in fixed-speed, low-power turbines. In contrast, blade pitch control actively modifies the blade

pitch angle to regulate aerodynamic lift and is the preferred solution for medium- and high-power variable-speed wind turbines.

Blade pitch control operates by adjusting the pitch angle β to a reference value β_{ref}, thereby regulating both the turbine rotational speed and the mechanical power output. The blades are oriented to face the wind at low wind speeds to maximize energy capture, whereas at high wind speeds they are pitched to reduce the power coefficient and limit the extracted power.

The pitch actuation system is commonly modeled as a first-order transfer function characterized by a time constant T_β. The corresponding actuator block diagram is shown in Figure 3-8. For safety and reliability, the pitch rate is typically constrained to approximately *10°/s* during normal operation and may reach *20°/s* under emergency conditions [13][16].

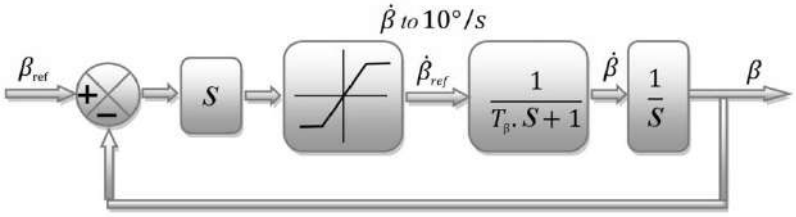


Figure 3-8 Block diagram of the blade pitch actuator.

The regulation of the pitch angle is designed to maintain the generated active power at its rated value P_{nom}. This is achieved by comparing the measured power P_{mes} with Pnom using a PI controller to generate the pitch angle reference β_{ref}. The resulting pitch rate reference $\dot{\beta_{ref}}$ is limited to ensure safe operation, and an integrator is then used to obtain the actual pitch angle β. The overall pitch control structure is presented in Figure 3-9, which illustrates the closed-loop regulation ensuring stable turbine operation under high wind conditions [13][16].

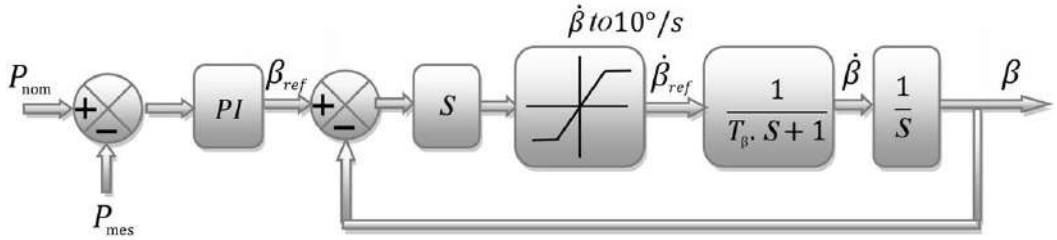


Figure 3-9 Block diagram of the pitch control regulation system.

3.5 Generator Constitution and Modeling for WECS

Efficient integration of WECS into the electrical grid requires appropriate generator structures and power conversion interfaces. In variable-speed wind turbines, the electrical generator plays a key role in maximizing energy extraction while ensuring compliant interaction with the grid. Wind generators used in modern WECS can be broadly classified according to their operating speed range and grid interface. Fixed-speed systems, typically based on squirrel-cage induction generators, offer limited controllability and reduced energy capture. In contrast, variable-speed configurations rely on power electronic converters to enable flexible

control of active and reactive power, improved efficiency, and reduced mechanical stress. Among variable-speed generator technologies, the Doubly-Fed Induction Generator (DFIG) and the Permanent Magnet Synchronous Generator (PMSG) have emerged as the dominant solutions in both onshore and offshore wind applications. This section presents these main generator types, with a particular focus on their physical constitution and mathematical modeling, highlighting their high performance, controllability, and compatibility with modern power electronic converters.

3.5.1 Permanent Magnet Synchronous Generator

a Physical Constitution and Operating Principle

The PMSG is a synchronous electrical machine in which the excitation magnetic field is provided by permanent magnets mounted on the rotor. The stator comprises three-phase distributed windings arranged in the stator slots, which generate electrical power when interacting with the rotor magnetic field [89]. The rotor carries surface-mounted or interior permanent magnets that establish a constant magnetic flux, eliminating the need for external excitation and reducing maintenance compared to conventional synchronous machines [18].

PMSGs are typically implemented in variable-speed wind energy conversion systems, allowing the generator to operate over a wide range of rotor speeds corresponding to fluctuating wind conditions. In direct-drive configurations, the rotor is directly coupled to the wind turbine shaft, avoiding mechanical losses associated with gearboxes, whereas medium-speed configurations may include a gearbox to match the turbine and generator speeds. The electrical output of the PMSG is interfaced with the grid through a full-scale power electronic converter, consisting of a generator-side rectifier, a DC-link capacitor, and a grid-side voltage source inverter (VSI). This configuration ensures complete decoupling between the generator and the grid, enabling independent control of active and reactive power, precise voltage regulation, and compliance with grid codes [18].

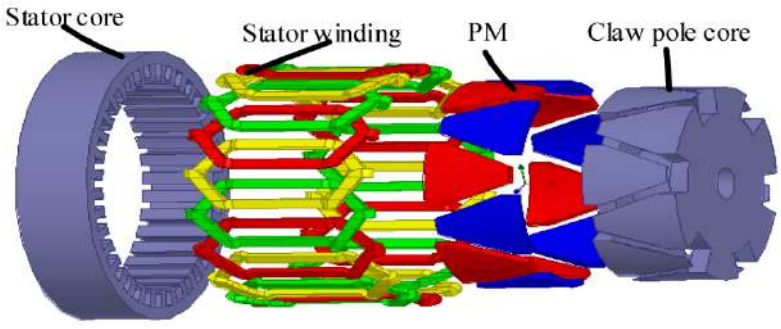


Figure 3-10 Physical constitution of a PMSG

b Electrical Modeling

The electrical dynamics of the PMSG in the synchronous rotating reference frame can be clearly interpreted using the equivalent circuits illustrated in Figure 3-11. These circuits provide a physical representation of the stator voltage equations along the d- and q-axes and highlight the inherent coupling introduced by the machine rotation [1][18][13].

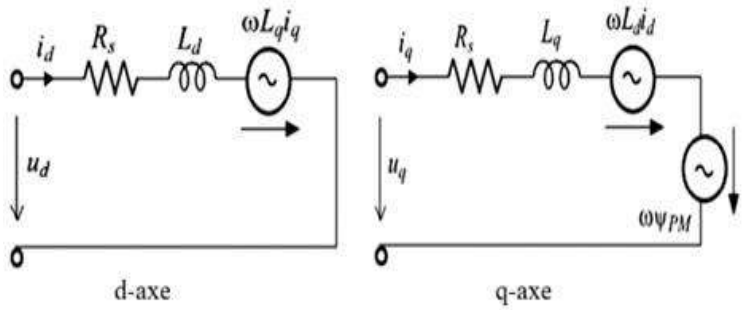


Figure 3-11 Equivalent circuit of the PMSG in the d-q reference frame

The electrical behavior of the PMSG in the three-phase stationary reference frame is governed by the stator voltage equation given in (3-16) [18][49].

$$u_{abc_s} = \frac{d\psi_{abc_s}}{dt} + R_s \,.\, i_{abc_s} \tag{3-16}$$

This equation relates the instantaneous stator voltages to the time derivative of the stator flux linkages and the voltage drop across the stator resistance. In this formulation, u_{abcs} denotes the instantaneous three-phase stator voltages, i_{abcs} represents the corresponding stator currents, R_s is the per-phase stator winding resistance, and ψ_{abcs} refers to the flux linkages generated by both the stator currents and the permanent magnets [18][39].

To simplify analysis and control, the three-phase quantities are transformed into the rotating synchronous d-q reference frame using the Park transformation. Applying this transformation to (3-16) yields the stator voltage equations expressed in the d-q frame, as presented in (3-17).

$$\begin{bmatrix} u_{d_s} \\ u_{q_s} \end{bmatrix} = [P(\theta_m)][R_s][P(\theta_m)]^{-1} i_{dq_s} + [P(\theta_m)][P(\theta_m)]^{-1} \frac{d}{dt}\left[\psi_{dq_s}\right] + [P(\theta_m)]\left(\frac{d}{dt}[P(\theta_m)]^{-1}\right)\left[\psi_{dq_s}\right] \tag{3-17}$$

This transformation introduces additional terms related to the rotation of the reference frame, which depend on the electrical angular position θ_m.

The Park transformation matrix $P(\theta_m)$, defined in (3-18), maps the three-phase stationary variables onto the two-axis rotating frame [13][49].

$$P(\theta_m) = \frac{2}{3}\begin{bmatrix} cos(\theta_m) & cos\left(\theta_m - \frac{2\pi}{3}\right) & cos\left(\theta_m + \frac{2\pi}{3}\right) \\ -sin(\theta_m) & -sin\left(\theta_m - \frac{2\pi}{3}\right) & -sin\left(\theta_m + \frac{2\pi}{3}\right) \\ \frac{1}{2} & \frac{1}{2} & \frac{1}{2} \end{bmatrix} \tag{3-18}$$

The angle θ_m represents the angular displacement between the stator reference axis and the rotating q-axis. In the synchronous frame, the stator flux linkages along the d- and q-axes are related to the stator currents through the respective inductances, as expressed in (3-19) [10].

$$\begin{bmatrix} \psi_{d_s} \\ \psi_{q_s} \end{bmatrix} = \begin{bmatrix} L_d & 0 \\ 0 & L_q \end{bmatrix} \begin{bmatrix} i_{d_s} \\ i_{q_s} \end{bmatrix} = \begin{bmatrix} \psi_f \\ 0 \end{bmatrix} \tag{3-19}$$

In this equation, L_d and L_q denote the stator inductances along the d- and q-axes, respectively, while ψ_f represents the constant flux linkage produced by the permanent magnets.

Furthermore, the derivative of the flux linkage vector in the rotating reference frame introduces a coupling term proportional to the electrical angular speed. As shown in (3-20), this term can be expressed as the product of the electrical angular speed ω_s and a transformed flux linkage vector $[\psi_{dqs}]'$ [89].

$$[P(\theta_m)][P(\theta_m)]^{-1} \frac{d}{dt}[\psi_{dq_s}] = \frac{d}{dt}(\theta_m) * P\left(\frac{\pi}{2}\right) * [\ \psi_{dq_s}] = \omega_s [\ \psi_{dq_s}\ ]' \tag{3-20}$$

The expression of this transformed vector is detailed in (3-21), where it is shown to depend on both the stator currents and the permanent magnet flux [89].

$$[\psi_{dq_s}]' = \begin{bmatrix} -L_q & 0 \\ 0 & L_d \end{bmatrix} \begin{bmatrix} i_{q_s} \\ i_{d_s} \end{bmatrix} + \begin{bmatrix} 0 \\ \psi_f \end{bmatrix} = \begin{bmatrix} -\psi_{q_s} \\ \psi_{d_s} \end{bmatrix} \tag{3-21}$$

By incorporating these relations, the stator voltage equations in the synchronous reference frame can be compactly written as in (3-22).

$$[\ u_{dq_s}] = [\ R_s\ ][\ i_{dq_s}\ ] + \frac{d}{dt}[\ \psi_{dq_s}] + \omega_s [\ \psi_{dq_s}\ ]' \tag{3-22}$$

Substituting the expression of the transformed flux linkage from (3-21) into (3-22) leads to the decoupled d- and q-axis voltage equations presented in (3-23) [10][18][49].

$$\begin{cases} u_{d_s} = -\omega_s \cdot \psi_{q_s} + (R_s + pL_d) i_{d_s} \\ u_{q_s} = \omega_s \cdot \psi_{d_s} + (R_s + pL_q) i_{q_s} \end{cases} \tag{3-23}$$

The electrical angular speed ω_s of the PMSG is directly related to the mechanical angular speed Ω_m by the number of pole pairs n_p, as defined in (3-24) [18].

$$\omega_s = n_p * \Omega_m \tag{3-24}$$

Here, ψ_{ds} and ψ_{qs} denote the stator flux linkages along the d- and q-axes, respectively.

By substituting the flux expressions given in (3-19) into the voltage equations of (3-23), the final form of the d-q stator voltage equations is obtained, as shown in (3-25) [18][81].

$$\begin{cases} u_{d_s} = -\omega_s . L_{q_s} i_{q_s} - \omega_s \cdot (R_s + pL_d) i_{d_s} \\ u_{q_s} = \omega_s . L_{d_s} i_{d_s} + (R_s + pL_q) i_{q_s} + E_s \end{cases} \tag{3-25}$$

In this formulation, L_{ds} and L_{qs} correspond to the stator inductances along the respective axes, i_{ds} and i_{qs} are the armature currents, p denotes the differential operator, and E_s represents the back electromotive force induced by the permanent magnets. Where E_s equal:

$$E_s = \omega_s \,.\, \psi_f \tag{3-26}$$

Finally, in the synchronous rotating reference frame, the electromagnetic torque developed by the PMSG is expressed by (3-27). This torque expression highlights the contribution of both the permanent magnet flux and the reluctance torque, the latter arising from the difference between the d- and q-axis inductances [10].

$$T_{em} = \frac{3}{2} n_p \left[\psi_d i_{q_s} + \left(L_d - L_q\right) i_{d_s} i_{q_s}\right] \tag{3-27}$$

3.5.2 Doubly-Fed Induction Generator

a Physical Constitution and Operating Principle

The DFIG is an asynchronous machine with a wound rotor equipped with a slip-ring and brush system. In this configuration, the stator is directly connected to the electrical grid, while the rotor consists of a three-phase winding connected in a star configuration and supplied through a power electronic converter. This structure enables independent control of the rotor currents and, consequently, control of the machine slip and electromagnetic torque [3].

The bidirectional power converter interfacing the rotor circuit may be implemented either as a direct AC–AC converter or as an indirect AC–DC–AC topology [51], commonly referred to as a back-to-back converter, composed of a rectifier and an inverter. The fundamental operating principle of the DFIG relies on controlling the rotor power, also known as slip power, which can be recovered and either injected into or absorbed from the grid depending on the operating mode. A key characteristic of the DFIG is that the frequency of the rotor currents f_r is proportional to the slip S and the stator frequency f_s, as expressed in (3-28) [3][52][92].

$$f_r = S \,.\, f_s \tag{3-28}$$

Hence, the slip can be written as:

$$S = \frac{f_r}{f_s} = \frac{\omega_r}{\omega_s} \tag{3-29}$$

Where the rotor electrical angular frequency ω_r is given by expression (3-30) [15].

$$\omega_r = \omega_s - \omega_m \tag{3-30}$$

In these expressions, ω_s denotes the stator electrical angular frequency, ω_r represents the rotor electrical angular frequency, and ω_m is the rotor electrical angular speed. The latter is related to the mechanical angular speed Ω_m by expression (3-31) [15].

$$\omega_m = p\,.\,\Omega_m \tag{3-31}$$

Where p is the number of pole pairs, and Ω_m is the mechanical rotational speed of the rotor.

The mechanical dynamics of the DFIG are governed by the motion equation (3-32) [30][92].

$$\frac{d\Omega_m}{dt} = \frac{(T_{em} - T_m)}{J} \tag{3-32}$$

Where J is the equivalent inertia of the mechanical system, T_{em} is the electromagnetic torque developed by the generator, and T_m is the turbine torque applied to the shaft [3].

b Mathematical Modeling

Using space vector theory, a dynamic model of the DFIG can be derived in the stationary $\alpha\beta$ reference frame. In this representation, the three-phase stator and rotor windings are modeled by two stator windings fixed in space and two rotor windings rotating at the mechanical speed. The stator and rotor voltage equations are given by (3-33) and (3-34), respectively [1][3][13][15][19][30][92].

$$\overrightarrow{V_s} = R_s\,\overrightarrow{\imath_s} + \frac{d\,\overrightarrow{\psi_s}}{d\,t} \rightarrow \begin{cases} v_{\alpha s} = R_s\,i_{\alpha s} + \frac{d\,\psi_{\alpha s}}{dt} \\ v_{\beta s} = R_s\,i_{\beta s} + \frac{d\,\psi_{\beta s}}{dt} \end{cases} \tag{3-33}$$

$$\overrightarrow{V_r} = R_r\,\overrightarrow{\imath_r} + \frac{d\,\overrightarrow{\psi_r}}{d\,t} - j\omega_m\overrightarrow{\psi_r} \rightarrow \begin{cases} v_{\alpha r} = R_r\,i_{\alpha r} + \frac{d\,\psi_{\alpha r}}{dt} + \omega_m\psi_{\beta r} \\ v_{\beta r} = R_r\,i_{\beta r} + \frac{d\,\psi_{\beta r}}{dt} - \omega_m\psi_{\alpha r} \end{cases} \tag{3-34}$$

The stator and rotor flux linkages are expressed in (3-35) and (3-36) [3][15][19][27][31][54].

$$\overrightarrow{\psi_s} = L_s\,\overrightarrow{\imath_s} + L_m\,\overrightarrow{\imath_r} \rightarrow \begin{cases} \psi_{\alpha s} = L_s\,i_{\alpha s} + L_m\,i_{\alpha s} \\ \psi_{\beta s} = L_s\,i_{\beta s} + L_m\,i_{\beta s} \end{cases} \tag{3-35}$$

$$\overrightarrow{\psi_r} = L_m\,\overrightarrow{\imath_s} + L_r\,\overrightarrow{\imath_r} \rightarrow \begin{cases} \psi_{\alpha r} = L_m\,i_{\alpha r} + L_r\,i_{\alpha r} \\ \psi_{\beta r} = L_m\,i_{\beta s} + L_r\,i_{\beta r} \end{cases} \tag{3-36}$$

The stator and rotor inductances L_s and L_r are related to the magnetizing inductance L_m and the leakage inductances $L_{\sigma s}$ and $L_{\sigma r}$ as follows [19][92]:

$$L_s = L_{\sigma s} + L_m \tag{3-37}$$

$$L_r = L_{\sigma r} + L_m \tag{3-38}$$

By expressing the flux and current dynamics in state-space form, the flux-based model of the DFIG in the $\alpha\beta$ frame is obtained as shown in (3-39), while the current-based formulation is given in (3-40) [10][13][17][92].

$$\frac{d}{dt}\begin{bmatrix}\psi_{\alpha s}\\ \psi_{\beta s}\\ \psi_{\alpha r}\\ \psi_{\beta r}\end{bmatrix}=\begin{bmatrix} -R_s/\sigma L_s & 0 & R_s L_m/\sigma L_s L_r & 0\\ 0 & -R_s/\sigma L_s & 0 & R_s L_m/\sigma L_s L_r\\ R_r L_m/\sigma L_s L_r & 0 & -R_r/\sigma L_r & -\omega_m\\ 0 & R_r L_m/\sigma L_s L_r & \omega_m & -R_r/\sigma L_r\end{bmatrix}\begin{bmatrix}\psi_{\alpha s}\\ \psi_{\beta s}\\ \psi_{\alpha r}\\ \psi_{\beta r}\end{bmatrix}+\begin{bmatrix}v_{\alpha s}\\ v_{\beta s}\\ v_{\alpha r}\\ v_{\beta r}\end{bmatrix} \tag{3-39}$$

$$\begin{aligned}\frac{d}{dt}\begin{bmatrix}i_{\alpha s}\\ i_{\beta s}\\ i_{\alpha r}\\ i_{\beta r}\end{bmatrix}&=\left(1/\sigma L_s L_r\right)\begin{bmatrix} -R_s L_r & \omega_m {L_m}^2 & R_r L_m & \omega_m L_m L_r\\ -\omega_m {L_m}^2 & -R_s L_r & -\omega_m L_m L_r & R_r L_m\\ R_s L_m & -\omega_m L_m L_s & -R_r L_s & -\omega_m L_m L_r\\ \omega_m L_m L_s & R_s L_m & \omega_m L_r L_s & -R_r L_s\end{bmatrix}\begin{bmatrix}i_{\alpha s}\\ i_{\beta s}\\ i_{\alpha r}\\ i_{\beta r}\end{bmatrix}\\ &+\left(1/\sigma L_s L_r\right)\begin{bmatrix} L_r & 0 & -L_m & 0\\ 0 & L_r & 0 & -L_m\\ -L_m & 0 & L_s & 0\\ 0 & -L_m & 0 & L_s\end{bmatrix}\begin{bmatrix}v_{\alpha s}\\ v_{\beta s}\\ v_{\alpha r}\\ v_{\beta r}\end{bmatrix}\end{aligned} \tag{3-40}$$

The leakage coefficient is defined by [10][34][92]:

$$\sigma=\frac{1-{L_m}^2}{L_s L_r} \tag{3-41}$$

The electromagnetic torque developed by the DFIG is expressed as in (3-42) [19][27][30].

$$T_{em}=\frac{3}{2}\,p\,\frac{L_m}{\sigma\,L_r L_s}\left(\psi_{\beta s}\,\psi_{\alpha r}-\psi_{\alpha s}\,\psi_{\beta r}\right)=\frac{3}{2}\,p\,L_m\left(i_{\beta s}\,i_{\alpha r}-i_{\alpha s}\,i_{\beta r}\right) \tag{3-42}$$

By selecting the stator and rotor currents as state variables, the state-space representation of the DFIG can be written as in (3-43), derived from (3-35) and (3-36).

$$\begin{bmatrix}i_{\alpha s}\\ i_{\beta s}\\ i_{\alpha r}\\ i_{\beta r}\end{bmatrix}=\begin{bmatrix} 1/\sigma L_s & 0 & -L_m/\sigma L_s L_r & 0\\ 0 & 1/\sigma L_s & 0 & -L_m/\sigma L_s L_r\\ -L_m/\sigma L_s L_r & 0 & 1/\sigma L_r & 0\\ 0 & -L_m/\sigma L_s L_r & 0 & 1/\sigma L_r\end{bmatrix}\begin{bmatrix}\psi_{\alpha s}\\ \psi_{\beta s}\\ \psi_{\alpha r}\\ \psi_{\beta r}\end{bmatrix} \tag{3-43}$$

The active and reactive powers exchanged on the stator and rotor sides are calculated using the following expressions [19][32][54]:

$$P_s=\frac{3}{2}(v_{\alpha s}\,i_{\alpha s}+v_{\beta s}\,i_{\beta s}) \tag{3-44}$$

$$P_r=\frac{3}{2}(v_{\alpha r}\,i_{\alpha r}+v_{\beta r}\,i_{\beta r}) \tag{3-45}$$

$$Q_s=\frac{3}{2}(v_{\beta s}\,i_{\alpha s}-v_{\alpha s}\,i_{\beta s}) \tag{3-46}$$

$$Q_r = \frac{3}{2}(v_{\beta r}\, i_{\alpha r} - v_{\alpha r}\, i_{\beta r}) \tag{3-47}$$

Figure 3-12 illustrates the block diagram of the DFIG dynamic simulation model. The inputs include stator and rotor phase voltages as well as the applied load torque, while the outputs consist of stator and rotor currents, flux linkages, electromagnetic torque, rotor speed, and rotor angular position [92].

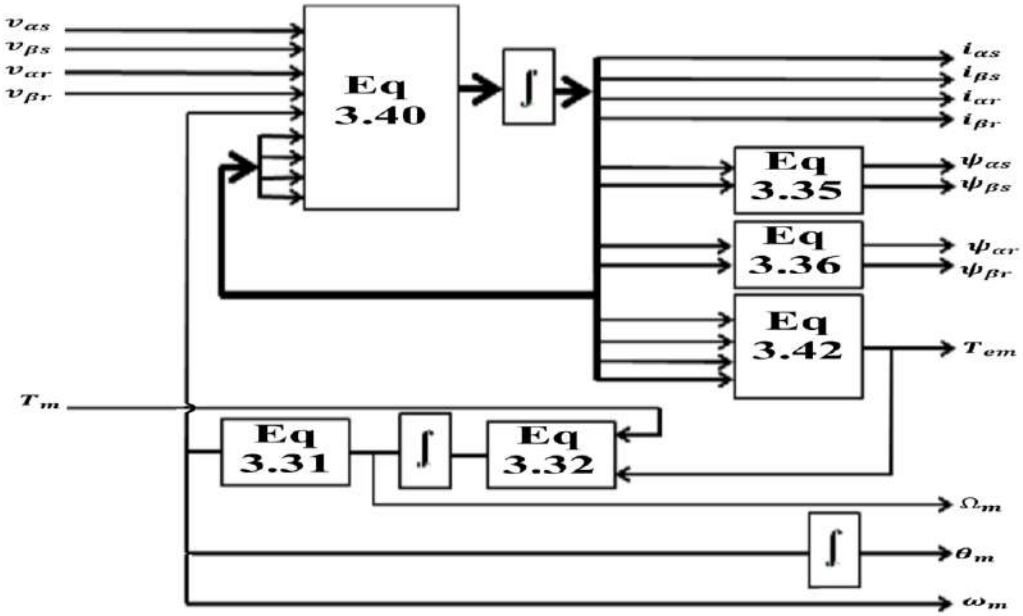


Figure 3-12 Block diagram of the DFIG dynamic simulation model

3.6 Grid-connected Wind Energy System Topologies based on PMSG and DFIG

The integration of wind energy conversion systems into the electrical grid relies on suitable generator technologies and power electronic interfaces capable of ensuring variable-speed operation, efficient power extraction, and compliance with grid codes. Among the available solutions, PMSG and DFIG-based systems are the most widely implemented. Each generator type is associated with specific grid-connected topologies, which are described in the following subsections together with their corresponding schematic representations [10].

3.6.1 PMSG-based Grid-Connected Wind Energy System Topologies

a PMSG with a Diode Rectifier and a Grid-Side Inverter

In this topology, the variable-frequency three-phase output of the Permanent Magnet Synchronous Generator is converted into DC power using an uncontrolled diode rectifier. The rectified voltage is smoothed by a DC-link capacitor and subsequently converted into grid-compatible AC by a voltage source inverter synchronized with the utility network. This configuration represents one of the simplest full-scale converter interfaces used in wind

energy systems and is typically adopted in small and medium power applications. The overall structure of this grid-connected PMSG system is illustrated in

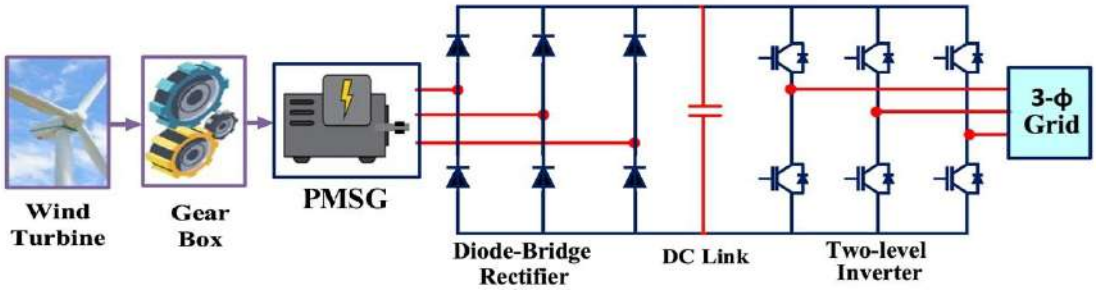


Figure **3-13**, which shows the wind turbine, the PMSG, the diode rectifier, the DC-link capacitor, and the grid-side inverter connected to the utility grid [13][89].

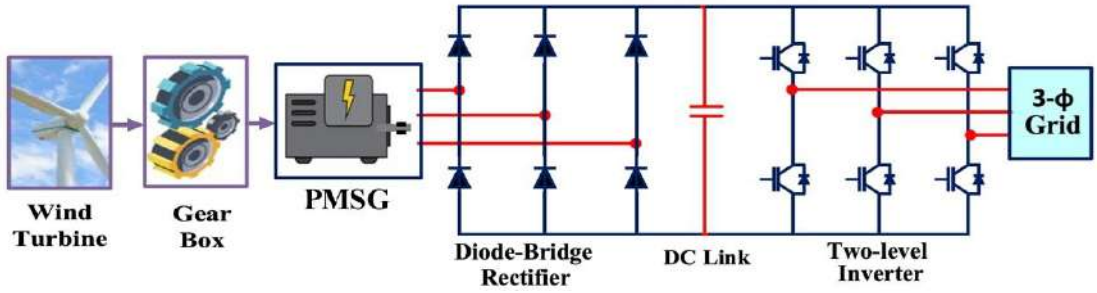


Figure 3-13 Grid-connected wind energy conversion system based on a PMSG with a diode rectifier and voltage source inverter.

b PMSG with Diode Rectifier and DC–DC Boost Converter

To enhance DC-link voltage regulation under variable wind conditions, a DC–DC boost converter can be inserted between the diode rectifier and the DC-link capacitor. In this topology, the boost converter adjusts the DC voltage level to ensure proper operation of the grid-side inverter while enabling effective maximum power point tracking. The presence of the DC–DC stage significantly improves system flexibility, particularly at low wind speeds, where the generator voltage may be insufficient for direct grid injection. The complete configuration of the PMSG system equipped with a diode rectifier and a boost converter is depicted in Figure 3-14, which highlights the additional DC–DC conversion stage and its role in stabilizing the DC link [5][13][16][22][82].

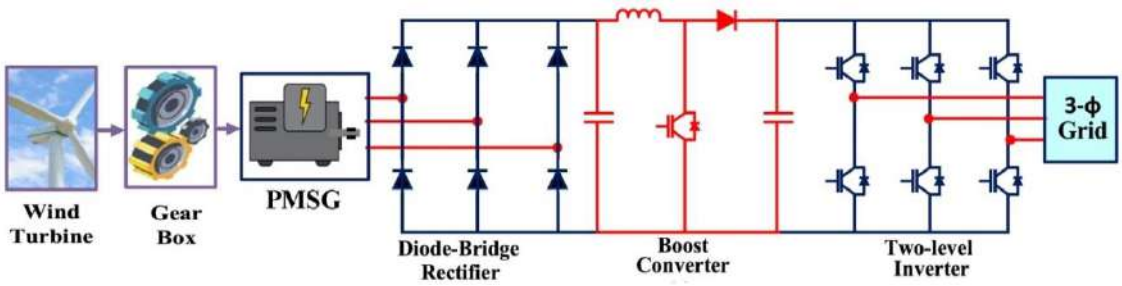


Figure 3-14 Grid-connected PMSG-based wind energy system employing a diode rectifier and DC–DC boost converter for DC-link voltage regulation.

c PMSG with Controlled Rectifier and Grid-Side Inverter

In this configuration, the uncontrolled diode rectifier is replaced by a controlled PWM rectifier based on power electronic switches. This modification allows direct control of the generator currents and electromagnetic torque, leading to improved dynamic performance and enhanced power quality. The controlled rectifier regulates the DC-link voltage and enables more accurate implementation of maximum power point tracking algorithms. Although this topology increases system complexity and cost, it is particularly suitable for high-performance wind energy conversion systems. The schematic representation of this grid-connected PMSG topology, including the controlled rectifier, DC-link capacitor, and grid-side inverter, is shown in Figure 3-15 [19].

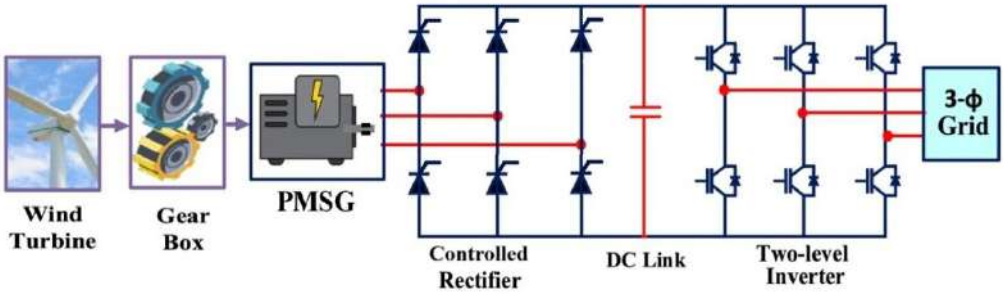


Figure 3-15 Grid-connected wind energy conversion system using a PMSG with controlled PWM rectifier and grid-side inverter.

d PMSG with a full-scale back-to-back converter

The most advanced PMSG-based grid-connected topology employs a full-scale back-to-back converter composed of a machine-side converter and a GSC connected through a common DC-link capacitor. The machine-side converter controls the generator currents and torque, while the grid-side converter regulates the DC-link voltage and manages active and reactive power exchange with the grid. This structure ensures complete electrical decoupling between the generator and the grid, resulting in superior power quality and compliance with modern grid codes. The overall architecture of the PMSG system using a full-scale back-to-back converter is presented in Figure 3-16, which clearly shows the dual converter structure and its connection to the utility grid [10][16][49][81].

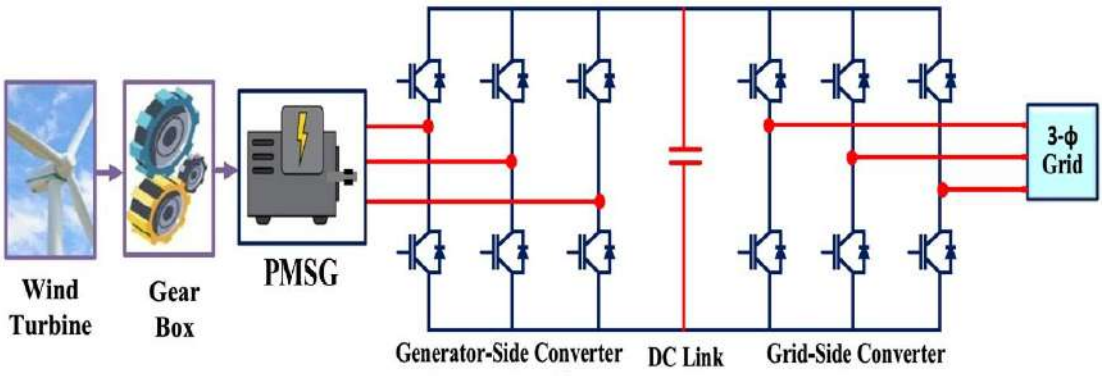


Figure 3-16 PMSG-based wind energy conversion system with full-scale back-to-back power converter for grid integration.

3.6.2 DFIG-Based Grid-Connected Wind Energy System Topologies

a Conventional DFIG with Back-to-Back Rotor Converter

In the conventional DFIG-based wind energy system, the stator windings are directly connected to the grid, while the rotor windings are interfaced through a partial-scale back-to-back converter [3][6][13]. This converter, composed of a rotor-side converter and a grid-side converter, allows control of the rotor currents and consequently enables regulation of active and reactive power. Since only the slip power is processed by the converters, the overall converter rating is significantly reduced compared to full-scale solutions. The structure of this widely adopted DFIG topology is illustrated in Figure 3-17, which shows the direct stator-grid connection and the rotor-side power electronic interface [17][18][19][25][28][51][59][60].

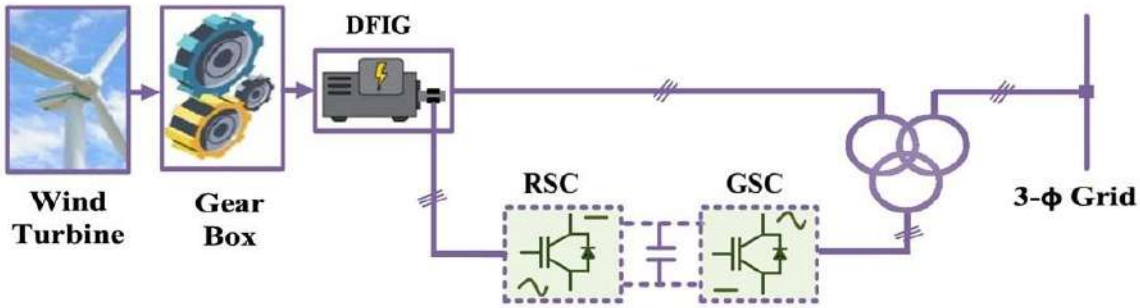


Figure 3-17 Conventional grid-connected DFIG-based wind energy system with partial-scale back-to-back rotor-side converter.

b DFIG with Multilevel Rotor-Side Converter

To improve power quality and reduce harmonic distortion in high-power applications, multilevel converter topologies can be employed on the rotor side of the DFIG. These converters generate output voltages with multiple levels, which reduces voltage stress on power switches and improves current waveform quality [13][15].

c DFIG with Direct AC–AC Rotor Converter

An alternative approach for rotor power control in DFIG systems involves the use of a direct AC–AC converter, such as a cycloconverter or matrix converter, which eliminates the DC-link capacitor. This topology reduces the number of passive components and increases power density, although it requires more complex control strategies and offers a limited frequency conversion range. The schematic diagram of a DFIG system employing a direct AC–AC rotor converter is shown in Figure 3-18, illustrating the absence of a DC link and the direct connection between the rotor and the grid [15].

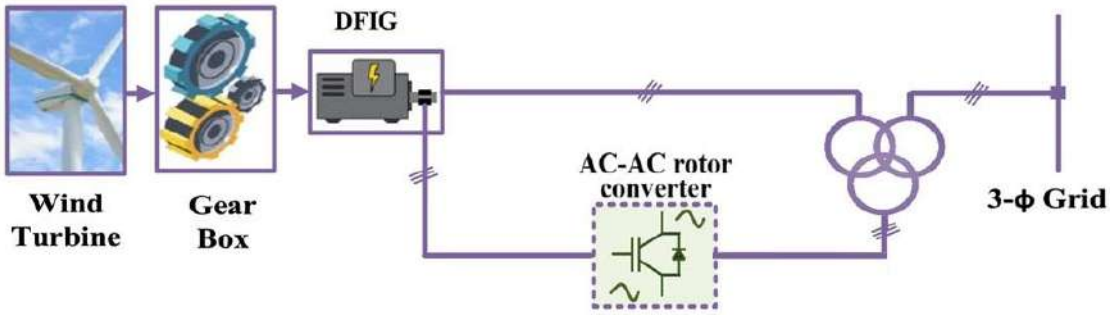


Figure 3-18 DFIG-based wind energy conversion system with direct AC-AC rotor converter and grid-connected stator.

3.7 Control Strategies for Wind Energy Systems

The control system of a wind energy conversion system is essential for ensuring stable operation, maximizing energy capture, and guaranteeing compliant interaction with the electrical grid. In grid-connected variable-speed wind turbines, control complexity increases due to the simultaneous requirements of maximum power point tracking and regulated power exchange with the utility network. The primary objectives of control in such systems are to extract the maximum available power from the wind, regulate the DC-link voltage, control the active and reactive power injected into the grid, and ensure proper synchronization with grid voltage and frequency [19]. In addition, modern wind energy systems must satisfy grid-code requirements, including voltage support and fault ride-through capability during grid disturbances. These objectives are achieved through coordinated control of the generator-side and grid-side converters. Consequently, this section presents the principal control strategies applied to DFIG- and PMSG-based wind energy systems, with particular emphasis on generator-side and grid-side converter control.

3.7.1 Rotor Side Control of DFIG-based Wind Energy Systems

In DFIG-based wind energy systems, variable-speed operation is achieved by controlling the rotor currents via a partial-scale back-to-back rotor-side converter (RSC), while the stator is directly connected to the grid. The RSC uses vector control in the synchronous d–q reference frame aligned with the stator flux, enabling independent regulation of active and reactive power [27][32].

In this configuration, the q-axis rotor current i_q^r regulates the electromagnetic torque and thus the active power output, while the d-axis rotor current i_d^r controls the reactive power exchanged with the grid. The converter employs a dual-loop structure, a voltage loop to control active and reactive power, and a current loop to ensure that rotor currents track their reference values. A PLL synchronizes the system with the grid to determine the reference frame angle θ, facilitating accurate dq-axis transformations [34][40][51].

MPPT is achieved by adjusting the rotor speed to maintain the turbine at its optimal operating torque T_{em_opt}, as expressed in (3-15), thereby maximizing energy extraction from the wind.

The rotor current references are defined in (3-48) and (3-49) for the d-axis and q-axis, respectively.

$$i_{d_ref}^{r} = 0 \tag{3-48}$$

$$i_{q_ref}^{r} = \frac{T_{em_opt}}{\frac{3}{2}.p.\frac{L_m}{L_s}.\left(\frac{V_s.\sqrt{2/3}}{2.\pi.f}\right)} \tag{3-49}$$

The RSC generates the required voltage commands using PI controllers along both d–q axes, as expressed in (3-50) and (3-51).

$$v_{d_ref} = \left[\left(K_p^r + \frac{1}{s}\,K_i^r\right).\left(i_{d_ref}^{r} - i_d^r\right) - \sigma.L_r.\omega_r.i_q^r\right]\left(\frac{2}{v_{dc}}\right) \tag{3-50}$$

$$v_{q_ref} = \left[\left(K_p^r + \frac{1}{s}\,K_i^r\right).\left(i_{q_ref}^{r} - i_q^r\right) + \sigma.L_r.\omega_r.i_d^r + \sqrt{\frac{2}{3}}.V_s.\frac{L_m}{L_s}.\frac{\omega_r}{\omega}\right]\left(\frac{2}{v_{dc}}\right) \tag{3-51}$$

Where K_p^r and K_i^r are the proportional and integral gains, L_r is the rotor inductance, σ is the leakage coefficient defined in expression (3-41), and V_{dc} is the DC-link voltage. This control strategy allows efficient energy extraction, precise active and reactive power regulation, and stable operation under varying wind conditions and grid disturbances.

3.7.2 Control Strategies for PMSG-Based Wind Energy Systems

PMSG-based wind energy systems employ full-scale power conversion interfaces that completely decouple the generator from the grid, enabling independent control of electrical and mechanical variables. On the generator side, the electrical power produced by the PMSG is commonly converted into DC using a diode rectifier, which provides a simple and reliable AC–DC conversion stage. This rectified power is subsequently processed by power electronic converters, allowing the implementation of various control strategies to regulate torque, current, and power output under variable wind conditions. Among the most widely adopted approaches are DTC, DPC, dq-axis control, and SRF control. Each of these methods can be combined with maximum power point tracking MPPT algorithms to ensure maximum energy capture, stable torque regulation, and accurate control of both active and reactive power. The choice of the control strategy depends on system requirements, desired dynamic performance, and implementation complexity.

The diode rectifier and DC–DC boost stage represent a simple and widely used configuration. The diode rectifier converts the three-phase AC output of the PMSG into DC, and the rectified DC voltage V_{DC} is given by expression (3-52).

$$V_{DC} = \frac{3\sqrt{2}}{\pi}.V_{LL} \tag{3-52}$$

Where V_{LL} is the line-to-line voltage of the generator. To stabilize the DC-link voltage and adapt it for grid connection, a DC–DC boost converter can be employed and controlled using various MPPT techniques. This stage ensures a constant DC voltage for the inverter while allowing efficient energy transfer under fluctuating wind conditions.

DTC represents an alternative control strategy for PMSG-based systems, offering fast dynamic response by directly selecting converter switching states without the use of coordinate transformations. Although this method improves transient performance, it requires high sampling frequencies and sophisticated switching logic. To enhance system reliability and reduce maintenance requirements, sensorless control techniques are often implemented, where rotor position and speed are estimated using back-electromotive force or observer-based methods instead of mechanical sensors [19].

DTC directly regulates the electromagnetic torque T_{em} and stator flux ψ_s without coordinate transformations. The torque and flux errors are defined in expressions (3-53) and (3-54).

$$\Delta T_{em} = T_{em_ref} - T_{em} \tag{3-53}$$

$$\Delta \psi_s = \psi_{s_ref} - \psi_s \tag{3-54}$$

Where T_{em_ref} and ψ_{s_ref} are obtained from the MPPT algorithm. The electromagnetic torque is calculated from the stator d–q currents and flux linkages as defined in expression (3-55).

$$T_{em} = \frac{3}{2} . p . (\psi_d . i_q - \psi_q . i_d) \tag{3-55}$$

Where p is the number of pole pairs. These errors are used to select the optimal converter voltage vector through a switching table, enabling fast torque response and reduced transient deviations.

3.7.3 Grid-Side Converter Control for DFIG and PMSG

The grid-side converter plays a crucial role in maintaining DC-link voltage stability and controlling power exchange with the grid in both DFIG- and PMSG-based systems. It is generally controlled in a synchronous reference frame synchronized with the grid voltage. In this control structure, the d-axis current component regulates the DC-link voltage by balancing active power flow, while the q-axis current component controls reactive power injection or absorption [32][34].

Accurate synchronization with the grid is achieved using phase-locked loop techniques, including conventional PLL or DSOGI-PLL, particularly under distorted grid conditions. To ensure compliance with power quality standards, the grid-side converter is commonly interfaced with the grid through a filter to reduce current harmonic distortion [40][51][60].

3.7.4 Advanced Control Techniques for Wind Energy Systems

To improve robustness under wind variability, parameter uncertainties, and grid disturbances, advanced control techniques have been increasingly adopted in wind energy systems. Intelligent approaches such as fuzzy logic control effectively handle nonlinear behavior without requiring precise mathematical models. Model predictive control optimizes converter switching by predicting future system behavior, while sliding mode control offers strong robustness against disturbances and parameter variations. Adaptive PI controllers are also employed to dynamically adjust controller gains and maintain optimal performance over a wide operating range [29][30][39][49][50][89].

3.8 Modeling of Grid-Connected Wind Energy System

This section presents the mathematical modeling of the grid-connected wind energy conversion system based on a PMSG. The system integrates a controlled generator-side rectifier, a DC-link stage, and a grid-side inverter with appropriate control strategies to ensure maximum power extraction, stable DC-link regulation, and high-quality power injection into the utility grid.

3.8.1 Description of the Grid-Connected Wind Energy System

As shown in Figure 3-19, the illustrated system represents a grid-connected wind energy conversion system based on a PMSG interfaced with the utility grid through a full-scale power electronic conversion chain. The architecture is designed to enable variable-speed operation, independent control of active and reactive power, and compliance with grid power quality requirements.

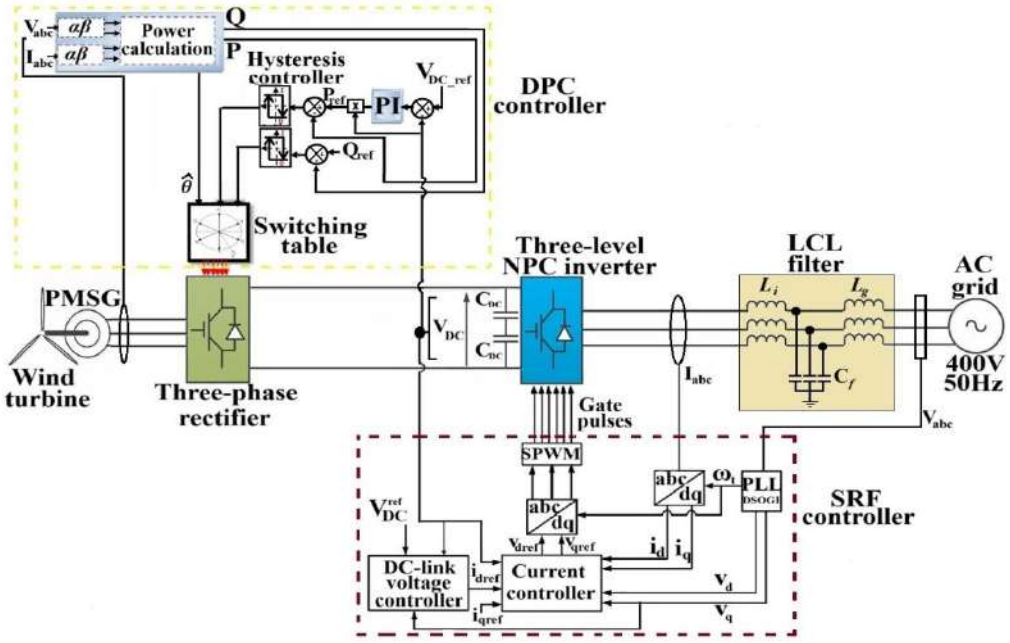


Figure 3-19 Configuration of the grid-connected PMSG-based wind energy system.

The wind turbine converts the kinetic energy of the wind into mechanical torque, which drives the PMSG. Due to the variable nature of wind speed, the generator operates at variable frequency and voltage, requiring a power electronic interface to ensure proper grid integration.

On the generator side, the three-phase output of the PMSG is connected to a three-phase controlled rectifier. This rectifier converts the variable-frequency AC voltage into DC power while allowing control of the generator current and electromagnetic torque. The generator-side control is based on DPC, where the instantaneous active and reactive powers are calculated in the stationary $\alpha\beta$ reference frame using measured stator voltages and currents. These power components are compared with their reference values, and hysteresis controllers generate switching signals through a predefined switching table. This control strategy ensures fast dynamic response and effective regulation of generator power without requiring coordinate transformations.

The rectified power is transferred to the DC-link stage, which consists of a DC-link capacitor. The DC-link acts as an energy buffer between the generator-side rectifier and the grid-side inverter, smoothing power fluctuations and maintaining a stable DC voltage. The DC-link voltage is a key variable for ensuring balanced power flow between both conversion stages.

On the grid side, a three-level NPC voltage source inverter is employed to inject power into the utility grid. The multilevel topology improves output voltage quality, reduces switching losses, and lowers harmonic distortion compared to conventional two-level inverters. The inverter is connected to the grid through an LCL filter, composed of inverter-side inductance, grid-side inductance, and a shunt capacitor. This filter effectively attenuates high-frequency switching harmonics and ensures that the injected grid current satisfies harmonic standards.

The grid-side inverter is controlled using an SRF control strategy. A DSOGI-PLL synchronizes the inverter with the grid voltage by providing the grid angle and frequency [40]. Measured grid currents are transformed into the dq reference frame, where the d-axis current is typically used to regulate the DC-link voltage (active power), while the q-axis current controls reactive power exchange with the grid. The current control loops generate reference voltages, which are converted into gate pulses using sinusoidal pulse-width modulation (SPWM)[25].

Overall, the proposed system combines DPC-based generator-side control with SRF and DSOGI-PLL-based grid-side control, enabling efficient maximum power extraction, stable DC-link regulation, precise active and reactive power control, and high-quality grid current injection under variable wind conditions.

3.8.2 Direct Power Control of the Three-Phase Rectifier

DPC is a nonlinear control strategy widely applied to three-phase rectifiers in grid-connected wind energy conversion systems due to its fast dynamic response and simple control structure. In DPC, the instantaneous active and reactive powers exchanged between the rectifier and the grid are directly controlled, without the use of inner current control loops or a modulation

stage. The switching states of the converter are selected directly from a predefined switching table. The general structure of a DPC-controlled rectifier is illustrated in Figure 3-19, which includes the power estimation block, hysteresis controllers, sector detection logic, and switching table used to generate the converter gating signals [2][18][19][50][84].

The instantaneous three-phase currents are first transformed into the stationary $\alpha\beta$ reference frame using the Concordia transformation. Based on the current components i_α and i_β, together with the corresponding voltage components v_α and v_β, the instantaneous active and reactive powers are calculated as expressed in equations (2-34) and (2-35). The inverse Concordia transformation is subsequently employed, when required, to reconstruct the phase voltages for voltage sector identification and switching decision purposes [2][19][83][84].

The instantaneous power errors are obtained by comparing the estimated active and reactive powers with their respective reference values, as defined in equations (3-56) and (3-57).

$$\Delta P = P_{ref} - P \tag{3-56}$$

$$\Delta Q = Q_{ref} - Q \tag{3-57}$$

The DC-link voltage regulation loop plays a key role in maintaining the DC bus voltage at its reference value by controlling the charging and discharging process of the DC-link capacitor. To ensure stable rectifier operation and a constant DC-link voltage, an outer control loop based on a PI regulator is implemented. The error between the reference DC voltage V_{DC_ref} and the measured DC voltage V_{DC} is processed by the PI controller to generate the maximum amplitude of the source current I_{max}. This current amplitude is then multiplied by the measured DC voltage V_{DC} to produce the active power reference P_{ref}. The PI controller parameters are given by equations (3-58) and (3-59), while the reactive power reference is set to zero ($Q_{ref}=0$) to ensure unity power factor operation [83][84].

$$K_P = 2.C_{DC}\,.\,{\omega_0}^2\,.\,\xi \tag{3-58}$$

$$K_i = C_{DC}\,.\,{\omega_0}^2 \tag{3-59}$$

Where K_P and K_I are the proportional and integral gains of the PI controller, respectively, C_{DC} is the DC-link capacitance, ξ is the damping factor, and ω_0 is the natural angular frequency of the control loop.

The active and reactive power errors are then processed through hysteresis controllers, which generate the binary control signals S_P and S_Q. These signals indicate whether the instantaneous powers must increase or decrease. The hysteresis control logic is defined in equation (3-60), where H_P and H_Q denote the hysteresis band widths [2][16][19][83].

$$S_p \begin{cases} 1, & P < P_{ref} - H_P \\ 0, & P > P_{ref} + H_P \end{cases}; \quad S_Q \begin{cases} 1, & Q < Q_{ref} - H_Q \\ 0, & Q > Q_{ref} + H_Q \end{cases} \tag{3-60}$$

Simultaneously, the angular position of the grid voltage vector is identified in the $\alpha\beta$ plane and divided into twelve sectors, as illustrated in Figure 3-20**.** The sector in which the voltage vector is located is determined based on the angle of the voltage vector with respect to the α-axis. This angle is computed using the inverse tangent function, as expressed in equation (3-61) [2][19][50][93].

$$\hat{\theta} = \tan^{-1}\left(\frac{v_{s\beta}}{v_{s\alpha}}\right) \tag{3-61}$$

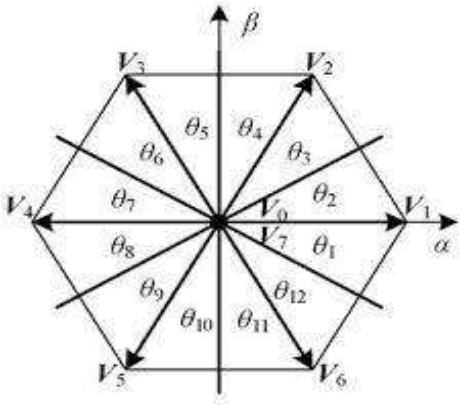


Figure 3-20 The division of the αβ plane into sectors.

Finally, the combination of the hysteresis outputs S_P and S_Q, together with the identified voltage sector, is used to select the appropriate switching state from the DPC switching table presented in Table 3-1. This table defines the optimal converter voltage vector V_k to be applied by the rectifier to drive the instantaneous active and reactive powers toward their reference values [2][19].

Table 3-1 Switching table.

S_P	S_Q	S_1	S_2	S_3	S_4	S_5	S_6	S_7	S_8	S_9	S_{10}	S_{11}	S_{12}
1	*0*	V_6 (101)	V_7 (111)	V_1 (100)	V_0 (000)	V_2 (110)	V_7 (111)	V_3 (010)	V_0 (000)	V_4 (011)	$V7$ (111)	$V5$ (001)	$V0$ (000)
	1	V_2 (110)	V_7 (111)	V_3 (010)	V_0 (000)	V_4 (011)	V_7 (111)	V_5 (001)	V_0 (000)	V_6 (101)	$V7$ (111)	$V1$ (100)	$V0$ (000)
0	*0*	V_6 (101)	V_1 (100)	V_1 (100)	V_2 (110)	V_2 (110)	V_3 (010)	V_3 (010)	V_4 (011)	V_4 (100)	$V5$ (001)	$V5$ (001)	$V6$ (101)
	1	V_1 (100)	V_2 (110)	V_2 (110)	V_3 (010)	V_3 (010)	V_4 (011)	V_4 0110	V_5 (001)	V_5 (001)	$V6$ (101)	$V6$ (101)	$V1$ (100)

3.8.3 DC-Link Capacitance Design

The DC-link capacitor in a three-level NPC inverter plays a fundamental role in maintaining a stable DC voltage and ensuring reliable operation of the grid-connected wind energy conversion system. It acts as an energy buffer between the generator-side converter and the grid-side inverter, absorbing power fluctuations caused by wind speed variations, switching actions, and transient operating conditions. Proper sizing of the DC-link capacitor is therefore essential to limit voltage ripple, guarantee neutral-point stability, and satisfy grid power quality requirements [44].

The design of the DC-link capacitance is primarily governed by the allowable DC voltage ripple, the rated power of the inverter, and the grid frequency. The capacitor must store sufficient energy to compensate for low-frequency power oscillations while maintaining the DC voltage within an acceptable range, typically limited to *2–5%* of the nominal DC-link voltage. For a grid-connected three-level NPC inverter, the minimum required DC-link capacitance can be estimated by expression (3-62).

$$C_{dc} \geq \frac{P}{V_{dc}.2.\pi\,.f_{grid}\,.\Delta V_{dc}} \tag{3-62}$$

Where P is the rated inverter power, V_{DC} is the nominal DC-link voltage, f_{grid} is the grid frequency, and ΔV_{DC} is the permissible DC voltage ripple.

In a three-level NPC topology, the DC-link is generally implemented using two series-connected capacitors in order to create the neutral point. Under balanced operating conditions, the total DC-link capacitance is equally shared between the two capacitors, such that:

$$C_1 = C_2 = \frac{C_{DC}}{2} \tag{3-63}$$

This configuration ensures symmetrical voltage distribution across the DC-link and contributes to stable neutral-point operation.

To further improve system stability and suppress oscillations caused by switching harmonics and resonance phenomena, damping resistors are commonly connected in series with the DC-link capacitors. These resistors reduce voltage and current oscillations without introducing excessive power losses. An appropriate value of the damping resistance can be approximated based on the capacitor impedance at the dominant ripple frequency, which is typically related to the inverter switching frequency, and is given by (3-64) [48][70][74].

$$R_d = \frac{1}{6.\pi.f_{sw}.C_{dc}} \tag{3-64}$$

Where f_{sw} denotes the inverter switching frequency. The inclusion of damping resistors enhances DC-link voltage stability and improves the overall dynamic performance of the NPC inverter under fluctuating wind and grid conditions.

3.8.4 LCL Filter Design

The LCL filter is a key component in grid-connected inverter-based wind energy systems, as it is specifically designed to attenuate high-frequency harmonics produced by the inverter switching process. The filter is composed of an inverter-side inductance L_i, a shunt-connected filter capacitor C_f, and a grid-side inductance L_g. This structure offers significantly better harmonic attenuation than a simple L filter, since the attenuation slope increases

proportionally to the square of the frequency. Proper selection of these elements ensures effective harmonic mitigation, stable system operation, and compliance with grid power quality standards [36][37][69][73][75].

The design of the LCL filter starts with defining the main system parameters, including the inverter rated power P, grid voltage V_g, switching frequency f_{sw}, grid frequency f_{grid}, and the maximum allowable total harmonic distortion, which is typically limited to *5%* according to IEEE 519 [21][76]. A critical aspect of the design is the selection of the resonance frequency f_{res}, which must be sufficiently higher than the grid frequency to avoid interaction with fundamental components, and sufficiently lower than the switching frequency to ensure effective harmonic attenuation. In practice, the resonance frequency is selected within the following range [69][78][93]:

$$10 \cdot f_{grid} \leq f_{res} \leq 0.5 \cdot f_{sw} \tag{3-65}$$

The resonance frequency of the LCL filter is determined by the inverter-side inductance, grid-side inductance, and filter capacitance, and is given by (3-66) [71][78][93].

$$f_{res} = \frac{1}{2\pi}\sqrt{\frac{L_i + L_g}{L_i \cdot L_g \cdot C_f}} \tag{3-66}$$

To evaluate the harmonic attenuation and stability characteristics of the filter, the frequency response is analyzed using its transfer function. Assuming the grid behaves as an ideal voltage source that absorbs harmonic components, the transfer function between the inverter voltage and the grid current, including damping resistance, can be expressed by transfer function (3-67) [70][71].

$$H_{LCL}(s) = \frac{C_f R_f\, s \;+\; 1}{L_i\, C_f\, L_g\, s^3 + \; C_f \;\; (L_i + L_g) R_f\, s^2 + (L_i + L_g) s} \tag{3-67}$$

The Bode plot of this transfer function is commonly used to verify the attenuation of switching harmonics and to ensure that resonance peaks are adequately damped [73].

The inverter-side inductance L_i is typically designed based on the allowable current ripple ΔI, which is usually selected between *10%* and *20%* of the rated current. A commonly used expression for L_i is given by (3-68) [72].

$$L_i = \frac{V_{dc}}{16.\, f_{sw}.\, \Delta I} \tag{3-68}$$

Where the ripple current is defined by expression (3-69) [72].

$$\Delta I = 0.1.\, I_{rated} \tag{3-69}$$

And the rated current of the inverter is calculated by expression (3-70).

$$I_{rated} = \frac{P.\sqrt{2}}{V_g} \tag{3-70}$$

The grid-side inductance L_g is usually chosen as a multiple of the inverter-side inductance to improve filtering performance and robustness against grid impedance variations, and is given by expression (3-71).

$$L_g = k.L_i \tag{3-71}$$

Where the ratio *k* generally lies between *3* and *5* [72].

The filter capacitance C_f is selected to provide sufficient attenuation of high-frequency harmonics while limiting the reactive power injected into the grid at the fundamental frequency. To satisfy grid code requirements, the reactive power absorbed by the capacitor is typically limited to 5% of the inverter's rated power, leading to expression (3-72) [69][72][80].

$$C_f \leq \frac{Q_{max}}{2\pi.f_{grid}.{V_g}^2} \tag{3-72}$$

With the maximum allowable reactive power defined by expression (3-73).

$$Q_{max} = 0.05\ P \tag{3-73}$$

To suppress resonance phenomena introduced by the interaction of the inductive and capacitive elements, a damping resistor R_{fd} is connected in series with the filter capacitor in each phase. This resistor provides passive damping and improves system stability without significantly affecting low-frequency performance. An approximate value of the damping resistance can be obtained by expression (3-74) [70][74].

$$R_{fd} = \frac{1}{6.\pi.f_{res}.C_f} \tag{3-74}$$

The appropriate design of the LCL filter based on these relations ensures effective harmonic attenuation, stable dynamic behavior, and compliance with grid power quality standards in grid-connected wind energy conversion systems [36].

3.9 Simulation Results of Grid-Connected Wind Energy System

The simulation results of the proposed grid-connected wind energy conversion system are presented to validate the effectiveness of the system modeling, control strategies, and power quality performance. The complete system was implemented in MATLAB/Simulink using the parameters listed in Table 3-2 (Annex II), and a time-varying wind speed profile, shown in Figure 3-21, was applied to emulate realistic operating conditions [38]. The analysis addresses both generator-side and grid-side behaviors, including DC-link voltage regulation, DSOGI-PLL synchronization, LCL filter frequency response, active and reactive power exchange, and

the quality of the injected grid current. The obtained results confirm stable operation, fast dynamic response, effective harmonic mitigation, and full compliance with grid interconnection standards under variable wind conditions.

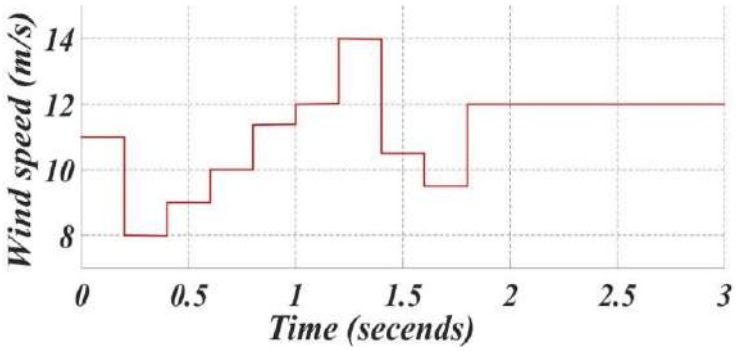


Figure 3-21 Variable wind speed profile.

3.9.1 DC-Link Voltage Regulation Performance

The regulation of the DC-link voltage is illustrated in Figure 3-22. The DC-link voltage was tightly regulated around its nominal value of *720V*, with a steady-state ripple maintained below *1%*, as observed in the simulation results. This high level of voltage stability is primarily attributed to the proper sizing of the DC-link capacitor (C_{dc}= *5600µF*) and the inclusion of a damping resistor (R_d = *1mΩ*), which effectively suppressed oscillatory behavior and mitigated resonance phenomena. Moreover, the DC-link voltage remained stable during transient operating conditions, such as sudden power variations and external disturbances, confirming the robustness of the DC voltage control loop and its ability to ensure reliable power balance between the generator-side and grid-side converters.

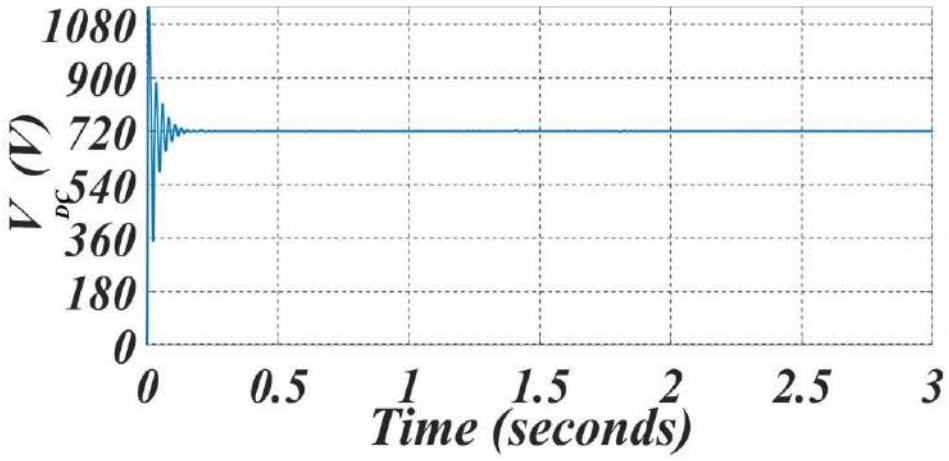


Figure 3-22 DC-link voltage response.

3.9.2 DSOGI-PLL Synchronization Performance

The synchronization capability of the grid-side control is evaluated through the frequency estimation provided by the DSOGI-PLL, as shown in Figure 3-23. At system startup, a short oscillatory transient appears due to the synchronization process; however, the estimated frequency rapidly converges to the nominal grid frequency of *50Hz* within approximately

0.1s. No overshoot, steady-state error, or long-term drift is observed. This fast and accurate frequency tracking confirms the robustness of the DSOGI-PLL under initial grid disturbances and ensures precise dq-axis alignment for synchronous reference frame control, which is critical for stable current regulation and secure grid interconnection [51].

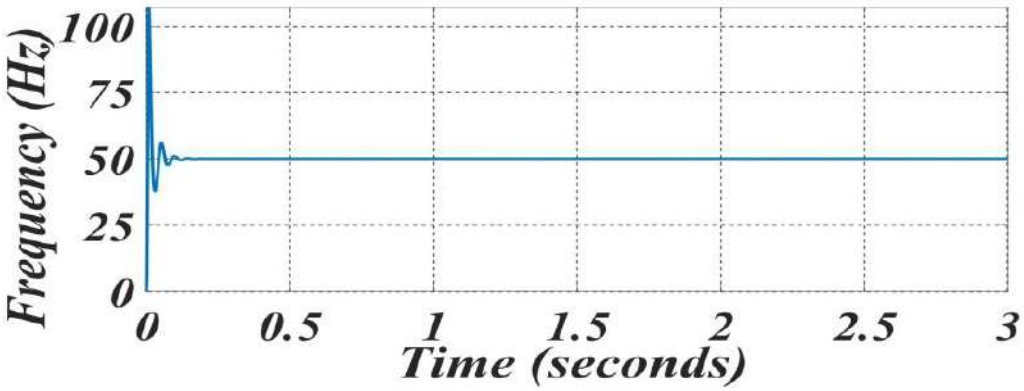


Figure 3-23 Estimated grid frequency using DSOGI-PLL.

3.9.3 LCL Filter Frequency Response Analysis

The frequency-domain performance of the LCL filter with damping is analyzed using the Bode diagram presented in Figure 3-24. The LCL filter, whose parameters (L_i=*0.1mH*, L_g=*0.5mH*, C_f=*100μF*, R_{fd}=*0.3 Ω*) were carefully tuned, exhibits a significant reduction of the resonance peak due to the introduction of a series damping resistor with the filter capacitor, resulting in a smoother magnitude response. At high frequencies, the phase response converges toward *−180°*, instead of *−230°*, indicating improved stability margins. The resonance frequency is observed around *1.5kHz*, which is well separated from the inverter switching frequency of *10kHz*, thereby ensuring effective harmonic attenuation. Furthermore, the analysis confirms that the closed-loop current control bandwidth should be limited to approximately 1 kHz, where the phase shift is close to *−90°*, in accordance with stability criteria reported in the literature. These results validate the effectiveness of the damping strategy and confirm that the LCL filter design achieves an optimal compromise between harmonic suppression and dynamic stability [73].

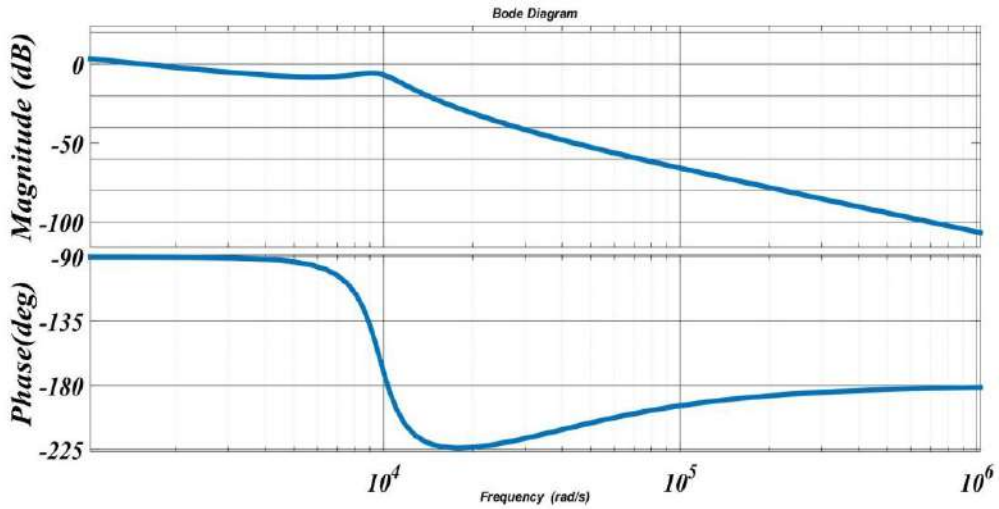


Figure 3-24 Bode diagram of the LCL filter transfer function.

3.9.4 Active and Reactive Power Exchange with the Grid and Efficiency

The active and reactive power exchanged with the utility grid are depicted in Figure 3-25. The active power closely follows the available wind energy, reaching values up to the rated system power of *120kW* under high wind conditions. This behavior demonstrates effective maximum power extraction and efficient power transfer to the grid. Meanwhile, the reactive power is maintained near zero, with fluctuations limited to less than *±1kVAr*, confirming unity power factor operation. The overall system efficiency exceeds *95%* over a wide operating range, reflecting reduced conduction and switching losses achieved through the adopted converter topology, optimized control strategy, and well-designed filter. These results validate compliance with grid code requirements and highlight the suitability of the proposed system for practical grid-connected wind energy applications.

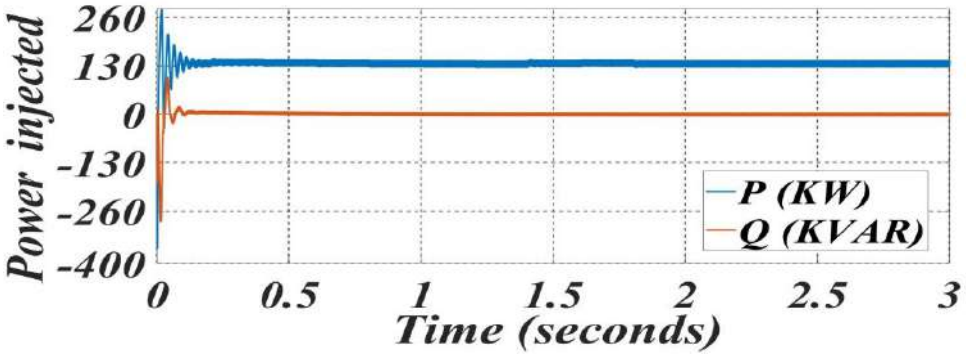


Figure 3-25 Active and reactive powers injected into the grid.

3.9.5 Grid Current Quality and Harmonic Distortion

The quality of the grid-injected current is assessed by examining both the current waveform and its THD, with a zoomed view of the waveform shown in Figure 3-26. The grid current exhibits a nearly sinusoidal shape, with a phase shift of *120* electrical degrees, and remains well synchronized with the grid voltage, indicating accurate PLL operation and effective current control. Harmonic analysis shows that the THD of the grid current remains below *1.5%*, which is well within the limits defined by IEEE 519 standards [21]. This low THD confirms the combined effectiveness of the LCL filter and the SRF control strategy in mitigating switching harmonics and maintaining high power quality.

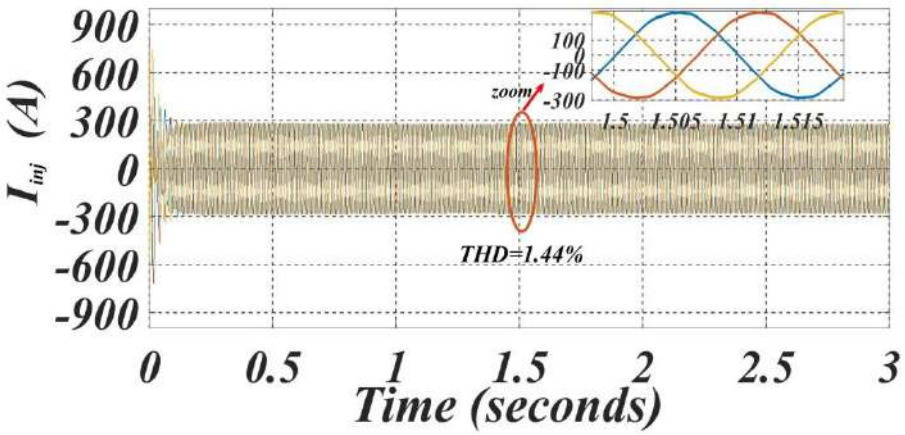


Figure 3-26 Current injected into the grid waveforms.

3.10 Simulation Results Discussion

The simulation results of the proposed grid-connected wind energy conversion system demonstrate the effectiveness of the system modeling, control strategies, and power quality performance. Under a time-varying wind profile, the system maintained stable operation, confirming the robustness of both generator-side and grid-side control schemes under realistic operating conditions.

The DC-link voltage remained tightly regulated throughout the simulation, showing minimal oscillations even during sudden changes in power or environmental disturbances. This indicates that the voltage control loop effectively maintains power balance between the generator-side and grid-side converters, ensuring system stability under dynamic conditions.

The grid synchronization achieved through the DSOGI-PLL exhibited fast and accurate frequency tracking, with negligible overshoot or steady-state error. This ensures precise alignment of the synchronous reference frame, which is essential for stable current regulation and reliable grid interconnection.

The LCL filter, combined with a damping strategy, effectively mitigated resonance phenomena and provided a smooth frequency response. The filter maintained stability across the operational frequency range and sufficiently separated resonance from switching harmonics, demonstrating a strong balance between harmonic suppression and dynamic response.

Active and reactive power behavior showed that the system effectively extracts available wind energy and delivers it to the grid with minimal reactive power exchange. The system operates near unity power factor and achieves high efficiency, reflecting the effectiveness of the adopted control strategies and filter design.

Finally, the grid current quality was excellent, with a near-sinusoidal waveform closely synchronized with the grid voltage. Harmonic distortion remained very low, highlighting the combined efficiency of the LCL filter and synchronous reference frame control in maintaining high power quality and meeting grid standards.

Overall, the results demonstrate that the proposed system ensures stable and efficient operation, reliable grid synchronization, effective harmonic mitigation, and high-quality power delivery under variable wind conditions, validating the proposed design and control methodology.

3.11 Conclusion

This chapter provided a detailed examination of the design, modeling, and control of grid-connected wind energy conversion systems, addressing both PMSG and DFIG technologies. Various MPPT strategies, from conventional methods to intelligent optimization algorithms, were evaluated through simulations to assess their performance under realistic operating conditions.

The comparative analysis highlighted that PMSG-based systems offer high efficiency and robust operation, albeit with increased cost and complexity, whereas DFIG-based systems provide enhanced grid support and economic scalability, though they are more sensitive to grid disturbances. Similarly, standalone PV and wind systems were compared, revealing that PV systems excel in modularity, cost, and ease of deployment, while wind systems offer superior energy yield and greater flexibility for grid integration.

These findings establish a foundation for the next chapter, which focuses on hybrid PV–wind systems. By combining the advantages of both technologies, hybrid systems can deliver reliable, cost-effective, and sustainable power for grid-connected applications.

Chapter 4 Design and Control of a Grid-Connected Hybrid PV–Wind System Based on a DFIG

4.1 Introduction

The increasing penetration of renewable energy sources into modern power systems has intensified the need for efficient, reliable, and grid-compliant energy conversion technologies. Among available solutions, the DFIG-based wind energy conversion system has attracted significant attention due to its high efficiency, reduced maintenance requirements, and ability to operate over a wide speed range. When combined with PV generation, hybrid PV–wind systems offer enhanced reliability and improved energy availability by compensating for the intermittent nature of individual renewable sources [23]. However, such hybrid configurations introduce technical challenges related to maximum power extraction, DC-link voltage regulation, power quality, and dynamic grid interaction under variable environmental conditions.

Recent advances in power electronic devices, particularly IGBTs, have enabled the practical implementation of sophisticated converter topologies and control strategies for hybrid renewable systems. PV arrays composed of series–parallel connected modules provide higher voltage and power levels but are inherently affected by irradiance and temperature variations, leading to fluctuations in output power. To address these issues, MPPT algorithms are essential for ensuring optimal energy extraction from PV systems. Similarly, wind energy systems based on DFIGs rely on effective rotor-side control strategies to maximize captured wind power while maintaining stable electrical performance. SRF-based control has emerged as a widely adopted technique for harmonic mitigation and precise regulation of active and reactive power in three-phase grid-connected systems.

This chapter presents a simplified yet effective hybrid PV–wind topology that integrates a DFIG-based wind energy conversion system with a PV array through a back-to-back converter and a single-stage grid-connected inverter. The RSC employs an indirect speed-based MPPT strategy to extract maximum wind power, while the GSC, controlled using the SRF approach, manages DC-link voltage regulation, harmonic reduction, and grid synchronization. The PV array is directly connected to the DC-link, eliminating the need for an intermediate DC–DC converter and reducing losses and control complexity. The proposed configuration aims to enhance system efficiency, maintain voltage and frequency stability, and deliver high-quality power to the grid under varying environmental conditions [33][34].

The chapter begins by describing the overall hybrid system and its fundamental operating principles. This is followed by a detailed presentation of the PV array subsystem, including modeling, operating characteristics, and environmental impacts on power generation. Next, the wind energy conversion subsystem is examined, with emphasis on wind turbine modeling, DFIG operation, and rotor-side control strategy. The back-to-back converter system and its role in interfacing the hybrid system with the grid are then discussed, followed by an analysis of the DFIG's steady-state behavior under different operating points [34]. The simulation scenarios and system parameters used for performance assessment are defined, and the mechanical dynamic response of the DFIG, including rotor speed and torque characteristics, is analyzed. Subsequently, the chapter evaluates the electrical performance of the hybrid system, covering PV subsystem performance, DC-link voltage behavior, power output and efficiency,

power quality, harmonic analysis, and voltage/frequency stability. Finally, the results are discussed, system limitations are highlighted, and key findings are summarized, demonstrating the effectiveness and practical applicability of the proposed hybrid PV–wind DFIG-based system. This structured approach ensures a clear progression from system design and modeling to detailed performance evaluation, providing a comprehensive understanding of the proposed system's robustness, efficiency, and grid compatibility.

4.2 System Description and Operating Principle

The proposed grid-connected hybrid photovoltaic-wind energy conversion system is designed to operate efficiently under variable wind speed and solar irradiance conditions. The overall system integrates a PV generator and a wind energy conversion system based on a DFIG, interconnected through a shared DC-link and a common grid interface. This hybrid configuration enables coordinated energy conversion, efficient power management, and enhanced power quality at the point of common coupling (PCC) [32][40][52].

The wind energy subsystem consists of a fixed-blade wind turbine mechanically coupled to a DFIG. The stator windings of the DFIG are directly connected to the utility grid, allowing stator currents to be injected at grid voltage and frequency without the need for additional power conversion stages. This direct stator–grid connection ensures inherent synchronization with the grid and contributes to high system efficiency. The rotor windings, on the other hand, are supplied through a pair of bidirectional power electronic converters arranged in a back-to-back configuration, operating under PWM. This converter structure, composed of an RSC, a DC-link capacitor, and a GSC, enables independent control of the rotor currents, electromagnetic torque, and reactive power, making it one of the most widely adopted topologies in modern wind energy conversion systems [30][34].

A key feature of the proposed architecture is the integration of the PV system directly into the DC-link of the back-to-back converter. By connecting the PV array to the DC bus, the grid-side converter is used as a multi-source inverter, responsible for injecting the combined power from both the PV and wind subsystems into the grid. This approach eliminates the need for an additional DC–DC converter for the PV system [27][28][33][52], thereby reducing conversion stages, power losses, and control complexity. Moreover, it allows the PV generator to share the same grid interface as the wind system, preserving the advantages of single-stage grid-connected PV topologies [45].

The photovoltaic subsystem is composed of series–parallel connected PV modules designed to provide the required voltage and power levels. An MPPT algorithm is implemented to ensure maximum power extraction under changing irradiance and temperature conditions. The wind turbine subsystem is controlled to maximize energy capture at low and medium wind speeds while limiting mechanical and electrical stresses during high wind speed operation, thus ensuring safe and reliable system performance.

The DC-link plays a central role in the proposed system, serving as the coupling point between the PV generator, the rotor-side converter, and the grid-side converter. A DC-link

capacitor is employed to smooth voltage fluctuations, store transient energy, and decouple the dynamic behavior of the wind and PV subsystems from the grid. Stable DC-link voltage regulation is essential for the proper operation of the converters and for maintaining power balance within the hybrid system.

The grid-side converter is responsible for regulating the DC-link voltage, controlling the active and reactive power exchanged with the grid, and ensuring high-quality current injection. An RL filter is placed between the GSC and the grid to attenuate switching harmonics and comply with grid power quality standards. Through appropriate control strategies, the GSC improves the grid-side power factor, minimizes current harmonic distortion, and maintains synchronization with the grid voltage [28].

As illustrated in Figure 4-1, the proposed hybrid topology combines the advantages of a DFIG-based wind system and a single-stage grid-connected PV system. In the following sections, detailed mathematical models of each component, namely the PV system and its MPPT control, the wind turbine, the DFIG, the DC-link, and the power converters, are presented to support the analysis and control design of the overall system [53][85].

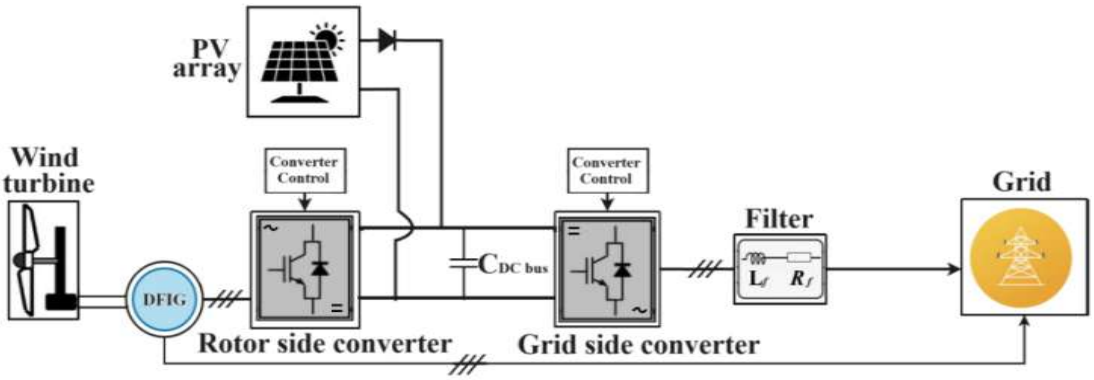


Figure 4-1 Block diagram of grid-connected PV/DFIG hybrid system.

4.3 Description and Operating Characteristics of the PV Array Subsystem

The PV array in the proposed hybrid system is composed of *43* series-connected modules per string and *100* parallel strings of *Kyocera KD 205GX-LP* modules, resulting in a total array capable of producing a maximum power of *882kW*. Under standard test conditions, each string operates at a voltage of *1144V* at maximum power V_{mp} and a current of *771A* at maximum power I_{mp} [85].

The performance of the PV array is highly influenced by environmental conditions. Increases in solar irradiance significantly raise both the output current and the maximum power of the modules, whereas variations in ambient temperature have a smaller effect, slightly reducing the open-circuit voltage and overall power. Because of this limited impact of temperature, simulations primarily focus on varying irradiance to study the array's behavior under realistic operating conditions, which allows a precise assessment of PV power fluctuations and their interaction with the wind subsystem. These irradiance-driven variations influence the overall hybrid system operation, as changes in PV output directly affect the DC-link voltage and consequently the power balance and control requirements of the wind generation unit.

To ensure the PV generator operates continuously at its MPP, the system employs an MPPT controller based on the INC algorithm. This controller monitors the PV array voltage and current and dynamically adjusts the operating point to maintain the MPP. The INC algorithm increases the reference voltage if the system is operating to the left of the MPP, decreases it if operating to the right, and keeps it unchanged when the MPP is reached. Furthermore, because the system is a single-stage configuration without a DC–DC boost converter, the INC-based MPPT is integrated directly with the SRF controller of the grid-connected inverter. This integration enables effective regulation of the DC-link voltage and grid-side current. By combining MPPT and SRF control, the PV subsystem continuously extracts optimal energy and delivers it efficiently to the grid, ensuring stable and maximum power contribution from the hybrid PV–wind system even under rapidly changing irradiance conditions.

4.4 Description and Operating Characteristics of the Wind Generator Subsystem

The wind subsystem of the proposed hybrid system is based on a variable-speed wind turbine coupled to a DFIG. The aerodynamic performance of the turbine is characterized by the power coefficient C_p, which reflects the efficiency of converting the kinetic energy of the wind into mechanical power. The analysis of the C_p characteristic as a function of the tip-speed ratio and blade pitch angle allows the identification of an optimal operating point. In this study, the turbine reaches a maximum power coefficient of $C_{p_max}=0.44$, which corresponds to an optimal tip-speed ratio of $\lambda_{opt}=7.2$ and a pitch angle $\beta=0$. Operation at this point ensures maximum aerodynamic efficiency and enables the turbine to deliver optimal mechanical power to the generator.

The turbine consists of three blades with a radius of *42m*, providing a large swept area suitable for high-power applications. A gearbox with a ratio of $N_G=100$ is used to adapt the low-speed rotation of the turbine shaft to the higher rotational speed required by the generator. The turbine is designed to operate at a nominal wind speed of *12.5m/s*, while the dynamic behavior of the turbine–generator assembly is influenced by a combined moment of inertia of $90kg{\cdot}m^2$ and a viscous friction coefficient of $0.1N{\cdot}m{\cdot}s$, which determines the transient response of the mechanical subsystem during wind speed variations.

The DFIG adopted in this study is a *2MW* machine operating at a nominal stator voltage of *690V* and a grid frequency of *50Hz*, corresponding to a synchronous speed of *1500rpm*. Its electrical and mechanical parameters, summarized in Table 4-1 (Annex III), are representative of industrial-scale wind turbines and ensure realistic steady-state and dynamic behavior in simulation.

The stator windings of the DFIG are directly connected to the grid, guaranteeing constant synchronization with grid voltage and frequency. In contrast, the rotor windings are connected through a bidirectional back-to-back power converter, enabling variable-speed operation over a wide wind speed range while requiring only partial-scale power electronic conversion. The operating characteristics of the wind subsystem are governed by an indirect speed control

strategy, which regulates the electromagnetic torque to maintain operation near the optimal aerodynamic point without direct measurement of wind speed.

Depending on the rotor speed relative to the synchronous speed, the DFIG operates in two distinct modes. In sub-synchronous operation, where the rotor speed is below synchronous speed, and the slip is positive, the rotor-side converter absorbs slip power from the grid to regulate rotor currents. In super-synchronous operation, when the rotor speed exceeds the synchronous speed, and the slip becomes negative, the excess slip power is transferred from the rotor to the grid. This slip-dependent bidirectional power flow enables smooth transitions between operating regions while maintaining grid synchronization through the stator connection.

The rotor-side converter employs vector control in the SRF to regulate rotor current components, allowing decoupled control of active and reactive power. This control strategy enables the wind subsystem to dynamically respond to grid requirements while maintaining stable regulation of the DC-link voltage shared with the photovoltaic subsystem. In the hybrid configuration, fluctuations in PV power caused by variations in solar irradiance directly affect the DC-link voltage and influence the control actions of the wind subsystem. Coordinated control between the DFIG indirect control and the grid-side SRF control, therefore, ensures balanced power sharing, enhanced system stability, and improved grid support under variable renewable energy conditions.

4.5 Description of the Back-to-Back Converter Part

Power electronic converters are essential for interfacing renewable energy sources with the electrical grid, particularly in hybrid systems where multiple generators share a common DC link. In the proposed hybrid PV–wind system, the DFIG is connected to the utility grid through a back-to-back two-level bidirectional converter based on PWM control. This converter enables variable-speed operation of the wind turbine and allows photovoltaic power to be injected into the same DC bus. The complete control structure of the back-to-back converter, including the RSC, GSC, DC-link capacitor, and synchronization blocks, is illustrated in Figure 4-2 [6][46][53][59][85][92].

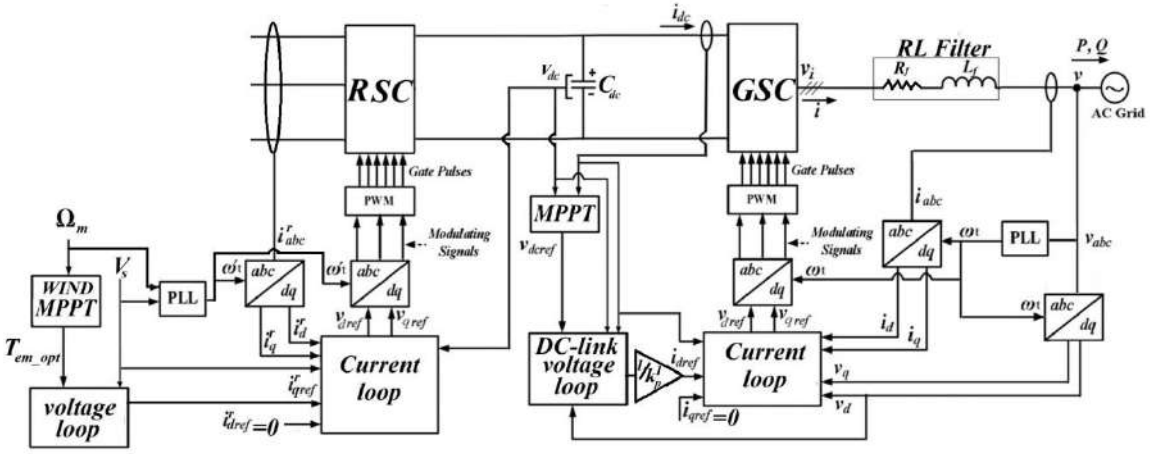


Figure 4-2 Block diagram of method controls for back-to-back converter.

The back-to-back converter consists of two voltage source inverters, namely the RSC and the GSC, interconnected through a common DC-link capacitor. Each inverter employs six IGBT switches with antiparallel diodes. Since only the rotor slip power is processed, the converter rating is limited to a fraction of the DFIG nominal power, which reduces converter losses and cost. The shared DC-link further enables direct coupling of the PV array without an additional DC-DC converter stage, as shown in Figure 4-1.

4.5.1 Rotor-Side Converter Control

As depicted in Figure 4-2, RSC regulates the wind energy conversion subsystem. Its main objectives are electromagnetic torque control, reactive power regulation, and coordination of active power through the DC link. The RSC employs an SRF control strategy, enabling decoupled regulation of the rotor current components along the d- and q-axes. The reference voltages applied to the PWM modulator are generated by PI current controllers and are expressed in (4-1) and (4-2) [6][13][25][53][59][92].

$$v_{d_ref} = \left[\left(K_p^r + \frac{1}{s}\, K_i^r\right).\left(i_{d_ref}^r - i_d^r\right) - \sigma.L_r.\omega_r.i_q^r\right]\left(\frac{2}{v_{dc}}\right) \tag{4-1}$$

$$v_{q_ref} = \left[\left(K_p^r + \frac{1}{s}\, K_i^r\right).\left(i_{q_ref}^r - i_q^r\right) + \sigma.L_r.\omega_r.i_d^r + \sqrt{\frac{2}{3}}.V_s.\frac{L_m}{L_s}.\frac{\omega_r}{\omega}\right]\left(\frac{2}{v_{dc}}\right) \tag{4-2}$$

To ensure decoupled torque and flux control, the d-axis rotor current reference is set to zero, while the q-axis rotor current reference is derived from the optimal electromagnetic torque obtained from the indirect speed-based MPPT algorithm [39][92].

$$i_{d_ref}^r = 0 \tag{4-3}$$

$$i_{q_ref}^r = \frac{T_{em_opt}}{-\frac{3}{2}.p.\frac{L_m}{L_s}.\frac{V_s.\sqrt{\frac{2}{3}}}{2.\pi.f}} \tag{4-4}$$

A PLL of RSC, presented in Figure 4-2, synchronizes the RSC rotating reference frame with the stator voltage. In this approach, the rotor mechanical angle is obtained by integrating the rotor mechanical speed Ω_m.

$$\theta_m = \frac{1}{s}\,\omega_m = \frac{1}{s}\;p.\Omega_m \tag{4-5}$$

The three-phase stator voltage V_s is measured and transformed into the dq synchronous reference frame as presented in (4-6).

$$\begin{bmatrix} V_d \\ V_q \end{bmatrix} = \frac{2}{3}\begin{bmatrix} 1 & -\frac{1}{2} & -\frac{1}{2} \\ 0 & \frac{\sqrt{3}}{2} & -\frac{\sqrt{3}}{2} \end{bmatrix}\begin{bmatrix} V_a \\ V_b \\ V_c \end{bmatrix} \tag{4-6}$$

The instantaneous stator voltage angle is computed from these dq components:

$$\theta_s = \tan^{-1}\left(\frac{V_q}{V_d}\right) \tag{4-7}$$

The rotor reference angle for the RSC is then calculated using both the stator voltage angle and the rotor mechanical angle:

$$\theta_r = \theta_s - \frac{\pi}{2} - p\,.\,\theta_m \tag{4-8}$$

This formulation explicitly links the measured stator voltage V_s with the rotor mechanical speed Ω_m to compute the rotor reference angle and frequency. The PLL ensures accurate synchronization of the RSC reference frame to the grid voltage, enabling precise rotor current control, optimal torque generation, and smooth bidirectional slip power exchange. By applying the control laws in (4-1) to (4-4), the RSC maintains stable operation in both sub-synchronous and super-synchronous modes under varying wind and grid conditions.

4.5.2 DC-Link and Energy Coupling

The DC-link capacitor provides energy buffering between the RSC and GSC, as illustrated in Figure 4-2, and plays a crucial role in maintaining a stable DC voltage during wind and solar power variations. Proper sizing of this capacitor limits voltage ripple and ensures dynamic stability of the hybrid system. The minimum required DC-link capacitance is determined using expression (4-9) [53][85].

$$C_{dc} \geq \frac{P_r}{2\,\omega_g\,V_{dc}\,\Delta V_{dc}} \tag{4-9}$$

Where P_r is the rated inverter power, ω_g is the grid pulsation, V_{dc} is the average DC voltage, and ΔV_{dc} is the allowable DC voltage ripple. Since the PV array is directly connected to the DC link, variations in solar irradiance directly affect V_{dc}, requiring coordinated control of both converters, as shown in Figure 4-2.

4.5.3 Grid-Side Converter Control

The GSC, illustrated in Figure 4-2, is responsible for regulating the DC-link voltage and ensuring high-quality power injection into the utility grid. To achieve these objectives, the GSC employs a cascaded control structure based on the SRF, consisting of an outer DC-link voltage control loop and an inner grid current control loop. This hierarchical arrangement enables fast dynamic response while ensuring effective decoupling between active and reactive power control [13][25][53].

In the proposed hybrid system, the INC MPPT algorithm associated with the photovoltaic subsystem is embedded within the GSC control scheme. The MPPT algorithm determines the optimal DC-link voltage reference V_{dc_ref} corresponding to the maximum available PV power. The GSC then adjusts the grid current components to balance the power exchanged through the DC link, thereby maintaining voltage stability under varying solar irradiance conditions.

The reference d-axis grid current, which governs active power flow and DC-link voltage regulation, is generated by the outer voltage control loop and is expressed by (4-10) [45][55].

$$i_{d\,ref} = \left(k_p^{dc} + \frac{1}{s}\, k_I^{dc}\right).\left(v_{dc\,ref} - v_{dc}\right).\frac{1}{k_p^I} + \left(\frac{2}{3}.\frac{v_{dc}\,.\,i_{dc}}{v_d}\right) \quad (4\text{-}10)$$

This formulation differs from the conventional SRF-based grid-connected PV control presented in Equation (2-51), where the proportional gain $k_p{}^I$ acts as a virtual resistor in the voltage loop [37]. In the present work, this modified expression improves DC-link voltage dynamics while preserving the overall structure of the current control loop, which remains consistent with the formulations given in Equations (2-49) and (2-50) [46].

The reactive power reference is set to zero, ensuring unity power factor operation and compliance with grid code requirements. Grid synchronization is achieved using a PLL, as shown in Figure 4-2, which aligns the control reference frame with the grid voltage. The voltage references generated by the SRF current controllers are subsequently transformed back into three-phase quantities and applied to the PWM modulator, which generates the appropriate gate signals for the GSC IGBT switches [45][46].

4.5.4 Role of the RL Filter

An RL filter is placed between the GSC and the utility grid to attenuate switching harmonics and limit current ripple. As illustrated in Figure 4-2, this filter ensures that the injected grid currents are sinusoidal and compliant with power quality standards. The dq-frame model of the RL filter is described by expressions (4-11) and (4-12) [18][40][53][55][85].

$$V_q = -R_f.i_d - L_f\frac{di_d}{dt} + L_f.\omega_g.i_q + V_{gd} \quad (4\text{-}11)$$

$$V_d = -R_f.i_q - L_f\frac{di_q}{dt} + L_f.\omega_g.i_d + V_{gq} \quad (4\text{-}12)$$

Where V_{gd}, V_{gq} are grid voltages, V_d, V_q are inverter output voltages, i_d, i_q are inverter output currents, ω_g is the grid pulsation, L_f represents the inductance of the filter, and R_f represents the resistor of the filter.

4.6 Steady-State Analysis of the DFIG

The DFIG offers a major advantage over conventional induction and synchronous machines due to its ability to operate efficiently over a wide speed range and in all four quadrants of the torque–speed plane. This flexibility enables both motor and generator operation under sub-synchronous and super-synchronous speed conditions. Unlike fixed-speed generators, the operating mode of the DFIG is not determined solely by mechanical speed but rather by the direction of power flow and the magnitude and sign of the slip. Through the back-to-back converter, the slip directly governs the exchange of power between the rotor circuit and the electrical grid, allowing independent control of active and reactive power [85][92].

In sub-synchronous generator operation ($S>0$), the rotor speed remains below the synchronous speed, corresponding to the positive slip region shown in the slip–speed characteristic of Figure 4-3(a). Under this condition, slip power is absorbed from the grid via

the rotor-side converter and injected into the rotor windings. Despite operating below synchronism, the aerodynamic power extracted from the wind turbine enables the DFIG to function in generator mode, delivering active power to the grid through the stator. As illustrated in Figure 4-3(c) and Figure 4-3(d), the stator supplies electrical power to the grid, while the rotor absorbs a portion of slip power to maintain electromagnetic coupling and ensure stable and flexible control.

In super-synchronous generator operation ($S<0$), the rotor speed exceeds the synchronous speed, as indicated by the negative slip region in Figure 4-3(a). In this operating mode, the increased mechanical input causes both the stator and rotor circuits to supply active power to the grid. The excess mechanical energy is transferred to the rotor and routed to the grid through the rotor-side and grid-side converters. This behavior is clearly reflected in Figure 4-3(c) and Figure 4-3(d), where both stator and rotor active powers become positive. Super-synchronous operation, therefore, enhances energy capture at higher wind speeds while avoiding full-scale power electronic conversion, since only the slip power is processed by the converters.

The electromagnetic torque behavior further characterizes the steady-state operation of the DFIG. Throughout generator operation, the electromagnetic torque remains negative, confirming continuous conversion of mechanical energy into electrical energy. The transition between sub-synchronous and super-synchronous modes occurs at the synchronous speed of *1500rpm*, which corresponds to a wind speed of approximately *9.2m/s* for the selected turbine. Below this speed, the system operates in sub-synchronous mode, whereas above it, super-synchronous operation is achieved.

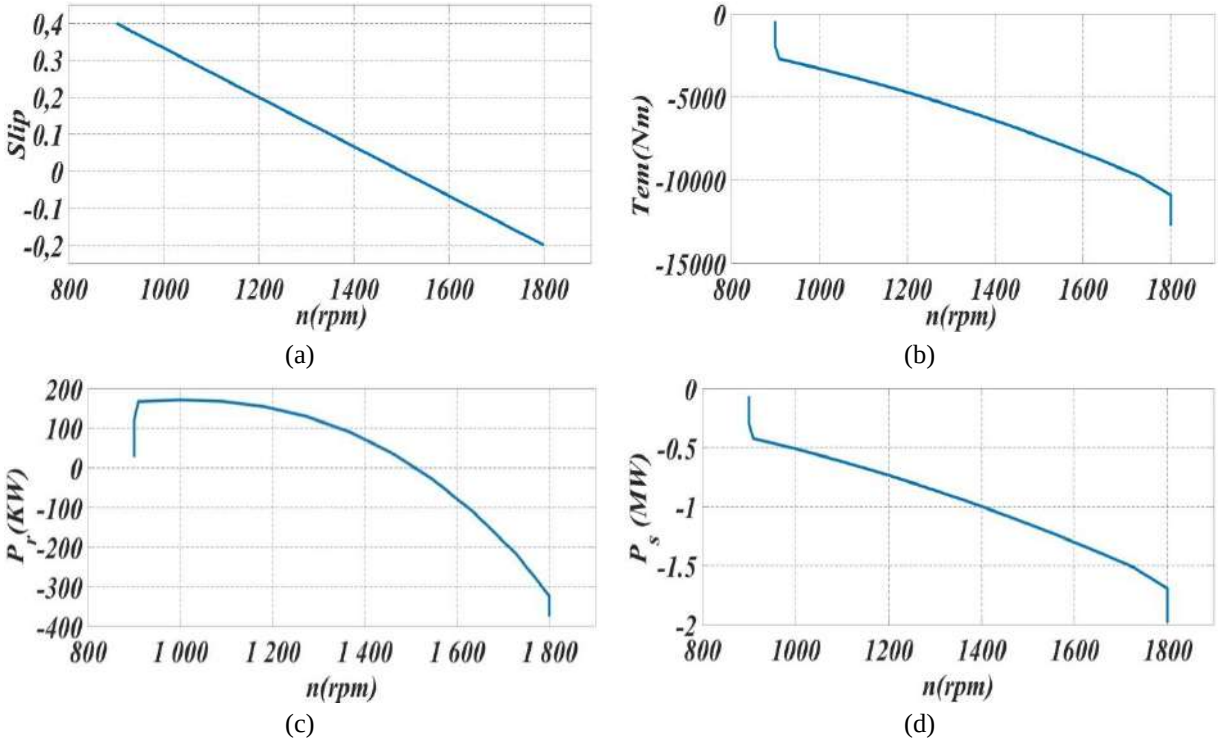


Figure 4-3 Steady-state magnitudes as a function of rotation speed: (a) Slip, (b) electromagnetic torque, (c) stator active power, and (d) rotor active power.

Overall, the steady-state analysis demonstrates that the DFIG enables efficient energy extraction over a wide range of wind speeds through controlled operation in both sub- and super-synchronous modes. This capability, combined with reduced converter ratings, bidirectional power flow, and flexible power control, makes the DFIG particularly well suited for grid-connected hybrid PV–wind energy systems.

4.7 Simulation Scenarios and Parameter Definition

For accurate and reproducible simulation outcomes, all system parameters are rigorously defined, encompassing the electrical grid, photovoltaic array, DFIG-based wind subsystem, DC-link, power converters, controllers, and the RL filter. The characteristics of the PV array, wind turbine, and DFIG are provided in Table 2-2 (Annex I), and Table 4-1 (Annex III), while the remaining parameters required for system modeling, control design, and dynamic performance evaluation are summarized in Table 4-2 (Annex III). These parameters include rated voltages and currents, switching frequencies, PI controller gains, and DC-link capacitance, ensuring realistic operation and stable system behavior under all investigated operating conditions.

To investigate the dynamic performance, stability, and energy management capabilities of the proposed grid-connected hybrid PV–wind system, four representative operating scenarios are defined. These scenarios reflect realistic variations in solar irradiance and wind speed and examine the system's response under different DFIG operating modes, including sub-synchronous $S>0$ and super-synchronous $S<0$ conditions. The analysis emphasizes power sharing between the PV array and DFIG, DC-link voltage regulation, grid power quality, and the robustness of the applied SRF-based control strategies.

Scenario 1: High Solar Irradiance and Low Wind Speed ($S>0$)
Under strong solar irradiation of $1kW/m^2$ and a low wind speed of $5m/s$, the photovoltaic array operates at its maximum power point through the INC-based MPPT algorithm. In this condition, the contribution of the wind energy subsystem is limited, and the DFIG operates in sub-synchronous generator mode with positive slip. The overall power delivered to the grid is therefore dominated by the PV system, while the rotor absorbs slip power through the back-to-back converter to sustain controlled operation.

Scenario 2: Low Solar Irradiance and High Wind Speed ($S<0$)
When solar irradiation decreases to $0.4kW/m^2$ and wind speed increases to $12m/s$, the wind energy subsystem becomes the dominant source of power. The DFIG operates in super-synchronous generator mode, allowing both the stator and rotor circuits to supply active power to the grid. The slip power extracted from the rotor is transferred to the DC link via the rotor-side converter and subsequently injected into the grid through the grid-side converter, ensuring stable DC-link voltage regulation and efficient energy transfer.

Scenario 3: High Solar and Wind Availability (Balanced Operation near Synchronous Speed)

With high solar irradiance of $1kW/m^2$ and a moderate wind speed of approximately $9.2m/s$, the DFIG operates close to synchronous speed. This operating condition enables coordinated power sharing between the photovoltaic array and the wind turbine. As a result, mechanical stress on the turbine is reduced, converter loading is balanced, and smooth and stable power injection into the grid is achieved.

Scenario 4: Rapid Variations in Solar Irradiance and Wind Speed (Dynamic Generator Transitions)

This scenario evaluates the robustness of the proposed system under rapidly changing environmental conditions. The DFIG dynamically transitions between sub-synchronous and super-synchronous operating modes in response to wind speed fluctuations, while the photovoltaic array experiences sudden changes in solar irradiance. These operating conditions test the effectiveness of the MPPT strategies, DC-link voltage regulation, and synchronous reference frame-based control in maintaining grid synchronization, power quality, and overall system stability.

4.8 Mechanical Dynamic Response of the DFIG

The mechanical behavior of the DFIG is analyzed through the responses shown in Figure 4-4, which depicts the electromagnetic torque, and Figure 4-5, which presents the corresponding rotor mechanical speed for the four investigated operating cases. The evaluation emphasizes transient dynamics, steady-state behavior, and overall mechanical stability in order to assess the impact of each control strategy on system performance [92].

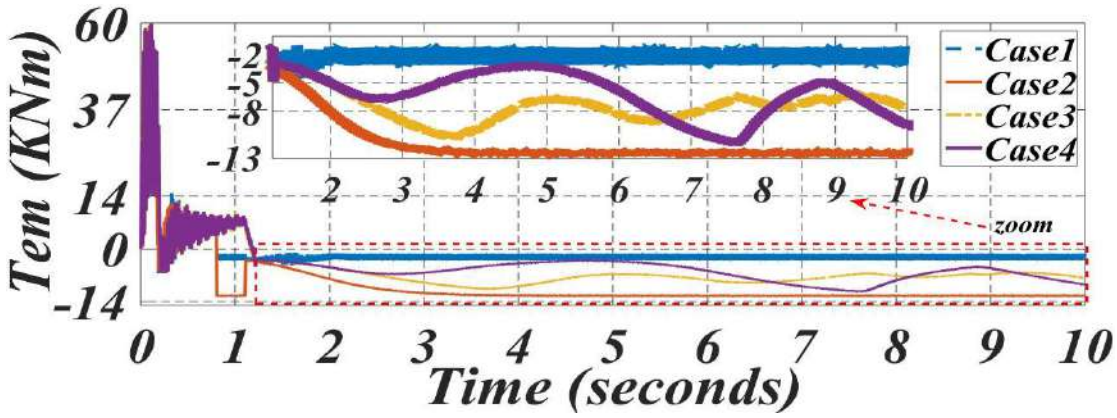


Figure 4-4 Electromagnetic torque.

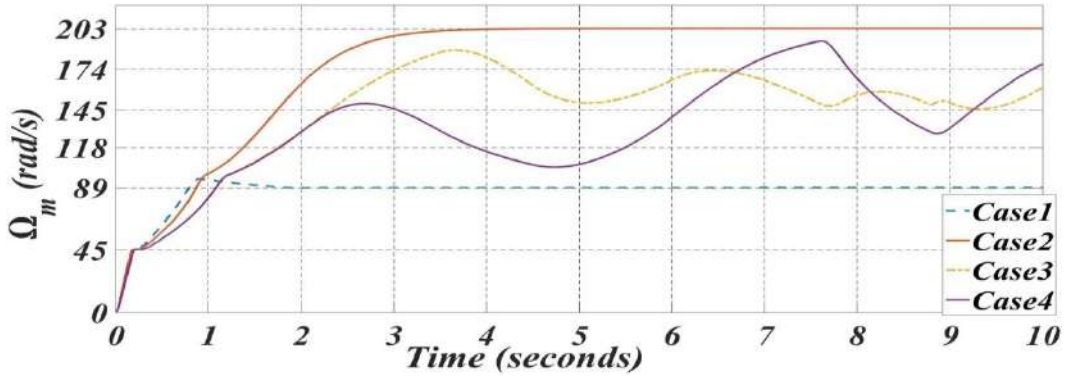


Figure 4-5 Mechanical rotational speed at the rotor.

In Case 1, the electromagnetic torque remains almost constant at approximately *10kN·m*, exhibiting a highly stable and well-damped profile throughout the simulation. The rotor speed is maintained near *90rad/s* with no noticeable transient dynamics. This behavior corresponds to a conservative operating mode, resembling fixed-speed operation, where mechanical stability is achieved at the expense of dynamic flexibility and responsiveness.

Case 2 exhibits the most favorable mechanical performance. During startup, the electromagnetic torque briefly reaches about *40kN·m* before rapidly settling to a steady value. In parallel, the rotor speed converges smoothly and rapidly to around *203rad/s* without overshoot or oscillations. This response reflects an effectively tuned control strategy, ensuring fast dynamic response, strong damping, and high mechanical stability.

In Case 3, the electromagnetic torque attains a peak of roughly *30kN·m*, followed by moderate oscillations before reaching steady state. The rotor speed shows an initial overshoot and then gradually stabilizes around *203rad/s* with damped oscillations. This case represents a compromise between response speed and stability; however, the observed oscillatory behavior indicates that further controller tuning would be beneficial to enhance damping.

Case 4 demonstrates the least satisfactory mechanical behavior. The electromagnetic torque exhibits a large overshoot exceeding *60kN·m* at startup and continues to fluctuate with significant amplitude during operation. Similarly, the rotor speed shows sustained oscillations without clear convergence. Such responses indicate insufficient damping and inadequate control design, which may lead to excessive mechanical stress and reduced system reliability.

Overall, the mechanical analysis confirms that the adopted control strategy has a decisive influence on the dynamic and steady-state behavior of the DFIG. Case 2 provides the best performance, combining rapid speed convergence, minimal torque overshoot, and stable operation, and therefore represents the most suitable control configuration. Case 3 offers acceptable performance but requires improved damping. Case 1 ensures mechanical stability but limits adaptability to variable wind conditions, while Case 4 highlights the consequences of poor control tuning, underscoring the necessity of proper controller design to guarantee stable and safe operation.

4.9 Electrical Performance Analysis of the Hybrid PV–Wind System

This section presents the electrical performance of the proposed grid-connected hybrid PV–wind system, including the dynamic behavior of the PV subsystem, DC-link voltage regulation, power output, efficiency, and power quality under four operational scenarios. The analysis highlights the interaction between the PV array, the DFIG-based wind subsystem, and the grid-side converter (GSC).

4.9.1 PV Subsystem Performance

The performance of the photovoltaic subsystem is analyzed under four distinct operating scenarios to evaluate its dynamic response, steady-state behavior, and interaction with the wind energy subsystem in the grid-connected hybrid configuration. The assessment is based

on the temporal evolution of the PV output current and power over a *10s* simulation interval, as illustrated in Figure 4-6 and Figure 4-7, respectively. Particular attention is given to the effectiveness of the MPPT strategy, the coordination between energy sources, and the resulting system stability.

As shown in Figure 4-6, the PV array exhibits a rapid transient response in all scenarios, with stabilization occurring within the first second of operation. This fast convergence reflects the high tracking capability of the implemented MPPT algorithm and its ability to promptly adapt to changes in operating conditions. Such behavior is essential in grid-connected hybrid systems, as it minimizes power disturbances and contributes to maintaining voltage and frequency stability at the point of common coupling.

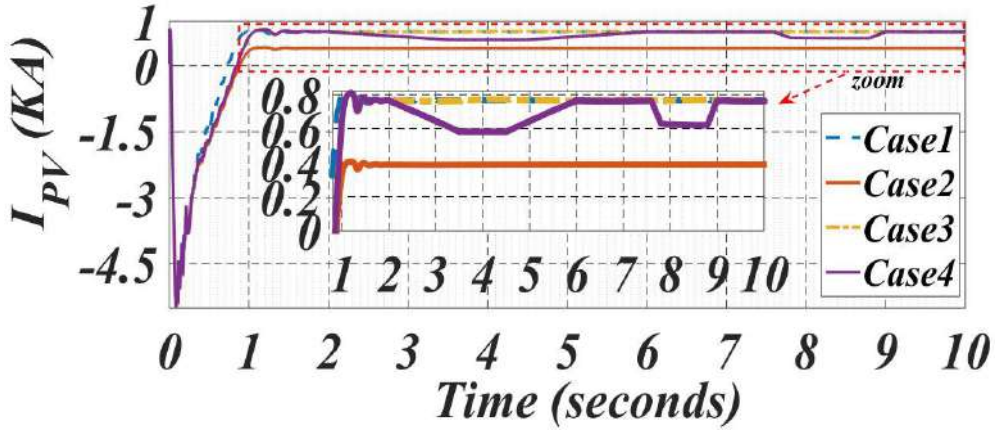


Figure 4-6 PV current.

Figure 4-7 presents the PV power injected into the DC bus for the four scenarios. Cases 1 and 3 demonstrate the best steady-state performance, with peak currents reaching approximately *770A* and power output close to *0.88MW*. These results indicate that under favorable irradiance conditions, the PV subsystem operates consistently near its maximum power point. The stable interaction between the PV array, the DC-link, and the wind subsystem further enhances power extraction efficiency, confirming the robustness and accuracy of the MPPT control strategy.

In Case 4, the PV subsystem exhibits a more dynamic behavior. Although the initial power level is comparable to that of Cases 1 and 3, noticeable reductions in current and power occur during the intervals from *2s* to *6s* and from *7.5s* to *9s*. These fluctuations are primarily caused by variations in solar irradiance. Nevertheless, the PV system rapidly recovers after each disturbance, demonstrating the adaptability of the MPPT controller and its ability to maintain stable operation under time-varying environmental conditions.

By contrast, Case 2 records the lowest PV output, with an average current of approximately *400A* and a power level of around *0.45MW*. This reduced contribution is associated with low solar irradiance and a system operating condition that favors wind energy production. Despite the limited PV contribution, the subsystem remains stable, highlighting the effectiveness of the hybrid architecture in ensuring continuous operation even when one renewable source is constrained.

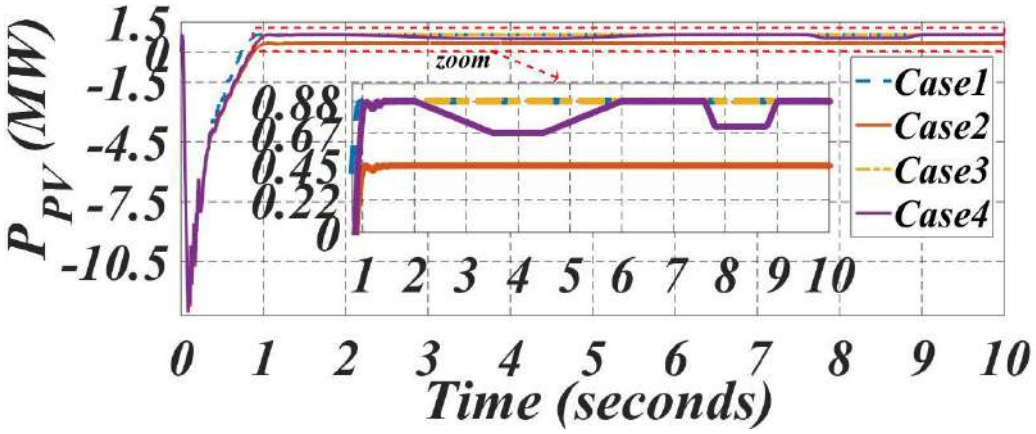


Figure 4-7 PV power injected into the DC bus.

Overall, the results confirm that effective MPPT implementation and proper coordination between the PV array and the DFIG-based wind subsystem are critical for achieving stable and optimal performance in hybrid PV–wind systems. The PV subsystem plays a key role in supporting DC-link voltage stability and enhancing total energy harvesting, particularly under high irradiance conditions, thereby contributing to the overall reliability and efficiency of the grid-connected hybrid system.

4.9.2 DC-link Voltage Behavior

The DC-link voltage response of the grid-connected hybrid PV–DFIG system is illustrated in Figure 4-8 for the four investigated operating scenarios. This analysis focuses on both the transient and steady-state behaviors in order to evaluate the effectiveness of the back-to-back converter control and the overall energy balance between the PV and wind subsystems.

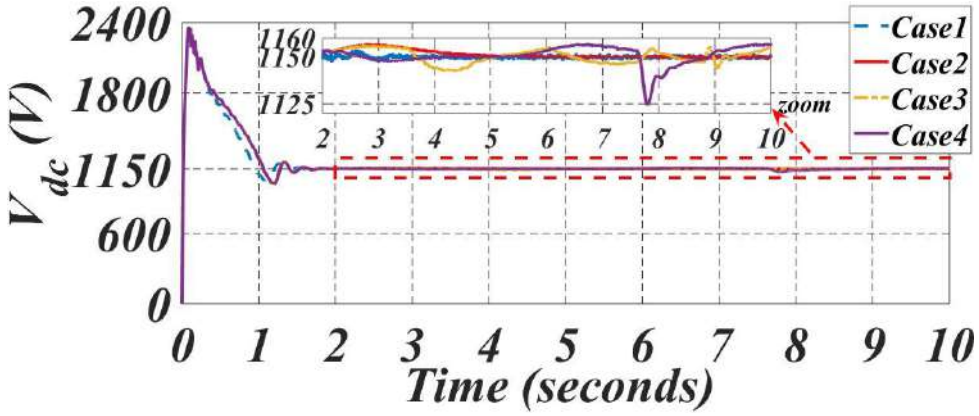


Figure 4-8 DC bus voltage.

During the initial transient interval (*0–2 s*), the DC-link voltage exhibits a rapid increase from its initial value and converges toward the nominal reference of *1150V*. This behavior reflects the fast dynamic response of the power electronic converters and the DC-link capacitor in regulating the exchanged power. Case 1 presents the largest overshoot, which is mainly attributed to the sudden and strong contribution of the PV subsystem under high irradiance conditions. In contrast, Case 2 shows the smoothest and fastest settling response, as the wind turbine provides a relatively steady power input, facilitating effective voltage regulation.

In the steady-state period, beyond *2s*, distinct behaviors can be observed among the scenarios. Case 2 maintains an almost constant DC-link voltage with minimal ripple, demonstrating robust regulation under dominant wind generation. Case 1 also achieves stable operation, although small oscillations persist due to variations in PV power. Case 3 exhibits more noticeable voltage fluctuations, which can be associated with the dynamic interaction between the PV array and the DFIG operating close to synchronous speed. Case 4 represents the most challenging condition, as a significant voltage dip occurs around *7.8s*, followed by a slower recovery. This response highlights the stress imposed on the converter control during rapid and simultaneous variations in solar irradiance and wind speed.

Overall, the results confirm that the DC-link voltage remains within acceptable limits across all scenarios. The coordinated operation of the DC bus capacitor, the RSC, and the GSC plays a critical role in maintaining voltage stability, attenuating power fluctuations, and ensuring reliable grid interaction. These findings also indicate that more adaptive or predictive control strategies could further enhance performance under highly dynamic hybrid generation conditions.

4.9.3 Power Output and Efficiency

The power flow characteristics and overall efficiency of the proposed hybrid PV–DFIG system are evaluated using the DFIG slip profile, the stator power injected into the grid, and the GSC output power, as illustrated in Figure 4-9, Figure 4-10, and Figure 4-11, respectively. These results provide insight into the system's operational modes, energy management capability, and conversion efficiency under different combinations of wind speed and solar irradiance.

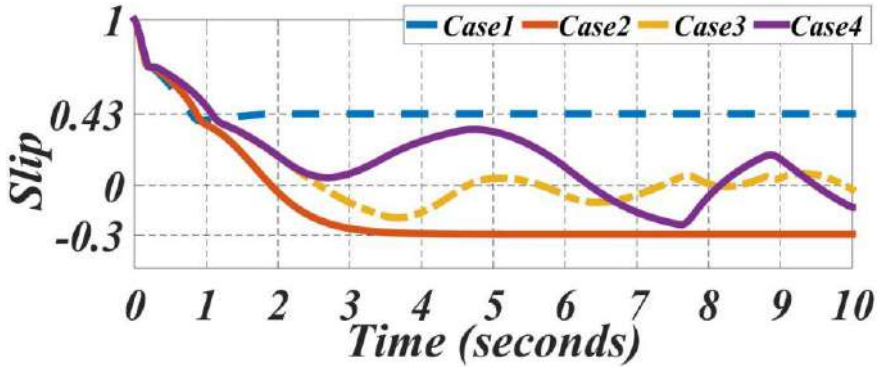


Figure 4-9 DFIG slip.

In Scenario 1, the DFIG operates in the hypo-synchronous generator mode, characterized by a positive slip value. In this condition, the rotor absorbs slip power from the grid through the rotor-side converter, while only the stator delivers active power to the grid. The PV array primarily supports DC-link voltage regulation, ensuring stable operation of the back-to-back converter, whereas the GSC manages controlled power injection. As shown in Figure 4-10 and Figure 4-11, an initial transient is observed, followed by rapid stabilization, indicating effective damping and converter control. Due to the unidirectional power flow from the stator, the overall efficiency is moderate, reaching approximately *80%*, yet the system remains stable and compliant with grid requirements.

Scenario 2 corresponds to hyper-synchronous generator operation, where the slip becomes negative, and the turbine speed exceeds synchronous speed. In this case, both the stator and rotor contribute active power to the grid, resulting in the highest power output among all scenarios. Figure 4-10 and Figure 4-11 show increased power levels with smooth steady-state behavior, confirming the effectiveness of the RSC in regulating rotor power and reactive power exchange. Despite a reduced contribution from the PV subsystem, the DFIG dominates power delivery, allowing the system to achieve a peak efficiency of approximately *96%*. This scenario demonstrates the capability of the hybrid system to operate efficiently even under low solar irradiance conditions.

In Scenario 3, coordinated operation between the PV array and the wind turbine is achieved, with both sources contributing to the DC bus. The GSC operates as a multi-source interface, enabling balanced and continuous power transfer to the grid. The stator and GSC power profiles exhibit minimal overshoot and stable steady-state behavior, highlighting the synergistic effect of hybrid energy integration. The DC-link capacitor further smooths short-term fluctuations, leading to improved power quality and an overall efficiency of around *92%*, while reducing dependence on a single energy source.

Scenario 4 involves dynamic transitions between hypo-synchronous and hyper-synchronous modes in response to rapid variations in wind speed and solar irradiance. This operating condition introduces stronger transients, which are reflected by temporary oscillations in the stator and GSC power curves. Nevertheless, the system quickly restores stable operation due to the combined action of adaptive MPPT for the PV subsystem, MPPT control for the wind turbine, and real-time inverter regulation. Although the presence of frequent transitions slightly reduces performance, the system maintains an efficiency of approximately *85%*, demonstrating a high level of robustness and flexibility.

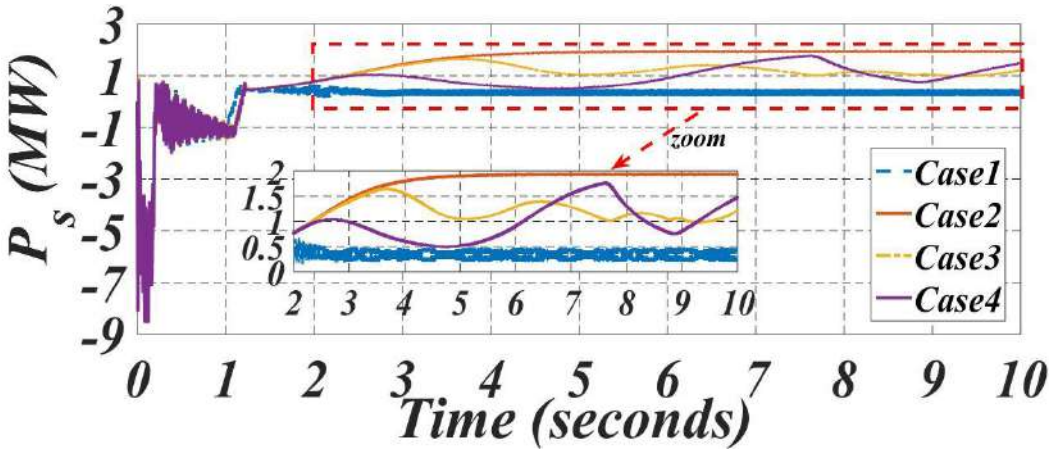


Figure 4-10 Stator power injected into the grid.

Overall, the comparative analysis confirms that the proposed hybrid PV–DFIG system effectively manages power flow and maintains high efficiency across a wide range of operating conditions. The coordinated control of the RSC, GSC, and MPPT algorithms enables stable grid interaction, efficient energy conversion, and reliable operation under both steady and rapidly changing environmental conditions.

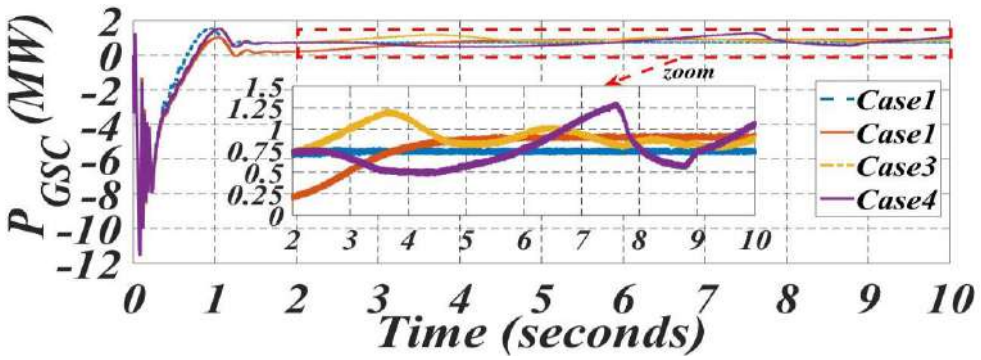


Figure 4-11 GSC power injected into the grid.

4.9.4 Power Quality and Harmonic Analysis

Power quality assessment is a critical aspect of grid-connected hybrid renewable energy systems, as it directly affects grid stability, equipment lifetime, and compliance with international standards. In this study, the quality of power injected by the GSC is evaluated under the four operating scenarios through the analysis of reactive power exchange, output current waveforms, and THD, as illustrated in Figure 4-12 to Figure 4-14. The evaluation follows the limits and recommendations of IEEE Std 519-2022 [21].

Figure 4-12 illustrates the reactive power injected into the grid by the GSC. In all scenarios, a short transient is observed during the first second, followed by rapid convergence toward zero reactive power. This behavior confirms the effectiveness of the GSC control strategy in decoupling active and reactive power and in maintaining near-unity power factor operation. Scenarios with higher and more stable renewable energy contributions exhibit faster damping of transients, reflecting improved dynamic performance and enhanced voltage support at the point of common coupling.

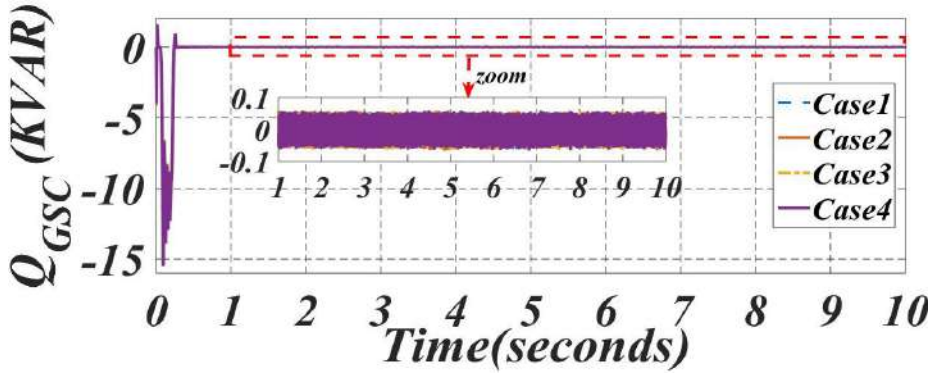


Figure 4-12 GSC reactive power injected into the grid.

The quality of the injected current waveforms is examined in Figure 4-13, which presents the GSC output line currents along with zoomed views over selected time intervals. In all cases, the currents exhibit a stable periodicity of *0.02s*, corresponding to the *50Hz* grid frequency, confirming accurate synchronization and phase locking. The waveforms remain predominantly sinusoidal, indicating effective modulation and filtering. Minor distortions are more noticeable in Scenario 4, where rapid variations in wind speed and solar irradiance lead to frequent operating mode transitions. In contrast, Scenarios 1 and 2 show smoother current profiles due to more stable operating conditions dominated by a single energy source.

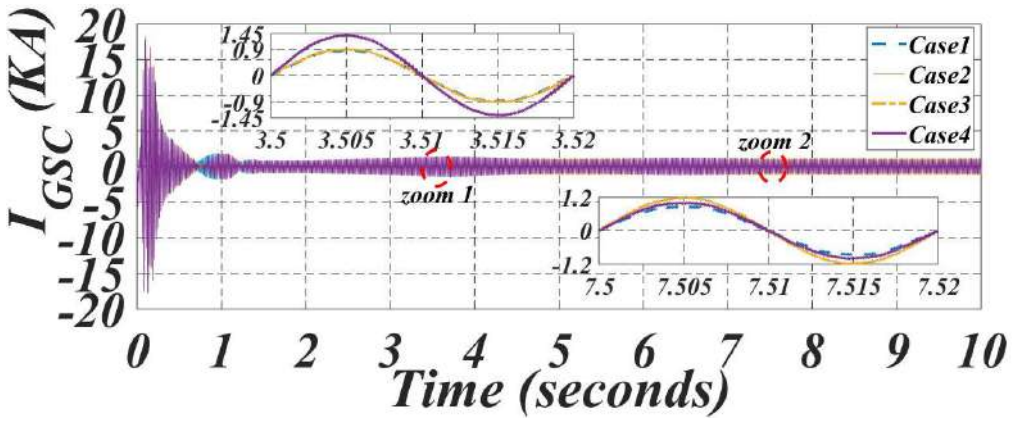
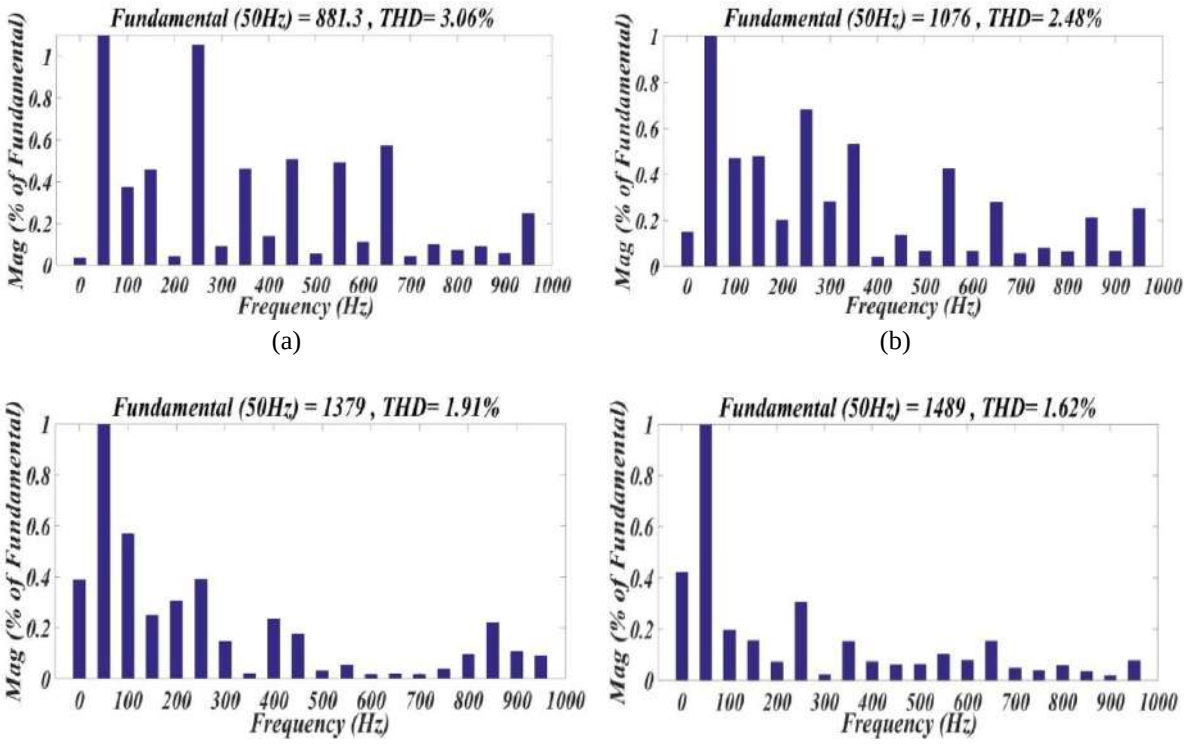


Figure 4-13 GSC output line current.

Further quantitative validation of power quality is provided by the THD analysis in Figure 4-14. In Scenarios 1 to 3, the THD of the GSC output currents remains below *3%*, indicating excellent harmonic performance under steady and coordinated operating conditions. In Scenario 4, which represents the most demanding dynamic case, the THD increases but remains within acceptable limits, not exceeding *4.24%*. These results demonstrate that the proposed control and filtering scheme maintains harmonic distortion well within IEEE Std 519-2022 requirements, even under fast-changing environmental conditions [21].



(a) (b)

(c) (d)

Figure 4-14 THD of GSC output currents.

To identify the dominant harmonic components, specific harmonic orders were examined. The 5^{th} (*250Hz*) and 7^{th} (*350 Hz*) harmonics were found to be the most significant, yet their magnitudes remained below the prescribed standard limits in all scenarios. The combined use

of SRF-based GSC control, optimized PWM switching, and passive LC filters tuned to the 5^{th} and 7^{th} harmonic frequencies ensures effective attenuation of these components without degrading the fundamental current [40]. Additionally, the DC-link capacitor contributes to smoothing power fluctuations and reducing harmonic propagation [29][31].

Finally, a correlation between electrical power quality and DFIG mechanical behavior is observed. Variations in rotor speed and electromagnetic torque influence current ripple and harmonic content, particularly during dynamic operating conditions. Nevertheless, the coordinated operation of the RSC, GSC, and filtering stages enables the system to preserve high-quality power injection, confirming the robustness, adaptability, and grid-code compliance of the proposed hybrid PV/wind energy conversion system.

4.9.5 Voltage and Frequency Stability

Voltage and frequency stability are key indicators of the suitability of grid-connected hybrid renewable energy systems for reliable and compliant operation. The behavior of the proposed PV–wind hybrid system is evaluated through the three-phase grid voltage shown in Figure 4-15, which illustrates the phase-to-phase voltages at the point of common coupling together with zoomed views for detailed assessment.

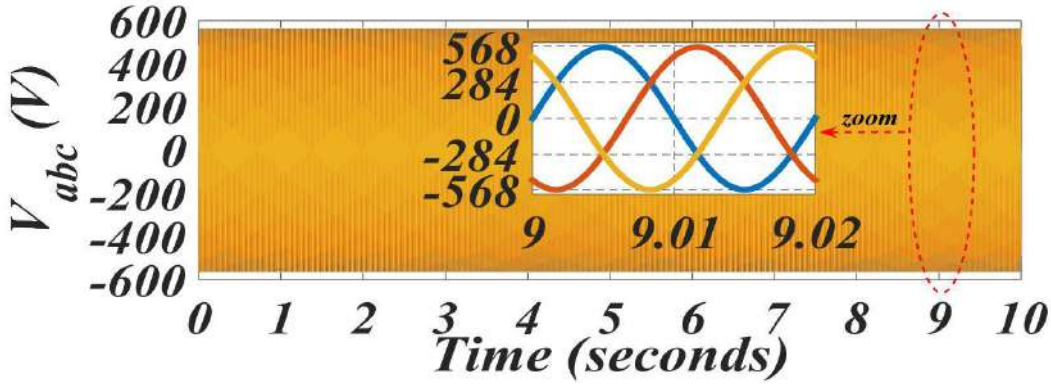


Figure 4-15 Three-phase grid voltage (phase-to-phase).

As observed in Figure 4-15, the grid voltage maintains a balanced and sinusoidal three-phase profile over the entire simulation period. The zoomed-in view clearly shows one complete voltage cycle within a *0.02s* interval, confirming a stable fundamental frequency of *50Hz*. The three-phase voltages are equal in magnitude and displaced by *120* electrical degrees, indicating proper synchronization with the grid and effective suppression of unbalance and waveform distortion.

This stable voltage behavior is preserved despite variations in solar irradiance and wind speed. The coordinated control strategy, which combines dedicated MPPT algorithms for the PV array and wind turbine with an SRF-controlled grid-side converter, effectively decouples source-side power fluctuations from the grid interface. As a result, disturbances originating from renewable intermittency do not propagate to the PCC, ensuring smooth voltage regulation and frequency stability [32][40].

Moreover, the employed converter topology provides fast dynamic compensation during transient conditions, allowing rapid correction of voltage deviations and maintaining

operation within acceptable limits. The observed voltage quality and frequency stability fully comply with IEEE Std 519-2022 requirements, confirming the effectiveness of the proposed control and power conversion architecture.

Overall, the results demonstrate that the hybrid PV–wind system is capable of delivering clean, stable, and well-regulated voltage at constant frequency under all operating scenarios. This validates its suitability for reliable grid integration and deployment in modern smart grid environments.

4.10 Discussion of Results

The simulation results comprehensively demonstrate the effectiveness of the proposed grid-connected hybrid PV–wind energy system based on a DFIG and coordinated power electronic control. The discussion integrates the mechanical, electrical, control, and power quality outcomes obtained under four representative operating scenarios characterized by different combinations of solar irradiance and wind speed.

From an energy conversion and control perspective, the results confirm that the hybrid architecture enables efficient and flexible power sharing between the PV array and the wind turbine. The PV subsystem exhibits fast dynamic response and accurate maximum power point tracking, as evidenced by the rapid stabilization of PV current and power in all scenarios. High irradiance conditions lead to maximum PV contribution, while reduced irradiance appropriately limits PV output without compromising system stability. This behavior highlights the robustness of the INC-based MPPT and its ability to adapt to abrupt irradiance variations.

The DFIG-based wind subsystem demonstrates strong operational flexibility through controlled transitions between sub-synchronous and super-synchronous modes. The slip profiles clearly indicate that power flow direction is governed by slip rather than mechanical speed alone, allowing the system to maximize wind energy capture over a wide speed range. In super-synchronous operation, the contribution of both stator and rotor circuits significantly enhances total power output while maintaining reduced converter ratings, confirming one of the principal advantages of DFIG technology in hybrid systems.

The DC-link voltage analysis shows that the coordinated action of the DC capacitor, rotor-side converter, and grid-side converter ensures stable voltage regulation under all scenarios. Although transient overshoots and dips appear during abrupt changes in generation, particularly under highly dynamic conditions, the voltage consistently converges to its nominal value. This demonstrates effective energy buffering and confirms that the control strategy successfully decouples source-side variability from the grid interface. Scenarios dominated by wind generation exhibit the smoothest DC-link behavior, underlining the stabilizing role of continuous wind power in hybrid configurations.

Mechanical performance analysis of the DFIG further emphasizes the importance of controller tuning. Stable torque and smooth rotor speed convergence are achieved in well-regulated cases, while poorly damped control leads to oscillatory behavior and excessive

torque peaks. These findings highlight that appropriate control design is not only essential for electrical performance but also critical for reducing mechanical stress and improving long-term system reliability.

Regarding power flow and efficiency, the hybrid system achieves its highest efficiency during super-synchronous operation, where both stator and rotor actively inject power into the grid. Coordinated PV–wind operation also yields high efficiency with balanced power delivery and reduced grid dependence. Even during dynamic transitions, the system maintains acceptable efficiency levels, demonstrating resilience and adaptability to real-world operating conditions.

Power quality analysis confirms that the proposed control strategy ensures compliance with grid standards. Reactive power is effectively regulated near zero, current waveforms remain sinusoidal and synchronized with the grid, and total harmonic distortion stays well within IEEE Std 519-2022 limits across all scenarios [21]. The reduction of THD with increasing fundamental current, combined with the mitigation of dominant low-order harmonics using PWM techniques and passive filtering, validates the effectiveness of the SRF-controlled GSC and the overall converter design. The observed correlation between rotor dynamics and harmonic behavior further underscores the strong coupling between mechanical and electrical subsystems in DFIG-based systems.

Finally, voltage and frequency stability results demonstrate that the hybrid system maintains balanced, sinusoidal grid voltages at a constant *50Hz* despite fluctuating renewable inputs. This confirms that the combined MPPT strategies and converter controls successfully isolate renewable variability from the grid, ensuring reliable and standards-compliant operation.

Overall, the discussion of results confirms that the proposed hybrid PV–wind DFIG-based system achieves high efficiency, robust dynamic performance, excellent power quality, and stable grid integration. The coordinated control architecture effectively manages the inherent intermittency of renewable sources, making the system well-suited for practical deployment in modern smart grid applications.

4.11 Limitations of the Proposed System

Although the proposed hybrid PV–wind energy system based on a DFIG and a simplified back-to-back converter demonstrates strong performance in terms of efficiency, stability, and power quality, several limitations should be acknowledged to provide a balanced and realistic assessment of the research outcomes.

First, the entire study is validated exclusively through simulation using MATLAB/Simulink. While detailed and widely accepted models are employed, simulation-based validation cannot fully represent real-world operating conditions. Practical issues such as sensor inaccuracies, signal delays, switching dead times, electromagnetic interference, thermal effects on power electronic components, and parameter drifts were not considered. Consequently, the system's robustness under actual hardware constraints remains to be experimentally verified through laboratory-scale prototypes or hardware-in-the-loop (HIL) testing.

Second, the proposed control strategy relies mainly on conventional MPPT techniques and PI-based controllers combined with SRF control. Although these methods offer simplicity, reliability, and ease of implementation, their performance may deteriorate under highly nonlinear or extreme operating conditions, such as severe grid faults, abrupt wind gusts, or partial shading of PV arrays with multiple local maximum power points. Advanced adaptive or intelligent control methods could potentially improve tracking accuracy and dynamic response in such cases, but were not addressed in this work.

Third, the wind energy conversion system is based on a DFIG topology, which inherently has limitations related to its partial-scale power converter. While this reduces converter rating and cost, it restricts the operating speed range and fault ride-through capability compared to full-scale converter-based generators. The study does not explicitly analyze compliance with modern grid codes related to low-voltage ride-through (LVRT), fault current injection, or grid support during deep voltage sags.

Fourth, the hybrid system does not include energy storage elements such as batteries or supercapacitors. As a result, the system's capability to smooth long-term power fluctuations, provide frequency support, or perform peak-shaving functions is limited. Under prolonged periods of low wind speed and low solar irradiance, the system remains dependent on the grid to maintain power balance, which may restrict its autonomy and flexibility in isolated or weak grid applications.

Fifth, the power quality analysis focuses primarily on harmonic distortion, reactive power control, and steady-state waveform quality under balanced grid conditions. Effects related to grid unbalance, voltage asymmetry, weak grid conditions, frequency deviations, and resonance phenomena due to grid impedance variations were not investigated. These factors can significantly influence converter performance and stability in real distribution networks.

Finally, the scalability and economic assessment of the proposed topology were not quantitatively analyzed. While the reduction in control loops and converter stages suggests lower cost and complexity, a detailed techno-economic analysis considering component sizing, losses, lifetime, and maintenance costs would be required to fully evaluate the system's commercial viability for large-scale deployment.

4.12 Conclusion

This chapter presented a comprehensive performance evaluation of the proposed grid-connected hybrid PV–wind energy system based on a DFIG and a simplified back-to-back converter topology. The analysis focused on both dynamic and steady-state behaviors under multiple operating scenarios characterized by varying solar irradiance and wind speed, intending to assess system stability, energy management efficiency, and power quality.

Detailed simulation results demonstrated that the PV subsystem, controlled by an MPPT algorithm, is capable of rapidly tracking the maximum power point and delivering stable power to the DC bus despite irradiance variations. Similarly, the wind energy conversion system based on the DFIG exhibited reliable operation in hypo-synchronous, hyper-

synchronous, and near-synchronous modes, ensuring effective power extraction and smooth transitions between operating regions. The coordinated operation of the rotor-side converter and grid-side converter enabled efficient regulation of active and reactive power while maintaining a stable DC-link voltage across all tested scenarios.

The DC-link voltage analysis confirmed the effectiveness of the proposed control strategy in decoupling the renewable sources from the grid interface. Despite transient disturbances and fast environmental changes, the DC bus voltage remained close to its nominal value, highlighting the crucial role of the DC-link capacitor and the coordinated action of the converters in mitigating fluctuations and ensuring continuous power flow.

Furthermore, the power quality assessment validated the ability of the SRF-controlled GSC to inject high-quality current into the grid. Low total harmonic distortion, effective reactive power compensation, and balanced sinusoidal voltages were achieved in compliance with IEEE standards [21]. The results also revealed a strong correlation between the mechanical dynamics of the DFIG and the electrical performance of the system, emphasizing the importance of integrated electromechanical control in hybrid renewable energy systems.

Overall, this chapter confirms that the proposed hybrid PV–wind DFIG-based system provides a robust, efficient, and grid-compliant solution for renewable energy integration. The simplified topology, combined with effective MPPT and SRF control strategies, achieves high efficiency, stable operation, and improved power quality under a wide range of operating conditions. These findings establish a solid foundation for future research aimed at further enhancing the proposed system and extending its application toward real-time implementation and large-scale grid-connected renewable energy systems.

General Conclusion

This doctoral thesis has addressed the technical and scientific challenges related to the integration of renewable energy sources into the electrical grid through a comprehensive study of grid-connected photovoltaic systems, wind energy conversion systems, and hybrid photovoltaic-wind–wind architectures. The research was motivated by the increasing penetration of renewable generation in modern power systems and the resulting requirements for enhanced stability, improved power quality, and reliable operation under variable environmental and grid conditions. To respond to these challenges, the work adopted a progressive research methodology that moved from fundamental concepts and modeling approaches toward advanced system-level architectures and coordinated control strategies, leading to original contributions in the field of hybrid renewable energy integration.

The first chapter established the theoretical, technological, and contextual framework of the thesis by presenting the fundamental principles of renewable energy sources, with particular emphasis on photovoltaic and wind technologies. The chapter examined their historical development, operating principles, technological classifications, and deployment trends at both global and national levels, with a specific focus on the Algerian energy context. The limitations associated with single-source renewable systems were analyzed, highlighting intermittency, reduced availability, and grid integration challenges. This analysis justified the adoption of hybrid renewable energy systems as an effective solution to improve energy reliability, reduce carbon emissions, and enhance grid compatibility. The conceptual foundation developed in this chapter provided a consistent reference for the modeling, control, and comparative analyses carried out in the subsequent chapters.

The second chapter was dedicated to grid-connected photovoltaic systems and contributed an in-depth modeling and performance analysis of photovoltaic generators operating under realistic environmental conditions. The nonlinear behavior of PV cells and arrays was analyzed with respect to variations in solar irradiance, temperature, and partial shading conditions, emphasizing the critical role of accurate modeling and efficient maximum power point tracking. The chapter investigated a wide range of power conversion architectures, including single-stage and two-stage configurations, as well as various inverter topologies. Advanced control strategies based on synchronous reference frame theory and modern grid synchronization techniques were examined and validated through large-scale simulation studies. The results provided a clear understanding of the trade-offs between efficiency, dynamic response, and control complexity, forming a solid basis for integrating photovoltaic generation within hybrid renewable energy systems.

The third chapter addressed grid-connected wind energy conversion systems and presented a comprehensive analysis of wind turbine modeling, aerodynamic behavior, and electrical energy conversion. Both permanent magnet synchronous generator and doubly-fed induction generator technologies were presented and compared in terms of structure, control flexibility, and grid integration capability. The steady-state analysis and detailed system modeling were primarily developed for a permanent magnet synchronous generator-based wind energy system, which employed a generator-side rectifier controlled by direct power control and a grid-side three-level neutral point clamped inverter. The inverter was controlled using the

synchronous reference frame strategy and synchronized with the grid through a dual second-order generalized integrator phase-locked loop. Simulation results demonstrated stable steady-state operation, effective DC-link regulation, and high-quality grid current injection, establishing a robust reference framework for advanced wind energy systems. The comparative presentation of PMSG and DFIG technologies provided the necessary technical justification for the selection of the DFIG topology in the hybrid system investigated later in the thesis.

The main original contributions of this doctoral work were realized in the fourth chapter, which proposed and validated a grid-connected hybrid photovoltaic and wind energy system based on a doubly-fed induction generator. The hybrid architecture enabled coordinated energy coupling between the photovoltaic array and the wind energy conversion system through a common DC-link, allowing efficient power sharing while limiting conversion stages and associated losses. Maximum power point tracking algorithms were applied to both renewable sources, while synchronous reference frame-based control ensured decoupled regulation of active and reactive power and effective stabilization of the DC-link voltage. The coordinated operation of the rotor-side and grid-side converters allowed the hybrid system to maintain stable operation under dynamic conditions characterized by rapid variations in wind speed and solar irradiance.

Extensive simulation results confirmed the robustness and effectiveness of the proposed hybrid system under both steady-state and transient operating conditions. The doubly-fed induction generator operated reliably across hypo-synchronous, hyper-synchronous, and near-synchronous regimes, with smooth transitions between operating modes and stable electromechanical behavior. The DC-link voltage remained tightly regulated despite fast environmental fluctuations, demonstrating the effectiveness of the energy coupling strategy and coordinated converter control. Power quality analysis revealed low harmonic distortion, balanced grid currents, and effective reactive power compensation in compliance with IEEE standards. The results further highlighted the strong coupling between mechanical dynamics and electrical performance, emphasizing the importance of integrated electromechanical control in hybrid renewable energy systems.

Overall, this thesis has demonstrated that advanced grid-connected photovoltaic, wind, and hybrid photovoltaic-wind energy systems can achieve high efficiency, stable operation, and superior power quality when supported by appropriately designed power electronic interfaces and coordinated control strategies. The combined presentation of permanent magnet synchronous generator and doubly-fed induction generator technologies, followed by the development of a DFIG-based hybrid system, represents an original and coherent contribution to the field of renewable energy integration. The proposed architectures and control approaches provide a solid foundation for future research, including experimental validation, integration of energy storage systems, enhancement of fault ride-through capabilities, and real-time implementation within smart grid environments.

Perspectives of Future Work

The results obtained in this work confirm the technical relevance of advanced power electronic interfaces and coordinated control strategies for grid-connected photovoltaic and wind energy systems. Nevertheless, several research directions remain open and offer opportunities to further enhance system performance, reliability, and applicability in real-world power networks [85].

A first natural extension of this research concerns experimental validation. While detailed simulations provide valuable insight into system dynamics and control effectiveness, real-time implementation would allow the assessment of controller robustness under practical constraints such as sensor noise, switching nonlinearities, parameter drift, and computational delays. Hardware-based validation on laboratory-scale or pilot installations would strengthen confidence in the proposed architectures and facilitate their adoption in industrial renewable energy systems.

Another important perspective lies in the evolution of control methodologies. The synchronous reference frame strategy combined with classical regulators ensures stable operation and effective decoupling of active and reactive power. However, adaptive and predictive control approaches may offer superior performance in terms of transient response, disturbance rejection, and robustness to operating point variations. Intelligent control techniques based on optimization or learning principles could further enhance power tracking accuracy and dynamic stability under rapidly changing environmental conditions.

Additional research may also focus on a deeper and more unified treatment of wind energy conversion technologies. Although both permanent magnet synchronous generator and doubly-fed induction generator systems are presented and analyzed within this work, further investigation into their coordinated operation, comparative behavior, and integration within hybrid configurations would provide valuable insight. Such studies could clarify the respective advantages of each technology in terms of efficiency, controllability, grid support capability, and suitability for different operating regimes.

The integration of energy storage constitutes another promising direction. Incorporating battery systems or supercapacitors at the DC-link level would enable improved power smoothing, enhanced voltage regulation, and increased resilience against renewable intermittency. Advanced energy management strategies could be developed to coordinate photovoltaic generation, wind power, storage units, and grid exchange, thereby ensuring optimal system operation under variable climatic conditions and load demands.

A particularly important perspective concerns fault analysis and grid disturbance behavior in grid-connected hybrid PV–wind systems. The interaction of the proposed system with nonideal grid conditions, including voltage sags, swells, unbalance, frequency deviations, and harmonic distortion, requires a comprehensive investigation. Analyzing system response during grid faults and transient disturbances would allow the evaluation of fault ride-through capability, current limiting behavior, and DC-link stability. Special attention should be given to weak grid conditions and high renewable penetration scenarios, where impedance variation and resonance phenomena may significantly affect stability and power quality. Enhancing

control strategies to ensure compliance with modern grid codes under such disturbances would significantly improve the grid-supportive functionality of hybrid renewable energy systems.

Finally, extending the analysis toward reliability and economic aspects would further strengthen the practical relevance of this research. Evaluating converter losses, thermal stress, component aging, and maintenance requirements would provide a clearer picture of long-term system performance. Integrating techno-economic criteria into the design and control process would support the development of optimized hybrid renewable energy solutions that are not only technically efficient but also economically sustainable.

Annex I

Table 2-2 Electrical Characteristics of the Kyocera KD205GX-LP Module (STC).

Parameter	Value
Maximum Power P_{mpp}	*205W*
Voltage at MPP V_{mpp}	*26.3V*
Current at MPP I_{mpp}	*7.8A*
Open-Circuit Voltage V_{oc}	*32.9V*
Short-Circuit Current I_{sc}	*8.6A*
Temperature T	*25°C*

Table 2-3 Simulation parameters of the two-stage inverter.

Component	Parameter	Value
PV Array	Power P_{MPP}	*100kW*
Boost Converter	Switching Frequency f_s	*5kHz*
	Input Voltage V_{PV}	*290-300V*
	Output Voltage V_{DC}	*600 V*
	Boost inductor L_{in}	*≥ 1.45mH*
	Boost capacitor C_{in}	*1000µF*
	DC bus capacitor C_{dc}	*≥ 3227µF*
Inverter	Switching Frequency f_{sw}	*10kHz*
	Control Method	*SRF-dq*
SRF Controller	PI Gains (Current Loop)	K_p*=20,* K_i*=10*
	PI Gains (Voltage Loop)	K_p^{dc}*=300,* K_i^{dc}*=0.25*
PLL	PI Gains	K_p*=50000,* K_i*=10*
LCL Filter	Inductor L_f	*500µH*
	Capacitor C_f	*100µF*
Grid	Voltage (Phase-to-Phase)	*400V*
	Frequency f	*50Hz*

Table 2-4 Simulation parameters of single-stage inverter.

Component	Parameter	Value
PV Array	Power P_{MPP}	*100 kW*
	Operating Voltage V_{MPP}	*≈700V*
Inverter	Switching Frequency f_{sw}	*10kHz*
	Control Method	*SRF-INC*
MPPT	Algorithm	*Incremental Conductance*
SRF Controller	PI Gains (Current Loop)	K_p*=5000,* K_i*=3.33*
	PI Gains (Voltage Loop)	K_p^{dc}*=0.001,* K_i^{dc}*=0.25*
PLL	PI Gains	K_p*=50000,* K_i*=10*
LCL Filter	Inductor L_f	*500µH*
	Capacitor C_f	*100µF*
Grid	Voltage (Phase-to-Phase)	*400V*
	Frequency f	*50Hz*

Annex II

Table 3-2 Simultion parameters of wind system

Parameters		**Values**
Wind turbine	Blade radius R [m]	*3*
	Number of blades	*3*
	Nominal wind speed [m/s]	*14*
	Gearbox ratio G	*5.4*
	Moment of inertia J [$Kg.m^2$]	*0.042*
	friction coefficient F [N.m/s]	*0.017*
PMSG	Direct stator inductances L_d [mH]	*4.5*
	Quadrature stator inductances L_q [mH]	*4.5*
	Stator phase resistance R_{st} [Ω]	*0.021*
	Number of pole pairs p	*30*
	Flux linkage established by magnets [$V.s$]	*0.433*
Rectifier And DPC controller	Rectifier output DC bus capacitor C_r [μF]	*3227*
	The interfacing filter inductor L [mH]	*2*
	The interfacing filter resistor R [Ω]	*0.5*
	gains of PI regulator k_p and k_i	*0.4/3.5*
	The reference voltage V_{DC_ref} [V]	*720*
Inverter and SRF controller	Split DC-link capacitors C_i [μF]	*5600*
	Damping Resistor R_d (in series with C_i) [Ω]	*0.001*
	Rated Power P_i [kW]	*120*
	Switching frequency f_s [kHz]	*10*
	The step size of the INC algorithm: ΔV_{DC_ref}	*0.001*
	Current loop PI K_i / K_p	*3.33 / 5000*
	Voltage loop PI K_i^{dc}/ K_p^{dc}	*0.25 / 0.001*
	PLL PI K_i^{PLL}/ K_p^{PLL}	*10 / 50000*
Filter LCL	The inverter-side inductor L_i [μH]	*100*
	The grid-side inductor L_g [μH]	*500*
	The Capacitor C_f [μF]	*100*
	Damping Resistor R_f (in series with C_f) [Ω]	*0.3*

Annex III

Table 4-1 DFIG parameters.

Parameters	Valus
Stator supply voltage *Vs* [*V*]	*690*
Stator frequency *fs* [*Hz*]	*50*
Nominal power P_n [*MW*]	*2*
Synchronism N_n [*rev/min*]	*1500*
Stator resistance R_s [$m\Omega$]	*2.9*
Stator leakage inductance $L_{\sigma s}$ [*mH*]	*0.087*
Magnetizing inductance L_m [*mH*]	*2.5*
Friction coefficient *F* [*N m s/rad*]	1×10^{-3}
Number of pole pairs *p*	*2*
Rotor resistance R_r [$m\Omega$]	*2.6*
Rotor leakage inductance $L_{\sigma r}$ [*mH*]	*0.087*
The inertia of rotor *J* [kg/m^2]	*127*

Table 4-2 Simulation parameters of the hybrid PV–wind grid-connected system.

Parameters		Values
Electrical grid	Grid RMS voltage (phase to phase) V_{abc} [*V*]	*690*
	Grid frequency *f* [*Hz*]	*50*
PV array	Series-connected modules per string	*43*
	Parallel strings	*100*
	The voltage at maximum power in standard conditions V_{mp} [*V*]	*1144*
	Current at maximum power I_{mp} [*A*]	*771*
	Power rating P_{mp} [*KW*]	*882*
DC bus	Rated voltage V_{dc} [*V*]	*1150*
	Maximum allowable voltage ripple $\overline{V_{dc}}$ [*V*]	*23*
	Power rating P_r [*MW*]	*1.2*
	DC capacitance C_{dc} [*mF*]	*80*
RSC and controller	Input voltage V_r [*V*]	*2070*
	Output voltage V_{dc} [*V*]	*1150*
	Rate power at MP *P* [*KW*]	*200*
	Switching frequency f_s [*KHz*]	*4*
	Current PI regulator K_P^r/K_I^r	*0.58/492*
GSC and controller	Rated power *P* [*MW*]	*1.2*
	Switching frequency f_s [*KHz*]	*4*
	Current loop PI regulator K_p/K_I	*0.3/57*
	Voltage loop PI regulator K_P^{dc}/K_I^{dc}	*-1000/-60000*
	Proportional regulator K_p^I (virtual resistor)	*834*
Filter RL	Filter inductor L_f [μH]	*400*
	Filter resistor R_f [$\mu\Omega$]	*20*

Bibliography

[1] S. Benhalima, “Modélisation et Contrôle des Systèmes Éoliens-Solaire Intégrés au Réseau VSC-HVDC”, doctoral thesis, Higher Technology School University of QUEBEC, 2019.

[2] M. R. Bengourina, “Commande avancée d’un filtre actif parallèle en utilisant une approche méta-heuristique: application aux systèmes photovoltaïques interconnectes au réseau ”, doctoral thesis, University of Science and Technology of ORAN - MOHAMED BOUDIAF, 2020.

[3] M. Hallouz, “Contribution à l’amélioration de la commande de la machine asynchrone à double alimentation”, doctoral thesis, Yahia Fares University of MEDEA, 2023.

[4] A. Yahiaoui, “Commande, analyse et optimisation d’une chaine photovoltaique a base d’un convertisseur de puissance”, doctoral thesis, Yahia Fares University of MEDEA, 2017.

[5] A. Ben Jemaa, “Coopération méta heuristique et logique floue pour le dimensionnement d'une installation hybride”, doctoral thesis, University of REIMS CHAMPAGNE-ARDENNE, 2015.

[6] M. Bechouche Ali, “Utilisation des techniques avancées pour l’observation et la commande d’une machine asynchrone : Application à une éolienne”, doctoral thesis, Mouloud Mammeri University of TIZI–OUZOU, 2013.

[7] P. Feyel, “Optimisation des correcteurs par les métaheuristiques - Application à la stabilisation inertielle de ligne de visée”, doctoral thesis, CentraleSupélec- Paris-Saclay University, 2015.

[8] D Sal y Rosas, “Etude et conception de convertisseurs réversiblesmulti-sources isolés pour l’interfaçage au réseau de sources d’énergies renouvelables et de moyens de stockage”, doctoral thesis, Grenoble Alpes University, 2017.

[9] G. Denis, “From grid-following to grid-forming: The new strategy to build 100% power-electronics interfaced transmission system with enhanced transient behavior”, doctoral thesis, Central School of Lille, 2017.

[10] S. Kahla, “Modélisation et commande d’un système éolien”, doctoral thesis, 8 mai 1945 University of GUELMA, 2018.

[11] S. Phommixay, “Optimisation de coût de production de l'électricité dans un micro réseau électrique”, doctoral thesis, University of Quebec in Trois-Rivières, 2021.

[12] N. Aouchiche, “Conception d’une commande MPPT optimale à base d’intelligence artificielle d’un système photovoltaïque”, doctoral thesis, Bourgogne Franche-Comte University, 2020.

[13] R. Rouabhi,“Contrôle des puissances générées par un système éolien à vitesse variable basé sur une machine asynchrone double alimentée”, doctoral thesis, University of BATNA 2, 2016.

[14] H. Sahraoui, “Modélisation et commande des convertisseurs DC-DC utilisés dans les systèmes photovoltaïques (Théorie et Expérimentation)”, doctoral thesis, University of BATNA 2, 2016.

[15] J. G. Slootweg, “Wind Power: Modeling and Impact on Power System Dynamics”, doctoral thesis, Delft University of Technology, 2003.

[16] S. Saib, “Contribution à l’optimisation d’un système hybride (PV/éolien) avec stockage d’énergie connecté au réseau électrique”, doctoral thesis, Ferhat Abbas University of Setif 1, 2018.

[17] L. Stoyanov, “Etude de différentes structures de systèmes hybrides à sources d’énergie renouvelables”, doctoral thesis, Pascal Paoli University, 2011.

[18] I. Toumi, “Contribution à l’amélioration de performance d’une chaine énergétique hybride (éolienne/ photovoltaïque) basée sur des techniques d’intelligence artificielle ”, doctoral thesis, Kasdi Merbah University of Ouargla, 2023.

[19] Y. Sahri, “ Contribution à la commande non linéaire et à la gestion d’énergie d’un système hybride d’énergies renouvelables”, doctoral thesis, Ahmed Mira University of Bejaia, 2022.

[20] H. Boutelli, “ Etude d’un système hybride à sources d'énergie renouvelables dans la région de Ouargla : Application au pompage de l’eau ”, doctoral thesis, Kasdi Merbah University of Ouargla, 2023.

[21] "IEEE Standard for Harmonic Control in Electric Power Systems," in IEEE Std 519-2022 (Revision of IEEE Std 519-2014), vol., no., pp.1-31, 5 Aug. 2022, doi: 10.1109/IEEESTD.2022.9848440.

[22] T. Thomas, M. K. Mishra, C. Kumar, and M. Liserre, "Control of a PV-Wind Based DC Microgrid With Hybrid Energy Storage System Using Lyapunov Approach and Sliding Mode Control," in IEEE Transactions on Industry Applications, vol. 60, no. 2, pp. 3746-3758, March-April 2024, doi: 10.1109/TIA.2023.3349359.

[23] T. Senthilkumar, S.S. Sivaraju, V. Ranganayaki, and T. Anuradha, "Voltage-Fed single stage inverter for generating systems with Multi-Input inverter using Pulse Width Modulation," Sustainable Energy Technologies and Assessments, Volume 60, 2023, 103483, ISSN 2213-1388, https://doi.org/10.1016/j.seta.2023.103483.

[24] N. C. Alluraiah and P. Vijayapriya, "Optimization, Design, and Feasibility Analysis of a Grid-Integrated Hybrid AC/DC Microgrid System for Rural

Electrification," in IEEE Access, vol. 11, pp. 67013-67029, 2023, doi: 10.1109/ACCESS.2023.3291010.

[25] C. R. Jiménez Román, E. Hernández Mayoral, and M. Madrigal Martínez, "Experimental Comparison of the Different Switching Techniques applied to Back-to-Back Converter connected to DFIG-based Wind Turbine for Harmonic Analysis," in IEEE Latin America Transactions, vol. 21, no. 1, pp. 142-150, Jan. 2023, doi: 10.1109/TLA.2023.10015136.

[26] Akif Karafil, "Thinned-out controlled IC MPPT algorithm for class E resonant inverter with PV system," Ain Shams Engineering Journal, Volume 14, Issue 5, 2023, 101992, ISSN 2090-4479, https://doi.org/10.1016/j.asej.2022.101992.

[27] Boni Satya Varun Sai, Rupali Mohanty, Satyajit Mohanty, Debashis Chatterjee, C. Dhanamjayulu, Ravikumar Chinthaginjala, Hossam Kotb, and Ali Elrashidi, "An efficient MPPT techniques for inter-harmonic reduction in grid-connected hybrid wind and solar energy systems," Heliyon, Volume 10, Issue 5,2024, e27312, ISSN 2405-8440, https://doi.org/10.1016/j.heliyon.2024.e27312.

[28] Mihir Mehta and Bhinal Mehta, "Control strategies for grid-connected hybrid renewable energy systems: Integrating modified direct torque control based doubly fed induction generator and ANFIS based maximum power point tracking for solar PV generation," e-Prime - Advances in Electrical Engineering, Electronics and Energy, Volume 8, 2024, 100575, ISSN 2772-6711, https://doi.org/10.1016/j.prime.2024.100575.

[29] F. M. A. Hadi and H. H. Aly, "Harmonics Forecasting of Renewable Energy System Using Hybrid Model Based on LSTM and ANFIS," in IEEE Access, vol. 12, pp. 50966-50985, 2024, doi: 10.1109/ACCESS.2024.3386092.

[30] R. Tharwin Kumar and C. Christober Asir Rajan, "Integration of hybrid PV-wind system for electric vehicle charging: Towards a sustainable future," e-Prime - Advances in Electrical Engineering, Electronics and Energy, Volume 6, 2023, 100347, ISSN 2772-6711, https://doi.org/10.1016/j.prime.2023.100347.

[31] F. M. A. Hadi, H. H. Aly, and T. Little, "Harmonics Forecasting of Wind and Solar Hybrid Model Based on Deep Machine Learning," in IEEE Access, vol. 11, pp. 100438-100457, 2023, doi: 10.1109/ACCESS.2023.3314742.

[32] A. Benali, M. Khiat, T. Allaoui, and M. Denaï, "Power Quality Improvement and Low Voltage Ride Through Capability in Hybrid Wind-PV Farms Grid-Connected Using Dynamic Voltage Restorer," in IEEE Access, vol. 6, pp. 68634-68648, 2018, doi: 10.1109/ACCESS.2018.2878493.

[33] A. Renjith, and P. Selvam, "Efficient maximum power tracking technique in grid-connected PV-wind system," Electric Power Systems Research, Volume 214, Part B, 2023, 108955, ISSN 0378-7796, https://doi.org/10.1016/j.epsr.2022.108955.

[34] Arjun Kumar, Shivashankar, and Keshavamurthy, "Design and control of autonomous hybrid wind solar system with DFIG supplying three-phase four-wire loads," Ain Shams Engineering Journal, Volume 12, Issue 3, 2021, Pages 2875-2890, ISSN 2090-4479, https://doi.org/10.1016/j.asej.2020.11.027.

[35] Korhan Kayisli, "Super twisting sliding mode-type 2 fuzzy MPPT control of solar PV system with parameter optimization under variable irradiance conditions," Ain Shams Engineering Journal, Volume 14, Issue 1, 2023, 101950, ISSN 2090-4479, https://doi.org/10.1016/j.asej.2022.101950.

[36] A. G. Paspatis, and G. C. Konstantopoulos, "SRF-based Current-Limiting Droop Controller for Three-Phase Grid-Tied Inverters," IECON 2018 - 44th Annual Conference of the IEEE Industrial Electronics Society, Washington, DC, USA, 2018, pp. 282-287, doi: 10.1109/IECON.2018.8591676.

[37] M. E. Benzoubir, A. Lashab, K. Rayane, M. Benmiloud, M. Bougrine, and A. Benalia, "Improved Performance and Voltage Stability of Islanded Inverters Using Single-Loop PI-Lead Controller," in IEEE Access, vol. 13, pp. 23851-23865, 2025, doi: 10.1109/ACCESS.2025.3537716.

[38] A. Al-Jodah and M. Alwan, "Robust Speed Control Methodology for Variable Speed Wind Turbines," 2021 11th IEEE International Conference on Control System, Computing and Engineering (ICCSCE), Penang, Malaysia, 2021, pp. 1-6, doi: 10.1109/ICCSCE52189.2021.9530958.

[39] H. Alghamdi, S. Ullah, A. Ali, G. Hafeez, L. Guanghua, and A. Ullah, "Variable-Gain Robust Exact Differentiator-Based Neuro-Adaptive Control Design for Dynamic Wind Power Optimization," in IEEE Access, vol. 12, pp. 2186-2197, 2024, doi: 10.1109/ACCESS.2023.3344451.

[40] J. Samanes, E. Gubia, J. Lopez, and R. Burgos, "Sub-Synchronous Resonance Damping Control Strategy for DFIG Wind Turbines," in IEEE Access, vol. 8, pp. 223359-223372, 2020, doi: 10.1109/ACCESS.2020.3043818.

[41] Y. Mchaouar, Y. Abouelmahjoub, A. Abouloifa, H. Abouobaida, A. Chellakhi, I. Lachkar, F. Giri, A. Elalli, C. Taghzaoui, S. El Beid, "Nonlinear control of single stage grid-tied photovoltaic systems based on a 3L-NPC topology," IFAC-PapersOnLine, Volume 55, Issue 12, 2022, Pages 538-543, ISSN 2405-8963, https://doi.org/10.1016/j.ifacol.2022.07.367.

[42] N. Kacimi, A. Idir, S. Grouni, and M. S. Boucherit, "Improved MPPT Control Strategy for PV Connected to Grid Using IncCond-PSO-MPC Approach," in CSEE Journal of Power and Energy Systems, vol. 9, no. 3, pp. 1008-1020, May 2023, doi: 10.17775/CSEEJPES.2021.08810.

[43] N. Güler and E. Irmak, "MPPT Based Model Predictive Control of Grid-Connected Inverter for PV Systems," 2019 8th International Conference on Renewable Energy Research and Applications (ICRERA), Brasov, Romania, 2019, pp. 982-986, doi: 10.1109/ICRERA47325.2019.8997105.

[44] B. Zhang, X. Du, J. Zhao, J. Zhou, and X. Zou, "Impedance modeling and stability analysis of a three-phase three-level NPC inverter connected to the grid," in CSEE Journal of Power and Energy Systems, vol. 6, no. 2, pp. 270-278, June 2020, doi: 10.17775/CSEEJPES.2019.02620.

[45] **F. Hadj Mihoub Sidi Moussa**, A. Morsli, A. Tlemçani, H. Belmili, and H. Nouri, "Performance Evaluation and Comparative Study of Single and Two Stages

Inverters Used in Grid-Connected Photovoltaic Systems," 2024 2nd International Conference on Electrical Engineering and Automatic Control (ICEEAC), Setif, Algeria, 2024, pp. 1-6, doi: 10.1109/ICEEAC61226.2024.10576442.

[46] **F. Hadj Mihoub Sidi Moussa**, A. Morsli, A. Tlemçani, H. Belmili, and H. Nouri, "A Comparison Analysis between Two and Three Levels Inverter to Grid-Connected Used the Photovoltaic System," 2023 2nd International Conference on Electronics, Energy and Measurement (IC2EM), Medea, Algeria, 2023, pp. 1-6, doi: 10.1109/IC2EM59347.2023.10419754.

[47] A. Morsli, A. Tlemcani, and H. Nouri, "Control of a shunt active power filter by the synchronous referential method connected with a photovoltaic solar energy", Nonlinear Dynamics and Systems Theory, vol. 22, no. 4, pp. 424-431, Oct 2022.

[48] M. Badoni, A. Singh, A. K. Singh, H. Saxena, and R. Kumar, "Grid Tied Solar PV System with Power Quality Enhancement Using Adaptive Generalized Maximum Versoria Criterion," in CSEE Journal of Power and Energy Systems, vol. 9, no. 2, pp. 722-732, March 2023, doi: 10.17775/CSEEJPES.2020.04820.

[49] I. U. Haq, Q. Khan, I. Khan, R. Akmeliawati, K. S. Nisar and I. Khan, "Maximum Power Extraction Strategy for Variable Speed Wind Turbine System via Neuro-Adaptive Generalized Global Sliding Mode Controller," in IEEE Access, vol. 8, pp. 128536-128547, 2020, doi: 10.1109/ACCESS.2020.2966053.

[50] Younes Sahri, Salah Tamalouzt, Sofia Lalouni Belaid, Mohit Bajaj, Sherif S.M. Ghoneim, Hossam M. Zawbaa, and Salah Kamel, "Performance improvement of Hybrid System based DFIG-Wind/PV/Batteries connected to DC and AC grid by applying Intelligent Control," Energy Reports, Volume 9, 2023, Pages 2027-2043, ISSN 2352-4847, https://doi.org/10.1016/j.egyr.2023.01.021.

[51] Jinmu Lai, Yang Liu, Xin Yin, Yaoqiang Wang, Jiaxuan Hu, Xianggen Yin, and Keliang Zhou, "A novel hybrid interlinking transformer-integrated DFIG wind power and energy storage system with flexible control strategy," International Journal of Electrical Power & Energy Systems, Volume 168, 2025, 110641, ISSN 0142-0615, https://doi.org/10.1016/j.ijepes.2025.110641.

[52] S. Kumar Tiwari, B. Singh, and P. K. Goel, "Design and Control of Micro-grid Fed by Renewable Energy Generating Sources," in IEEE Transactions on Industry Applications, vol. 54, no. 3, pp. 2041-2050, May-June 2018, doi: 10.1109/TIA.2018.2793213.

[53] B. Pangedaiah, Y. P. Obulesu, and Venkata Reddy Kota, "New Architecture Topology for Back-to-Back Grid-Connected Hybrid Wind and PV System," Journal of Electrical Engineering & Technology, Volume 16, Pages 1457–1467, 2021, https://doi.org/10.1007/s42835-021-00685-w.

[54] G. B. Arjun Kumar and Shivashankar, "Optimal power point tracking of solar and wind energy in a hybrid wind solar energy system," International Journal of Energy and Environmental Engineering, Volume 13, Pages 77–103, 2022. https://doi.org/10.1007/s40095-021-00399-9.

[55] Y. Kebbati, and L. Baghli, "Design, modeling and control of a hybrid grid-connected photovoltaic-wind system for the region of Adrar, Algeria," International Journal of Environmental Science and Technology, Volume 20, Pages 6531–6558, 2023, https://doi.org/10.1007/s13762-022-04426-y.

[56] Saheb Ghanbari Motlagh, Fatemeh Razi Astaraei, Mohammad Montazeri, Mohsen Bayat, "COVID-19 impact on wind and solar energy sector and cost of energy prediction based on machine learning," Heliyon, Volume 10, Issue 17, 2024, e36662, ISSN 2405-8440, https://doi.org/10.1016/j.heliyon.2024.e36662.

[57] Chong Xu, Yuchen Gao, Zengqiang Qin, Zhiwen Li, Shaojie Pan, and Linlin Qi, "Historical characteristics and projection of global renewable energy consumption," Renewable Energy, Volume 234, 2024, 121222, ISSN 0960-1481, https://doi.org/10.1016/j.renene.2024.121222.

[58] M. Sarvi, A. Azadian, "A comprehensive review and classified comparison of MPPT algorithms in PV systems," Energy Systems, Volume 13, Pages 281–320, 2022, https://doi.org/10.1007/s12667-021-00427-x.

[59] X. Zhang, Y. Zhang, R. Fang, and D. Xu, "Impedance Modeling and SSR Analysis of DFIG Using Complex Vector Theory," in IEEE Access, vol. 7, pp. 155860-155870, 2019, doi: 10.1109/ACCESS.2019.2949198.

[60] M. W. K. Mbukani and N. Gule, "PLL-Based Sliding Mode Observer Estimators for Sensorless Control of Rotor-Tied DFIG Systems," in IEEE Transactions on Industry Applications, vol. 55, no. 6, pp. 5960-5970, Nov.-Dec. 2019, doi: 10.1109/TIA.2019.2931970.

[61] A. Vasanth, and V. Sheeja, “Comparative analysis of SRF, PI and AWPI controllers for hybrid standalone microgrid,” IEEE International Conference on Power Electronics and Renewable Energy Applications (PEREA), IEEE, 2020, pp. 1-6.

[62] L. Chen, A. Amirahmadi, Q. Zhang, N. Kutkut, and I. Batarseh, “Design and implementation of three-phase two-stage grid-connected module integrated converter, ” IEEE Transactions On Power Electronics, vol.29, No.8, pp.3881-3892, Aug. 2014.

[63] D. Saravanan, D. Singh, S. Sinha, R. Nath Shaw, and K. Prabu, “A comprehensive study of well-known maximum power point tracking techniques, ” IEEE

International Conference on Computing, Power and Communication Technologies (GUCON), Galgotias University, Greater Noida, UP, India. Oct 2-4, 2020.

[64] K. Kalyan Kumar, R. Bhaskar, and H. Koti, "Implementation of MPPT algorithm for solar photovoltaic cell by comparing short-circuit method and incremental conductance method," The 7th International Conference Interdisciplinarity in Engineering, Procedia Technology,2014, pp. 705 – 715.

[65] A. Loukriz, M. Haddadi, and S. Messalti, "Simulation and experimental design of a new advanced variable step size incremental conductance MPPT algorithm for PV systems," ISA Transactions, Elsevier, Vol 62, pp. 30-38, May 2016.

[66] F. Lahouar, J. Ben Hadj Slama, M. Hamouda, and F.Ben Mustapha, "Comparative study between two and three-level topologies of grid-connected photovoltaic converters," in Proceedings of the 5th International Renewable Energy Congress (IREC), IEEE, Hammamet, Tunisia, 2014, pp. 1–6.

[67] D. Gurav Rutuja, B. Morey Suryakant, and P. M. Joshi, "3-Ph 2-level VSI with sinusoidal pulse width modulation," 3rd International Conference for Convergence in Technology, Pune, India, pp. 1-4, Apr 06-08. 2018.

[68] G. Jani Rushiraj, and P. N. Kapil, "Analysis of different modulation techniques for multilevel inverters," International Conference on Electrical, Electronics, and Optimization Techniques, 2016, pp.3017-3022.

[69] X. Liu, Z. Chen, and W. Wang, "Optimized LCL filter design for grid-connected photovoltaic inverters," IEEE Transactions on Power Electronics, vol. 35, no. 4, pp. 1205–1214, 2021.

[70] J. Wu, F. Zhuo, and H. Wang, "An improved damping method for LCL-filtered single-phase grid-tied inverters," in Proc. IEEE Energy Conversion Congress and Exposition (ECCE), Atlanta, GA, USA, 2020.

[71] R. K. Singh and A. K. Gupta, "Harmonic attenuation using passive LCL filters in single-stage PV inverters," IEEE Journal of Emerging and Selected Topics in Power Electronics, vol. 8, no. 2, pp. 945–955, 2020.

[72] Q. Zhang, Y. Zhang, and J. Yang, "A new approach to parameter optimization for LCL filters in single-phase PV inverters," IEEE Access, vol. 7, pp. 105421–105430, 2019.

[73] J. Wu, Y. Zhang, and J. Yang, "Design and optimization of LCL filters for grid-connected PV inverters," IEEE Transactions on Power Electronics, vol. 36, no. 7, pp. 8111–8123, July 2021.

[74] S. S. A. H. Sadeghi, S. S. G. H. Shabani, and A. B. R. M. Sharifian, “A novel passive damping strategy for LCL filters in three-phase grid-connected photovoltaic inverters,” IEEE Transactions on Industrial Electronics, vol. 69, no. 4, pp. 4125–4136, Apr. 2022.

[75] Q. Zhang, Y. Li, and X. Yuan, “Design of LCL filters for high-efficiency grid-connected photovoltaic inverters,” IEEE Journal of Emerging and Selected Topics in Power Electronics, vol. 9, no. 3, pp. 1604–1616, Sept. 2021.

[76] H. C. Chiu, Y. L. Hsu, and K. Y. Hsiao, “Optimization of LCL filter design for three-phase grid-connected photovoltaic inverters considering harmonics and cost,” IEEE Transactions on Sustainable Energy, vol. 12, no. 2, pp. 1453–1464, Apr. 2021.

[77] J. Zhang and X. Zhang, “Harmonic reduction in three-phase grid-connected PV systems with LCL filters: A practical approach,” IEEE Transactions on Energy Conversion, vol. 35, no. 5, pp. 2101–2110, May 2020.

[78] H. Wang, Z. Chen, and Y. Liu, ”A robust design method for LCL filters in photovoltaic grid-connected inverters,” IEEE Transactions on Industrial Electronics, vol. 68, no. 2, pp. 1234–1243, Feb. 2021.

[79] R. A. Muhammed and D. Sulaiman, “Particle Swarm Optimization (PSO) Based MPPT Controller Modeling and Design of Photovoltaic Modules, ” Majlesi Journal of Electrical Engineering, vol. 16, no. 4, pp. 45–52, 2022.

[80] N. F. Ibrahim, M. M. Mahmoud, M. H. Al Thaiban Ali, A. B. Barnawi, Z. M. S. Elbarbary, and A. I. Omar, “Operation of Grid-Connected PV System With ANN-Based MPPT and an Optimized LCL Filter Using GRG Algorithm for Enhanced Power Quality,” in IEEE Access, vol. 11, pp. 106859-106876, 2023.

[81] B. Fekkak, M. Menaa, A. Loukriz, and A. Kouzou, “Control of grid-connected PMSG-based wind turbine system with back-to-back converters topology using a new PIL integration method,” Int Trans Electr Energ Syst,e12882, 2021.

[82] M. Rahimi, “Modeling, control and stability analysis of grid-connected PMSG based wind turbine assisted with diode rectifier and boost converter, ” International Journal of Electrical Power & Energy Systems, vol. 93, pp. 84-96, 2017.

[83] M. Moumna, R. Taleb, and Z. Boudjema, “Output voltage control of a PMSG with the DPC-SVM technique and high-order sliding mode,” Indonesian Journal of Electrical Engineering and Computer Science, vol. 23, no.2, pp. 772-781, 2021.

[84] H. Salime, B. Bossoufi, S. Motahhir, and Y. El Mourabit, A novel combined FFOC-DPC control for wind turbine based on the permanent magnet synchronous generator, Energy Reports, vol. 9, pp. 3204-3221, 2023.

[85] **F. Hadj Mihoub Sidi Moussa**, A. Morsli, and A. Tlemçani, "Optimized grid-connected hybrid PV-wind system with DFIG-based and advanced control strategies for dynamic power quality and grid stability", Wind Engineering. 2025, doi:10.1177/0309524X251391968.

[86] Bloomberg New Energy Finance, Energy Transition Investment Trends 2025: Tracking global investment in the low-carbon transition, Jan. 30, 2025. https://data.bloomberglp.com/professional/sites/24/951623_BNEF-Energy-Transition-Trends-2025-Abridged.pdf.

[87] Global Wind Energy Council, Global Wind Report 2025, Global Wind Energy Council, Brussels, Belgium, 2025. https://www.gwec.net/reports

[88] International Renewable Energy Agency and International Labour Organization, Renewable Energy and Jobs: Annual Review 2024, Abu Dhabi/Geneva,Oct.2024. https://www.irena.org/Publications/2024/Oct/Renewable-energy-and-jobs-Annual-review-2024

[89] D. Rekioua, Wind Power Electric, Green Energy and Technology series, London, UK: Springer, 2017.

[90] A. Keyhani, Design of Smart Power Grid Renewable Energy Systems, Hoboken, NJ, USA: John Wiley & Sons, Inc., 2011, ISBN: 978-0470-62761-7.

[91] Y. Yang, K. A. Kim, F. Blaabjerg, and A. Sangwongwanich, Advances in Grid-Connected Photovoltaic Power Conversion Systems. Cambridge, UK: Woodhead Publishing, 2018, Woodhead Publishing Series in Energy, ISBN: 9780128032121.

[92] G. Abad, J. López, M. A. Rodríguez, L. Marroyo, and G. Iwanski, Doubly Fed Induction Machine: Modeling and Control for Wind Energy Generation. Hoboken, NJ, USA: John Wiley & Sons, 2011, ISBN: 978-0-470-76865-5.

[93] H. Abu-Rub, M. Malinowski, and K. Al-Haddad, Power Electronics for Renewable Energy Systems, Transportation and Industrial Applications, 1st ed. Hoboken, NJ, USA: Wiley-IEEE Press, 2014, ISBN: 978-1-118-63403-5.